

Deutsches Zentrum
für Luft- und Raumfahrt e.V.

Forschungsbericht 2004-05

Comparison of polarimetric methods
in image classification and
SAR interferometry applications

Vito Alberga

Institut für Hochfrequenztechnik
und Radarsysteme
Oberpfaffenhofen



Comparison of polarimetric methods in image classification and SAR interferometry applications

Vito Alberga

Institut für Hochfrequenztechnik
und Radarsysteme
Oberpfaffenhofen

171 Seiten
49 Bilder
87 Tabellen
90 Literaturstellen

Comparison of polarimetric methods in image classification and SAR interferometry applications

Zur Erlangung des akademischen Grades eines
Doktoringenieurs (Dr.-Ing.)
von der Fakultät für Elektrotechnik und Informationstechnik
der Technischen Universität Chemnitz
genehmigte Dissertation von

Dott. Vito Alberga

Referent: Prof. Dr.-Ing. G. Wanielik
Korreferent: Prof. Dr. M. Chandra
Korreferent: Dr. E. Krogager

Tag der Einreichung: 29. Juli 2003
Tag der mündlichen Prüfung: 23. Januar 2004

Abstract

In this thesis, an analysis of the various parameters derivable from polarimetric SAR measurements is reported. The theory related to polarimetry and the state of the art of its application to remote sensing of the Earth by means of SAR systems are thoroughly discussed.

The experimental part of this work pursues the task of analyzing all the relevant polarimetric parameters. In the first part of the thesis, a systematic study of the different ways of examining polarimetric data has been performed. The main aim was to evaluate possible differences among the various polarimetric observables and the amount and usefulness of the information they contain. In this context, these observables have been compared by means of the accuracy estimates resulting from classification tests of real polarimetric SAR data. In the analysis proposed here, such accuracy estimates act as an objective measure of the “utility” of the observables.

In the second part, some of the aforementioned polarimetric observables have been used for interferometric applications. The main objective was to determine if a characterization of volume scattering, one of the terms affecting the interferometric coherence, is possible. Once again a comparison of the selected parameters has been done in terms of their capability to reduce the effects of volume scattering in interferometric coherence images.

Since this work is intended as a general survey of polarimetric observables, completeness has been an important goal, which the author hopes to have achieved. The twofold view of the investigations reported here, oriented both to classification and interferometry, contributes to a comprehensive understanding of the parameters under study.

Keywords: Radar imaging, synthetic aperture radar (SAR), SAR polarimetry, SAR interferometry, polarimetric SAR interferometry, image classification.

Kurzfassung

In dieser Arbeit wird über die Analyse von unterschiedlichen Parametern, ermittelt vom polarimetrischen SAR, berichtet. Die Theorie der Polarimetrie und der Stand der Technik in der Radarfernerkundung der Erdoberfläche, die auf SAR-Systemen beruht, ist gründlich dargestellt.

Der experimentelle Anteil dieser Arbeit beinhaltet die Analyse von allen relevanten polarimetrischen Parametern. Der erste Teil ist eine systematische Untersuchung von polarimetrischen Daten, wobei unterschiedliche Wege analysiert werden. Die Hauptaufgabe besteht darin, sowohl die möglichen Unterschiede zwischen den verschiedenen Eingangsparametern als auch die Anzahl von Parametern und deren Nutzen zur Informationsgewinnung zu untersuchen. Demzufolge wurden die Eingangsparameter hinsichtlich ihrer Klassifikationsgenauigkeit auf vorhandene SAR Daten verglichen. In der vorgeschlagenen Untersuchung stellen die Genauigkeitsanalysen ein objektives Kriterium für den sogenannten “Nutzen” der Eingangsparameter dar.

Im zweiten Teil wurden die zuvor genannten polarimetrischen Eingangsparameter für die interferometrische Anwendung eingesetzt. Im Vordergrund stand die Bestimmung der Volumenstreuung und deren Einfluss auf eines der Elemente der interferometrischen Kohärenz. Auch hier fand ein Vergleich der ausgesuchten Parameter in Bezug auf ihre Fähigkeit, den Effekt der Volumenstreuung in der interferometrischen Kohärenz zu reduzieren, statt.

Diese Arbeit möchte eine allgemeine Erfassung von polarimetrischen Eingangsparametern geben, wobei ein wichtiger Punkt, vom Autor hoffentlich erreicht, die Vollständigkeit ist. Die doppelte Sicht der vorgestellten Untersuchungen, angelehnt an die Polarimetrie und Interferometrie, trägt zu einem umfassenden Verständnis der Parameter in dieser Arbeit bei.

Stichworte: Abbildendes Radar, Synthetisches Apertur Radar (SAR), SAR-Polarimetrie, SAR-Interferometrie, Polarimetrische SAR-Interferometrie, Klassifikation.

“Tan cerca que tu mano sobre mi pecho es mía”
Pablo Neruda

“...It’s never over,
My kingdom for a kiss upon her shoulder
It’s never over,
All my riches for her smiles when I slept so soft against her
It’s never over,
All my blood for the sweetness of her laughter...”
Jeff Buckley

Acknowledgements

This is a report of the work done during the period from 1999 to 2002 at the Microwaves and Radar Institute of the German Aerospace Centre (DLR) in Oberpfaffenhofen, Germany.

The results here collected would have not been possible without the help of a great number of people. Foremost, I am indebted to my advisors Prof. Madhu Chandra and Prof. Gerd Wanielik from the Technical University of Chemnitz. The former was my group leader at DLR during my first three years there in the frame of the EU funded Training and Mobility of Researchers (TMR) project that he directed. He accepted the application for a pre-doc position from a guy from a never-heard-of-before town in Southern Italy and supported his work with a lot of “*a priori*” trust in his capabilities. I am very grateful for that. The latter agreed to take me as PhD fellow and gave me the chance to make further profit of my work in Oberpfaffenhofen.

Sincere thanks to the people that permitted and sustained my stay at DLR: Dr. Wolfgang Keydel and Prof. Alberto Moreira that followed each other as directors of the Institute and always guaranteed their support; Dr. David Hounam and Rudi Schmid, who practically took charge of my position within the EU project and Marian Werner who offered me the opportunity of a new interesting job and to complete this thesis.

I wish to thank those people who helped me in revising the manuscript and who taught me, or at least tried to teach me, something (my ability in forgetting things is astonishing!): Dr. Ernst Lüneburg for carefully going through the whole work and fundamentally influencing its writing, I regret I could not follow all his suggestions for further research, we should have started our collaboration earlier; Dr. José Luis Álvarez-Pérez, “Padre Álvarez”, for his kindness and attention, I almost do not remember a single “I don’t know” or “I can’t help you” from him; Dr. Kostas Papathanassiou, for his explanations on polarimetric SAR, interferometry and penguin hunting, he also gave me several practical suggestions regarding this and other works; Dr. Jürgen Holzner for his comments on the chapter on interferometry; Dr. Eleni Paliouras for a final English grammar check. Thanks also to Dr. Ernst Krogager from the Danish Defence Research Establishment (DDRE) in Copenhagen and to Dr. William Cameron from Boeing Defence and Space Group in Seattle for the discussions on target decomposition theory.

A special thank goes to Annette Wächter, Luis Ruby, Andrea Pelizzari and Dr. Katja Lamprecht for their German first-aid help, to Marco Quartulli and Herbert Daschiel for technical troubleshooting and for their company at coffee breaks and to Luca Pipia from the University of Cagliari (Italy, not Canada!), who tolerated me as graduation thesis supervisor, for the long talks on science and other (less “noble”) subjects.

Thanks to Dr. Irena Hajnsek for providing me with some figures, to Ralf Horn for the picture of the DLR aeroplane and to Dr. Valeria Radicci from the University of Bari for helping me in formatting them. I am also grateful to Birgit Wilhelm for saving data, burning CDs, printing slides, etc. on many occasions and to Laura Carrea (Technical University of Chemnitz) for solving all the bureaucratic questions concerning the presentation of this work and the academic title.

A mention is worth for Prof. Francesco Posa from the University of Bari and for Alma Blonda and Giuseppe Satalino from the Institute of Intelligent Systems for Automation (ISSIA) of the National Research Council (CNR) in Bari, through them I was introduced to remote sensing and image classification: everything started with them.

I do not want to forget those people that “simply” offered me their friendship, or more, during this adventure abroad: Sonia, Silvia, Antonio, Millah, Zsófi, Dani, Sandro, Ana Paula, Kais, Sara, Andrea, Christine, Paolo, José, Rafael, Josef, Adele, Licio, Axel, Sascha, Michael, Heike, Ewan, Carlos, Emiliano (I really hope nobody is missing).

Alla mia famiglia va la mia gratitudine per avermi sempre e comunque appoggiato.

Thanks, again, to everybody,

Wolf

Contents

1	Introduction	1
2	Foundations of radar polarimetry	7
2.1	Description of electromagnetic waves	7
2.2	Scattering of electromagnetic waves	16
2.3	Change-of-basis theory and characteristic polarizations	19
2.4	Scattering vectors and second order matrices	23
2.5	Target decomposition theorems	26
3	SAR polarimetry	31
3.1	Basics	31
3.1.1	SAR sensors	31
3.1.2	Early experimental results	32
3.1.3	Calibration techniques	34
3.2	Interactions with the Earth surface	35
3.3	Entropy/ α analysis	37
3.4	Polarimetric SAR interferometry	40
4	Analysis of polarimetric parameters: image classification	47
4.1	Introduction	47
4.2	Classification theory and accuracy assessment	48
4.2.1	Classification theory basics	48
4.2.2	Parallelepiped classification	49
4.2.3	Maximum likelihood classification	50
4.2.4	Minimum distance classification	52
4.2.5	Classification accuracy assessment	52
4.3	Overview on polarimetric parameters	54
4.4	Experimental approach	55
4.5	Data sets and test areas	56
4.6	Backscattered wave amplitude	59

4.7	Ratios of the scattering matrix elements	61
4.8	Characteristic polarizations	64
4.9	Parameters of the coherent target decomposition theorems	66
4.10	Entropy/ α parameters	71
4.11	Comparisons and conclusions	76
5	Analysis of polarimetric parameters: interferometry	79
5.1	Overview	79
5.2	Theoretical aspects	79
5.2.1	Interferograms generation	80
5.2.2	Decorrelation sources	83
5.2.3	Interferometric coherence enhancement	84
5.3	Interferometric coherence analysis	88
5.3.1	General correlation properties	88
5.3.2	Volume decorrelation	95
5.4	Interferometric phase analysis	98
5.5	Final considerations	105
6	Conclusions	107
A	Relationships among polarization geometrical parameters	109
B	Target decomposition theorems	113
B.1	Krogager decomposition	113
B.2	Cameron decomposition	115
C	Classification results	119
C.1	Backscattered wave amplitude	120
C.2	Characteristic polarizations	126
C.3	Parameters of the coherent target decomposition theorems	132
C.4	Entropy/ α parameters	150
	Bibliography	163

List of Figures

1.1	Overview of spaceborne SAR missions.	3
2.1	General bistatic scattering geometry and local coordinate systems.	10
2.2	Detailed view of the transmitting local coordinate system, with projection in the $\hat{h}_1\hat{v}_1$ -plane of the track described by the tip of the \vec{E}_T vector (with the hypothesis that the relative phase δ_T of the electric field components is different from 0).	11
2.3	Polarization ellipse.	12
2.4	The Poincaré sphere.	14
2.5	The Deschamps sphere.	15
3.1	SAR imaging geometry.	32
3.2	Scattering behaviour relative to: (a) smooth, (b) rough, (c) very rough surfaces (courtesy of I. Hajnsek [Haj01]).	36
3.3	Diagram for determining the phase difference between two parallel waves scattered from different points on a rough surface (courtesy of I. Hajnsek [Haj01]).	36
3.4	Scheme of the α angle interpretation.	39
3.5	H/α plane.	40
3.6	Interferometric SAR imaging geometry.	41
3.7	Interferometric SAR imaging creation (courtesy of M. Quartulli [Qua98]).	42
4.1	The DLR Dornier DO 228-212 aircraft and the displacement of the different SAR antennae mounted on board (courtesy of R. Horn).	57
4.2	Optical picture of the Oberpfaffenhofen test site (the yellow rectangle defines the area corresponding to the SAR data).	58
4.3	Accuracy estimation of the classification tests based on the amplitudes of the three $[S]$ matrix elements: (a) overall accuracy; (b) Kappa (October '99).	59
4.4	Classification maps based on the amplitudes of the three $[S]$ matrix elements (15×15 -pixel averaging window): (a) maximum likelihood; (b) minimum distance; (c) parallelepiped (October '99).	60
4.5	ZDR image of the Oberpfaffenhofen test site (October '99).	62

4.6	Mean values and standard deviations of the polarization ratios in the selected regions of interest: (a) Munich; (b) Oberpfaffenhofen (October '99). The ratios have been calculated, respectively, for the values relative to a 5×5 -pixel averaging window and on a single-pixel basis.	63
4.7	Accuracy estimation of the classification tests based on the co- and cross-polar nulls terms: (a) overall accuracy; (b) Kappa (October '99). . .	64
4.8	Classification maps based on the co- and cross-polar nulls terms (15×15 -pixel averaging window): (a) maximum likelihood; (b) minimum distance; (c) parallelepiped (October '99).	65
4.9	Accuracy estimation of the classification tests based on the three coefficients of the Krogager decomposition: (a) overall accuracy; (b) Kappa (October '99).	66
4.10	Accuracy estimation of the classification tests based on the three coefficients of the Pauli decomposition: (a) overall accuracy; (b) Kappa (October '99).	67
4.11	Accuracy estimation of the classification tests based on the norm of the two scattering vectors representing the Cameron decomposition terms: (a) overall accuracy; (b) Kappa (October '99).	67
4.12	Classification maps based on the Krogager decomposition terms (15×15 -pixel averaging window): (a) maximum likelihood; (b) minimum distance; (c) parallelepiped (October '99).	68
4.13	Classification maps based on the Pauli decomposition terms (15×15 -pixel averaging window): (a) maximum likelihood; (b) minimum distance; (c) parallelepiped (October '99).	69
4.14	Classification maps based on the Cameron decomposition terms (15×15 -pixel averaging window): (a) maximum likelihood; (b) minimum distance; (c) parallelepiped (October '99).	70
4.15	H/α plane and its division in sub-regions according to the scattering types (courtesy of I. Hajnsek).	71
4.16	Accuracy estimation of the classification tests based on the H and $\bar{\alpha}$ parameters: (a) overall accuracy; (b) Kappa (October '99).	73
4.17	Accuracy estimation of the classification tests based on the H , $\bar{\alpha}$ and A parameters: (a) overall accuracy; (b) Kappa (October '99).	73
4.18	Classification maps based on the H and $\bar{\alpha}$ parameters (10×10 -pixel averaging window): (a) maximum likelihood; (b) minimum distance; (c) parallelepiped (October '99).	74
4.19	Classification maps based on the H , $\bar{\alpha}$ and A parameters (10×10 -pixel averaging window): (a) maximum likelihood; (b) minimum distance; (c) parallelepiped (October '99).	75
5.1	Range history $R(R', x - x')$ of a point scatterer belonging to an extended target.	80
5.2	Range coordinate system for a fixed point in azimuth.	81

5.3	Front view of the interferometric data-take geometry.	82
5.4	Schematic representation of the random volume over ground scattering model proposed in [PC01].	86
5.5	Interferometric coherence derived from: (a) the S_{hh} elements of the sphere term; (b) the S_{hh} elements of the diplane term; (c) the S_{hh} elements of the helix term; (d) the unitary polarization vectors representing the sphere term; (e) the unitary polarization vectors representing the diplane term; (f) the unitary polarization vectors representing the helix term (May '98; baseline: 15 m).	89
5.6	Interferometric coherence derived from the S_{hh} elements of the diplane term (October '99; baseline: 12 m).	90
5.7	Interferometric coherence derived from: (a) the 1st Pauli term; (b) the 2nd Pauli term; (c) the 3rd term; (d) the scattering vectors of Cameron most dominant symmetric term; (e) the scattering vectors of Cameron least dominant symmetric term (May '98; baseline: 15 m).	92
5.8	Interferometric coherence derived from: (a) the 1st optimal value; (b) the 2nd optimal value; (c) the 3rd optimal value; (d) the original S_{hh} elements; (e) the original S_{hv} elements; (f) the original S_{vv} elements (May '98; baseline: 15 m).	93
5.9	Histograms of the interferometric coherence of the whole area derived from: (a) the S_{hh} of the SDH decomposition terms; (b) the scattering vectors of the SDH decomposition terms; (c) the Pauli decomposition coefficients; (d) the scattering vectors of the Cameron decomposition terms; (e) the optimal polarizations; (f) the original polarimetric data (May '98; baseline: 15 m).	94
5.10	Histograms of the interferometric coherence for urban areas derived from: (a) the S_{hh} of the SDH decomposition terms; (b) the scattering vectors of the SDH decomposition terms; (c) the Pauli decomposition coefficients; (d) the scattering vectors of the Cameron decomposition terms; (e) the optimal polarizations; (f) the original polarimetric data (May '98; baseline: 15 m).	96
5.11	Histograms of the interferometric coherence for forested areas derived from: (a) the S_{hh} of the SDH decomposition terms; (b) the scattering vectors of the SDH decomposition terms; (c) the Pauli decomposition coefficients; (d) the scattering vectors of the Cameron decomposition terms; (e) the optimal polarizations; (f) the original polarimetric data (May '98; baseline: 15 m).	97
5.12	Interferometric phases of: (a) the S_{hh} elements of the sphere term; (b) the S_{hh} elements of the diplane term. (c) Difference of the two interferometric phases (May '98, baseline: 15 m).	100
5.13	Interferometric phases of: (a) the unitary polarization vectors representing the sphere term; (b) the unitary polarization vectors representing the helix term. (c) Difference of the two interferometric phases (May '98, baseline: 15 m).	101

5.14	Interferometric phases of: (a) the 1st Pauli term; (b) the 2nd Pauli term. (c) Difference of the two interferometric phases (May '98, baseline: 15 m).	102
5.15	Interferometric phases of: (a) the scattering vectors of Cameron most dominant symmetric term; (b) the scattering vectors of Cameron least dominant symmetric term. (c) Difference of the two interferometric phases (May '98, baseline: 15 m).	103
5.16	Interferometric phases of: (a) the 1st optimal value; (b) the 2nd optimal value. (c) Difference of the two interferometric phases (May '98, baseline: 15 m).	104
A.1	Polarization ellipse.	110

List of Tables

4.1	Confusion matrix relative to the Min. Dist. classification test performed on the amplitudes of the three [S] matrix elements, with a 15×15 -pixel averaging window (values in percentage).	53
4.2	Main E-SAR system parameters.	56
4.3	Accuracy estimates of all the classification tests relative to the 15×15 -pixel averaging window.	76
C.1	Pr. Acc. and Us. Acc. estimates relative to the Max. Lik. classification test performed on the the three [S] matrix elements (single-pixel basis). . . .	120
C.2	Commission and omission error estimates relative to the Max. Lik. classification test performed the three [S] matrix elements (single-pixel basis). . . .	120
C.3	Pr. Acc. and Us. Acc. estimates relative to the Min. Dist. classification test performed on the the three [S] matrix elements (single-pixel basis). . . .	121
C.4	Commission and omission error estimates relative to the Min. Dist. classification test performed the three [S] matrix elements (single-pixel basis). . . .	121
C.5	Pr. Acc. and Us. Acc. estimates relative to the Parall. classification test performed on the the three [S] matrix elements (single-pixel basis). . . .	122
C.6	Commission and omission error estimates relative to the Parall. classification test performed the three [S] matrix elements (single-pixel basis). . . .	122
C.7	Pr. Acc. and Us. Acc. estimates relative to the Max. Lik. classification test performed on the the three [S] matrix elements (15×15 -pixel averaging window).	123
C.8	Commission and omission error estimates relative to the Max. Lik. classification test performed the three [S] matrix elements (15×15 -pixel averaging window).	123
C.9	Pr. Acc. and Us. Acc. estimates relative to the Min. Dist. classification test performed on the the three [S] matrix elements (15×15 -pixel averaging window).	124
C.10	Commission and omission error estimates relative to the Min. Dist. classification test performed the three [S] matrix elements (15×15 -pixel averaging window).	124
C.11	Pr. Acc. and Us. Acc. estimates relative to the Parall. classification test performed on the the three [S] matrix elements (15×15 -pixel averaging window).	125

C.12	Commission and omission error estimates relative to the Parall. classification test performed the three [S] matrix elements (15×15-pixel averaging window).	125
C.13	Pr. Acc. and Us. Acc. estimates relative to the Max. Lik. classification test performed on the [S] matrix co- and cross-polar nulls (single-pixel basis).	126
C.14	Commission and omission error estimates relative to the Max. Lik. classification test performed on the [S] matrix co- and cross-polar nulls (single-pixel basis).	126
C.15	Pr. Acc. and Us. Acc. estimates relative to the Min. Dist. classification test performed on the [S] matrix co- and cross-polar nulls (single-pixel basis).	127
C.16	Commission and omission error estimates relative to the Min. Dist. classification test performed on the [S] matrix co- and cross-polar nulls (single-pixel basis).	127
C.17	Pr. Acc. and Us. Acc. estimates relative to the Parall. classification test performed on the [S] matrix co- and cross-polar nulls (single-pixel basis).	128
C.18	Commission and omission error estimates relative to the Parall. classification test performed on the [S] matrix co- and cross-polar nulls (single-pixel basis).	128
C.19	Pr. Acc. and Us. Acc. estimates relative to the Max. Lik. classification test performed on the [S] matrix co- and cross-polar nulls (15×15-pixel averaging window).	129
C.20	Commission and omission error estimates relative to the Max. Lik. classification test performed on the [S] matrix co- and cross-polar nulls (15×15-pixel averaging window).	129
C.21	Pr. Acc. and Us. Acc. estimates relative to the Min. Dist. classification test performed on the [S] matrix co- and cross-polar nulls (15×15-pixel averaging window).	130
C.22	Commission and omission error estimates relative to the Min. Dist. classification test performed on the [S] matrix co- and cross-polar nulls (15×15-pixel averaging window).	130
C.23	Pr. Acc. and Us. Acc. estimates relative to the Parall. classification test performed on the [S] matrix co- and cross-polar nulls (15×15-pixel averaging window).	131
C.24	Commission and omission error estimates relative to the Parall. classification test performed on the [S] matrix co- and cross-polar nulls (15×15-pixel averaging window).	131
C.25	Pr. Acc. and Us. Acc. estimates relative to the Max. Lik. classification test performed on the SDH decomposition terms (single-pixel basis).	132
C.26	Commission and omission error estimates relative to the Max. Lik. classification test performed on the SDH decomposition terms (single-pixel basis).	132

C.27 Pr. Acc. and Us. Acc. estimates relative to the Min. Dist. classification test performed on the SDH decomposition terms (single-pixel basis).	133
C.28 Commission and omission error estimates relative to the Min. Dist. classification test performed on the SDH decomposition terms (single-pixel basis).	133
C.29 Pr. Acc. and Us. Acc. estimates relative to the Parall. classification test performed on the SDH decomposition terms (single-pixel basis).	134
C.30 Commission and omission error estimates relative to the Parall. classification test performed on the SDH decomposition terms (single-pixel basis).	134
C.31 Pr. Acc. and Us. Acc. estimates relative to the Max. Lik. classification test performed on the SDH decomposition terms (15×15-pixel averaging window).	135
C.32 Commission and omission error estimates relative to the Max. Lik. classification test performed on the SDH decomposition terms (15×15-pixel averaging window).	135
C.33 Pr. Acc. and Us. Acc. estimates relative to the Min. Dist. classification test performed on the SDH decomposition terms (15×15-pixel averaging window).	136
C.34 Commission and omission error estimates relative to the Min. Dist. classification test performed on the SDH decomposition terms (15×15-pixel averaging window).	136
C.35 Pr. Acc. and Us. Acc. estimates relative to the Parall. classification test performed on the SDH decomposition terms (15 × 15-pixel averaging window).	137
C.36 Commission and omission error estimates relative to the Parall. classification test performed on the SDH decomposition terms (15 × 15-pixel averaging window).	137
C.37 Pr. Acc. and Us. Acc. estimates relative to the Max. Lik. classification test performed on the Pauli decomposition terms (single-pixel basis).	138
C.38 Commission and omission error estimates relative to the Max. Lik. classification test performed on the Pauli decomposition terms (single-pixel basis).	138
C.39 Pr. Acc. and Us. Acc. estimates relative to the Min. Dist. classification test performed on the Pauli decomposition terms (single-pixel basis).	139
C.40 Commission and omission error estimates relative to the Min. Dist. classification test performed on the Pauli decomposition terms (single-pixel basis).	139
C.41 Pr. Acc. and Us. Acc. estimates relative to the Parall. classification test performed on the Pauli decomposition terms (single-pixel basis).	140
C.42 Commission and omission error estimates relative to the Parall. classification test performed on the Pauli decomposition terms (single-pixel basis).	140

C.43 Pr. Acc. and Us. Acc. estimates relative to the Max. Lik. classification test performed on the Pauli decomposition terms (15×15 -pixel averaging window).	141
C.44 Commission and omission error estimates relative to the Max. Lik. classification test performed on the Pauli decomposition terms (15×15 -pixel averaging window).	141
C.45 Pr. Acc. and Us. Acc. estimates relative to the Min. Dist. classification test performed on the Pauli decomposition terms (15×15 -pixel averaging window).	142
C.46 Commission and omission error estimates relative to the Min. Dist. classification test performed on the Pauli decomposition terms (15×15 -pixel averaging window).	142
C.47 Pr. Acc. and Us. Acc. estimates relative to the Parall. classification test performed on the Pauli decomposition terms (15×15 -pixel averaging window).	143
C.48 Commission and omission error estimates relative to the Parall. classification test performed on the Pauli decomposition terms (15×15 -pixel averaging window).	143
C.49 Pr. Acc. and Us. Acc. estimates relative to the Max. Lik. classification test performed on the Cameron decomposition terms (single-pixel basis). . .	144
C.50 Commission and omission error estimates relative to the Max. Lik. classification test performed on the Cameron decomposition terms (single-pixel basis).	144
C.51 Pr. Acc. and Us. Acc. estimates relative to the Min. Dist. classification test performed on the Cameron decomposition terms (single-pixel basis).	145
C.52 Commission and omission error estimates relative to the Min. Dist. classification test performed on the Cameron decomposition terms (single-pixel basis).	145
C.53 Pr. Acc. and Us. Acc. estimates relative to the Parall. classification test performed on the Cameron decomposition terms (single-pixel basis). . .	146
C.54 Commission and omission error estimates relative to the Parall. classification test performed on the Cameron decomposition terms (single-pixel basis).	146
C.55 Pr. Acc. and Us. Acc. estimates relative to the Max. Lik. classification test performed on the Cameron decomposition terms (15×15 -pixel averaging window).	147
C.56 Commission and omission error estimates relative to the Max. Lik. classification test performed on the Cameron decomposition terms (15×15 -pixel averaging window).	147
C.57 Pr. Acc. and Us. Acc. estimates relative to the Min. Dist. classification test performed on the Cameron decomposition terms (15×15 -pixel averaging window).	148

C.58 Commission and omission error estimates relative to the Min. Dist. classification test performed on the Cameron decomposition terms (15×15 -pixel averaging window).	148
C.59 Pr. Acc. and Us. Acc. estimates relative to the Parall. classification test performed on the Cameron decomposition terms (15×15 -pixel averaging window).	149
C.60 Commission and omission error estimates relative to the Parall. classification test performed on the Cameron decomposition terms (15×15 -pixel averaging window).	149
C.61 Pr. Acc. and Us. Acc. estimates relative to the Max. Lik. classification test performed on the H and $\bar{\alpha}$ parameters (3×3 -pixel averaging window). .	150
C.62 Commission and omission error estimates relative to the Max. Lik. classification test performed on the H and $\bar{\alpha}$ parameters (3×3 -pixel averaging window).	150
C.63 Pr. Acc. and Us. Acc. estimates relative to the Min. Dist. classification test performed on the H and $\bar{\alpha}$ parameters (3×3 -pixel averaging window).151	151
C.64 Commission and omission error estimates relative to the Min. Dist. classification test performed on the H and $\bar{\alpha}$ parameters (3×3 -pixel averaging window).	151
C.65 Pr. Acc. and Us. Acc. estimates relative to the Parall. classification test performed on the H and $\bar{\alpha}$ parameters (3×3 -pixel averaging window). .	152
C.66 Commission and omission error estimates relative to the Parall. classification test performed on the H and $\bar{\alpha}$ parameters (3×3 -pixel averaging window).	152
C.67 Pr. Acc. and Us. Acc. estimates relative to the Max. Lik. classification test performed on the H and $\bar{\alpha}$ parameters (15×15 -pixel averaging window). 153	153
C.68 Commission and omission error estimates relative to the Max. Lik. classification test performed on the H and $\bar{\alpha}$ parameters (15×15 -pixel averaging window).	153
C.69 Pr. Acc. and Us. Acc. estimates relative to the Min. Dist. classification test performed on the H and $\bar{\alpha}$ parameters (15×15 -pixel averaging window). 154	154
C.70 Commission and omission error estimates relative to the Min. Dist. classification test performed on the H and $\bar{\alpha}$ parameters (15×15 -pixel averaging window).	154
C.71 Pr. Acc. and Us. Acc. estimates relative to the Parall. classification test performed on the H and $\bar{\alpha}$ parameters (15×15 -pixel averaging window). 155	155
C.72 Commission and omission error estimates relative to the Parall. classification test performed on the H and $\bar{\alpha}$ parameters (15×15 -pixel averaging window).	155
C.73 Pr. Acc. and Us. Acc. estimates relative to the Max. Lik. classification test performed on the H , $\bar{\alpha}$ and A parameters (3×3 -pixel averaging window). 156	156

C.74	Commission and omission error estimates relative to the Max. Lik. classification test performed on the H , $\bar{\alpha}$ and A parameters (3×3 -pixel averaging window).	156
C.75	Pr. Acc. and Us. Acc. estimates relative to the Min. Dist. classification test performed on the H , $\bar{\alpha}$ and A parameters (3×3 -pixel averaging window).	157
C.76	Commission and omission error estimates relative to the Min. Dist. classification test performed on the H , $\bar{\alpha}$ and A parameters (3×3 -pixel averaging window).	157
C.77	Pr. Acc. and Us. Acc. estimates relative to the Parall. classification test performed on the H , $\bar{\alpha}$ and A parameters (3×3 -pixel averaging window).	158
C.78	Commission and omission error estimates relative to the Parall. classification test performed on the H , $\bar{\alpha}$ and A parameters (3×3 -pixel averaging window).	158
C.79	Pr. Acc. and Us. Acc. estimates relative to the Max. Lik. classification test performed on the H , $\bar{\alpha}$ and A parameters (15×15 -pixel averaging window).	159
C.80	Commission and omission error estimates relative to the Max. Lik. classification test performed on the H , $\bar{\alpha}$ and A parameters (15×15 -pixel averaging window).	159
C.81	Pr. Acc. and Us. Acc. estimates relative to the Min. Dist. classification test performed on the H , $\bar{\alpha}$ and A parameters (15×15 -pixel averaging window).	160
C.82	Commission and omission error estimates relative to the Min. Dist. classification test performed on the H , $\bar{\alpha}$ and A parameters (15×15 -pixel averaging window).	160
C.83	Pr. Acc. and Us. Acc. estimates relative to the Parall. classification test performed on the H , $\bar{\alpha}$ and A parameters (15×15 -pixel averaging window).	161
C.84	Commission and omission error estimates relative to the Parall. classification test performed on the H , $\bar{\alpha}$ and A parameters (15×15 -pixel averaging window).	161

1 Introduction

Research in the field of radar remote sensing has been a promising area for several decades. In particular, imaging radar systems have become a powerful tool for studying the Earth and its environment. The reasons which make radars useful may be summarized as follows:

- radars are *active* systems: this means that they generate electromagnetic (EM) wave beams whose scattering by targets is the object of study and that they can operate independently of daylight (unlike, for example, optical sensors).
- Frequency, polarization, power and direction of the transmitted beam can be chosen at will. Radars operate within the microwave (MW) region of the EM spectrum that ranges from frequencies of about 3 MHz up to 300 GHz, with corresponding wavelengths λ from 100 m down to 1 mm. However, most of the civil systems nowadays in use limit themselves to a main set of frequency bands: X ($f \approx 10$ GHz or $\lambda \approx 3$ cm), C ($f \approx 6$ GHz or $\lambda \approx 5$ cm), S ($f \approx 3$ GHz or $\lambda \approx 10$ cm), L ($f \approx 2$ GHz or $\lambda \approx 15$ cm) and P ($f \approx 0.5$ GHz or $\lambda \approx 60$ cm).
- Radars can provide (for certain values of moisture and density of the ground) information from beneath the ground surface (sub-surface information). In the same way, they can go through vegetation canopies and give information on their characteristics and on the terrain beneath. Indeed, the penetration depth of an EM wave is a function of the density and moisture content of the penetrated medium as well as of the frequency and polarization of the wave itself.
- In most of the common radar frequency bands, these sensors are almost independent of weather conditions, as the attenuation of the atmosphere is negligible for wavelengths $\lambda > 3$ cm.

Synthetic aperture radar (SAR) systems can provide better results than conventional direct aperture radars. Whereas the resolution of an airborne or spaceborne radar depends on antenna dimensions and on the distance from the targets, SAR devices can simulate antenna dimensions much larger than the real ones and can make the resolution along the flight-path direction independent from the sensor-to-target distance.

Conventional imaging radars (including SAR) operate with a single fixed-polarization antenna for both transmission and reception of radar signals. In this way, for each resolution element in the image, a single scattering coefficient is measured for a specific combination of transmit and receive polarization states used for recording the radar echo; hence, a scalar processing is applied to the power backscattered from

the observed targets. The use of polarization-sensitive devices is the logical development that follows from the consideration of the vector nature of the EM waves. Fully polarimetric radars are indeed able to transmit and receive both the orthogonal components of an EM wave. This ensures that the complete scattering information carried by radar echo signals is fully used to enhance targets detection and identification.

A brief digression on polarimetry history, covering the last 50 years, would now be useful.

Although the discovery of polarimetric phenomena in light dates back to the seventeenth century, the earliest studies on polarimetric radars appeared at the end of the 40s. Worth mentioning are in particular those reported by Kennaugh [Ken54], Sinclair [Sin50], Deschamps [Des51], Graves [Gra56] and Copeland [Cop60] which anticipated the classic PhD work by Huynen [Huy70] in 1970. Kennaugh's contribution was probably the most meaningful; unfortunately it was for several years classified and only at the end of the 70s made available for the scientific community. A detailed review of all these contributions was later conducted by Boerner [BEACM81], [eae85], [eae92]. However, the potential of radar polarimetry remained underestimated until the end of the 80s, mainly because of technological limits restricting practical applications. A fundamental turning point was represented by the NASA/JPL airborne AIRSAR [ZvZH87], [ZvZ91] that was the first imaging polarimetric SAR system ever operated and the forerunner to a series of others by different research institutions (see Figure 1.1).

Thus, concrete applications of polarimetric techniques became possible only recently, when developments in technology (among others the availability of digital data recording systems and general purpose computers for data reduction) permitted the implementation of fully polarimetric imaging radars. Even more important has been the solution of the problems related to the coherent analysis of the waves, i. e., the exact measurement of the signal phase. With regard to the role played by phase, backscattered signals depend completely on the nature of the targets and two extreme situations are possible: point scatterers and Gaussian scatterers. In the first case, the resolution cell may be treated as point-like when determining its position and no uncertainties in phase are present. Backscattering from Gaussian scatterers is, on the contrary, due to a number of elementary random scatterers among which none provides a contribution clearly dominating the others. The evaluation of the phase is in this case the result of an integration over the various contribution from the chosen resolution cell.

It is currently possible to distinguish different branches of what are generally called polarimetric studies. Regardless of the common basis they share, there are troubles in relating them partly due to the different conventions adopted in radar and optical polarimetry. For example, the very definition of polarization handedness can lead to confusion and misunderstandings.¹

¹"...Circularly polarized waves have either a right-handed polarization or a left-handed polarization, which is defined by convention. The TELSTAR satellite sent out circularly polarized microwaves. When it first passed over the Atlantic, the British station at Goonhilly and the French station at Pleumeur Bodou both tried to receive its signals. The French succeeded, because their definition of sense of polarization agreed with the American definition. The British station was set up to receive the wrong polarization because their definition of sense of polarization was contrary to our definition..."

from J. R. Pierce, *"Almost everything about waves"*. Cambridge, Massachusetts USA; MIT Press, 1974, pages 130-131.

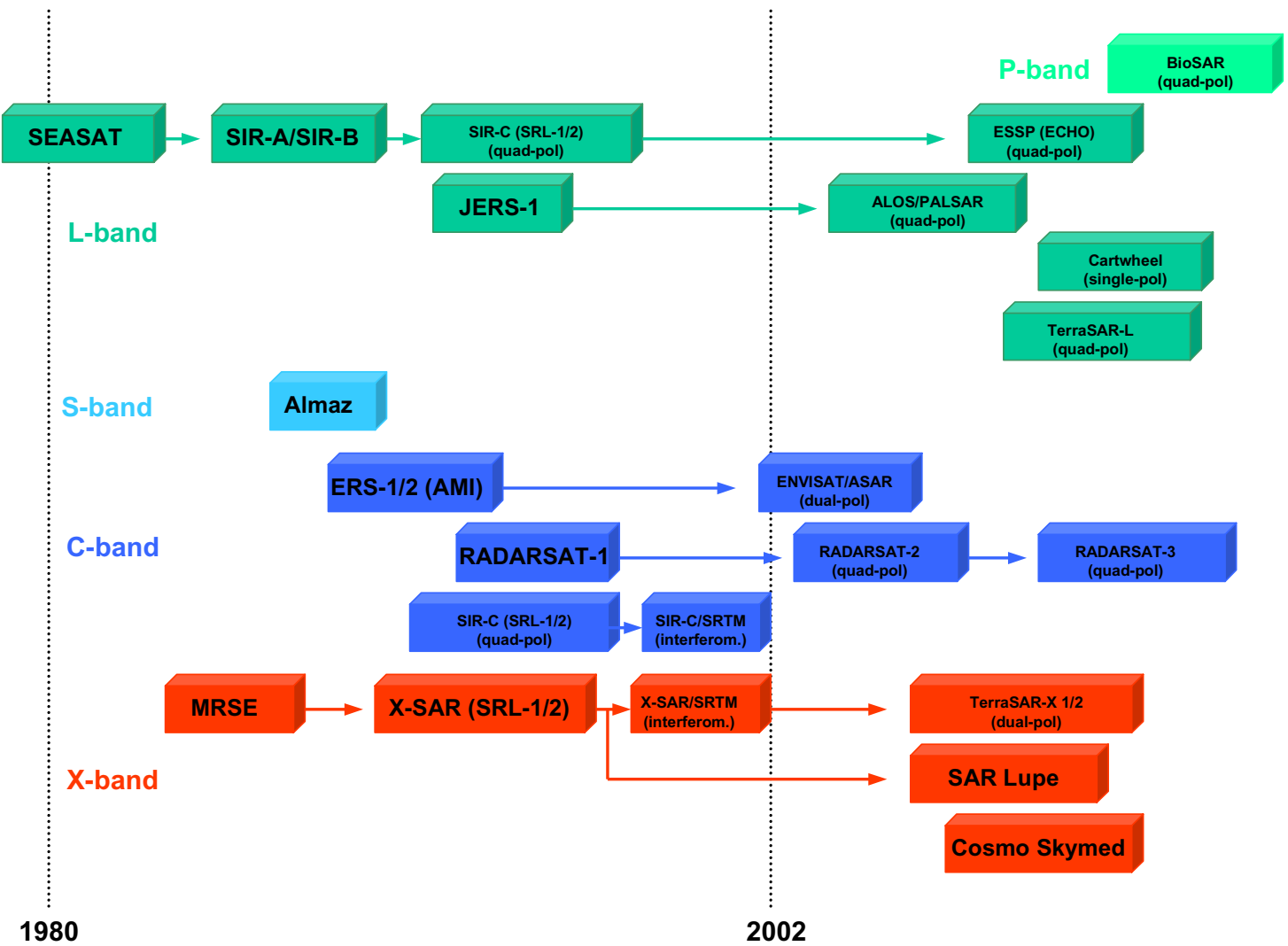


Figure 1.1: Overview of spaceborne SAR missions.

Let us now define the main branches of polarimetry that can be identified, this short summary will also serve as a guideline for the organization of the theoretical part of this work:

General polarimetry theory. It is the most general field of study, comprising very basic polarimetry concepts valid for all radar applications, from weather radars to

remote sensing systems. In this context, the EM waves may be described either using two-dimensional Jones vectors or four-dimensional Stokes vectors and, accordingly, their scattering interactions will be represented by means of scattering or Stokes matrices. The theory explaining the relations among different representations and the operations of change-of-basis also have a general relevance.

SAR polarimetry. As anticipated, the principles of synthetic aperture have been applied also to polarimetric radars giving new momentum to the microwave remote sensing of the Earth. In some cases, the full scattering matrices or the Kennaugh matrices can be measured. Technological aspects as well as those connected to applications of the data are developing rapidly. Much attention is paid, for example, to calibration and signal processing or to classification and pattern recognition methods.

Scatterer property modelling. This is the “ultimate” part of the research, which involves both theoretical and experimental aspects: modelling the scattering behaviour of point and distributed targets and the interactions using few parameters only, and developing algorithms to invert the models for retrieving physical quantities from the measurements.

Polarimetric interferometry. A recent development of polarimetry arises from its association with interferometric techniques. Their combined application yields notable results: polarimetric analysis makes it possible to separate different scattering mechanisms within a given resolution cell, whereas interferometric techniques allow for a topographical characterization of the scattering contributions. These properties can then be used for improving digital elevation models (DEM) or for biomass estimation.

Finally, tomographic and holographic techniques are also applicable to SAR data [RM00], [Rei01] and can be combined with interferometric tools, as they share the common goal of achieving elevation maps or 3-D images of the observed scenes.

The following two chapters will be devoted to a review, as complete as possible, of the theory concerning these and other issues. *The aim is to define, for each branch, the established knowledge and the possible future developments of research.*

The experimental part of this work will pursue another task. Given the different possibilities of expressing polarimetric data, *we will consider them in a systematic way, trying to see if substantial differences exist among the various polarimetric observables in terms of the amount of information they can provide and of its usefulness.* For this reason, in Chapter 4 we have compared a set of these quantities by means of measures of classification accuracy. In other words, we have tested different classification algorithms on observables extracted by airborne polarimetric SAR data. The chosen algorithms are not specifically suited for this kind of data but, considering our approach, this is only of secondary importance. Indeed, with our tests *we want to have a measure (hence, some objective quantities) of the “utility” of the studied observables.* A further reason for this choice was that the classification algorithms used are well-established and in general use in the remote sensing scientific community. In this way we may also get some idea of the potential for wider use of polarimetric SAR data.

Following this systematic overview, we will consider in Chapter 5 some of the polarimetric observables and examine them in combination with interferometry. *The goal is to determine whether in this way a characterization of volume scattering, one of the terms affecting the interferometric coherence, is possible. Again, a comparison of the chosen polarimetric quantities has been done and an attempt to estimate their usefulness is performed.*

As indicated by its general scheme, this work is intended as a survey of polarimetric observables and one of its merits is hopefully its completeness. Finally, to provide a better understanding about the observables, these have been considered from different points of view, namely in classification and SAR interferometry applications.

2 Foundations of radar polarimetry

2.1 Description of electromagnetic waves

Comprehensive introductions to polarimetry theory may be found in classics by Born and Wolf [BW85], Kennaugh [Ken52], [Ken54], Huynen [Huy70], Azzam and Bashara [AB77] and Mott [Mot92]. Also a great number of journal publications have been dedicated during the years to general theoretical aspects; noteworthy examples are those by Cloude [Clo83], [Clo86], van Zyl et al. [vZZE87] and by Kostinski and Boerner [KB86] whose title we borrow for this chapter. These works are all interesting descriptions of the state of the art in this field during the eighties and collect almost all the basic equations of polarimetry. Other reviews of the main concepts of radar polarimetry have been later presented in [AB89], [vZZ90], [BYXY91] and [Hub94].

As a first step we will introduce EM waves and see how they can be represented and how different representations are related to each other.

All aspects of macroscopic electromagnetic phenomena may be described in terms of the set of the *Maxwell equations* that in MKSA units have the form [Str41], [Jac75], [Kon86]:

$$\vec{\nabla} \times \vec{E}(\vec{r}, t) = -\frac{\partial}{\partial t} \vec{B}(\vec{r}, t), \quad (2.1)$$

$$\vec{\nabla} \times \vec{H}(\vec{r}, t) = \vec{J}(\vec{r}, t) + \frac{\partial}{\partial t} \vec{D}(\vec{r}, t), \quad (2.2)$$

$$\vec{\nabla} \cdot \vec{B}(\vec{r}, t) = 0, \quad (2.3)$$

$$\vec{\nabla} \cdot \vec{D}(\vec{r}, t) = \varrho(\vec{r}, t), \quad (2.4)$$

where:

- \vec{E} is the electric field intensity vector in *Volt/meter*,
- \vec{B} is the magnetic flux density vector in *Tesla*,
- \vec{H} is the magnetic field intensity vector in *Ampere/meter*,
- \vec{D} is the current displacement vector in *Coulomb/meter²*,
- \vec{J} is the electric current density vector in *Ampere/meter²* and
- ϱ is the electric charge density in *Coulomb/meter³*.

\vec{E} , \vec{B} , \vec{H} , \vec{D} , \vec{J} and ϱ are all real-valued functions of time t and spatial location \vec{r} , with \vec{r} being a position vector defined with respect to a specified coordinate system.

If the field vectors are linearly related, the medium is said to be *linear* and one has:

$$\vec{B}(\vec{r}, t) = \bar{\mu}(\vec{r}) \vec{H}(\vec{r}, t), \quad (2.5)$$

$$\vec{D}(\vec{r}, t) = \bar{\epsilon}(\vec{r}) \vec{E}(\vec{r}, t), \quad (2.6)$$

indicating with $\bar{\mu}(\vec{r})$ (expressed in *Farad/meter*) and $\bar{\epsilon}(\vec{r})$ (in *Henry/meter*), respectively the dielectric tensor and the magnetic permeability tensor of the medium. In a *homogeneous* medium $\bar{\mu}$, and $\bar{\epsilon}$ are constant and in an *isotropic* medium they are scalar quantities.

Generation, propagation and interactions of EM waves with matter are governed by these laws. Indeed, by means of simple combinations of the Maxwell equations and using further relationships among the above defined quantities, one can prove that for the vector fields in a homogeneous isotropic medium a wave motion equation holds such as:

$$\nabla^2 \vec{\Psi}(\vec{r}, t) - \frac{1}{v^2} \frac{\partial^2}{\partial t^2} \vec{\Psi}(\vec{r}, t) = \vec{g}(\vec{r}, t), \quad (2.7)$$

with $\vec{\Psi}$ being one of the fields, v the wave propagation velocity and \vec{g} a function of the sources generating the wave.¹

In a linear, source-free (i. e., for $\varrho(\vec{r}, t) = 0$ and in absence of externally applied electric currents), homogeneous isotropic medium, the wave equation is homogeneous for every component of \vec{E} :

$$\nabla^2 \vec{E}(\vec{r}, t) - \frac{1}{v^2} \frac{\partial^2}{\partial t^2} \vec{E}(\vec{r}, t) = 0, \quad (2.12)$$

with:

$$v = \frac{1}{\sqrt{\mu\epsilon}}. \quad (2.13)$$

¹Let us show how an equation similar to (2.7) can be derived for the electric field \vec{E} in a homogeneous isotropic medium. From Equations (2.1) and (2.5) it follows:

$$\vec{\nabla} \times (\vec{\nabla} \times \vec{E}(\vec{r}, t)) = \vec{\nabla} \times \left(-\frac{\partial}{\partial t} \vec{B}(\vec{r}, t) \right) = \vec{\nabla} \times \left(-\mu \frac{\partial}{\partial t} \vec{H}(\vec{r}, t) \right) = -\mu \frac{\partial}{\partial t} (\vec{\nabla} \times \vec{H}(\vec{r}, t)). \quad (2.8)$$

Applying the vector identity $\vec{\nabla} \times (\vec{\nabla} \times \vec{a}) = \vec{\nabla}(\vec{\nabla} \cdot \vec{a}) - \nabla^2 \vec{a}$, and substituting $\vec{\nabla} \times \vec{H}(\vec{r}, t)$ from Equation (2.2) one has:

$$\vec{\nabla}(\vec{\nabla} \cdot \vec{E}(\vec{r}, t)) - \nabla^2 \vec{E}(\vec{r}, t) = -\mu \frac{\partial}{\partial t} \vec{J}(\vec{r}, t) - \mu \frac{\partial^2}{\partial t^2} \vec{D}(\vec{r}, t), \quad (2.9)$$

that by means of (2.6) becomes:

$$\nabla^2 \vec{E}(\vec{r}, t) - \vec{\nabla}(\vec{\nabla} \cdot \vec{E}(\vec{r}, t)) - \mu\epsilon \frac{\partial^2}{\partial t^2} \vec{E}(\vec{r}, t) = \mu \frac{\partial}{\partial t} \vec{J}(\vec{r}, t). \quad (2.10)$$

Using Equation (2.4) and assuming $\vec{\nabla} \varrho(\vec{r}, t) = 0$, Equation (2.10) may be written as:

$$\nabla^2 \vec{E}(\vec{r}, t) - \mu\epsilon \frac{\partial^2}{\partial t^2} \vec{E}(\vec{r}, t) = \mu \frac{\partial}{\partial t} \vec{J}(\vec{r}, t), \quad (2.11)$$

known as the *inhomogeneous scalar wave* or *Helmholtz equation*.

Equation (2.12) allows as a solution any function of the type:

$$\vec{\Psi}(\vec{r}, t) = \vec{\Psi}_+(\omega t - \vec{k} \cdot \vec{r}) + \vec{\Psi}_-(\omega t + \vec{k} \cdot \vec{r}). \quad (2.14)$$

$\vec{\Psi}_+$ and $\vec{\Psi}_-$ represent waves propagating in opposite directions and are twice differentiable functions of:

$$\phi_{\pm} = \omega t \mp \vec{k} \cdot \vec{r}, \quad (2.15)$$

where ω and \vec{k} are respectively the angular frequency and the propagation vector of the wave defined concordantly to the position vector; hence, a real-valued solution of the wave equation of the electric field may be written as:

$$\vec{E}(\vec{r}, t) = \vec{E}_{real} \cos(\omega t - \vec{k} \cdot \vec{r}) \quad (2.16)$$

(here only one of the two terms of the sum in (2.14) has been considered).

For practical reasons, it is however customary to adopt a complex representation (this is always possible due to the linearity of the wave equation):

$$\vec{E}(\vec{r}, t) = \vec{E} \exp j(\omega t - \vec{k} \cdot \vec{r}), \quad (2.17)$$

taking both $\vec{E}(\vec{r}, t)$ and \vec{E} as complex, and to assign physical meaning only to its real part, $Re[\vec{E}(\vec{r}, t)]$. This is the convention that we too will use in the following.

For a given real vector \vec{k} , one can determine a phase front of $\vec{E}(\vec{r}, t)$ by setting $\vec{k} \cdot \vec{r} = \text{constant}$ and note that it coincides with a plane orthogonal to \vec{k} . Indeed, with this condition the amplitude of the electric field is the same for all points on the plane and varies in time, remaining constant on this surface. Such waves are known as *plane waves* and Equation (2.17) represents their general form.

Let us consider now a simple physical system such as the one in Figure 2.1, composed of a transmitting antenna, a target and a receiving antenna and let us define a global Cartesian coordinate system, with basis vectors \hat{x} , \hat{y} and \hat{z} , with its origin within the target. The plane containing the directions of propagation of the transmitted and scattered waves is the *scattering plane*; referring to it, the complex transverse components of the electric field illuminating the scatterer are expressed in terms of a local right-handed coordinate system $(\hat{h}_1, \hat{v}_1, \hat{n}_1)$, coincident with the transmitting antenna, defined so that the n_1 -axis is directed towards the target. In a similar way a local coordinate system $(\hat{h}_2, \hat{v}_2, \hat{n}_2)$ is defined with its origin in the receiving system.

In the far field and for small (compared with distances r) targets, waves can be treated as planar; thus, the electric fields of three monochromatic (i. e., completely polarized) waves may be expressed as follows:

$$\vec{E}_T = (E_{Th_1}^2 + E_{Tv_1}^2)^{1/2} [\cos \alpha_T \hat{h}_1 + \sin \alpha_T e^{j\delta_T} \hat{v}_1] \cdot \exp j(\omega t - \vec{k} \cdot \vec{r}_1 + \phi_T), \quad (2.18)$$

$$\vec{E}_R = (E_{Rh_2}^2 + E_{Rv_2}^2)^{1/2} [\cos \alpha_R \hat{h}_2 + \sin \alpha_R e^{j\delta_R} \hat{v}_2] \cdot \exp j(\omega t + \vec{k} \cdot \vec{r}_2 + \phi_R), \quad (2.19)$$

$$\vec{A} = (A_{h_2}^2 + A_{v_2}^2)^{1/2} [\cos \alpha_A \hat{h}_2 + \sin \alpha_A e^{j\delta_A} \hat{v}_2] \cdot \exp j(\omega t - \vec{k} \cdot \vec{r}_2 + \phi_A), \quad (2.20)$$

where, in all the equations, $\alpha = \arctan(E_v/E_h)$ (E_h and E_v being the absolute values of the complex components of the electric field), δ and ϕ are the relative and absolute

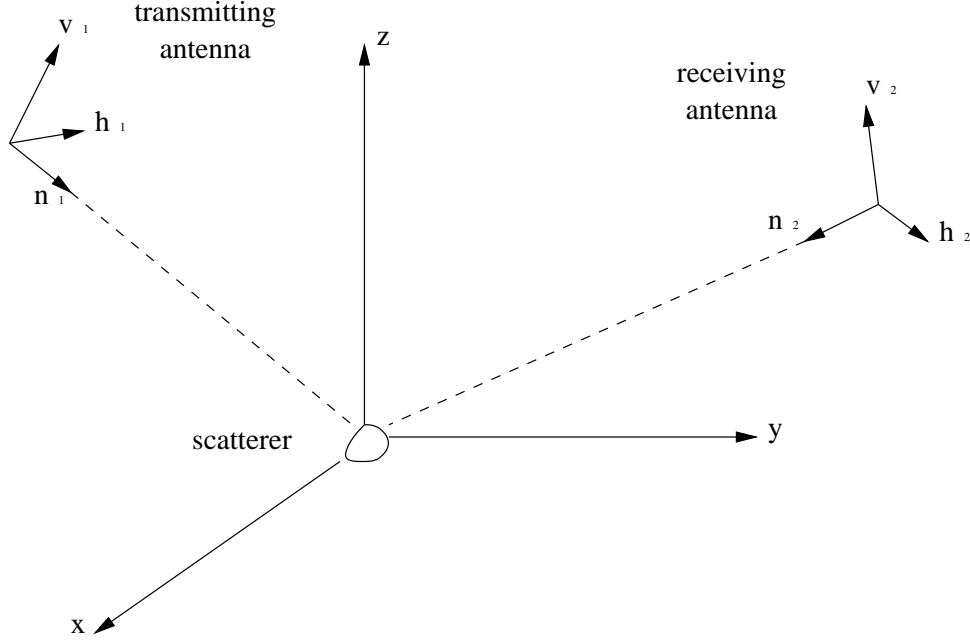


Figure 2.1: General bistatic scattering geometry and local coordinate systems.

phases respectively, subscripts T and R stand for transmitter and receiver, subscripts 1 and 2 specify the coordinate system and \vec{A} , the *antenna height*, is the wave that the receiving antenna would radiate in the $+\hat{n}_2$ direction if it acted as a transmitter (for a better understanding of the terms involved in the equations above, see also Figure 2.2 and later on in this paragraph).

The three waves propagate in the $+\hat{n}_1$, $-\hat{n}_2$ and $+\hat{n}_2$ directions respectively. In the case of backscattering, $\vec{E}_T \propto \vec{A}$ only if the same antenna is used for transmitting and receiving. When this condition is held to be true, one can then write [Ken54]:

$$\vec{E}_T = \frac{Z_0 I_t}{2\lambda r} \vec{A}, \quad (2.21)$$

where Z_0 is the impedance of the medium, I_t the terminal antenna current, λ the wavelength and $r = r_1 = r_2$.

For every monochromatic EM wave, the tip of the vector representing the electric field describes an ellipse on each generic fixed plane normal to the direction of propagation (i. e., when one considers the evolution in time). According to the IEEE standard definitions [IEE83], the polarization of a wave receding from an observer is denoted *right-handed* if the electric field vector appears to be rotating clockwise in this plane and *left-handed* if it appears to be rotating counterclockwise on the chosen perpendicular plane. Therefore, assuming $\alpha = \pi/4$ and $\delta = \pi/2$, we may define \vec{A} as a left-handed circularly polarized wave (because of its $+\hat{n}_2$ propagation) and \vec{E}_R as a right-handed one (as it propagates along the $-\hat{n}_2$ direction).

Before going further with the description of the scattering process, it is useful to introduce some alternative representations of the EM waves. Let \vec{E} be a generic wave of the form:

$$\vec{E} = (E_h^2 + E_v^2)^{1/2} [\cos \alpha \hat{h} + \sin \alpha e^{j\delta} \hat{v}] \cdot \exp j(\omega t - \vec{k} \cdot \vec{r} + \phi). \quad (2.22)$$

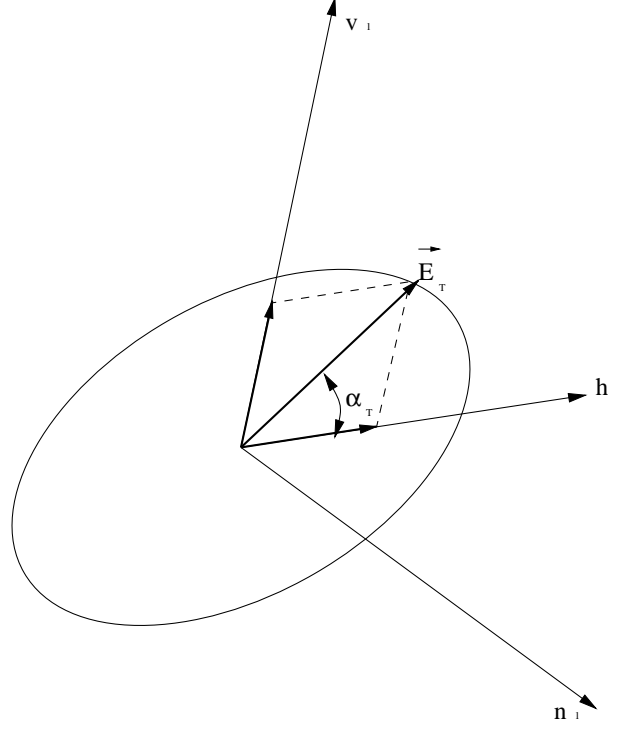


Figure 2.2: Detailed view of the transmitting local coordinate system, with projection in the $\hat{h}_1\hat{v}_1$ -plane of the track described by the tip of the \vec{E}_T vector (with the hypothesis that the relative phase δ_T of the electric field components is different from 0).

This equation, which is similar to the ones above, can also be rewritten as:

$$\vec{E} = (E_h^2 + E_v^2)^{1/2} [\cos \alpha e^{j\delta_h} \hat{h} + \sin \alpha e^{j\delta_v} \hat{v}] \cdot \exp j(\omega t - \vec{k} \cdot \vec{r}), \quad (2.23)$$

when each component is expressed with its own absolute phase, i. e. considering:

$$\delta_h = \phi \quad (2.24)$$

and

$$\delta = \delta_v - \delta_h = \delta_v - \phi. \quad (2.25)$$

One example of the different ways to represent \vec{E} is the *Jones vector* representation, which is related to the particular choice we made of the wave local coordinate system. This is obtained by writing the wave as a complex two-dimensional column vector like:

$$\mathbf{E} = (E_h^2 + E_v^2)^{1/2} e^{j\phi} \begin{bmatrix} \cos \alpha \\ \sin \alpha e^{j\delta} \end{bmatrix} = (E_h^2 + E_v^2)^{1/2} \begin{bmatrix} \cos \alpha e^{j\delta_h} \\ \sin \alpha e^{j\delta_v} \end{bmatrix}. \quad (2.26)$$

In fact, an isomorphism exists relating generic two-dimensional vectors to two-dimensional column vectors (for which we adopted respectively the notations: \vec{V} and \mathbf{V}). In many cases, the Jones vectors are defined as normalized vectors, hence dividing (2.26) by $(E_h^2 + E_v^2)^{1/2}$.

The term in square brackets, the *polarization state* (PS) of the wave, completely determines its polarization ellipse at a fixed point in space, but does not contain the direction of propagation, which must be recovered from the exponent appearing in (2.22).

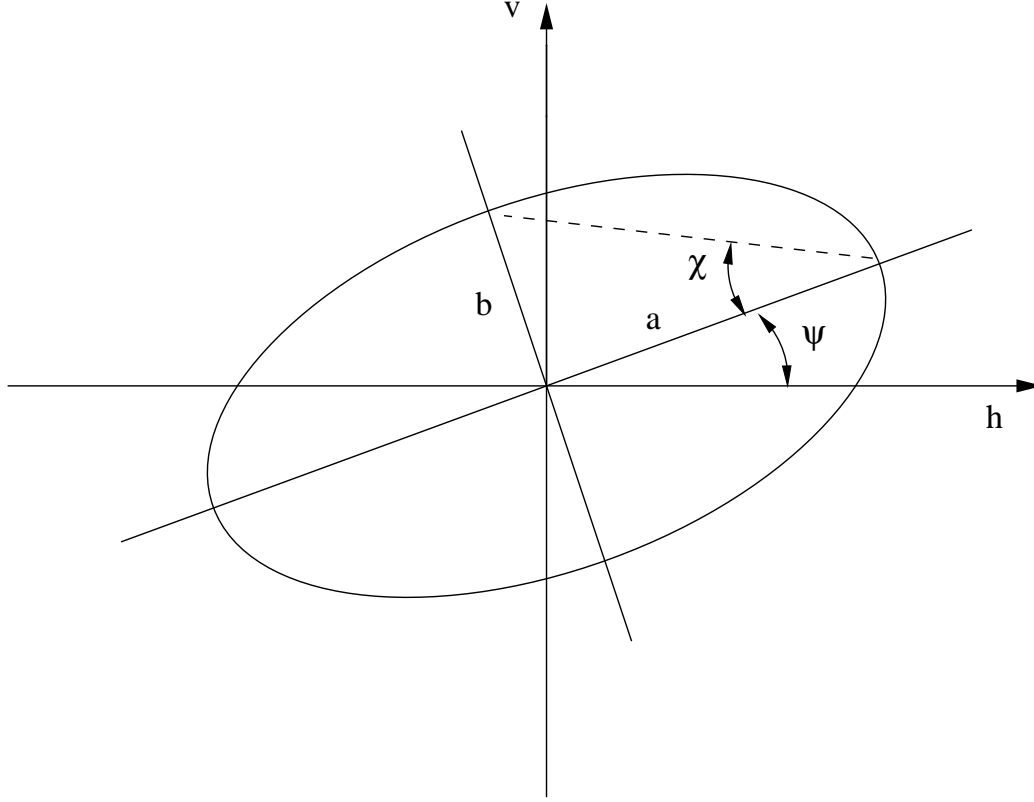


Figure 2.3: Polarization ellipse.

Hence, the only polarimetric information which cannot be reconstructed from the Jones vectors is the handedness, since handedness involves the definition of the direction of propagation.

To avoid the lack of consistency caused by this insufficiency, the Jones vectors can be complemented by the subscripts “+” and “−” in order to distinguish between two directions of propagation: \mathbf{E}_+ should indicate waves propagating in the $+\vec{k}$ direction and \mathbf{E}_- in the $-\vec{k}$ direction:

$$\vec{E}_+ = \mathbf{E}_+ \exp j(\omega t - \vec{k} \cdot \vec{r}) \quad (2.27)$$

$$\vec{E}_- = \mathbf{E}_- \exp j(\omega t + \vec{k} \cdot \vec{r}). \quad (2.28)$$

The vectors \mathbf{E}_\pm are known as *directional Jones vectors* [Gra56]. \mathbf{E}_+ and \mathbf{E}_- represent the same state of polarization referring to opposite propagation directions if they are related by the complex conjugation operation, i. e.:

$$\mathbf{E}_\pm = \mathbf{E}_\mp^*. \quad (2.29)$$

It should be stressed that this relation is valid only for linear polarization bases.

The equation of the polarization ellipse can be derived from the general expression (2.22). This new representation of the generic wave \vec{E} , a geometrical one (see Figure 2.3), is characterized by two parameters expressing the ellipticity, i. e., the ratio of the minor semi-axis b to the major semi-axis a [BEACM81], [BW85]:

$$\tan \chi = \frac{b}{a} \quad (2.30)$$

and inclination angle ψ of the major axis. These parameters are related to those of the Jones vector by means of:²

$$\tan 2\psi = \tan 2\alpha \cos \delta, \quad (2.31)$$

$$\sin 2\chi = \sin 2\alpha \sin \delta \quad (2.32)$$

and using them, the PS of \vec{E} (the first column vector that appears in (2.26)) can be expressed as:

$$\mathbf{p} = \begin{bmatrix} \cos \psi & -\sin \psi \\ \sin \psi & \cos \psi \end{bmatrix} \begin{bmatrix} \cos \chi \\ j \sin \chi \end{bmatrix}. \quad (2.33)$$

Values of χ between $-\pi/4$ and $+\pi/4$, and values of ψ between 0 and $+\pi$ (or equivalently between $-\pi/2$ and $+\pi/2$) are sufficient to describe all possible polarization states. According to the convention adopted above, a wave propagating in the $+\vec{k}$ direction is right-handed if $-\pi/4 \leq \chi < 0$ and left-handed if $0 < \chi \leq \pi/4$.

It is now easier to understand the meaning of Equation (2.29): the conjugation of the Jones vectors implies a change in the sign of the phase difference $\delta = \delta_v - \delta_h$ and, via (2.32), in the sign of the ellipticity angle χ . Hence, the handedness of the PS also changes accordingly.

Another representation of the waves closely related to the one we have just introduced, is the *Stokes vector*³ representation. Such vectors are defined in the following way:

$$\mathbf{g} = \begin{bmatrix} g_0 \\ g_1 \\ g_2 \\ g_3 \end{bmatrix} = \begin{bmatrix} I \\ Q \\ U \\ V \end{bmatrix} \stackrel{\text{def}}{=} \begin{bmatrix} |\underline{E}_h|^2 + |\underline{E}_v|^2 \\ |\underline{E}_h|^2 - |\underline{E}_v|^2 \\ 2 \operatorname{Re}\{\underline{E}_h^* \underline{E}_v\} \\ 2 \operatorname{Im}\{\underline{E}_h^* \underline{E}_v\} \end{bmatrix}, \quad (2.34)$$

where \underline{E}_h and \underline{E}_v are the complex components of \vec{E} .

Each component⁴ of \mathbf{g} describes a characteristic of the EM wave, in detail:

- I represents the total wave intensity,
- Q is the difference between horizontal and vertical intensities,
- U is the difference between $\pm \frac{\pi}{2}$ linear polarizations (the tendency of the wave to be $\pm \frac{\pi}{2}$ linear polarized),
- V is the difference of intensities between right and left polarizations (the tendency to be left- or right-handed)

and it can be shown that they are not independent and furthermore that, for a completely polarized wave (which is the case we are hitherto considering), it results:

$$g_0 = (g_1^2 + g_2^2 + g_3^2)^{1/2}. \quad (2.35)$$

²Mathematical details on the derivation of Equations (2.31) and (2.32) are reported in Appendix A.

³A word of caution in the use of the term “vector” is required when referring to the Stokes vectors. Since the common rules of addition of vectors and of product by a scalar cannot be defined, the Stokes vectors are not really vectors.

⁴The definition of \mathbf{g} chosen here has been widely used in optics [BW85] and also seems to have become common in radar polarimetry in recent years. The definition preferred by Huynen [Huy70] and others [Giu86] is instead obtained by substituting as follows: $g_1 \rightarrow g_2$, $g_2 \rightarrow g_3$ and $g_3 \rightarrow g_1$.

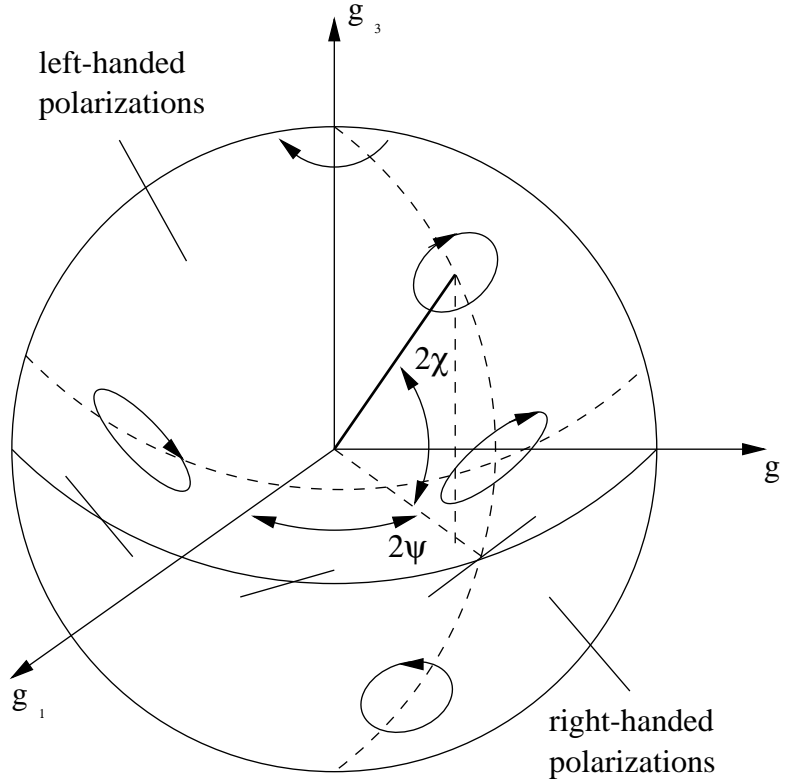


Figure 2.4: The Poincaré sphere.

The relationship with the previous geometrical representation may be brought together by using (2.31) and (2.32), so that (2.34) can be rewritten as:

$$\mathbf{g} = \begin{bmatrix} E_h^2 + E_v^2 \\ E_h^2 - E_v^2 \\ 2E_h E_v \cos \delta \\ 2E_h E_v \sin \delta \end{bmatrix} = E^2 \begin{bmatrix} 1 \\ \cos 2\psi \cos 2\chi \\ \sin 2\psi \cos 2\chi \\ \sin 2\chi \end{bmatrix}. \quad (2.36)$$

In (2.36), $E^2 = E_h^2 + E_v^2$ is the total intensity of the wave.

The Stokes vector can be represented graphically by reference to the *Poincaré sphere*.

All the possible polarizations of a wave with total intensity $E^2 = g_0$ are described in a three-dimensional Cartesian system (see Figure 2.4). Each PS is represented by a point on a sphere of radius g_0 whose Cartesian coordinates are (g_1, g_2, g_3) . On this sphere the angles 2ψ and 2χ represent the longitude and the latitude of the point defining the PS. The equator of the Poincaré sphere thus represents linear polarizations, the poles represent circular polarizations and all left-handed (right-handed) elliptical polarizations are mapped onto the northern (southern) hemisphere. The extremes of each diameter correspond to a pair of orthogonal polarizations [IEE83].

As a final example of the different ways to describe an EM wave, we introduce the concept of *complex polarization ratio*, defined as the ratio of the orthogonal complex electric field components [AB77]:

$$\rho \stackrel{\text{def}}{=} \underline{E}_v / \underline{E}_h = E_v e^{j\delta_v} / E_h e^{j\delta_h} = \tan \alpha e^{j\delta} = |\rho| e^{j\delta}, \quad (2.37)$$

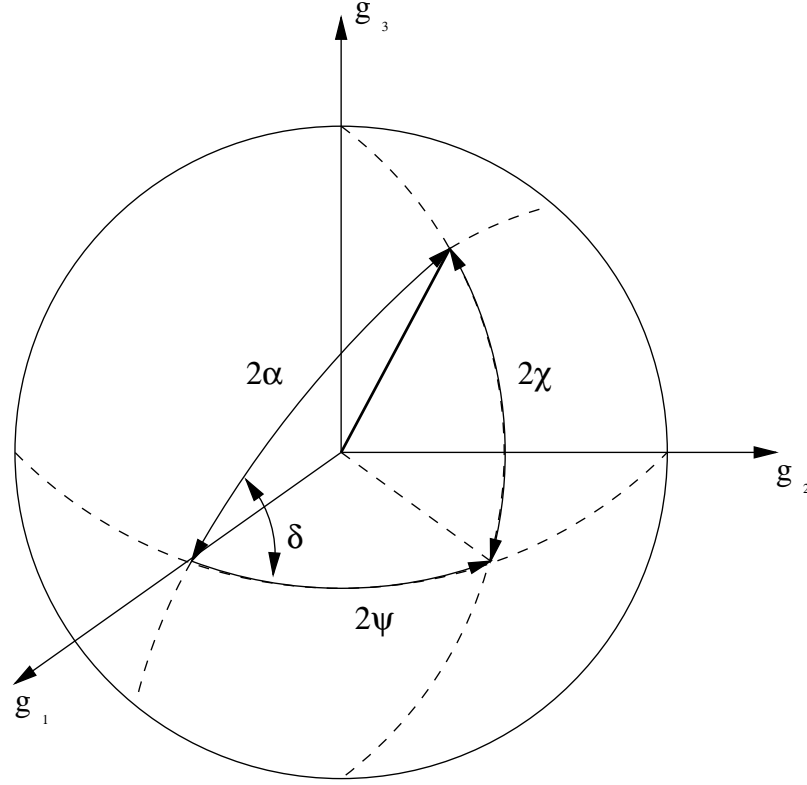


Figure 2.5: The Deschamps sphere.

where $0 \leq \alpha < \pi/2$ and $0 \leq \delta < 2\pi$. The two angles α and δ are now defined as *Deschamps parameters* [Des51] and determine the polarization state of a wave in terms of the amplitude ratio and phase difference. Since these parameters can also be geometrically represented by means of a sphere, the *Deschamps sphere*, it is easy to visualize the relationship between them and ψ and χ (see Figure 2.5). Using ρ , the two-dimensional column vector becomes:

$$\mathbf{E} = e^{j\delta_h} \frac{(E_h^2 + E_v^2)^{1/2}}{\sqrt{1 + \rho\rho^*}} \begin{bmatrix} 1 \\ \rho \end{bmatrix}. \quad (2.38)$$

The previously mentioned “orthogonality” of complex vectors (referred to PSs or generic vectors) may be defined in terms of an inner product of the form:

$$\langle \mathbf{a} | \mathbf{b} \rangle \equiv a_x^* b_x + a_y^* b_y, \quad (2.39)$$

where \mathbf{a} and \mathbf{b} are two generic column vectors, such that they are orthogonal if:

$$\langle \mathbf{a} | \mathbf{b} \rangle = 0 \quad (2.40)$$

Now, according to the complex polarization ratio representation, a new definition of orthogonality of two PSs, denoted by m and n , can be introduced:

$$\rho_m \rho_n^* = -1 \iff \rho_m = -\frac{1}{\rho_n^*}, \quad (2.41)$$

by means of some very general mathematical considerations (Feynman related it to the analogous condition for the angular coefficients of two real straight lines [Fey96]).

2.2 Scattering of electromagnetic waves

Taking into account all the definitions above, we can now continue with the description of the interactions among the elements of the system in Figure 2.1.

Under the far field assumption, it has been shown that a general EM scattering process can be described in terms of a matrix equation of the form [Mot92]:

$$\mathbf{E}_R = \lim_{r/\lambda \rightarrow \infty} \frac{\lambda}{(4\pi)^{1/2}r} [\mathbf{S}] \mathbf{E}_T, \quad (2.42)$$

where the distance between the receiving antenna and the target is denoted by r , λ is the operating wavelength and $[\mathbf{S}]$ is a 2×2 complex matrix, i. e.:

$$[\mathbf{S}] = \begin{bmatrix} S_{h_2 h_1} & S_{h_2 v_1} \\ S_{v_2 h_1} & S_{v_2 v_1} \end{bmatrix}. \quad (2.43)$$

$[\mathbf{S}]$ is the *scattering matrix* and completely defines the interaction; it introduces a *mapping* connecting the vectors representing the incident and scattered waves. Its elements are, in general, complicated and sensitive functions of frequency, target orientation and shape, relative orientation of the polarization planes in the bistatic case, etc. The diagonal elements $S_{h_2 h_1}$, $S_{v_2 v_1}$ and the off-diagonal ones $S_{h_2 v_1}$, $S_{v_2 h_1}$ are called respectively *co-* and *cross-polarized* components. Note that the fractional term causes $[\mathbf{S}]$ to be dimensionless, but (2.42) can be expressed in different ways and $[\mathbf{S}]$ can also have the dimension of a length. However, this proportional term will be omitted from here on and (2.42) written in the simplified form:

$$\mathbf{E}_R = [\mathbf{S}] \mathbf{E}_T. \quad (2.44)$$

In the most general case, there are seven independent parameters in the bistatic scattering matrix: four amplitudes and three phases. Indeed, an overall absolute phase may be neglected, since the power received from the scatterer is independent of this phase. In the backscatter (or *monostatic*) case, one has that $h_1 \equiv h_2$ and $v_1 \equiv v_2$ and reciprocity dictates that $S_{h_2 v_1} = S_{v_2 h_1}$ and there are only five independent parameters in the scattering matrix.

Another fundamental equation of radar polarimetry comes from a different element of the system: the receiving antenna network. It relates the voltage measured at a receiving antenna to the polarization of an incoming EM wave (which, in turn, may be scattered). A formal statement of the voltage equation is [Ken54]:

$$V = \mathbf{A}^t \mathbf{E}_R = \mathbf{A}^t [\mathbf{S}] \mathbf{E}_T, \quad (2.45)$$

where the notation $\mathbf{a}^t \mathbf{b} \equiv a_x b_x + a_y b_y$ is for column vectors and superscript t denotes the transpose. At the beginning of this paragraph, the antenna height \mathbf{A} was introduced as the polarization state of a wave transmitted by the receiving antenna towards the target. Thus, \mathbf{A} is a measurable quantity and is defined on the basis of the radiation pattern of that antenna. The squared absolute value of V ,

$$P_R = |V(\mathbf{A}, \mathbf{E}_R)|^2, \quad (2.46)$$

is described as the *power transfer equation*.

In [KB86], Kostinski and Boerner dealt with the voltage optimization question, which is the problem of finding which polarizations of the transmitting and receiving antennae maximize the value of P for a target with a known scattering matrix. It must be noted that in (2.45) there is not an inner product because \mathbf{A} is not conjugated; hence, for normalized vectors the maximum condition for $|V|^2$ is [Ken52]:

$$\mathbf{A} \propto \mathbf{E}_R^*. \quad (2.47)$$

The physical meaning of this formulation is easily understood if we consider that conjugation of any PS reverses the sense of rotation of the wave. Hence, the condition $\mathbf{A} \propto \mathbf{E}_R^*$ means that the returned wave is matched to the receiving antenna when its polarization ellipse is oriented in space identically with the one due to \mathbf{A} (radiated by the receiving antenna when used as a transmitter) and when they have opposite senses of rotation when both looked at from the same viewpoint.

Kostinski and Boerner provided a general solution for the voltage optimization problem which enables one to treat symmetric, asymmetric, monostatic and bistatic cases in an identical manner (further details on the optimal polarization problem and other solutions can be found in [Huy70], [AB89] and [BYXY91]). The approach proposed by the two authors has the principal advantage of not requiring diagonalization of the scattering matrix and therefore the use of change-of-basis formulae. This important aspect of polarimetry theory will be dealt with in the next paragraph.

When dealing with power measurements, Equation (2.42) may be expressed in terms of Stokes vectors and of the corresponding 4×4 matrix $[\mathbf{K}]$, the so-called *Kennaugh matrix*, whose elements can be derived from the ones of $[\mathbf{S}]$ by means of [vdH81], [BEACM81]:

$$[\mathbf{K}] = [\mathbf{A}]^*([\mathbf{S}] \otimes [\mathbf{S}]^*)[\mathbf{A}]^{-1}, \quad (2.48)$$

where \otimes denotes the Kronecker product of the two matrices and $[\mathbf{A}]$ is defined as:

$$[\mathbf{A}] = \begin{bmatrix} 1 & 0 & 0 & 1 \\ 1 & 0 & 0 & -1 \\ 0 & 1 & 1 & 0 \\ 0 & j & -j & 0 \end{bmatrix}. \quad (2.49)$$

For completely polarized waves there is a one-to-one correspondence between the scattering matrix $[\mathbf{S}]$ and the Kennaugh matrix $[\mathbf{K}]$.

In forward scattering cases, $[\mathbf{K}]$ must be substituted by the *Mueller matrix* which is related to the Kennaugh one by:

$$[\mathbf{M}] = [\mathbf{C}][\mathbf{K}] \quad \text{or} \quad [\mathbf{K}] = [\mathbf{C}][\mathbf{M}], \quad (2.50)$$

with:

$$[\mathbf{C}] = \begin{bmatrix} 1 & 0 & 0 & 0 \\ 0 & 1 & 0 & 0 \\ 0 & 0 & 1 & 0 \\ 0 & 0 & 0 & -1 \end{bmatrix}. \quad (2.51)$$

Before proceeding any further, it is now worthwhile to define some characteristics of the waves we are considering.

All of the equations introduced in the previous paragraphs refer to monochromatic waves that cannot be considered as typical real phenomena. Real systems work with partially polarized waves, which can be expressed, via Fourier integrals, as a superposition of plane monochromatic waves. This is the importance of plane waves that, in this sense, are the basic elements of all wave problems.

When a partially polarized wave is involved, Equation (2.35) must be replaced by:

$$g_0 \geq (g_1^2 + g_2^2 + g_3^2)^{1/2} \quad (2.52)$$

and the values of the Stokes parameters have to be derived using average estimates of the measurements, in order to correctly express the statistical variations of the polarization. Partially polarized waves are generated, typically, after scattering from real targets which have to be considered as distributed sets of scatterers varying either in space or in time. They are referred to as *non-deterministic* or *partial* or also *random* scatterers. In this case it was shown that the average Stokes parameters of the backscattered wave are related to those of the illuminating one through an averaged Kennaugh matrix. This matrix can be calculated by averaging the elements of $[\mathbf{K}]$ (we will indicate this operation using angular brackets $\langle \rangle$, that should not be confused with those defining the inner product of two vectors), but this process does not preserve the relationship with $[\mathbf{S}]$. Hence, the unique connection between the scattering matrix and the Stokes matrix representation is lost. In such a case, no equivalent scattering matrix exists for the average Kennaugh matrix [Huy70], [vZZE87], [Mot92].

Taking now into account the considerations above, we can show how the received power at the antenna terminal is related to the average Kennaugh matrix. In the most general case of Figure 2.1, it holds:

$$P_R = |V|^2 = |\mathbf{A}^t \mathbf{E}_R|^2 = |\langle \mathbf{A} | \mathbf{E}_R \rangle|^2, \quad (2.53)$$

which, for a monostatic system with fixed polarization, yields:

$$P_R = |\langle \mathbf{E}_T | \mathbf{E}_R \rangle|^2 = |\langle \mathbf{E}_T | [\mathbf{S}] \mathbf{E}_T \rangle|^2. \quad (2.54)$$

Using the Stokes vectors, (2.54) may be written in a similar way:

$$P_R = \mathbf{g}_T^t \langle [\mathbf{K}] \rangle \mathbf{g}_T, \quad (2.55)$$

with $\mathbf{g}_T = \mathbf{g}_T(\psi_T, \chi_T)$ according to (2.36). The value of P_R is usually the sum of several power measurements to reduce statistical variations due to non-deterministic scatterers inside an image resolution cell, so that $\langle [\mathbf{K}] \rangle$ is the average Kennaugh matrix.

The received power can also be expressed in terms of an area associated with the scatterer, called *scattering cross section* σ , such that:

$$\sigma = \lim_{r \rightarrow \infty} (4\pi r^2) \left(\frac{P_R}{P_T} \right). \quad (2.56)$$

At a fixed polarization, i. e., the same polarization of the transmitting and receiving antennae, σ is a function of ψ_T and χ_T only (by means of (2.36)). In the most general case, one would expect different polarizations and hence: $\sigma = \sigma(\psi_R, \chi_R, \psi_T, \chi_T)$.

2.3 Change-of-basis theory and characteristic polarizations

Let us introduce now some relations that will be extensively used later and let us refer, for instance, to the wave represented by (2.26). We defined it using a linear basis but, of course, it would be possible to consider other bases and represent \mathbf{E} according to them.

What must be stressed is that, regardless of the basis we choose, and therefore of the form in which we represent it, we are dealing with the same wave and there are some rules to follow in order to guarantee proper comparison of measurements taken with different antenna sets. The following requirement must be satisfied while changing basis: *all measurable quantities such as voltage, energy density, etc. must remain invariant under the change-of-basis.*

In general, defining a vector in two different bases requires us to find the relationship between its components in the two bases; this relationship is usually expressed by a matrix which maps the components of the vector in one basis to the components in the other basis.

The fulfillment of the conditions above imposes some constraints on the matrices which can be used as change-of-basis matrices: for orthogonal bases, they have to be *unitary matrices*.

It will be remembered that the *adjoint matrix* $[\mathbf{B}]^\dagger$ of a generic complex matrix $[\mathbf{B}]$ is defined as the complex conjugate of its transpose, i. e.:

$$[\mathbf{B}]^\dagger \stackrel{\text{def}}{=} [\mathbf{B}]^{t*} \quad (2.57)$$

and for unitary matrices the following properties hold:⁵

$$[\mathbf{U}]^\dagger \equiv [\mathbf{U}]^{t*} = [\mathbf{U}]^{-1}, \quad (2.58)$$

$$[\mathbf{U}]^\dagger [\mathbf{U}] = [\mathbf{U}] [\mathbf{U}]^\dagger = [\mathbf{I}], \quad (2.59)$$

$$|\det[\mathbf{U}]| = 1. \quad (2.60)$$

In the 2×2 complex case, the unitarity requirement imposes four constraints on eight parameters. Hence, $[\mathbf{U}]$ is, in general, a function of four variables. In radar polarimetry it was shown that an appropriate calibration of the system further leads to the following condition:

$$\det[\mathbf{U}] = 1. \quad (2.61)$$

It is then possible to reduce the number of parameters so that, in terms of the complex polarization ratio, $[\mathbf{U}]$ can be expressed by:

$$[\mathbf{U}] = \frac{1}{\sqrt{1 + \rho\rho^*}} \begin{bmatrix} e^{j\delta_h} & -\rho^* e^{-j\delta_h} \\ \rho e^{j\delta_h} & e^{-j\delta_h} \end{bmatrix}. \quad (2.62)$$

Let us consider Equation (2.44) and see more in depth how the scattering matrix behaves under change-of-basis transformations, starting from the forward scattering.

⁵Equations (2.58) and (2.59) are necessary and sufficient conditions for unitarity whereas (2.60) is only necessary (but not sufficient).

In such a case, the vectors \mathbf{E}_R and \mathbf{E}_T will undergo the transformations:

$$\mathbf{E}_R = [\mathbf{U}]\mathbf{E}'_R, \quad (2.63)$$

$$\mathbf{E}_T = [\mathbf{U}]\mathbf{E}'_T, \quad (2.64)$$

where the primes indicate quantities expressed in the new polarization basis.

What we require is an obvious physical invariance, namely, that the measured voltage at the receiving antenna terminals remains unchanged under the change-of-basis transformation and that the scattering matrix in (2.44) connects the same physical polarization states as in the old basis. One then obtains:

$$\mathbf{E}_R = [\mathbf{S}]\mathbf{E}_T \Rightarrow \quad (2.65)$$

$$[\mathbf{U}]\mathbf{E}'_R = [\mathbf{S}][\mathbf{U}]\mathbf{E}'_T \Rightarrow \quad (2.66)$$

$$\mathbf{E}'_R = [\mathbf{U}]^{-1}[\mathbf{S}][\mathbf{U}]\mathbf{E}'_T, \quad (2.67)$$

leading to the unitary similarity transformation for the scattering matrix $[\mathbf{S}]$:

$$[\mathbf{S}'] = [\mathbf{U}]^{-1}[\mathbf{S}][\mathbf{U}], \quad (2.68)$$

which expresses the invariance of the properties of the target operator $[\mathbf{S}]$ following the change-of-basis.

Significant differences characterize the scattering equation in the monostatic case. Also for backscattering, the two polarization states (of the transmitted and of the received wave) can be referred to using the same reference system and expressed in the same basis but, obviously, correspond to waves propagating in opposite directions. It is then important to correctly define their handedness. This is possible by means of the directional Jones vectors. In a linear basis, keeping in mind that $\mathbf{E}_{\pm} = \mathbf{E}_{\mp}^*$ (see (2.29)), Equation (2.44) must be rewritten as:

$$\mathbf{E}_{R,-} = [\mathbf{S}]\mathbf{E}_{T,+} = [\mathbf{S}]\mathbf{E}_{T,-}^*. \quad (2.69)$$

According to this new expression (we will assume that, for a correct comparison, the waves propagate in the same direction and for simplicity we will ignore the subscript “-”), the change-of-basis relation for the scattering matrix becomes:

$$\mathbf{E}_R = [\mathbf{S}]\mathbf{E}_T^* \Rightarrow \quad (2.70)$$

$$[\mathbf{U}]\mathbf{E}'_R = [\mathbf{S}]([\mathbf{U}]\mathbf{E}'_T)^* \Rightarrow \quad (2.71)$$

$$\mathbf{E}'_R = [\mathbf{U}]^{-1}[\mathbf{S}][\mathbf{U}]^*\mathbf{E}'_T, \quad (2.72)$$

which again leads to:

$$[\mathbf{S}'] = [\mathbf{U}]^{-1}[\mathbf{S}][\mathbf{U}]^* = [\mathbf{U}]^{\dagger}[\mathbf{S}][\mathbf{U}]^*. \quad (2.73)$$

Simply changing the name of $[\mathbf{U}]^*$ and letting $[\mathbf{U}]^* = [\mathbf{U}_1]$, it becomes evident that the representation of the scattering matrix $[\mathbf{S}']$ in the new polarization basis is obtained by a unitary congruence transformation of the original scattering matrix $[\mathbf{S}]$:

$$[\mathbf{S}'] = [\mathbf{U}_1]^t[\mathbf{S}][\mathbf{U}_1]. \quad (2.74)$$

This relation plays a central role in radar theory since most of systems have a monostatic configuration.

The use of the change-of-basis formulae permits the expression of the scattering matrix in diagonalized forms; hence, one has access to particular representations of the interactions where the backscattered power is concentrated only in some of the components of $[S]$.

Let us consider the matrix transformation from the (\hat{h}, \hat{v}) linear basis into a generic one with basis vector (\hat{e}_1, \hat{e}_2) :

$$\begin{aligned} [S] &= \frac{1}{N} \begin{bmatrix} 1 & \rho \\ -\rho^* & 1 \end{bmatrix} \begin{bmatrix} S_{hh} & S_{hv} \\ S_{vh} & S_{vv} \end{bmatrix} \begin{bmatrix} 1 & -\rho^* \\ \rho & 1 \end{bmatrix} = \\ &= \frac{1}{N} \begin{bmatrix} 1 & \rho \\ -\rho^* & 1 \end{bmatrix} \begin{bmatrix} S_{hh} + \rho S_{hv} & -\rho^* S_{hh} + S_{hv} \\ S_{vh} + \rho S_{vv} & -\rho^* S_{vh} + S_{vv} \end{bmatrix} = \\ &= \frac{1}{N} \begin{bmatrix} S_{hh} + \rho S_{hv} + \rho S_{vh} + \rho^2 S_{vv} & -\rho^* S_{hh} + S_{hv} - \rho \rho^* S_{vh} + \rho S_{vv} \\ -\rho^* S_{hh} + S_{vh} - \rho \rho^* S_{hv} + \rho S_{vv} & \rho^* \rho^* S_{hh} - \rho^* S_{hv} - \rho^* S_{vh} + S_{vv} \end{bmatrix}, \end{aligned} \quad (2.75)$$

where:

$$N = 1 + \rho \rho^* \quad (2.76)$$

(we will no longer add the numerical subscripts to the $[S]$ matrix elements, adopting the broadly used convention of considering the first subscript related to the receiving system and the second one to the transmitting system).

As reported in [Ken54], the two cross-polar nulls, which define the polarization vectors whose reflected wave has zero cross-polar components, coincide with the co-polar maxima. To obtain them, one has to impose one of the following zeroing conditions on the cross-polar terms of (2.75) (due to reciprocity, in the monostatic case they are equivalent):

$$-\rho^* S_{hh} + S_{hv} - \rho \rho^* S_{vh} + \rho S_{vv} = 0 \quad (2.77)$$

$$-\rho^* S_{hh} + S_{vh} - \rho \rho^* S_{hv} + \rho S_{vv} = 0 \quad (2.78)$$

Considering the former, taking its complex conjugate and subtracting the latter:

$$\begin{cases} (\rho^* S_{hh} - S_{hv} + \rho \rho^* S_{vh} - \rho S_{vv}) S_{hv}^* = 0 \\ (\rho S_{hh}^* - S_{hv}^* + \rho \rho^* S_{vh}^* - \rho^* S_{vv}^*) S_{hv} = 0 \end{cases} \quad (2.79)$$

results in [BEACM81]:

$$\rho^* S_{hh} S_{hv}^* + \rho^* S_{vv}^* S_{hv} - \rho S_{vv} S_{hv}^* - \rho S_{hh}^* S_{hv} = 0 \Rightarrow \quad (2.80)$$

$$\rho^* (S_{hh} S_{hv}^* + S_{vv}^* S_{hv}) = \rho (S_{hh}^* S_{hv} + S_{vv} S_{hv}^*) \Rightarrow \rho^* A^* = \rho A, \quad (2.81)$$

being:

$$A = S_{hh}^* S_{hv} + S_{vv} S_{hv}^*. \quad (2.82)$$

Now, taking again (2.77) and multiplying it by A^* :

$$\rho^* A^* S_{hh} + \rho \rho^* A^* S_{hv} - S_{vh} A^* - \rho A^* S_{vv} = 0 \Rightarrow \quad (2.83)$$

$$\rho^2 A S_{hv} + \rho (A S_{hh} - A^* S_{vv}) - S_{vh} A^* = 0 \Rightarrow \quad (2.84)$$

$$\begin{aligned} &\rho^2 A S_{hv} + \rho (S_{hh}^* S_{hv} S_{hh} + \\ &+ S_{vv} S_{hv}^* S_{hh} - S_{hh} S_{hv}^* S_{vv} - S_{vv}^* S_{hv} S_{vv}) - S_{vh} A^* = 0 \Rightarrow \end{aligned} \quad (2.85)$$

$$\rho^2 A + \rho (|S_{hh}|^2 - |S_{vv}|^2) - A^* = 0. \quad (2.86)$$

Equation (2.86) has two possible complex solutions in terms of ρ :

$$\rho_{1,2}^{(p,q)} = \frac{|S_{vv}|^2 - |S_{hh}|^2 \pm \sqrt{(|S_{hh}|^2 - |S_{vv}|^2)^2 + 4|A|^2}}{2A} \quad (2.87)$$

that lead to two diagonalized $[S]$ matrices:

$$\rho_1^{(p,q)} \Rightarrow [S]_{(p_1, q_1)} = \begin{bmatrix} p_1 & 0 \\ 0 & q_1 \end{bmatrix}, \quad (2.88)$$

$$\rho_2^{(p,q)} \Rightarrow [S]_{(p_2, q_2)} = \begin{bmatrix} p_2 & 0 \\ 0 & q_2 \end{bmatrix}, \quad (2.89)$$

where the values of the two pairs of eigenvalues, are obtained by substituting the two solutions found with (2.87) into (2.75).

It can also be shown that the cross-polar nulls are always mutually orthogonal, indeed:

$$\begin{aligned} (\rho_1^{(p,q)}) \cdot (\rho_2^{(p,q)})^* &= \left[\frac{-B + \sqrt{B^2 + 4|A|^2}}{2A} \right] \left[\frac{-B - \sqrt{B^2 + 4|A|^2}}{2A} \right]^* = \\ &= \frac{B^2 - B^2 - 4|A|^2}{4AA^*} = -1, \end{aligned} \quad (2.90)$$

with:

$$B = |S_{hh}|^2 - |S_{vv}|^2. \quad (2.91)$$

The other group of characteristic polarizations is represented by the $[S]$ matrix co-polar nulls. As in the previous case, they can be calculated by setting both the co-polar terms of (2.75) to zero:

$$S_{hh} + 2\rho S_{hv} + \rho^2 S_{vv} = 0 \quad (2.92)$$

$$S_{vv} - 2\rho^* S_{hv} + (\rho^*)^2 S_{hh} = 0. \quad (2.93)$$

The solutions of these two equations lead to two pairs of values for ρ , respectively $(\rho_1^{(x)}, \rho_2^{(x)})$ and $(\rho_1^{(y)}, \rho_2^{(y)})$, and to two pairs of matrices which differ only in their phase terms. Indeed one gets:

$$\rho_1^{(x)} \Rightarrow [S]_{x_1} = \begin{bmatrix} 0 & x_1 \\ x_1 & a_1 \end{bmatrix}, \quad (2.94)$$

$$\rho_2^{(x)} \Rightarrow [S]_{x_2} = \begin{bmatrix} 0 & x_2 \\ x_2 & a_2 \end{bmatrix}, \quad (2.95)$$

$$\rho_1^{(y)} \Rightarrow [S]_{y_1} = \begin{bmatrix} b_1 & y_1 \\ y_1 & 0 \end{bmatrix}, \quad (2.96)$$

$$\rho_2^{(y)} \Rightarrow [S]_{y_2} = \begin{bmatrix} b_2 & y_2 \\ y_2 & 0 \end{bmatrix}, \quad (2.97)$$

with:

$$|x_1| = |x_2| = |y_1| = |y_2| \quad (2.98)$$

and

$$|a_1| = |a_2| = |b_1| = |b_2|. \quad (2.99)$$

It is important to note here that a more formal approach to the diagonalization of the scattering matrix is possible (for instance, by means of Takagi's theorem [HJ85]) which prevents some limits of the equations and derivations above. Indeed, these fail when diagonalizing some special scattering matrices. It is nevertheless possible to use them since in the majority of the cases, as it has been proven with experimental data, they do operate correctly.

In summary, by measuring the target scattering matrix at a fixed observation geometry and frequency, the invariant target parameters may be calculated and the resulting target information used to improve signal-to-clutter ratio or to provide the basis for target identification using pattern recognition techniques. These properties will be applied to real data in order to test their capability to describe natural scenes.

2.4 Scattering vectors and second order matrices

So far our attention has been mainly directed toward the scattering matrix. However, other representations of scattering phenomena, based on second order matrices, prove to be useful since they can better deal with the real case of partially polarized waves. It is worthwhile to introduce them before considering, in the next chapter, practical applications of SAR polarimetry.

Let us begin by rewriting the scattering matrix as a *scattering vector*, by means of the following relation [Clo86], [CP96]:

$$\mathbf{k}_{(4)} = \begin{bmatrix} k_0 \\ k_1 \\ k_2 \\ k_3 \end{bmatrix} \stackrel{\text{def}}{=} \frac{1}{2} \begin{bmatrix} \text{Trace}([\mathbf{S}][\Psi_0]) \\ \text{Trace}([\mathbf{S}][\Psi_1]) \\ \text{Trace}([\mathbf{S}][\Psi_2]) \\ \text{Trace}([\mathbf{S}][\Psi_3]) \end{bmatrix}, \quad (2.100)$$

where $\text{Trace}[\mathbf{B}]$ is the sum of the diagonal elements of whatever matrix $[\mathbf{B}]$ and $\Psi = ([\Psi_0], [\Psi_1], [\Psi_2], [\Psi_3])$ is a set of 2×2 complex matrices that form an orthogonal basis.

Among the basis sets used in the literature the most important ones are the following:

$$\Psi_L = \left(2 \begin{bmatrix} 1 & 0 \\ 0 & 0 \end{bmatrix}, 2 \begin{bmatrix} 0 & 1 \\ 0 & 0 \end{bmatrix}, 2 \begin{bmatrix} 0 & 0 \\ 1 & 0 \end{bmatrix}, 2 \begin{bmatrix} 0 & 0 \\ 0 & 1 \end{bmatrix} \right) \quad (2.101)$$

and

$$\begin{aligned} \Psi_P &= \left(\sqrt{2} [\sigma_0], \sqrt{2} [\sigma_1], \sqrt{2} [\sigma_2], \sqrt{2} [\sigma_3] \right) = \\ &= \left(\sqrt{2} \begin{bmatrix} 1 & 0 \\ 0 & 1 \end{bmatrix}, \sqrt{2} \begin{bmatrix} 1 & 0 \\ 0 & -1 \end{bmatrix}, \sqrt{2} \begin{bmatrix} 0 & 1 \\ 1 & 0 \end{bmatrix}, \sqrt{2} \begin{bmatrix} 0 & -j \\ j & 0 \end{bmatrix} \right). \end{aligned} \quad (2.102)$$

The former is a straightforward lexicographic ordering of the elements of $[\mathbf{S}]$, while the latter is based on the Pauli matrices.

Performing the vectorization of $[\mathbf{S}]$ using (2.100), two different scattering vectors can be derived from the bases above:

$$\mathbf{k}_{(4)L} = \begin{bmatrix} S_{hh} \\ S_{hv} \\ S_{vh} \\ S_{vv} \end{bmatrix}, \quad (2.103)$$

$$\mathbf{k}_{(4)P} = \frac{1}{\sqrt{2}} \begin{bmatrix} S_{hh} + S_{vv} \\ S_{hh} - S_{vv} \\ S_{hv} + S_{vh} \\ j(S_{hv} - S_{vh}) \end{bmatrix}. \quad (2.104)$$

Particular attention must be paid to the Pauli matrix basis: as will be shown later, its elements are related to elementary scattering mechanisms so that the scattering vectors can be immediately associated with concrete physical phenomena. For this reason it is also interesting to express the matrix $[\mathbf{S}]$ in terms of the elements of the Pauli scattering vector:

$$[\mathbf{S}] = \begin{bmatrix} k_0 + k_1 & k_2 - jk_3 \\ k_2 + jk_3 & k_0 - k_1 \end{bmatrix}. \quad (2.105)$$

The multiplication factors 2 and $\sqrt{2}$, which appear in (2.101) and (2.102), are needed in order to keep the norm of the scattering vector, which is equal to the total scattered power, independent of the chosen matrix basis Ψ ; in fact:

$$\begin{aligned} \|\mathbf{k}_{(4)}\|^2 &= \langle \mathbf{k}_{(4)} | \mathbf{k}_{(4)} \rangle = \text{Span}([\mathbf{S}]) = \\ &= \text{Trace}([\mathbf{S}][\mathbf{S}]^\dagger) = \text{Trace}([\mathbf{S}]^\dagger[\mathbf{S}]) = \\ &= |S_{hh}|^2 + |S_{hv}|^2 + |S_{vh}|^2 + |S_{vv}|^2. \end{aligned} \quad (2.106)$$

Again, as seen for the change-of-basis of the PSs (see page 19), the transformation from the lexicographic into the Pauli representation of the scattering vectors can be obtained by means of a relation of the type:

$$\mathbf{k}_{(4)P} = [\mathbf{D}_{(4)}]\mathbf{k}_{(4)L}, \quad (2.107)$$

where $[\mathbf{D}_{(4)}]$ is a unitary matrix defined as [CP96]:

$$[\mathbf{D}_{(4)}] = \frac{1}{\sqrt{2}}[\mathbf{A}] \quad (2.108)$$

with the matrix $[\mathbf{A}]$ given by (2.49).

We anticipated on page 18 that real systems involve scatterers situated in dynamic environments and subject to space and/or time variations (non-deterministic scatterers). This causes the EM waves to be partially polarized and prevents the scattering process from being described by a single matrix $[\mathbf{S}]$ only and hence by a single scattering vector.

In order to study such phenomena, it is useful to introduce some new matrices, starting from the *covariance matrix*, obtained by performing the outer product of the

lexicographic scattering vectors:

$$\begin{aligned}
 [\mathbf{C}_{(4)}] &\stackrel{\text{def}}{=} \langle \mathbf{k}_{(4)L} \mathbf{k}_{(4)L}^\dagger \rangle = \\
 &= \begin{bmatrix} \langle |S_{hh}|^2 \rangle & \langle S_{hh} S_{hv}^* \rangle & \langle S_{hh} S_{vh}^* \rangle & \langle S_{hh} S_{vv}^* \rangle \\ \langle S_{hv} S_{hh}^* \rangle & \langle |S_{hv}|^2 \rangle & \langle S_{hv} S_{vh}^* \rangle & \langle S_{hv} S_{vv}^* \rangle \\ \langle S_{vh} S_{hh}^* \rangle & \langle S_{vh} S_{hv}^* \rangle & \langle |S_{vh}|^2 \rangle & \langle S_{vh} S_{vv}^* \rangle \\ \langle S_{vv} S_{hh}^* \rangle & \langle S_{vv} S_{hv}^* \rangle & \langle S_{vv} S_{vh}^* \rangle & \langle |S_{vv}|^2 \rangle \end{bmatrix}. \quad (2.109)
 \end{aligned}$$

A similar expression can be derived by means of the Pauli scattering vectors, which brings to the *coherency matrix* $[\mathbf{T}_{(4)}]$:

$$[\mathbf{T}_{(4)}] \stackrel{\text{def}}{=} \langle \mathbf{k}_{(4)P} \mathbf{k}_{(4)P}^\dagger \rangle. \quad (2.110)$$

Of course, the ensemble averaging becomes redundant for deterministic scatterers; both matrices are by definition Hermitian positive semidefinite.

The relation between $[\mathbf{C}_{(4)}]$ and $[\mathbf{T}_{(4)}]$ follows from straightforward mathematics:

$$\begin{aligned}
 [\mathbf{T}_{(4)}] &= \langle \mathbf{k}_{(4)P} \mathbf{k}_{(4)P}^\dagger \rangle = \langle [\mathbf{D}_{(4)}] \mathbf{k}_{(4)L} \mathbf{k}_{(4)L}^\dagger [\mathbf{D}_{(4)}]^\dagger \rangle = \\
 &= [\mathbf{D}_{(4)}] \langle \mathbf{k}_{(4)L} \mathbf{k}_{(4)L}^\dagger \rangle [\mathbf{D}_{(4)}]^\dagger = [\mathbf{D}_{(4)}] [\mathbf{C}_{(4)}] [\mathbf{D}_{(4)}]^\dagger. \quad (2.111)
 \end{aligned}$$

We know that in the backscattering case the reciprocity theorem constrains scattering matrices to be symmetric, i. e. $S_{hv} = S_{vh}$; in such a case the dimensions of the scattering vectors, and hence of the coherency and covariance matrices, may be reduced as follows:

$$\mathbf{k}_{(3)L} = [\mathbf{Q}] \mathbf{k}_{(4)L} = \begin{bmatrix} S_{hh} \\ \sqrt{2} S_{hv} \\ S_{vv} \end{bmatrix}, \quad (2.112)$$

where:

$$[\mathbf{Q}] = \begin{bmatrix} 1 & 0 & 0 & 0 \\ 0 & 1/\sqrt{2} & 1/\sqrt{2} & 0 \\ 0 & 0 & 0 & 1 \end{bmatrix} \quad (2.113)$$

(with $[\mathbf{Q}][\mathbf{Q}]^t = [\mathbf{I}_{(3)}]$), and in a similar way:

$$\mathbf{k}_{(3)P} = \frac{1}{\sqrt{2}} \begin{bmatrix} S_{hh} + S_{vv} \\ S_{hh} - S_{vv} \\ 2S_{hv} \end{bmatrix}. \quad (2.114)$$

This leads to covariance and coherency matrices of smaller dimensions, 3×3 , defined as:

$$\begin{aligned}
 [\mathbf{C}_{(3)}] &\stackrel{\text{def}}{=} \langle \mathbf{k}_{(3)L} \mathbf{k}_{(3)L}^\dagger \rangle = \\
 &= \begin{bmatrix} \langle |S_{hh}|^2 \rangle & \sqrt{2} \langle S_{hh} S_{hv}^* \rangle & \langle S_{hh} S_{vv}^* \rangle \\ \sqrt{2} \langle S_{hv} S_{hh}^* \rangle & 2 \langle |S_{hv}|^2 \rangle & \sqrt{2} \langle S_{hv} S_{vv}^* \rangle \\ \langle S_{vv} S_{hh}^* \rangle & \sqrt{2} \langle S_{vv} S_{hv}^* \rangle & \langle |S_{vv}|^2 \rangle \end{bmatrix} \quad (2.115)
 \end{aligned}$$

and

$$\begin{aligned}
 [\mathbf{T}_{(3)}] &\stackrel{\text{def}}{=} \langle \mathbf{k}_{(3)P} \mathbf{k}_{(3)P}^\dagger \rangle = \\
 &= \frac{1}{2} \begin{bmatrix} \langle |S_{hh} + S_{vv}|^2 \rangle & \langle (S_{hh} + S_{vv})(S_{hh} - S_{vv})^* \rangle & 2\langle S_{hv}^*(S_{hh} + S_{vv}) \rangle \\ \langle (S_{hh} + S_{vv})^*(S_{hh} - S_{vv}) \rangle & \langle |S_{hh} - S_{vv}|^2 \rangle & 2\langle S_{hv}^*(S_{hh} - S_{vv}) \rangle \\ 2\langle S_{hv}(S_{hh} + S_{vv})^* \rangle & 2\langle S_{hv}(S_{hh} - S_{vv})^* \rangle & 4\langle |S_{hv}|^2 \rangle \end{bmatrix}.
 \end{aligned} \tag{2.116}$$

The transformation from one representation to the other is again obtained using a unitary matrix, so that:

$$\mathbf{k}_{(3)P} = [\mathbf{D}_{(3)}] \mathbf{k}_{(3)L} \tag{2.117}$$

and

$$[\mathbf{T}_{(3)}] = [\mathbf{D}_{(3)}][\mathbf{C}_{(3)}][\mathbf{D}_{(3)}]^\dagger, \tag{2.118}$$

with:

$$[\mathbf{D}_{(3)}] = \frac{1}{\sqrt{2}} \begin{bmatrix} 1 & 0 & 1 \\ 1 & 0 & -1 \\ 0 & \sqrt{2} & 0 \end{bmatrix}. \tag{2.119}$$

2.5 Target decomposition theorems

By means of the new representations provided by the scattering vectors and the covariance and coherency matrices, it is now possible to discuss the *target decomposition (TD) theorems*. These methods provide a physical interpretation of the scattered signals, that is achieved by considering them as superpositions of several contributions and trying to recognize each of them. This approach was first outlined by Chandrasekhar for light scattering by small anisotropic particles and later applied to polarized MW by Huynen [Huy70].

Following Huynen's fundamental contribution, several decomposition techniques were proposed, some of them attempting to overcome some limitations of Huynen's method.

According to [CP96], three primary classes of such decompositions may be defined:

- *coherent* theorems, that decompose the $[\mathbf{S}]$ matrix into the sum of elementary matrices;
- Huynen type decompositions, which attempt to extract a single scattering matrix from the average Kennaugh matrix;
- eigenvector decompositions of the coherency or covariance matrices.

Coherent decomposition theorems use $[\mathbf{S}]$ matrices, and their underlying principle is to consider a generic scattering matrix as a linear combination of several others, each defining a simple deterministic scatterer. Unlike the above mentioned decompositions of power reflection matrices, decompositions of the scattering matrix are particularly suited for cases where the scattering is due to few dominant scattering centres.

For example, using the Pauli matrices it is possible to write:

$$\begin{aligned} [\mathbf{S}] &= \begin{bmatrix} a+b & c-jd \\ c+jd & a-b \end{bmatrix} = \\ &= a \begin{bmatrix} 1 & 0 \\ 0 & 1 \end{bmatrix} + b \begin{bmatrix} 1 & 0 \\ 0 & -1 \end{bmatrix} + c \begin{bmatrix} 0 & 1 \\ 1 & 0 \end{bmatrix} + d \begin{bmatrix} 0 & -j \\ j & 0 \end{bmatrix}, \end{aligned} \quad (2.120)$$

where a , b , c and d are all complex and correspond to the elements of the Pauli scattering vector (see Equation (2.105)).

According to the hypotheses that have been made, this decomposition yields the coherent sum of four scattering mechanisms: the first being single scattering from a plane surface, the second and third being diplane scattering from corner reflectors with a relative orientation of 45° and the final element being all the antisymmetric components of the matrix $[\mathbf{S}]$ (which corresponds to a scatterer that transforms every incident polarization into its orthogonal state). As it causes $[\mathbf{S}]$ to be non-symmetric, the last term disappears, of course, in reciprocal backscattering cases.

Another example of a coherent TD method was presented by Krogager [Kro92], [Kro93]. His approach was based on the observation that any complex, symmetric scattering matrix can be decomposed into three components, as if the scattering were due to a sphere, a diplane and a right- or left-rotating helix. This can be shown by manipulating the real and imaginary parts of the elements of $[\mathbf{S}]$, resulting in the following formulation:

$$[\mathbf{S}] = k_s[\mathbf{S}]_{\text{sphere}} + e^{j\phi}(k_d[\mathbf{S}]_{\text{diplane}} + k_h[\mathbf{S}]_{\text{helix}}), \quad (2.121)$$

where k_s , k_d and k_h are real quantities and ϕ represents a relative phase which is equal to the displacement of the diplane and the helix relative to the sphere.⁶

The sphere, diplane and helix (henceforth denoted SDH) terms are related to measurable and familiar quantities, in that k_s and k_d can be measured directly using circular polarizations. In relation to target imaging, this decomposition provides a means for representing the target return in three different images, each characterizing different scattering mechanisms. The advantage is that for those cases where one of the types of scattering is predominant, the image corresponding to that type will be the only one containing significant response from the resolution cell in question. A resulting colour composite image would behave in this way, providing a valid classification system based on the relative contribution of the three mechanisms. This is particularly useful for practical applications, because the radar scattering can often be ascribed to one or more individual scatterers within each resolution cell. These individual contributions are typically due to major surfaces and to two- or three-sided corners reflectors (dihedral and trihedral). The role of the helix in the above decomposition becomes apparent from the fact that helix-like scattering may be produced by two or more dihedrals, depending on their relative orientation angles and displacements. On the other hand, helices as such are rarely found in practice. This means that, for resolution cells where a significant amount of helix-like scattering is found, one may conclude that the scattering from those resolution cells is mainly due to two or more even-bounce reflection mechanisms. For diagnostic purposes such information is obviously useful. Likewise

⁶In Appendix B are reported the exact expressions of the k coefficients as well as details on the following example of coherent decomposition, the Cameron one.

it is very useful to be able to determine whether the dominating scattering from a resolution cell is due to a single bounce mechanism or to a double bounce mechanism [vZZE87], [vZ89].

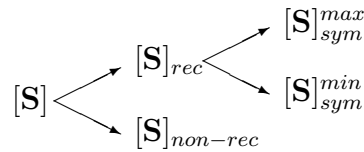
The approach proposed by Cameron [CL90], [CYL96] may be considered as a more generalized example of the “model fitting” seen with the SDH decomposition. Given a generic matrix $[S]$ (not only in the monostatic case), one can characterize it by its tendency of being more or less symmetric according to the reciprocity rule and split it into two terms representing reciprocal and non-reciprocal scattering mechanisms. Using the $\mathbf{k}_{(4)L}$ vector corresponding to $[S]$ this decomposition is expressed by:

$$\mathbf{k}_{(4)L} = \mathbf{k}_{rec} + \mathbf{k}_{non-rec} . \quad (2.122)$$

In turn, the reciprocal term (the one usually available after calibrating monostatic radar data) represents a target which is more or less symmetric with respect to an axis in the plane orthogonal to the radar line-of-sight and again a distinction can be made between the most dominant and the least dominant symmetric target components,⁷ that is:

$$\mathbf{k}_{rec} = \mathbf{k}_{sym}^{max} + \mathbf{k}_{sym}^{min} . \quad (2.123)$$

Hence, the decomposition follows the scheme:



The degrees of reciprocity and symmetry are evaluated in terms of projection angles of the scattering vectors onto the corresponding subspace and subsets via proper projection operators. In a similar way, one may compare an arbitrary scattering matrix to a model scattering matrix. In [CL90], this principle was further pursued leading to a matrix classification scheme able to assign $[S]$ to one of eleven classes according to the degree of reciprocity, symmetry and resemblance to a set of model matrices.

In contrast to coherent methods, Huynen decomposition [Huy70] acts on the Kennaugh matrix and is based on two key principles: to consider distributed targets for which $\langle [K] \rangle$ has no single equivalent scattering matrix; to try and extract from this average a “single” Kennaugh matrix (and hence a corresponding $[S]$ matrix) and a “N-targets” (i. e., random) contribution. This idea was expressed in mathematical terms in the following way:

$$\langle [K] \rangle = [K_s] + \langle [K_N] \rangle . \quad (2.124)$$

One of the limits of this approach is that, in general, it does not provide the invariance of the residue N-matrix under all possible unitary transformations [Clo92].

In fact, Huynen decomposition can also be performed using an equivalent coherency matrix representation; as this other form can be used to generate a diagonal coherency

⁷One should note the difference in the use of the word “symmetry” when referred to scattering matrices and to targets. Indeed, according to the Cameron decomposition, scattering matrices which are symmetric due to the reciprocity constraint may refer to targets which are *geometrically* more or less symmetric in the plane orthogonal to the radar line-of-sight (in the case of a helix, a symmetric scattering matrix describes a target which is not geometrically symmetric).

matrix, which may be physically interpreted as statistical independence between a set of target vectors, such an approach yields a general decomposition into independent scattering processes. The general expression of this diagonalization is the following:

$$[\mathbf{T}_{(3)}] = [\mathbf{U}_{(3)}][\mathbf{\Lambda}][\mathbf{U}_{(3)}]^{-1}, \quad (2.125)$$

where:

$$[\mathbf{\Lambda}] = \begin{bmatrix} \lambda_1 & 0 & 0 \\ 0 & \lambda_2 & 0 \\ 0 & 0 & \lambda_3 \end{bmatrix} \quad (2.126)$$

is the diagonal matrix with elements the real non-negative eigenvalues, $0 \leq \lambda_1 \leq \lambda_2 \leq \lambda_3$, of $[\mathbf{T}_{(3)}]$ (the coherency matrix is, indeed, Hermitian positive semidefinite) and

$$[\mathbf{U}_{(3)}] = [\mathbf{e}_1 \quad \mathbf{e}_2 \quad \mathbf{e}_3] \quad (2.127)$$

is the unitary eigenvector matrix built using as columns the eigenvectors of $[\mathbf{T}_{(3)}]$. The eigenvectors are orthogonal since the coherency matrix is Hermitian.

By means of the diagonalization of $[\mathbf{T}_{(3)}]$, which is in general of rank 3, the interaction is represented by the non-coherent sum (see the definition (2.116) of $[\mathbf{T}_{(3)}]$) of three independent (in the sense that they are connected to orthogonal vectors) coherency matrices $[\mathbf{T}_{(3)i}]$, each weighted by its eigenvalue:

$$[\mathbf{T}_{(3)}] = [\mathbf{U}_{(3)}][\mathbf{\Lambda}][\mathbf{U}_{(3)}]^{-1} = \sum_{i=1}^3 \lambda_i [\mathbf{T}_{(3)i}] = \sum_{i=1}^3 \lambda_i \mathbf{e}_i \mathbf{e}_i^\dagger. \quad (2.128)$$

For each $[\mathbf{T}_{(3)i}]$ matrix it is possible to define a corresponding scattering matrix (i. e., a deterministic scattering contribution), while the choice of the eigenvectors for building the unitary matrix $[\mathbf{U}_{(3)}]$ always guarantees an orthogonal basis set. The correspondence between the resulting coherency matrices and their respective scattering matrices may be referred as well to the relative eigenvectors so that also these can be used to represent scattering mechanisms as the $[\mathbf{S}]$ matrices.

3 SAR polarimetry

3.1 Basics

In this section, SAR systems for polarimetric applications will be introduced. At first, a general review of the SAR sensors presently operating will be made, of the single-polarization systems as well as of the multi-polarimetric ones. Then, only polarimetric SARs will be considered and some aspects of their practical applications will be analyzed. This should provide a first insight on the potentials of these systems.

Theoretical questions which derive from the complexity of the topic, will be discussed later on in this chapter.

3.1.1 SAR sensors

As stated before, synthetic aperture radars present important advantages with respect to conventional ones. Thus, since the beginning of the eighties, a great deal of work has been performed using these systems. At present, there are several SAR sensors in operation: single-polarization systems as well as multi-polarimetric ones. Noteworthy examples in the first group are the satellite mounted SAR systems: ERS-2 (by ESA, operating in C-band), JERS-1 (Japanese, L-band) and RADARSAT-1 (Canadian, C-band) and various airborne systems, namely: TOP-SAR (NASA/JPL, C- and L-band), IFSARE (Environmental Research Institute of Michigan, X-band), C/X-SAR (CCRS, Canada, X- and C-band), EMI-SAR (Danish Defence Research Establishment, C-band), E-SAR (DLR, X-, C-, L- and P-band), DoSAR (Dornier, Germany, X- and C-band), AeS-1 (AeroSensing, Germany, X-band), RAMSES (Onera, France, X-band), AER-II (FGAN, Germany, X-band) and ESR (DERA, UK, X-band). In the second group are included the airborne radars: AIRSAR (by NASA/JPL, which operates in fully polarimetric mode in C-, L- and P-band and which has to be mentioned as the forerunner of all polarimetric SAR), EMI-SAR (DDRE, Denmark, C- and L-band), E-SAR (DLR, L- and P-band) and NABC/ERIM SAR (ERIM, USA, X-, C- and L-band), and the ASAR C-band sensor mounted on the ESA ENVISAT satellite. To both groups belongs the Shuttle Imaging Radar SIR-C/X-SAR, which was flown twice in April and October 1994 and later, in February 2000, with a second antenna mounted on a 60 m boom for the Shuttle Radar Topography Mission (SRTM): part of the data of the missions were acquired in fully polarimetric mode in C- and L-band.

The main advantages of SAR systems arise from their imaging geometry, which requires a moving antenna (see Figure 3.1). Scene imaging with a moving device permits

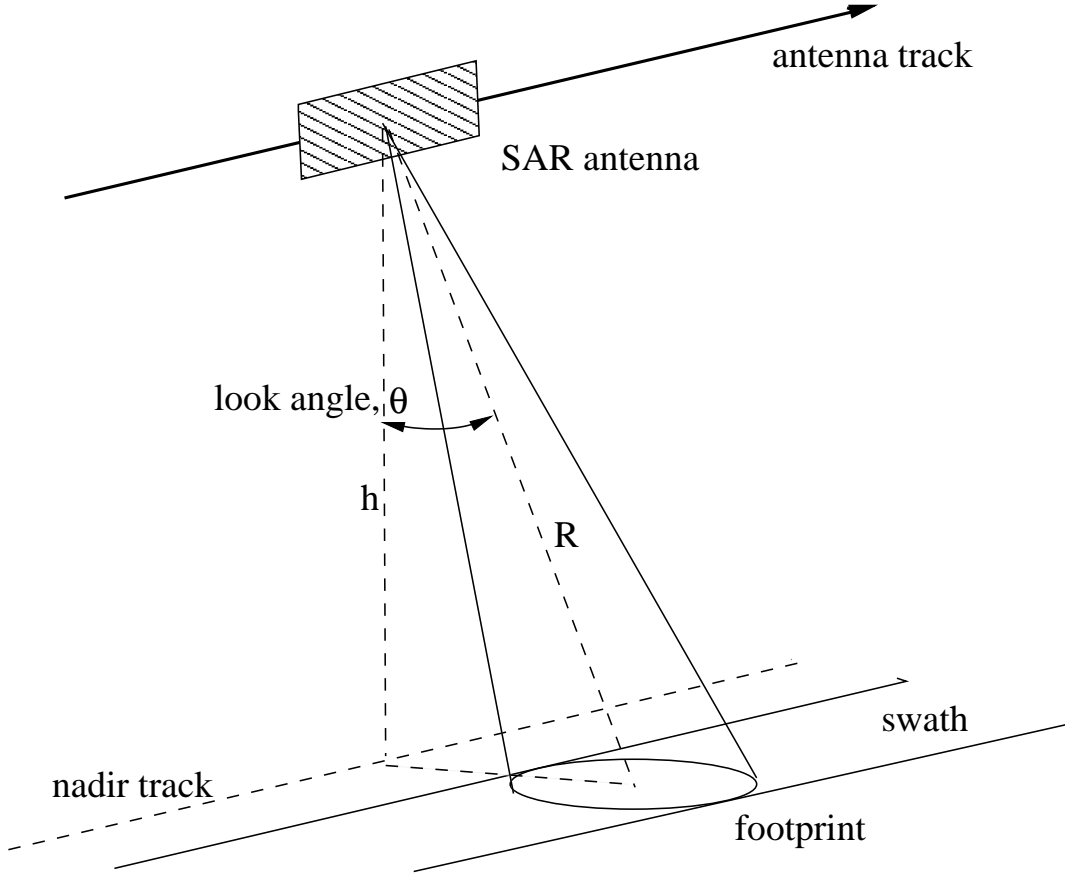


Figure 3.1: SAR imaging geometry.

the simulation of antenna dimensions much larger than the real ones and makes resolution along the flight-path independent of the sensor-target distance.

3.1.2 Early experimental results

Some of the earliest results obtained with SAR polarimetric systems were presented in a series of related papers by Zebker et al. [ZvZH87], van Zyl et al. [vZZE87] and Evans et al. [EFvZZ88], following data acquisition campaigns of the NASA/JPL high-resolution airborne imaging polarimetric SAR (further details on this apparatus, operating mainly in L-band and later extended to C- and P-band, can be found in [ZvZ91]). In particular, van Zyl et al. [vZZE87] reported experimental proofs of some basic scattering models: from a large, smooth dielectric surface, from a rough surface and from a dihedral corner reflector.

In [vZZE87], the scattering cross section $\sigma = \sigma(\psi_T, \chi_T)$ introduced with (2.56) is called the *polarization signature* of the scatterer and is widely used as it provides a really useful graphical representation of the behaviour of different targets. Indeed, the information contained in $\sigma(\psi_T, \chi_T)$ may be displayed as three-dimensional figures expressing the intensity of the backscattering from a target for varying ellipticity χ_T and ellipse orientation ψ_T of the transmitted wave.

The polarization signature, through its plots, has proven to be a valid tool in pat-

tern recognition. For example, a dihedral corner reflector, where the transmitted wave suffers two reflections, has a polarization signature which differs significantly from that of a wave which is scattered by a rough surface. With respect to these models, backscatter from ocean exhibits a polarization signature similar to that predicted by the one of scattering by a slightly rough dielectric surface. Urban regions exhibit the characteristics expected from dihedral corner reflectors and their polarization signature is quite different from that of the ocean or of the single-reflection slightly rough model [EFvZZ88], [ZvZ91].

Rough surface scattering presents an interesting behaviour: in this case, the three-dimensional plot of $\sigma(\psi_T, \chi_T)$ has minima which never go to null (as happens for other model scatterers). Hence, a “pedestal” of power returns always greater than zero appears in the polarization signature of rough surfaces. As pointed out in [vZZE87], this means that there is some portion of the return which cannot be nulled by changing the polarization of the transmitting and receiving antennae. In polarimetric observations, the presence of a pedestal in the signature means that the individual measured matrices used to calculate the signature were not identical. The more different the individual matrices, the higher the resulting pedestal. In radar images, this variation of scattering properties results from various different effects which all cause the measured scattering, and hence Kennaugh matrices of adjacent resolution elements, to be slightly different. The most obvious cause of such a variation is when adjacent pixels really contain different types of scatterers. Other causes include diffuse (that is, multiple) scattering and the presence of noise [vZZ90].

Based on these results, an unsupervised classification¹ algorithm able to distinguish between scattering with even number of reflections, odd number of reflections and diffuse scattering, was tested with good results and presented in a paper by van Zyl in 1989 [vZ89]. It was shown, for example, that information about the health of forests can be retrieved without ancillary data, just using this broad class division.

Unfortunately, polarization signatures are not unique. For instance, the polarization signature of a dielectric sphere has the same form as that of a smooth dielectric surface at normal incidence. It is also conceivable that different combinations of various scattering mechanisms may yield the same resulting $\sigma(\psi_R, \chi_R, \psi_T, \chi_T)$. However, under a more general point of view, it was evident that different polarizations (i. e., different transmitting and receiving settings) would provide different information according to the characteristics of the observed scene.

Further aspects of pattern recognition and image interpretation methods will be analyzed in following sections of this work as this area of study frequently overlaps with those of the inversion methods and, when used for these purposes, of the interferometric applications.

As stated before, an important characteristic of radar devices is that they permit measurements of the phase of the signal at a receiving antenna. In this way, besides studies on the scattered power (as the series reported above), it is possible to analyze the phase of both the orthogonal components of an EM wave.

An interesting example of these possibilities was reported in a paper by Ulaby et al. in 1987 [UHD⁺87]. Again the data used were those of the JPL L-band SAR, but the

¹A definition of unsupervised classification may be found in Paragraph 4.2.

attention was there devoted to the statistical behaviour of the phase difference between the hh -polarized and the vv -polarized backscattered signals:

$$\phi_{hhvv} = \phi_{hh} - \phi_{vv}. \quad (3.1)$$

Measurements were performed over agricultural test sites. While for the overwhelming majority of cases the ϕ_{hhvv} distribution was symmetrical and centered around a zero mean value, a different pattern was observed for corn fields: the mean phase difference was different from zero and increased with increasing look angle θ (see Figure 3.1). The explanation proposed for this variation was that the corn canopy, most of whose mass is contained in its vertical stalks, acts like uniaxial crystal characterized by different velocities of propagation for waves with horizontal and vertical polarization. Hence, assuming further that the observed backscatter was contributed by direct backscatter from plants, direct backscatter from soil and double-bounce reflection on soil and plants, a good agreement was found between measurements and model-derived expectation values.

About the expected distribution of ϕ_{hhvv} , a valid model was later proposed by Sarabandi [Sar92]. According to his general hypotheses, the probability density functions of the phase differences of the scattering matrix elements were derived from the average Kennaugh, assuming that the elements of $[S]$ are jointly Gaussian. As a result, the expressions defined for the co- and cross-polarized phase differences were similar in form and could be considered analogous to the Gaussian distribution for periodic random variables.

It must be stressed that, regardless of the interesting features related to this kind of analysis, studies on the phase behaviour of the scattered signals have not been fully exploited and can be considered as a promising subject for further investigations.

3.1.3 Calibration techniques

A completely different research topic on SAR polarimetric data arises from the calibration problem [ZvZ91], [Fre92] (the latter also for a particularly rich bibliography on this subject).

A fully polarimetric radar measures the full scattering matrix for every resolution element in an image. The increase of information with respect to “scalar” radar comes at a price, not only in the increase in complexity of the design and in the cost of building the radar system and processing the data, but also in the amount of effort needed to calibrate the data. Moreover, calibration is specific and peculiar to each apparatus since each has its own calibration needs.

In [vZ90], a technique was described which used the theoretical result that, for natural targets with azimuthal symmetry, the co- and cross-polarized components of the scattering matrix are uncorrelated. Representing this in mathematical form, this means that:

$$\langle S_{hh}^* S_{hv} \rangle = 0 \quad (3.2)$$

and

$$\langle S_{vv}^* S_{vh} \rangle = 0, \quad (3.3)$$

where, again, $\langle \rangle$ represents the ensemble average over an extended area (i. e., over several resolution elements).

The tests reported in [vZ90] confirmed the validity of the assumptions (3.2) and (3.3) for several terrain types, including desert surfaces, ocean surfaces, grasslands and sea ice, and only showed departures for heavily vegetated areas. The main advantage of this calibration technique was that it does not require any external calibration device to be deployed in the observed area before imaging. Besides this, the whole calibration process resulted in being separable in several independent stages and the cross-talk calibration to be a well defined part of it.

The already cited paper by Freeman [Fre92] is, instead, a more general survey on calibration problem, with a wide descriptive purpose; along with other techniques available for polarimetric data, examples are provided also for methods for calibrating interferometric SAR data.

3.2 Interactions with the Earth surface

When describing the first experimental applications of polarimetric SAR, we referred several times to “smooth” and “rough” surfaces. Let us now see more carefully what we meant with these terms and how the roughness of a surface actually influences the scattering of an EM wave.

In general, all natural surfaces may be considered as rough but roughness is not an intrinsic property of the scattering surfaces since it depends on the properties of the incident wave. Indeed, both the frequency and the incidence angle of the transmitted wave determine how rough or smooth a certain surface appears to be.

Considering constant wavelength and local incidence angle, the interaction of an EM wave with surfaces of different roughness may be simplified as follows: the rougher the surface, the more diffuse the scattering or the smoother the surface, the more directional the scattering. The case of an ideal smooth boundary surface between two dielectric media, for instance the air and a homogeneous soil, was explained by Fresnel who also determined the reflection coefficient of the horizontal and vertical components of an incoming wave as:

$$\Gamma_h(\theta) = \frac{\mu \cos \theta - \sqrt{\mu\epsilon - \sin^2 \theta}}{\mu \cos \theta + \sqrt{\mu\epsilon - \sin^2 \theta}}, \quad (3.4)$$

$$\Gamma_v(\theta) = \frac{\epsilon \cos \theta - \sqrt{\mu\epsilon - \sin^2 \theta}}{\epsilon \cos \theta + \sqrt{\mu\epsilon - \sin^2 \theta}}, \quad (3.5)$$

where μ and ϵ are, respectively, the dielectric constant and the magnetic permeability of the soil and θ the wave incidence angle.

In natural environments, the hypothesis of smooth boundary surface is hardly met so that also the scattering presents different characteristics. The backscattered EM wave from a natural surface consists of two components: a reflected, coherent part and a diffused, incoherent one (see Figure 3.2). The former resembles the behaviour of specular reflection on a smooth surface and thus, in the case of a monostatic radar,

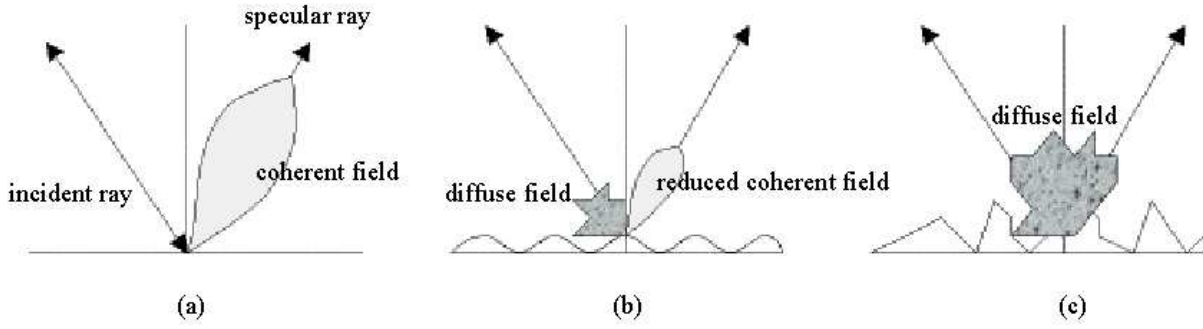


Figure 3.2: Scattering behaviour relative to: (a) smooth, (b) rough, (c) very rough surfaces (courtesy of I. Hajnsek [Haj01]).

gives no scatter return; the latter is a diffuse scatter and distributes the scattered power in all directions. As the surface becomes rougher, the coherent component becomes negligible and the incoherent one consists of only diffuse scattering.

From an electromagnetic point of view, the definition of a surface as rough or smooth is somewhat arbitrary. Nevertheless, in the literature two main criteria can be found to define the roughness of a surface: the Rayleigh and the Fraunhofer criterion [UMF82]. Considering a plane monochromatic wave transmitted at some angle θ onto a rough surface as represented in Figure 3.3, one can easily calculate the phase difference $\Delta\phi$ between two rays scattered from different points on the surface:

$$\Delta\phi = 2h \frac{2\pi}{\lambda} \cos \theta, \quad (3.6)$$

where h expresses the standard deviation of the roughness height with respect to a reference plane and λ is the wavelength of the incident wave. The Rayleigh criterion states that if the phase difference $\Delta\phi$ is less than $\pi/2$ radians, i. e., if

$$h < \frac{\lambda}{8 \cos \theta}, \quad (3.7)$$

then the surface may be considered as smooth. The Fraunhofer criterion is more strin-

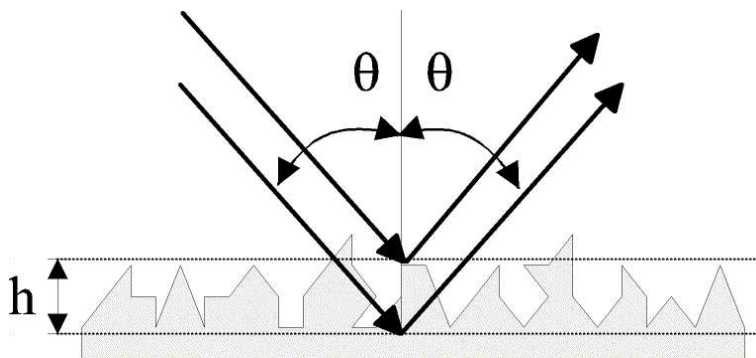


Figure 3.3: Diagram for determining the phase difference between two parallel waves scattered from different points on a rough surface (courtesy of I. Hajnsek [Haj01]).

gent and requires a $\Delta\phi$ less than $\pi/8$ radians to define a surface as smooth, hence:

$$h < \frac{\lambda}{32 \cos \theta}. \quad (3.8)$$

3.3 Entropy/ α analysis

Among the theoretical methods that have been recently applied to the interpretation of SAR polarimetric data, the entropy/ α analysis seems to be particularly promising and interesting.

Using the eigenvector-based decomposition of the coherency matrix discussed on page 29, the relative importance of each scattering mechanism (within a given resolution cell) is expressed by means of its eigenvalues. Indeed, whereas the eigenvectors discriminate the presence of different scattering behaviours, the eigenvalues underline the intensity of each mechanism. A quantity that measures the randomness of these scattering processes is the *polarimetric scattering entropy*² H defined as follows:

$$H = \sum_{i=1}^3 -P_i \log_3 P_i, \quad (3.9)$$

where:

$$P_i = \frac{\lambda_i}{\sum_{l=1}^3 \lambda_l}. \quad (3.10)$$

P_i represents the “appearance probability” of each contribution. H ranges from 0 to 1:

- an entropy equal to 0 corresponds to a deterministic scattering process ($[\mathbf{T}_{(3)}]$ has only one non-vanishing eigenvalue);
- an entropy equal to 1 indicates a degenerated eigenvalue spectrum, typical of random noise processes ($[\mathbf{T}_{(3)}]$ has three identical eigenvalues).

To estimate the relative importance of the different scattering mechanisms, a second polarimetric indicator has been introduced, the *polarimetric anisotropy* A :

$$A = \frac{\lambda_2 - \lambda_3}{\lambda_2 + \lambda_3}. \quad (3.11)$$

When H tends to 1 (i. e., when: $\lambda_1 \simeq \lambda_2 \simeq \lambda_3$) or to 0 ($\lambda_2 \simeq \lambda_3 \simeq 0$), A gives no further information except for low and medium H ($\lambda_1 > \lambda_2, \lambda_3$), whereas the entropy says nothing about the relationship between the two minor eigenvalues; the anisotropy supplies this information. Thus, a medium entropy means that more than a single scattering mechanism contributes to the back-scattered signal, but it is not clear how many additional mechanisms are present (one or two). A high A states that only the

²The scattering entropy formulation was first introduced to describe the depolarization degree of an EM wave (see [BW85]).

second scattering mechanism is important, whereas a low A indicates a remarkable contribution of the third one as well.

It is important to note that the set of orthogonal components represented by the three eigenvectors has no direct physical significance in terms of real scattering mechanism. In order to provide a physical interpretation, one needs to relate the degrees of freedom of the mathematical problem to the observed scattering process [Pap99]. One should first observe that, in the general bistatic case, the 4×4 covariance and coherency matrices contain sixteen independent parameters, namely four real power values and six complex cross-correlations; in the backscattering case the matrices reduce to 3×3 ones and contain nine independent parameters. On page 16, we have seen that a coherent matrix $[S]$ has instead seven independent parameters in the bistatic case and five in the reciprocal monostatic one. It is then evident that some limits exist for a single scattering matrix to represent a partial scatterer since the latter has, at least, four more degrees of freedom. The question is then how to interpret these extra degrees of freedom which the coherency (or covariance) matrix seems to take into account.

Let us reconsider the backscattering case and the \mathbf{k} vector derived in the Pauli matrix basis as expressed by Equation (2.114).

The terms that there appear are simply the three complex elements of the $[S]$ matrix: S_{hh} , S_{vv} and S_{hv} . This implies that the scattering vector is characterized by six independent parameters.

Further, $\mathbf{k}_{(3)P}$ can be written as:

$$\mathbf{k}_{(3)P} = \|\mathbf{k}_{(3)P}\| \mathbf{w}, \quad (3.12)$$

introducing the normalized vector \mathbf{w} which has only five degrees of freedom because of the normalization constraint. Since each generic \mathbf{k} vector is associated with an $[S]$ matrix, and hence to a scattering mechanism, so is each \mathbf{w} vector. The five independent parameters may be associated with five angles, so that:

$$\mathbf{w} = \begin{bmatrix} \cos \alpha \exp(-j\phi) \\ \sin \alpha \cos \beta \exp(-j\delta) \\ \sin \alpha \sin \beta \exp(-j\gamma) \end{bmatrix}. \quad (3.13)$$

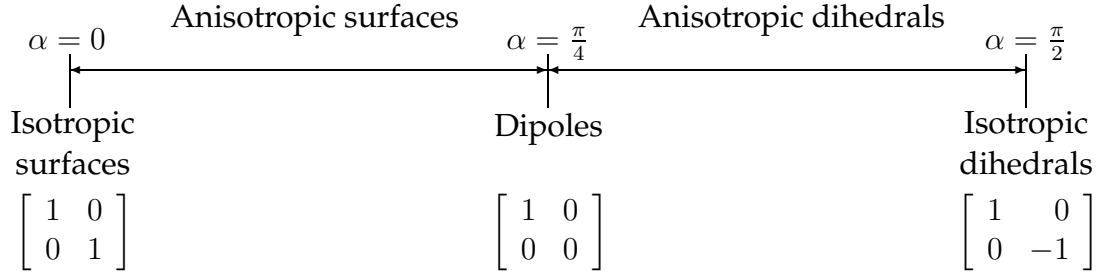
A change $\Delta\alpha$ and $\Delta\beta$ of the two angles α and β causes a transformation of \mathbf{w} described by two rotation matrices:

$$\mathbf{w}' = \begin{bmatrix} \cos \Delta\alpha & -\sin \Delta\alpha & 0 \\ \sin \Delta\alpha & \cos \Delta\alpha & 0 \\ 0 & 0 & 1 \end{bmatrix} \mathbf{w} \quad (3.14)$$

and

$$\mathbf{w}' = \begin{bmatrix} 1 & 0 & 0 \\ 0 & \cos \Delta\beta & -\sin \Delta\beta \\ 0 & \sin \Delta\beta & \cos \Delta\beta \end{bmatrix} \mathbf{w}. \quad (3.15)$$

This observation leads to the *scattering vectors reduction theorem*: it is always possible to reduce an arbitrary scattering mechanism, represented by a complex unitary vector

Figure 3.4: Scheme of the α angle interpretation.

\mathbf{w} , to the identity $\begin{bmatrix} 1 & 0 & 0 \end{bmatrix}^t$ by means of the following transformations:

$$\begin{bmatrix} 1 \\ 0 \\ 0 \end{bmatrix} = \begin{bmatrix} \cos \alpha & \sin \alpha & 0 \\ -\sin \alpha & \cos \alpha & 0 \\ 0 & 0 & 1 \end{bmatrix} \begin{bmatrix} 1 & 0 & 0 \\ 0 & \cos \beta & \sin \beta \\ 0 & -\sin \beta & \cos \beta \end{bmatrix} \begin{bmatrix} e^{j\phi} & 0 & 0 \\ 0 & e^{j\delta} & 0 \\ 0 & 0 & e^{j\gamma} \end{bmatrix} \mathbf{w}. \quad (3.16)$$

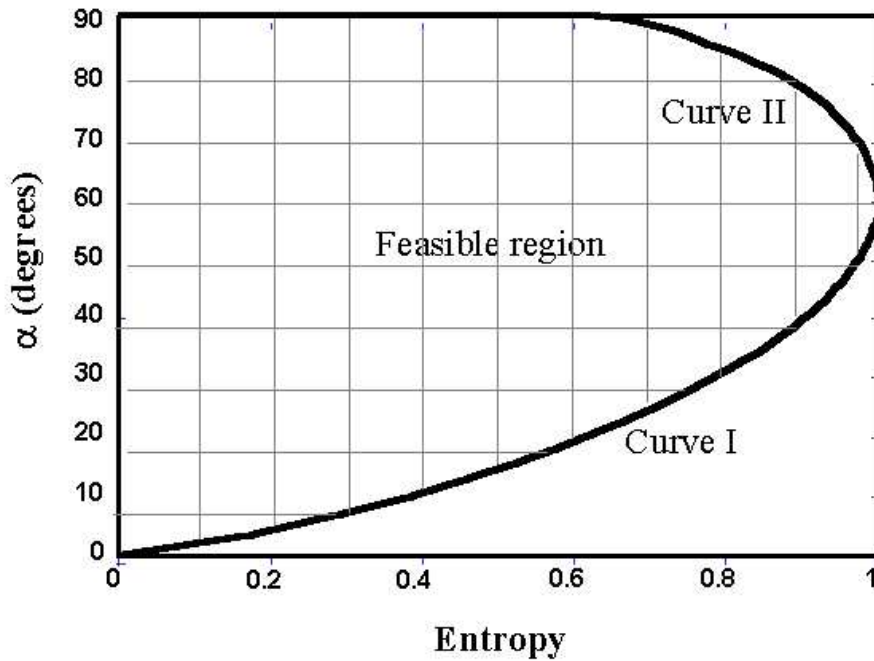
The third matrix represents a set of scattering phase angles, whereas the first and the second ones are canonical forms of plane rotations. Physically only one of them, β , which ranges from $-\pi$ to π , corresponds to a physical rotation of the sensor coordinates. Indeed, as long as we use the Pauli basis for the vectorization of the scattering matrix, β represents the physical orientation of the scatterer about the line-of-sight [Pap99]. Hence, by calculating β , one may obtain a direct estimate of the target orientation angles (a much simpler way than the polarimetric signature or the Stokes reflection matrix to determine the target orientation).

The parameter α is not related to the target orientation but represents an internal degree of freedom of the scatterer. It is associated with the “type” of scattering mechanism and can vary in the range $[0, \pi/2]$. $\alpha = 0$ stands for isotropic surfaces, $\alpha = \pi/2$ for isotropic diplanes or helices. Low values of α represent all-anisotropic scattering mechanisms with S_{hh} different from S_{vv} . The boundary between anisotropic surfaces and diplanes is represented by the case $\alpha = \pi/4$, which describes an horizontal dipole. Finally, the information provided by α about the scatterer is independent of its orientation β , and hence unaffected also by eventual misplacements between radar and scatterer reference.

When multiple scattering mechanisms are present in the same coherency matrix (i. e., when more than one eigenvalue appearing in (2.128) is different from zero), the target is represented by $[\mathbf{S}]$ matrices that occur with the probabilities P_i just seen. In this case, a description of the overall scattering is possible by applying the parameterization (3.13) to each eigenvector of $[\mathbf{T}_{(3)}]$ and then evaluating the mean of these parameters. In particular, the average $\bar{\alpha}$:

$$\bar{\alpha} = P_1 \alpha_1 + P_2 \alpha_2 + P_3 \alpha_3 \quad (3.17)$$

results as the most useful quantity. Target behaviour may indeed be studied in a two-dimensional H/α space. Here, since some limits exist to the variation of $\bar{\alpha}$ as a function of H , not all the space actually represents real scatterers (i. e., not all the values of entropy and $\bar{\alpha}$ have a physical meaning). The curves I and II of Figure 3.5 limit the feasible space [CFLSS99]. In turn, boundaries can be drawn between sub-areas of this

Figure 3.5: H/α plane.

region referring to targets with well-defined characteristics (expressed by their values of $\bar{\alpha}$ and H); the partition among various regions of the H/α space can actually be used as a classification method as reported in [CP97].

As we have seen, the unitary matrices needed for the change-of-basis relations can be derived only by means of the vectors of the bases involved, so that building a unitary matrix using three orthogonal vectors \mathbf{w} yields $3 \times 5 = 15$ parameters and six constraints due to orthogonality: this means nine degrees of freedom (eight considering also the special unitarity constraint, $\det[\mathbf{U}_{(3)}] = 1$). Thus, bearing in mind these characteristics of the change-of-basis matrices, it is possible to interpret the difference in number of independent parameters between the scattering and coherency (or covariance) matrices. In order to fully describe these additional degrees of freedom, they are no longer assigned to the “wave” representation, but to the projection matrices (the unitary matrices) of the scattering vectors onto the chosen basis of orthogonal vectors \mathbf{w} (i. e., to the chosen ensemble of scattering mechanisms).

3.4 Polarimetric SAR interferometry

This paragraph will introduce the theory concerning the use of polarimetric data for interferometric applications. Here, only some basic concepts will be given and a more sophisticated treatment will follow later in this work.

Relatively few examples of interferometric applications of polarimetric SAR data have been until recently reported in the literature. The main results in this field, to which this section is dedicated, are those presented by Cloude’s research group [CP98], [Pap99], [PRC99a], [PRC99b]. At present, also the potential of interferometry with single-polarization systems is actively investigated (for example, the use of interfero-

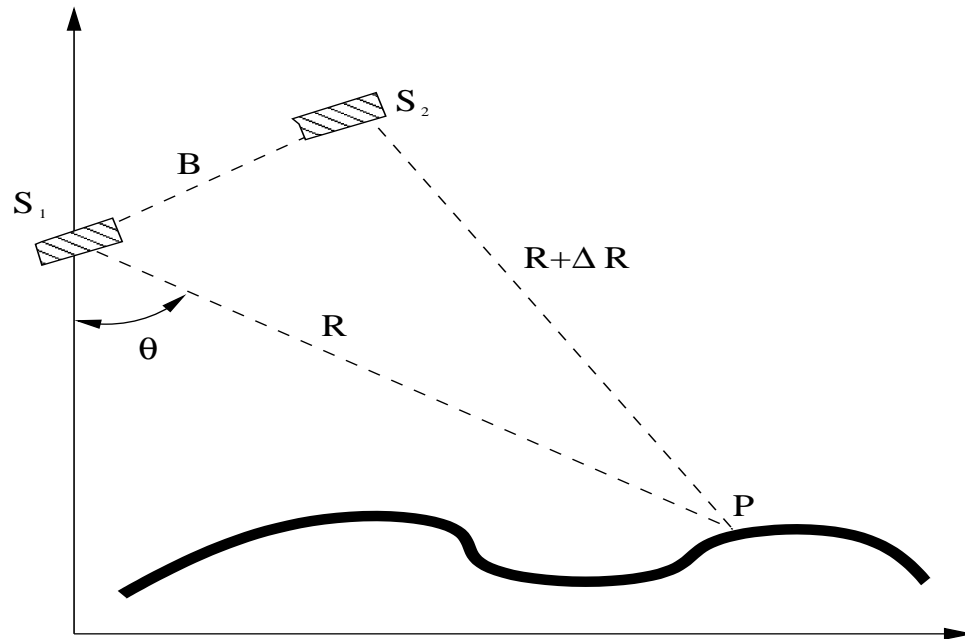


Figure 3.6: Interferometric SAR imaging geometry.

metric coherence images coupled with intensity images to improve thematic land classification [Alb98], [BSA⁺99]).

The fundamental idea of radar interferometry consists of an accurate phase analysis of the radar signals backscattered by a target and acquired by two antennae placed in different positions, S_1 and S_2 , as represented in Figure 3.6. This situation can be realized both by using actually two antennae separated by a fixed distance and by using only a single antenna mounted on a spaceborne or airborne device which gets data twice of the same area while moving along two slightly different tracks. In the second case, besides the exact control of the phase of the transmitted MW beam, the knowledge of the position of the antenna is very important in order to determine the distance, the *interferometric baseline* B , between the two “virtual” antennae.

The analysis performed on the signals follows the well-known rules also valid for optical interferometry. In particular, when two complex images of the same area acquired from two slightly different points of view are processed together, the result is a fringe structure similar to those observed in optical experiments. This analogy is so exact that, for example, it is possible to define a direct parallelism between the Young two slits experiment and the operation of a SAR interferometer:

- the partially coherent light source is replaced by the resolution cells on the ground which, when reached by the coherent radar signal, transmit its echo towards the two receiving antennae;
- the slits are substituted by the two antennae in the positions that they assume when they receive the pair of images used to synthesize the interferogram;
- the screen where the optic fringes appear is replaced by the whole electronic system of data acquisition and processing and by the one needed for the interferogram creation.

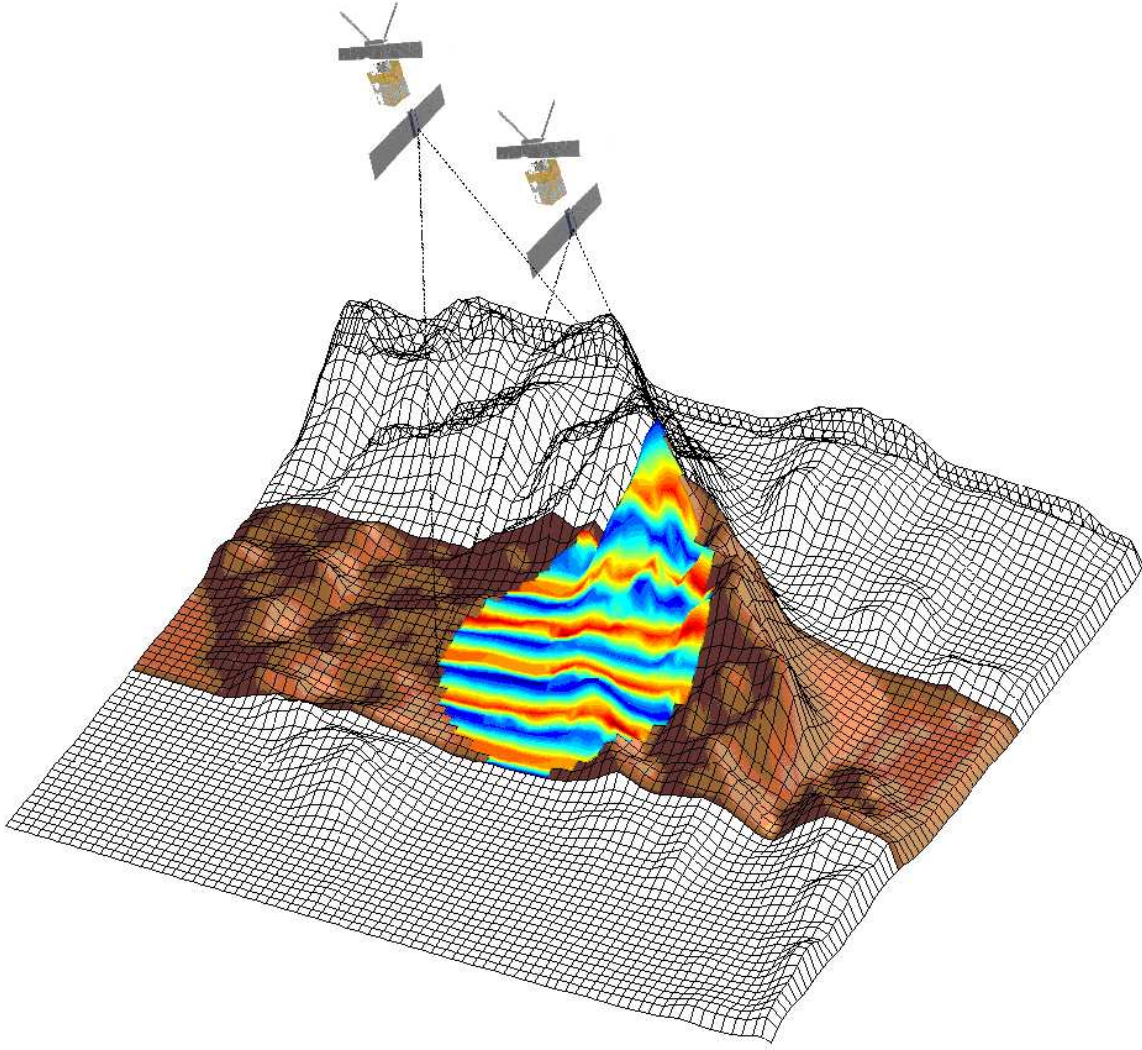


Figure 3.7: Interferometric SAR imaging creation (courtesy of M. Quartulli [Qua98]).

As a result of the coupled imaging and interferogram synthesis, the interferometric phase (i. e., the phase difference of the two signals coming from the same resolution cell) and the interferometric coherence (which is a normalized expression of this phase difference) may be calculated. The importance of these quantities lies in the fact that they are related to key parameters of the observed scene, for instance the vertical ground elevation.

Let us consider at first a single-polarization processing. For each resolution cell of two images, I_1 and I_2 , of the same area, this involves a complex scalar signal of the form:

$$s = |s|e^{j\delta}. \quad (3.18)$$

Thus, it is possible to define a Hermitian positive semidefinite coherency matrix as [CP98]:

$$[\mathbf{J}] = \left\langle \begin{bmatrix} s_1 \\ s_2 \end{bmatrix} \begin{bmatrix} s_1^* & s_2^* \end{bmatrix} \right\rangle = \begin{bmatrix} \langle s_1 s_1^* \rangle & \langle s_1 s_2^* \rangle \\ \langle s_2 s_1^* \rangle & \langle s_2 s_2^* \rangle \end{bmatrix} \quad (3.19)$$

using the two involved signals.

From the elements of $[\mathbf{J}]$, the interferometric coherence and the expected interfero-

metric phase are derived in the following ways:

$$\gamma = |\gamma'| = \frac{|\langle s_1 s_2^* \rangle|}{\sqrt{\langle s_1 s_1^* \rangle \langle s_2 s_2^* \rangle}} = \frac{|J_{12}|}{\sqrt{J_{11} J_{22}}} \quad (3.20)$$

and

$$\phi = \arctan \left(\frac{\text{Im} \langle s_1 s_2^* \rangle}{\text{Re} \langle s_1 s_2^* \rangle} \right). \quad (3.21)$$

The term γ' , also referred to as *correlation coefficient*, which represents the complex cross-correlation between the signals is introduced here as:

$$\gamma' = \gamma \exp(j\phi) \quad (3.22)$$

and the interferometric coherence γ is defined as its absolute value. With the definition above it holds as well that:

$$0 \leq \gamma \leq 1. \quad (3.23)$$

To extend these concepts to vector signals, let us call \mathbf{k}_1 and \mathbf{k}_2 the scattering vectors derived from the polarimetric data received from a resolution element of the imaged scene (for the sake of simplicity we drop the subscripts which refer to the dimensions of the vector and to the chosen matrices basis). The expression of such vectors in the Pauli matrix basis is given by Equation (2.114).

The analogue of $[\mathbf{J}]$ in this case can then be defined as:

$$[\mathbf{T}_{(6)}] = \left\langle \begin{bmatrix} \mathbf{k}_1 \\ \mathbf{k}_2 \end{bmatrix} \begin{bmatrix} \mathbf{k}_1^\dagger & \mathbf{k}_2^\dagger \end{bmatrix} \right\rangle = \begin{bmatrix} [\mathbf{T}_{11}] & [\mathbf{R}_{12}] \\ [\mathbf{R}_{12}]^\dagger & [\mathbf{T}_{22}] \end{bmatrix}. \quad (3.24)$$

$[\mathbf{T}_{(6)}]$ is a block matrix, Hermitian and positive semidefinite, the elements of which are the 3×3 matrices:

$$[\mathbf{T}_{11}] = \langle \mathbf{k}_1 \mathbf{k}_1^\dagger \rangle, \quad (3.25)$$

$$[\mathbf{T}_{22}] = \langle \mathbf{k}_2 \mathbf{k}_2^\dagger \rangle \quad (3.26)$$

and

$$[\mathbf{R}_{12}] = \langle \mathbf{k}_1 \mathbf{k}_2^\dagger \rangle. \quad (3.27)$$

According to their definition, $[\mathbf{T}_{11}]$ and $[\mathbf{T}_{22}]$ are the Hermitian coherency matrices of I_1 and I_2 (see Equation (2.116)), while $[\mathbf{R}_{12}]$ is a complex matrix which takes into account the interferometric phase relations of the different polarimetric channels between both images. $[\mathbf{R}_{12}]$ is not Hermitian since in general:

$$\mathbf{k}_1 \neq \mathbf{k}_2, \quad (3.28)$$

hence:

$$[\mathbf{R}_{12}] = \langle \mathbf{k}_1 \mathbf{k}_2^\dagger \rangle \neq \langle \mathbf{k}_2 \mathbf{k}_1^\dagger \rangle = [\mathbf{R}_{12}]^\dagger. \quad (3.29)$$

The next step is to take two normalized complex vectors, \mathbf{w}_1 and \mathbf{w}_2 (see also page 38), to generate two complex scalars, μ_1 and μ_2 , as the projections of the scattering vectors \mathbf{k}_1 and \mathbf{k}_2 onto \mathbf{w}_1 and \mathbf{w}_2 respectively:

$$\mu_1 = \mathbf{w}_1^\dagger \mathbf{k}_1, \quad (3.30)$$

$$\mu_2 = \mathbf{w}_2^\dagger \mathbf{k}_2. \quad (3.31)$$

By means of these scalars it is possible to redefine $[\mathbf{J}]$ for polarimetric quantities by replacing s_1 and s_2 in (3.19) by μ_1 and μ_2 :

$$\begin{aligned} [\mathbf{J}] &= \left\langle \begin{bmatrix} \mu_1 \\ \mu_2 \end{bmatrix} \begin{bmatrix} \mu_1^* & \mu_2^* \end{bmatrix} \right\rangle = \\ &= \left\langle \begin{bmatrix} \mathbf{w}_1^\dagger \mathbf{k}_1 \\ \mathbf{w}_2^\dagger \mathbf{k}_2 \end{bmatrix} \begin{bmatrix} (\mathbf{w}_1^\dagger \mathbf{k}_1)^* & (\mathbf{w}_2^\dagger \mathbf{k}_2)^* \end{bmatrix} \right\rangle = \\ &= \begin{bmatrix} \mathbf{w}_1^\dagger [\mathbf{T}_{11}] \mathbf{w}_1 & \mathbf{w}_1^\dagger [\mathbf{R}_{12}] \mathbf{w}_2 \\ \mathbf{w}_2^\dagger [\mathbf{R}_{12}]^\dagger \mathbf{w}_1 & \mathbf{w}_2^\dagger [\mathbf{T}_{22}] \mathbf{w}_2 \end{bmatrix}, \end{aligned} \quad (3.32)$$

where it must be noted that, for example:

$$(\mathbf{w}_1^\dagger \mathbf{k}_1)^* = (\mathbf{w}_1^\dagger \mathbf{k}_1)^\dagger, \quad (3.33)$$

since this is a scalar quantity.

Thus, the expressions of the interferometric coherence and of the expectation value of the interferometric phase may again be derived from the elements of $[\mathbf{J}]$:

$$\begin{aligned} \gamma &= \frac{|\langle \mu_1 \mu_2^* \rangle|}{\sqrt{\langle \mu_1 \mu_1^* \rangle \langle \mu_2 \mu_2^* \rangle}} = \frac{|J_{12}|}{\sqrt{J_{11} J_{22}}} = \\ &= \frac{|\langle \mathbf{w}_1^\dagger [\mathbf{R}_{12}] \mathbf{w}_2 \rangle|}{\sqrt{\langle \mathbf{w}_1^\dagger [\mathbf{T}_{11}] \mathbf{w}_1 \rangle \langle \mathbf{w}_2^\dagger [\mathbf{T}_{22}] \mathbf{w}_2 \rangle}} \end{aligned} \quad (3.34)$$

and

$$\phi = \arg \langle \mu_1 \mu_2^* \rangle = \arg \langle \mathbf{w}_1^\dagger [\mathbf{R}_{12}] \mathbf{w}_2 \rangle. \quad (3.35)$$

About the \mathbf{w} vectors one can note that using (2.114):

$$\mathbf{w}_{hh} = \begin{bmatrix} 1/\sqrt{2} \\ 1/\sqrt{2} \\ 0 \end{bmatrix}, \quad (3.36)$$

$$\mathbf{w}_{vv} = \begin{bmatrix} 1/\sqrt{2} \\ -1/\sqrt{2} \\ 0 \end{bmatrix} \quad (3.37)$$

and

$$\mathbf{w}_{hv} = \begin{bmatrix} 0 \\ 0 \\ 1 \end{bmatrix}, \quad (3.38)$$

that is, according to (3.30) and (3.31), the hh linear polarization corresponds to a projection of the given scattering vector onto the normalized vector \mathbf{w}_{hh} and so on for the other polarizations.

Given these fundamental expressions, which provide us with a theoretical basis for studying polarimetric interferometry, let us review what the main experimental results obtained to date have been.

In [CP98] and [Pap99] a method was presented to optimize the degree of correlation of an interferometric pair of images. It consisted of an eigenvalue analysis of the two equations (with the same eigenvalues) derived by imposing a maximization constraint on (3.34). According to this technique, for each image of the pair, it is usually possible to define three vectors \mathbf{w} which are eigenvectors of these equations and which represent different scattering mechanisms; the optimal coherence value is then obtained using the eigenvectors corresponding to the maximum eigenvalue. As the eigenvectors of a matrix are not uniquely defined, but do admit an arbitrary phase, one should add an additional condition which fixes the phase difference between the two eigenvectors \mathbf{w}_1 and \mathbf{w}_2 corresponding to the same mechanism; a sufficient one is to require that their phase difference be null, that is:

$$\arg\{\mathbf{w}_1^\dagger \mathbf{w}_2\} = 0. \quad (3.39)$$

The physical meaning of the coherence optimization is the definition of scattering mechanisms that would have the closest correspondence to a single point scatterer.

A very interesting result arises from the evaluation of the interferometric phase using the unitary vectors \mathbf{w} which maximize (3.34). As a major source of decorrelation results to be that due to the height distribution of the scattering coefficient above the chosen reference plane [ZV92], [BH98], one sees that the coherence optimization partly resolves just this height distribution. In fact, applying Equation (3.35) to the i th and j th mechanism and calculating its difference, i. e.:

$$\Delta\phi_{ij} = \arg\{\mu_{1_i}\mu_{2_i}^*\} - \arg\{\mu_{1_j}\mu_{2_j}^*\}, \quad (3.40)$$

it is in some cases possible to measure the height difference associated to $\Delta\phi_{ij}$. When applied to the estimation of forests height, this approach shows limits that depend on the properties of the scattering components. Indeed, while propagation through a random volume (that of the branches and layers of leaves where, usually, no preferential direction is present) is unaffected by changes of polarization, the ground scattering is polarization dependent; but as no polarization presents only one of the two contributions, it is not possible to completely separate them and estimate their difference in height through their interferometric phase difference [PRC99a], [PRC99b].

We have already said that, at present, few reports on applications of polarimetric SAR interferometry have been published; hence, this section has provided only a short, but fairly up-to-date description of the state of the art in this study area. Further original examples of such applications will be presented in Chapter 5.

The research related to scalar interferometry is, instead, more advanced. Though some of its features are similar to vector interferometry (for instance, *phase unwrapping* methods) we will not deal with them in this work in order to focus our attention on polarimetry. Nevertheless, starting from scalar technology achievements, several new topics can be suggested for future vector applications such as *differential polarimetric interferometry*, as proposed in [Pap99], or the use of polarimetric coherence images for pattern recognition and classification.

4 Analysis of polarimetric parameters: image classification

4.1 Introduction

As already seen, an electromagnetic wave may be described in different ways and each of them has a particular representation of its scattering interactions. Due to the vectorial nature of EM waves, the interactions are expressed in terms of matrices and again some matrices connect the various descriptions. We have also seen that some rules exist which impose constraints on these representations and on the transformation matrices, so that the number of the independent parameters, i. e., the carriers of physically relevant information, remains constant. The next question becomes: are the various representations absolutely equivalent? Why choose a particular representation? Are there parameters which are intrinsically more significant than others?

The answers to these questions should take into account also other considerations. In fact, the choice between two or more representations depends on the target to be detected and, in this sense, no absolute best descriptor is given. In the context of classification applications, the decision whether to use a linearly or an elliptically polarized base representation may depend on the fact that one is more interested in detecting, for example, buildings rather than trees. Hence, each problem has to be solved individually.

In the following, we will analytically study the various polarimetric parameters, trying to make this review as comprehensive as possible. In order to compare them and have an objective estimate of how well they may describe a certain target, some classification tests will be performed. In other words, an attempt to measure the amount of information provided by the different polarimetric parameters is made. It should be stressed that the main topic of our research will remain the polarimetric parameters, rather than the adopted classification techniques (of which only the indispensable notions will be given for sake of completeness) and their results; indeed, their exact knowledge will prove itself useful to better understand the scattering phenomena in connection with the characteristics of the wave and of the representation used.

The rest of this chapter is organized as follows: in the next section, the basics on classification theory and on the classification algorithms used in this work will be given; then the parameters under study will be briefly reviewed and the experimental setup described; finally the results of the tests will be reported and discussed for each polarimetric parameter considered.

4.2 Classification theory and accuracy assessment

Let us introduce here those basic concepts of image classification which are necessary to understand the tests performed later on in this chapter. Among others, the classification algorithms used will be described and some methods for classification accuracy assessment explained.

4.2.1 Classification theory basics

In general, the classification of an image is a process implying the identification of the different spectral classes¹ present in it and their connection to some specific ground cover types [Ric94]. Usually, this is accomplished using general mathematical pattern recognition and pattern classification techniques, though more specific methods have been developed especially suited for various sensors (as in the case of one based on the H/α parameters for polarimetric SARs [CP97]). The patterns are the pixels themselves that contain the values corresponding to the measured parameters; it is a common practice to represent them through column vectors like:

$$\mathbf{x} = \begin{bmatrix} x_1 \\ x_2 \\ \vdots \\ x_n \end{bmatrix}, \quad (4.1)$$

where x_1, x_2, \dots, x_n are the spectral values of the pixel vector \mathbf{x} in bands 1 to n , respectively. Therefore, classification involves labelling the pixels as belonging to particular spectral (and thus information) classes using the spectral characteristics of the available data.

During classification, each pixel of an image is no longer identified by its position in the chosen spatial reference system but by means of the vector belonging to the feature space relative to the spectral values. One then establishes a set of rules to label the pixels according to their particular properties in this space. To derive these rules, it is also necessary to define boundaries among the different classes in the n -dimensional feature space.

Two main types of classification procedures may be identified: the *supervised* and the *unsupervised classification* methods. Each type finds application in the analysis of remote sensing image data. These may be used as alternative approaches but are also often combined into hybrid methodologies.

Unsupervised classification is a means by which pixels are assigned to spectral classes without foreknowledge of the existence and properties of classes. Most often it is performed using clustering methods. These procedures can be used to determine at first the number and location of the spectral classes into which the data fall and then the spectral class of each pixel. The user finally identifies those classes *a posteriori*, by associating a sample of pixels in each class with available data, for instance maps and information from ground truth.

¹"Spectral classes" are defined by similar image pixel values, which may be related to the various ground coverages in a scene.

Clustering procedures are generally computationally expensive, they are nevertheless central to the analysis of remote sensing imagery. An interesting aspect of these methods is that whilst the ground cover classes, for a certain application, are usually known, the corresponding spectral classes are not. Unsupervised classification is therefore useful for determining spectral class composition of the data prior to any further detailed analysis with supervised methods. Examples of proposed algorithms for unsupervised classification are the K-means and the isodata [TG74]. Other approaches, not based on clustering, use inherent characteristics of the data used; for polarimetric SAR data, are worth mentioning the already cited methods by van Zyl [vZ89] and Cloude and Pottier [CP97].

Supervised classification is the procedure most often used for quantitative analysis of remote sensing image data. It is usually based on an important assumption, namely that each spectral class can be described by a probability distribution in the multispectral space; this will be a multivariable distribution with as many variables as the dimensions of the space. Such a distribution describes the chance of finding a pixel belonging to that class at any given location in the multispectral space. Almost all the algorithms used for this purpose consist of the same series of basic steps:

1. decide the set of ground coverages into which the image is to be segmented. The examples in this work are the classes: "water", "houses", "roads", "trees", "grass", "field 1" and "field 2".
2. A set of prototype pixels, the *training data*, is then selected for each class of the desired set. This choice may be done using information from ground surveys, aerial photographs, topographic maps or any other source of reference data.
3. The following step consists of describing each class by means of some particular parameters, mainly statistical ones such as the first and second order moments, depending on the chosen classifier. These parameters characterize the adopted probability model or directly define the partition of the multispectral space. The set of parameters for a given class is sometimes called the *signature* of that class.
4. Using the trained classifier labels, every pixel of the image is assigned to one of the desired ground cover types (information classes). In practice, the complete image is automatically classified after the user has directly identified just a portion of it in the second step when defining the training data.
5. Produce tabular summaries or thematic maps summarizing the classification results.

A variety of algorithms that perform supervised classification are available: parallelepiped, maximum likelihood, minimum distance, Mahalanobis classifier, etc. Here, we will briefly describe only the first three methods as they are those used in this work.

4.2.2 Parallelepiped classification

The *parallelepiped* (*Parall.*) classifier is a very simple supervised classification technique; in principle, the classifier is trained by inspecting histograms of the individual spectral

components of the selected training data. The upper and the lower significant bounds of the histograms are identified as the edges of a multidimensional parallelepiped for each class. If, on classification, pixels are found to lie in such a parallelepiped they are labelled as belonging to that class.

Relevant problems of this criteria are that pixels in regions between parallelepipeds cannot be assigned to any class and pixels in overlapping areas cannot be separated: in both cases, these pixels are not classified. No statistical constraints in the definition of the class membership are taken into account here.

4.2.3 Maximum likelihood classification

Maximum likelihood (Max. Lik.) classification is based on the estimation of the statistical distributions of the spectral components [Ric94]. This allows to evaluate the chance of finding a pixel belonging to a certain class at any given location in the multispectral space.

The working hypothesis usually adopted is that the probability distribution for each class is a multidimensional normal, or Gaussian, distribution. Hence, the probability of finding a pixel belonging to a given class ω_i in a position \mathbf{x} of the multispectral space is described by a function like:

$$p(\mathbf{x}|\omega_i) = \frac{1}{(2\pi)^{n/2}(\det [\Sigma_i])^{1/2}} \exp \left\{ -\frac{1}{2}(\mathbf{x} - \mathbf{m}_i)^t [\Sigma_i]^{-1}(\mathbf{x} - \mathbf{m}_i) \right\}, \quad (4.2)$$

where $i = 1, 2, \dots, l$ is the index identifying the l ground cover classes, \mathbf{m}_i the mean vector of the data in class ω_i and $[\Sigma_i]$ the *covariance matrix* for that class. For each i , the $[\Sigma]$ matrix is defined as:

$$[\Sigma] = \langle (\mathbf{x} - \mathbf{m})(\mathbf{x} - \mathbf{m})^t \rangle = \frac{1}{r-1} \sum_{j=1}^r (\mathbf{x}_j - \mathbf{m})(\mathbf{x}_j - \mathbf{m})^t, \quad (4.3)$$

being r the total number of pixel of the class. The multidimensional normal distribution is completely specified by its mean vector and its covariance matrix.

The covariance matrix introduced here is different from the one associated to polarimetric data. It allows, for instance, to see if a correlation exists between the responses of a pair of spectral bands: if they are correlated, the corresponding off-diagonal elements of the covariance matrix are large with respect to the diagonal terms (whereas little correlation yields off-diagonal terms close to zero). Let us now see how these hypotheses and expression are actually used by the classifier.

In trying to determine the class or category to which a pixel characterized by a vector \mathbf{x} belongs, it is strictly the conditional probabilities

$$p(\omega_i|\mathbf{x}), \quad i = 1, 2, \dots, l \quad (4.4)$$

that are of interest. As already said, the vector \mathbf{x} describes the pixel as a point in the multispectral space with coordinates defined by the values of the parameters. The probability $p(\omega_i|\mathbf{x})$ gives the likelihood that the correct class is ω_i for the pixel at position \mathbf{x} . Hence, the classification is performed assigning a pixel vector \mathbf{x} to class ω_i

when the condition:

$$p(\omega_i|\mathbf{x}) > p(\omega_j|\mathbf{x}) \quad \forall j \neq i \quad (4.5)$$

is verified. The problem is then to estimate the probabilities $p(\omega_i|\mathbf{x})$ that are unknown.

If sufficient training data are available for each class (each ground cover type defined by the user), the probability distribution, which describes the chance of finding a pixel from ω_i at the position \mathbf{x} , can be calculated. This new probability distribution is indicated with $p(\mathbf{x}|\omega_i)$. The desired $p(\omega_i|\mathbf{x})$ and the estimated $p(\mathbf{x}|\omega_i)$ are related by the *Bayes theorem* [Pap65]:

$$p(\omega_i|\mathbf{x}) = \frac{p(\mathbf{x}|\omega_i)p(\omega_i)}{p(\mathbf{x})}, \quad (4.6)$$

where $p(\omega_i)$ is the probability that class ω_i occurs in the image and $p(\mathbf{x})$ is the probability of finding a pixel from any class at the location \mathbf{x} . The $p(\omega_i)$ are called *a priori* or *prior* probabilities, since they express the probabilities with which the class membership of a pixel could be predicted before classification. By adopting the same interpretation principle, the $p(\omega_i|\mathbf{x})$ are *posterior* probabilities.

Using (4.6), the classification rule of (4.5) may be written as:

$$\mathbf{x} \in \omega_i \quad \text{if} \quad p(\mathbf{x}|\omega_i)p(\omega_i) > p(\mathbf{x}|\omega_j)p(\omega_j) \quad \forall j \neq i. \quad (4.7)$$

Mathematical convenience results if *discriminant functions* like:

$$g_i(\mathbf{x}) = \ln\{p(\mathbf{x}|\omega_i)p(\omega_i)\} = \ln\{p(\mathbf{x}|\omega_i)\} + \ln\{p(\omega_i)\} \quad (4.8)$$

are used, so that (4.7) is restated as:

$$\mathbf{x} \in \omega_i \quad \text{if} \quad g_i(\mathbf{x}) > g_j(\mathbf{x}) \quad \forall j \neq i. \quad (4.9)$$

At this stage it is assumed that the probability distributions for each class are of the form of the multivariate normal model, see (4.2). This is an assumption, rather than a demonstrable property for natural spectral or information classes; however it is chosen because it leads to mathematical simplifications and moreover it is a distribution for which properties of the multivariate form are well-known. The final form for the discriminant function, based upon the assumption of normal statistics, is then:

$$g_i(\mathbf{x}) = \ln p(\omega_i) - \frac{1}{2} \ln(\det[\Sigma_i]) - \frac{1}{2}(\mathbf{x} - \mathbf{m}_i)^t [\Sigma_i]^{-1} (\mathbf{x} - \mathbf{m}_i). \quad (4.10)$$

The boundaries among different classes, because of the second order equation that characterizes the discriminant function, are quadratic curves such as parabolas, circles and ellipses. As will be shown later, the boundaries in the minimum distance approach are expressed by linear equations, hence, the higher order decision rules make the maximum likelihood classification more efficient for partitioning multispectral space than the minimum distance one.

It is also possible to introduce a threshold in the case that insufficient training data are available to estimate the parameters of the class distributions; the threshold of each class is calculated from the knowledge of its *a priori* probability and its covariance matrix.

4.2.4 Minimum distance classification

The effectiveness of maximum likelihood classification is related to the accuracy in the estimation of the mean vector \mathbf{m} and the covariance matrix $[\Sigma]$ for each spectral class [Ric94]. This, in turn, depends upon having a sufficient number of training pixels for each of those classes. If this condition is not satisfied, an inaccurate estimate of $[\Sigma]$ results, leading to poor classification results. When the number of training samples per classes is limited, it is then worth trying to use a classification approach based only on the use of \mathbf{m} , whose evaluation, even for small quantities of samples, can be more accurate than that of the covariance matrix elements. A classifier which needs only the mean vectors of the various classes to be estimated is the *minimum distance (Min. Dist.)*, which should be more precisely indicated as *minimum distance to class means* classifier. Indeed, this algorithm operates by placing a pixel in the class of the nearest mean in the multispectral measurement space.

An advantage of this method with respect to the maximum likelihood classification is its computational speed. The main disadvantage stems from the fact that it does not use the covariance matrix and it therefore models only symmetric classes in the multispectral space; hence, classes with a well-defined data spread in a particular spectral direction cannot be represented correctly.

The discriminant function for the minimum distance classifier is derived from the expression of the squared Euclidean distance between the position of the generic pixel \mathbf{x} to be classified and the mean value \mathbf{m}_i of i -th class:

$$d(\mathbf{x}, \mathbf{m}_i)^2 = (\mathbf{x} - \mathbf{m}_i)^t (\mathbf{x} - \mathbf{m}_i). \quad (4.11)$$

Expanding the product gives:

$$d(\mathbf{x}, \mathbf{m}_i)^2 = \mathbf{x}^t \mathbf{x} - 2\mathbf{m}_i^t \mathbf{x} + \mathbf{m}_i^t \mathbf{m}_i. \quad (4.12)$$

Classification is performed on the basis of:

$$\mathbf{x} \in \omega_i \quad \text{if} \quad d(\mathbf{x}, \mathbf{m}_i)^2 < d(\mathbf{x}, \mathbf{m}_j)^2 \quad \forall j \neq i. \quad (4.13)$$

As $\mathbf{x}^t \mathbf{x}$ is common to all $d(\mathbf{x}, \mathbf{m}_i)^2$, it can be neglected. By reversing the signs of the expressions above, the assignment to a class is again expressed by the condition (4.9) with:

$$g_i(\mathbf{x}) = 2\mathbf{m}_i^t \mathbf{x} - \mathbf{m}_i^t \mathbf{m}_i. \quad (4.14)$$

As a consequence of the linearity of the discriminant functions, the decision surfaces for this classifier are planes in the n -dimensional spectral space. The minimum distance classification is proven to be of value when the number of training samples is limited and, in such a case, can lead to better results than the maximum likelihood procedure.

Finally, the possibility of adopting a definition for the distance other than the Euclidean is also worth mentioning.

4.2.5 Classification accuracy assessment

The final step in any classification procedure is an accuracy assessment. This should not be meant as an afterthought but as an integral part of any classification project, which explains and completes the results of the classifier used.

ber of “correct pixels” in a category is divided by the total number of pixels classified in that category, then this result gives a measure of the commissions. This measure, called *user’s accuracy* (*Us. Acc.*), is indicative of the probability that a pixel on the image actually represents that category on the ground.

It is also common practice to normalize the error matrices by an iterative proportional fitting procedure that forces each row and column in the matrix to sum to one. In this way, differences in sample sizes used to generate the matrices are eliminated and, therefore, individual cell values within the matrix are comparable. In addition, the resulting normalized matrix is more indicative of the off-diagonal cell values (i. e., the errors of omission and commission).

Another measure of the accuracy of a classification procedure is the *Kappa coefficient* defined as:

$$K = \frac{N \sum_{i=1}^r x_{ii} - \sum_{i=1}^r (x_{i+} \cdot x_{+i})}{N^2 - \sum_{i=1}^r (x_{i+} \cdot x_{+i})}, \quad (4.15)$$

where r is the number of rows in the matrix, x_{ii} is the number of observations in row i and column i , x_{i+} and x_{+i} are the marginal totals of row i and column i , respectively, and N is the total number of observations. For $0.4 < K < 0.75$ the accuracy of the classification is good and it is excellent for $K > 0.75$ [Con91].

In general, it is not possible to give clear-cut rules indicating when each measure should be used. Each accuracy measure incorporates different information about the error matrix and therefore must be used as a different computation attempting to explain the errors performed in the classification.

4.3 Overview on polarimetric parameters

Now that the theoretical bases to our tests and to their interpretation have been provided, it is possible to explain in detail the adopted analysis strategy and comment upon the results.

As a first step, it is helpful to summarize the parameters that can be extracted from a fully polarimetric SAR data set, i. e., those different ways in which these data can be visualized and analyzed:

Backscattered intensity. This is the observable directly detected by the sensor and gives the most immediate picture of the observed scene. The use of different polarization bases can be meaningful as far as intensities are concerned.

Ratios of the [S] matrix elements. One may use this approach in order to enhance and study the relative behaviour of the polarization channels. In particular, in this work, we will calculate for SAR data some quantities usually derived for weather radar data, like the *linear depolarization ratios* (LDR), i. e., the ratios between cross-polar channels and co-polar ones, and the *differential reflectivity* (ZDR), that is, the ratio between two co-polar channels (an example of a ZDR image is shown in Figure 4.5).

Characteristic polarizations. The co- and cross-polar nulls of the scattering matrix may be calculated to enhance image quality and to retrieve orthogonality properties of the polarizations.

Parameters of the coherent target decomposition theorems. In general, the application of such theorems leads to pictures that express the intensity of various scattering mechanisms. Higher or lower intensity values of one component are connected to the predominance of a mechanism with respect to the others.

Entropy/ α parameters. This approach involves the generation of the coherency matrix and the calculation of the eigenvalues and other related quantities. Their interpretation follows the principles proposed by Cloude and Pottier [CP97].

One should note that, although each parameter provides relevant information about the scatterers, none seems to be sufficient to fully interpret the response of a scene on its own, so that their joint use is a common practice. In the recent research literature the use of Entropy/ α method for classification purposes has been reported and carefully investigated [CP97], [Hel00]. The application of coherent methods for achieving similar purposes, however, appears to have remained neglected and basically untested. This is the reason why, in this contribution, we wish to address this issue, in an attempt to complete the knowledge of all the considered polarimetric parameters.

4.4 Experimental approach

A series of classification tests has been carried out for each one of the different approaches listed in Paragraph 4.3 [AC00], [PAC⁺02], [ACP02b]. Since the main interest of this research is not the theory of pattern recognition and image classification itself, we have considered these techniques simply as a tool to compare different polarimetric parameters or, rather, to have a first numerical estimation of their “potential”. Hence, we have chosen classification algorithms widely used in the field of remote sensing, though not specifically intended for SAR data, namely the parallelepiped, the minimum distance and the maximum likelihood. As previously seen, these algorithms assign the pixels of the images to selected ground cover types according to some statistical quantities (mean, variance, maxima and minima) extracted from prototype pixels belonging to these classes. For the Parall. and Min. Dist. classifiers no further assumptions are made on the statistical properties of the data or of the pixels belonging to the classes in particular. Conversely, the Max. Lik. algorithm is based on the hypothesis, reasonable in most of the cases for remotely sensed data, that the probability distributions for each class are in the form of multivariate normal models. Since this condition is hardly met for SAR polarimetric data [FMYS97], the use of this algorithm is controversial and the results presented here must be carefully interpreted.

An original aspect of this work is the study of the dependence of the classification results on the size of averaging windows of pixels, i. e., all the tests have been performed using images where the values of the pixels have been averaged considering square windows of increasing size, namely: 3×3 , 5×5 , 10×10 and 15×15 pixels. Such an analysis will permit to prove if the chosen polarimetric parameters provide a description only of “point-like” physical properties of the targets or if they also contain

“extended”, local information. Indeed, in the first case we expect good accuracy only for single-pixel or small averaging windows based classification, whereas the presence and recognition of extended parameters characteristics would lead to enhanced classification accuracy also for larger averaging windows.

Finally, the comparison among different polarimetric parameters will contribute to the search of targets and/or ground cover classes that are better recognized and unambiguously characterized by one parameter rather than another.

Regarding the outlined classification approach, it may be objectionable that the adopted techniques may not be adequate to the data (as we admitted for the Max. Lik. algorithm) and that more sophisticated approaches could better account for the statistical properties of targets. Similar doubts could be raised also by the fact that little or no attention was paid to noise removal or speckle reduction. However, there is a heuristic component in any polarimetric approach developed to date and, at this point, results seem to justify assumptions. Thus, by means of our tests, it is still possible to accomplish our tasks: to study the influence of the averaging windows dimensions and to broadly establish what kind of features are better detected by a given polarimetric parameter.

4.5 Data sets and test areas

The experimental data used for our tests are the following:

- Single-look complex (SLC) data sets of the area of Oberpfaffenhofen, Germany, acquired by the E-SAR airborne sensor operated by DLR during a measurement campaign in October '99. The data consist of L-band scattering matrices measured in the hv-basis.

The imaged area is situated approximately 25 km South West of the city of Munich and includes several interesting features: the DLR centre, the former Fairchild Dornier aeroplane factory and the airfield shared by the two firms (see Figure 4.2).

Table 4.2: Main E-SAR system parameters.

RF-band	L
Centre frequency	1.3 GHz
Wavelength	23 cm
Bandwidth	100 MHz
Mode	Quad Pol (hh, vh, vv, hv)
PRF	400 Hz (per channel)
Transmit peak power	360 W
Antenna gain	17 dB
Range resolution	1.5 m
Azimuth resolution	0.89 m

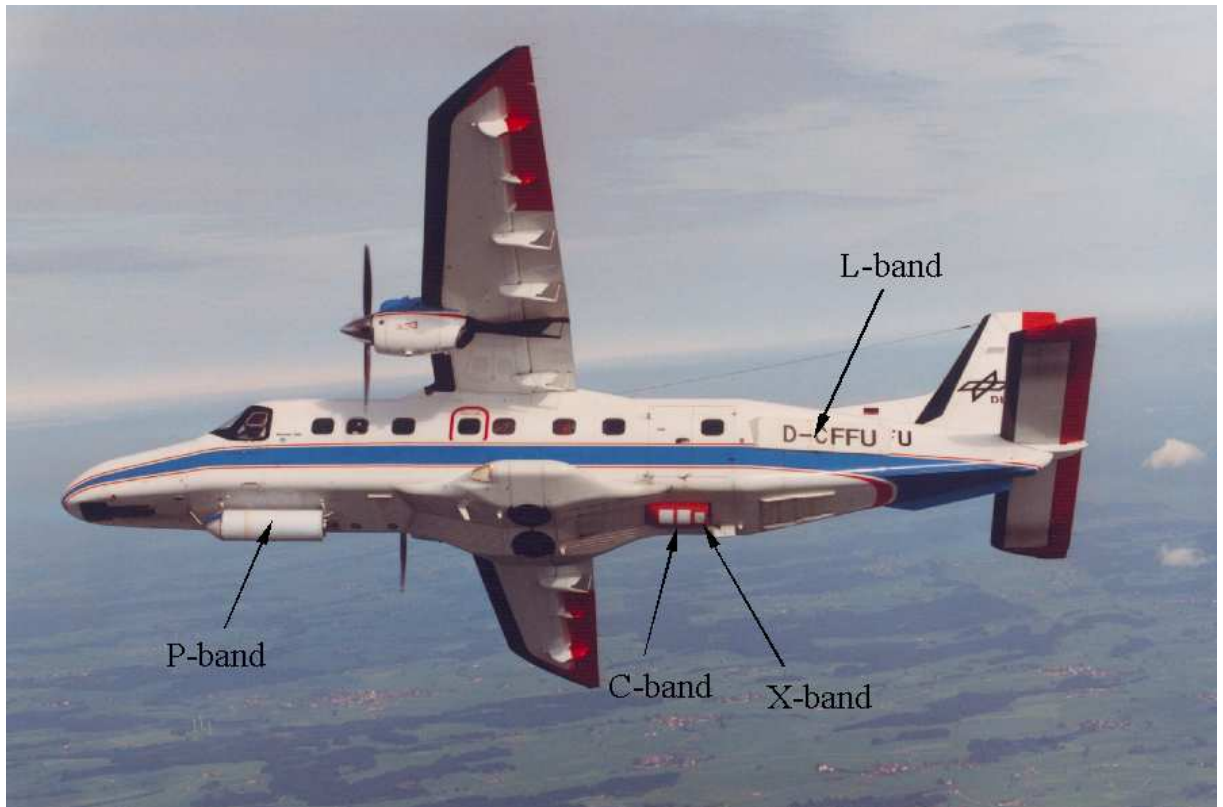


Figure 4.1: The DLR Dornier DO 228-212 aircraft and the displacement of the different SAR antennae mounted on board (courtesy of R. Horn).

Not far from them is situated the town of Gilching. Other important man-made features are the motorway and the railway line stretching across the image. The vegetation patches consist of coniferous and mixed forests, meadows and crops.

- Similar data of the same sensor acquired over the urban area of Munich. The scene contains mainly buildings, but green areas are also present.

Aerial photographs were also used as ground truth and complementary sources of information.

About the ground cover classes, we will concentrate on those types that are usually investigated in the literature:

- Urban areas and man-made artifacts (even when isolated);
- forests (trying to distinguish among dense, coniferous and sparse, deciduous ones);
- sparse vegetation;
- agricultural crops;
- water.

Whenever possible, some other distinctions have been made inside the types described above in order to refine this broad grouping (for example, to try to recognize

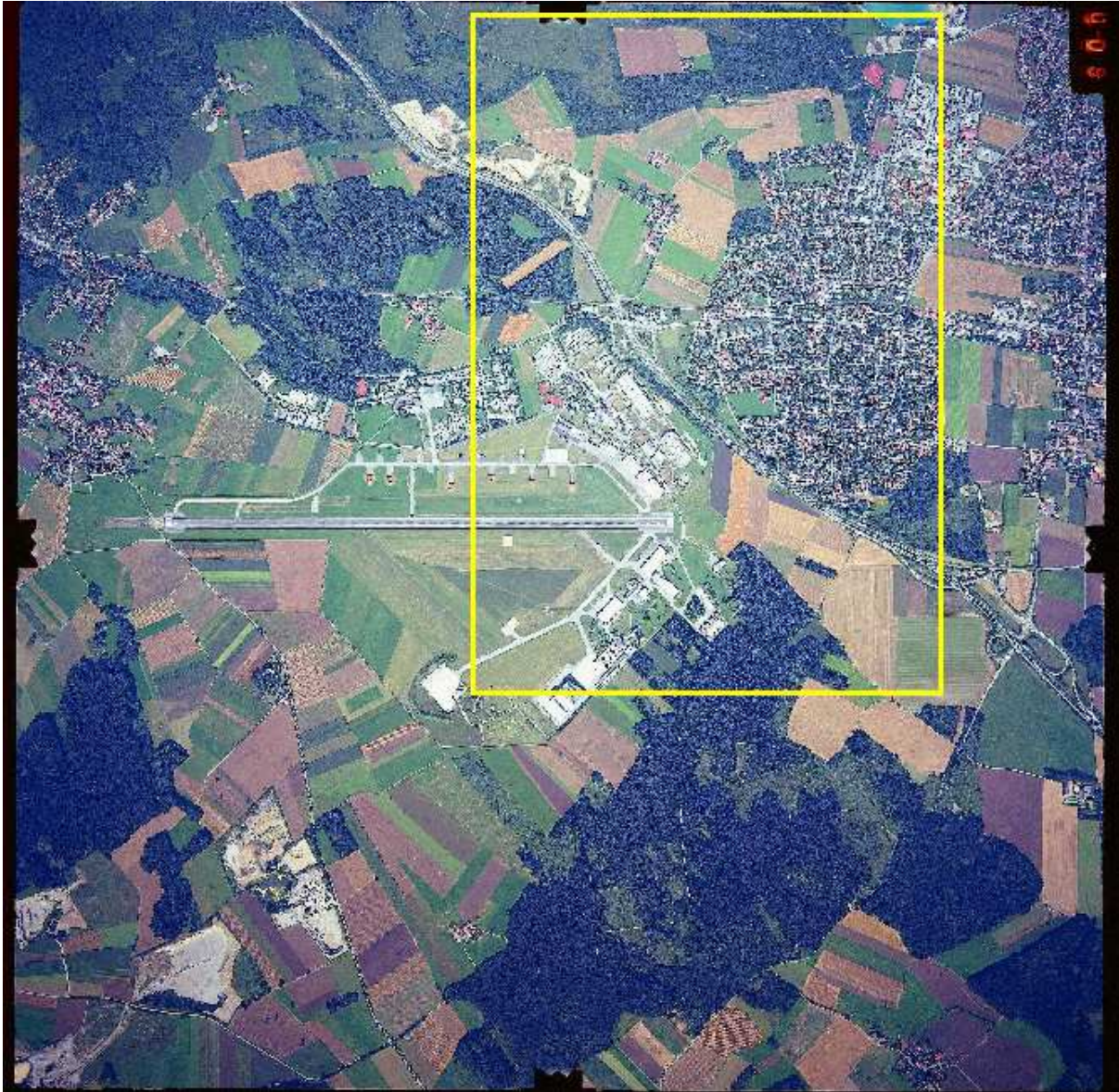


Figure 4.2: Optical picture of the Oberpfaffenhofen test site (the yellow rectangle defines the area corresponding to the SAR data).

different crop types or woods). This was done, in particular, when using the $[S]$ matrix elements ratios.

The optical images served as ground truth data, since no more precise information taken on the ground was available. The classes mentioned (forests, water, grass, etc.) have been identified by direct interpretation of these aerial photographs. Regarding the class indicated later on as “houses”, this definition refers to quite homogeneous areas characterized by family houses surrounded by gardens (often including trees).

4.6 Backscattered wave amplitude

A common analysis procedure was adopted for all the polarimetric parameters. At first, seven ground cover classes (a more refined set with respect to the coarse one previously outlined) were defined: “water”, “houses”, “roads”, “trees”, “grass”, “field 1” and “field 2”. Then, the corresponding prototype pixels from each class were selected and passed as training samples to each classification algorithm. Finally all of the data were classified. These last two steps were repeated five times, on a single-pixel basis and also considering the 3×3 , 5×5 , 10×10 and 15×15 -pixel averaging windows. Tables summarizing the most meaningful results of all the tests are reported in Appendix C.

In this section we will start by analyzing the backscattered wave amplitude, i. e., the data directly detected by the sensor and which provide the most immediate pictures of the observed scene [PAC⁺02]. The series of tests was performed giving the three amplitude images in the hv-linear basis, $|S_{hh}|$, $|S_{vv}|$ and $|S_{hv}|$, as input to the classifiers. Only the data of the Oberpfaffenhofen test site were taken into account.

Figure 4.3 shows the classification accuracy assessments in terms of overall accuracy and Kappa coefficient. It is clear that increasing the dimensions of the averaging window the classification accuracy improves; nevertheless, almost all the methods, independent of window dimensions, do not reach satisfactory accuracy degrees. Indeed, they all remain below or near the threshold of $K > 0.4$ which indicates a good classification accuracy and only the Max. Lik. classifier, for window dimensions larger than 5×5 pixel, clearly exceeds this threshold.

Let us limit ourselves to the case corresponding to the best results: the 15×15 -pixel window. The classes giving rise to the main recognition problems are: “water”, “roads” and “grass” (see Appendix C.1). These are the ones corresponding to ground cover types and samples giving the lowest backscattered intensity. The “grass” training pixels correspond to the flat area near the runway that, although rougher than the other two, still tend to reflect most of the incoming MWs away from the backscattering direction. Basically, the bad classification results for these three classes are due to their low *signal-to-noise ratio* (SNR). In particular, the Parall. classifier, the algorithm based

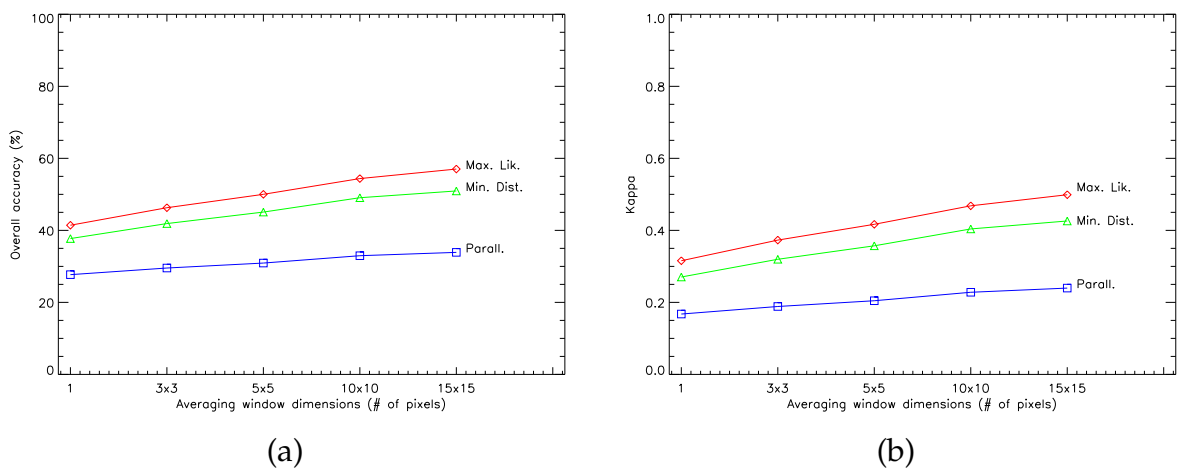


Figure 4.3: Accuracy estimation of the classification tests based on the amplitudes of the three $[S]$ matrix elements: (a) overall accuracy; (b) Kappa (October '99).

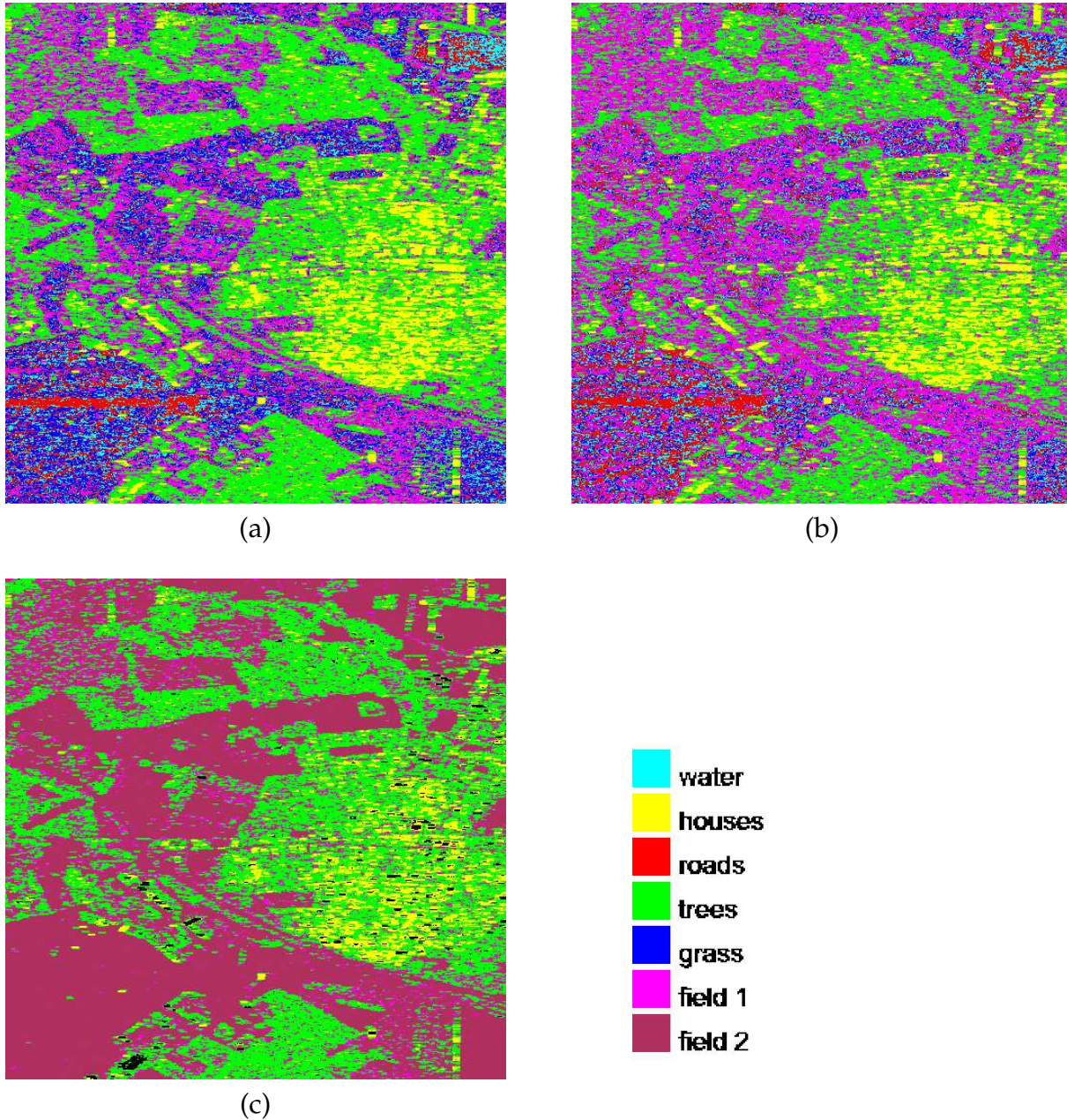


Figure 4.4: Classification maps based on the amplitudes of the three $[S]$ matrix elements (15×15 -pixel averaging window): (a) maximum likelihood; (b) minimum distance; (c) parallelepiped (October '99).

on the simplest feature space partition, fails to recognize all the samples belonging to them.

The best results in terms of both the producer's accuracy and the user's accuracy are obtained for the class "trees": 85.42% and 64.13%, respectively, for the Parall. and 76.42% and 65.08% for the Min. Dist. classifier. This means that most of the pixels belonging to this class have been correctly classified and that few samples from other training areas have been erroneously labelled as "trees". Hence, it seems that the $[S]$ matrix elements amplitudes are sufficient to characterize the targets associated with that ground cover type. Conversely, none of the other classes yields such good results;

for the “houses”, whereas the Us. Acc. is quite high for all the classifiers, the Pr. Acc. remains low.

As shown in the accuracy assessment graphs, for smaller averaging windows, the values of Kappa and Ov. Acc. are such that the classification results cannot be considered valuable.

4.7 Ratios of the scattering matrix elements

Let us now consider the backscattered intensity data from a different point of view and concentrate on the relative behaviour of the polarization channels [AC00]. In order to do this, some simple mathematical ratios will be used, namely the linear depolarization ratios:

$$\text{LDR}(1) = 10 \log \frac{|S_{hv}|^2}{|S_{vv}|^2} = 10 \log \frac{\sigma_{hv}}{\sigma_{vv}} \quad (4.16)$$

and

$$\text{LDR}(2) = 10 \log \frac{|S_{hv}|^2}{|S_{hh}|^2} = 10 \log \frac{\sigma_{hv}}{\sigma_{hh}} \quad (4.17)$$

and the differential reflectivity:

$$\text{ZDR} = 10 \log \frac{|S_{hh}|^2}{|S_{vv}|^2} = 10 \log \frac{\sigma_{hh}}{\sigma_{vv}} . \quad (4.18)$$

As already mentioned, these polarimetric observables have been extensively used in weather radar applications: for classifying hydrometeors [SCM88] and for estimating meteorological quantities like the drop size distribution and rain-rates [SBAK79] via solving inversion problems. Particularly relevant are propagation studies, including attenuation studies and studies on the depolarization behaviour of scatterers, like raindrops or ice crystals, along a propagation path [Hol84]. However, to our knowledge, the application of the ratios of the [S] matrix elements to the remote sensing of the Earth surface has been limited [ROvZJ93], [DvZE95].

Some other ratios could also be considered, such as those relating the [S] matrix elements expressed in different bases, for example, the RL-circular one as reported in [ROvZJ93].

The classification results obtained using different averaging windows do not lead to meaningful accuracy values for any of the classification algorithms. This may be due to the very limited variance of the ratio values among the classes. To verify this, we decided to study the polarization ratios more thoroughly, defining an extended set of classes for the Oberpfaffenhofen test site and using also other data relative to the Munich urban area.

The training areas selected in the Oberpfaffenhofen scene were labelled as follows: “water”, “houses”, “bare asphalt”, “trees”, “grass”, “field 1”, “field 2”, “field 3”, “field 4” and “field 5”. The “bare asphalt” is represented by the airfield, whereas the number of fields, which have different optical behaviour, have been extended to five. One can broadly distinguish harvested soil from not harvested but, unfortunately, the lack of direct information on the ground, like crop height or humidity, does not allow

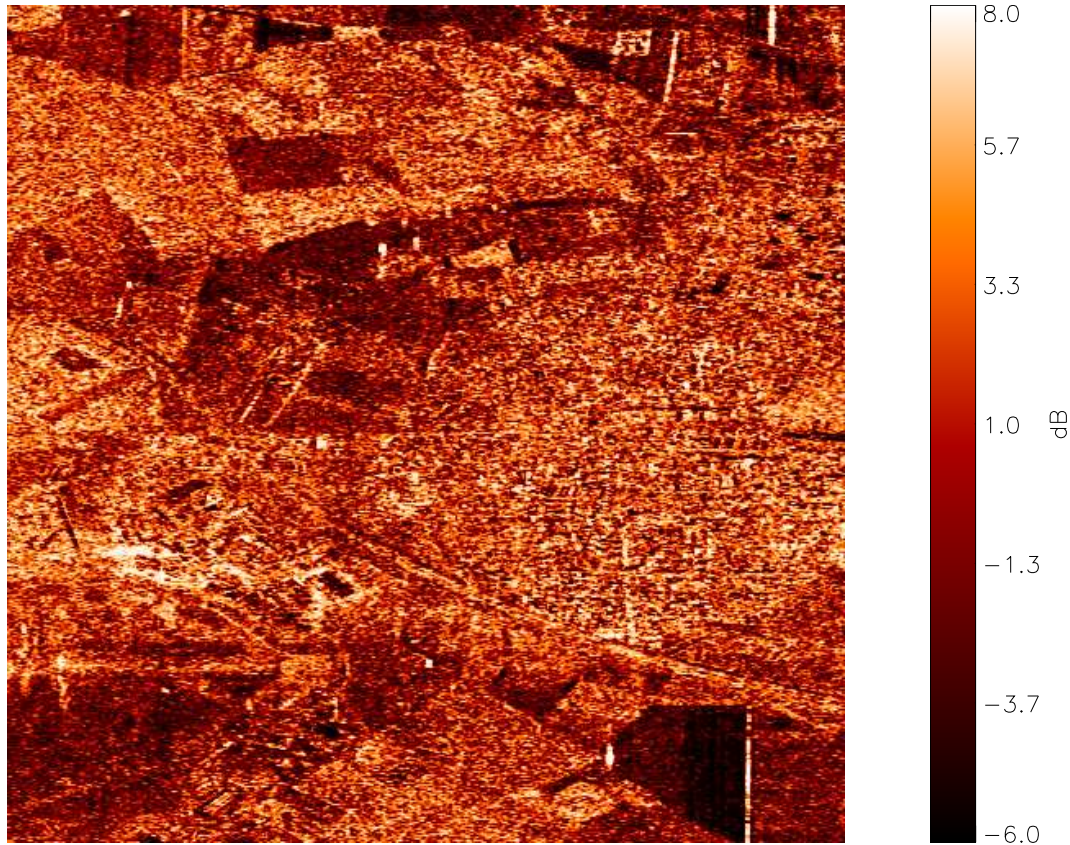


Figure 4.5: ZDR image of the Oberpfaffenhofen test site (October '99).

to fully explain the different backscattering signals. Hence, it is only possible to note the variations of the values in the images and register them without providing but a hypothetical interpretation.

In the Munich test site, the total number of training areas is lower than in the Oberpfaffenhofen one. Again, areas representative of the classes “water”, “houses”, “trees” and “grass” could be found. The class “buildings” has been introduced to define some bigger buildings, blockhouses and big sheds, which could in no way be associated with the class “houses” and whose response, especially in the hh -channel, is particularly high. We reiterate here that the class “houses” was associated to quite homogeneous areas characterized by family houses surrounded by gardens.

Figure 4.6 (a) reports the mean polarization ratios relative to a 5×5 -pixel averaging window, whereas the values in Figure 4.6 (b) refer to single-pixel estimates. In both cases, it is evident that the mean values of the three ratios do not vary significantly among the various classes. Considering also the standard deviations, to have a range of variation for each class, one can see that these ranges always overlap. This confirms our hypothesis and explains why none of the ratios suffices to distinguish a class from the others (at least among the ones we have defined here). As a consequence, classification based on these images only is unlikely to provide valuable results. Referring, for instance, to the quantities averaged on a 5×5 -pixel window, the test with the Min. Dist. classifier gives for the Oberpfaffenhofen site an Ov. Acc. around 28 % and a value for the Kappa coefficient of 0.242, and for Munich a slightly better result of Ov. Acc. =

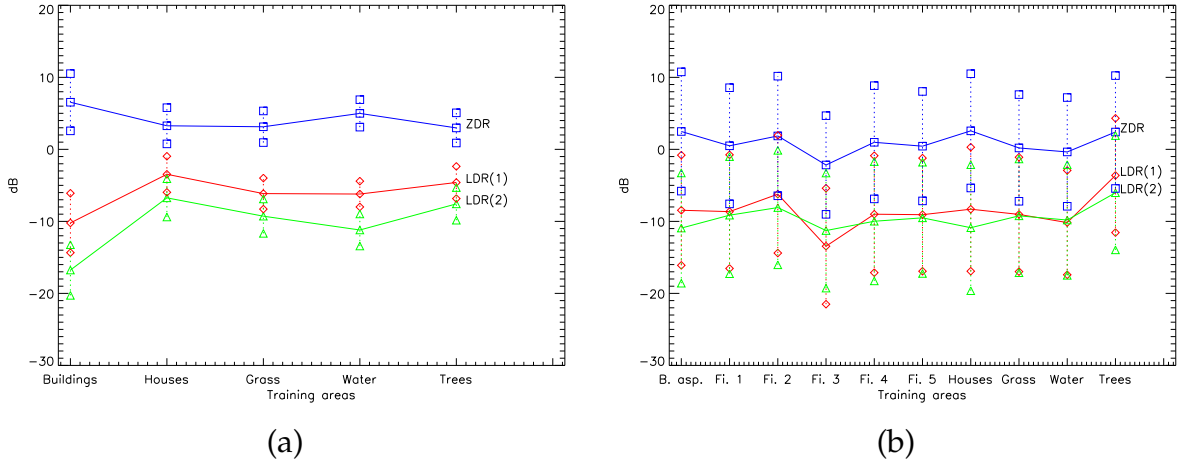


Figure 4.6: Mean values and standard deviations of the polarization ratios in the selected regions of interest: (a) Munich; (b) Oberpfaffenhofen (October '99). The ratios have been calculated, respectively, for the values relative to a 5×5 -pixel averaging window and on a single-pixel basis.

57.4 % and $K = 0.476$ (results far from, or just at the limit of, the range $0.4 < K < 0.75$ which indicates a good accuracy).

Almost everywhere the hh -channel response is slightly higher than the vv -one. Hence, it seems that a real polarization isotropy of the backscattered signal, of which the ZDR is a function [SCM88], is rarely present.

According to the theory [CM91], [BW85], [UMF82], the predominance of one term over the other is connected to the type of scattering on the illuminated surface. More precisely, $|S_{hh}| > |S_{vv}|$ when the incident beam is scattered according to the Fresnel model, valid for surfaces almost flat, whereas the case of $|S_{hh}| < |S_{vv}|$ is verified for scattering from rough surfaces described by the Bragg model. The hypothesis of Fresnel scattering applies, for example, to the “buildings” (ZDR high and LDR(2) low). Also the class “bare asphalt” seems to follow this trend, although with less pronounced evidence. Conversely, the only observed case of significantly negative ZDR average (and of LDR(1) values lower than the LDR(2) ones) refers to a field where we may suppose a recent ploughing and, for this reason, an enhanced roughness.

The class “trees”, from which we expected one of the highest average values for the LDR ratios (assuming the presence of the best conditions to have depolarization effects due to multiple scattering phenomena) shows clearly this tendency in the Oberpfaffenhofen test site and less evidently in the Munich test site. The reason for this difference can be the type of trees present in the two scenes: mainly coniferous (at least in the selected sample) in the Oberpfaffenhofen scene, deciduous in the Munich sample. On the acquisition date, beginning of October, the trees in Munich would have already lost their leaves and one can expect from them a less probable evidence of multiple bounce (and hence depolarization) phenomena.

4.8 Characteristic polarizations

The co- and cross-polar nulls were introduced in Paragraph 2.3 where we saw that by their means it was possible to express the scattering matrix in diagonalized forms, and thereby to better deal with representations of the interactions where the backscattered power is concentrated only in some of the components of $[S]$.

Referring more in particular to the results of the zeroing constraints, we obtained two solutions, i. e., two different matrices, with cross-polar null elements (see Equations (2.88) and (2.89)) and four with co-polar null elements ((2.94), (2.95), (2.96) and (2.97)). These last four matrices differ only in phase terms (see (2.98) and (2.99)). Thus, we have selected only some elements of the derived matrices to perform our tests, namely, the two complex terms appearing in (2.88) which were indicated as p_1 and q_1 and the two of (2.94) named x_1 and a_1 . The amplitudes of the four chosen elements have been provided as inputs to the classifiers with the usual repeated tests on different averaging window dimensions.

When using the co- and cross-polar nulls one gets, in general, better classification results than with the original amplitudes of the $[S]$ matrix elements [PAC⁺02], [ACP02b]. This is more evident for the larger averaging windows, as can be seen in Figure 4.7. For windows of 5×5 pixel or larger, the value of Kappa of the Min. Dist. and Max. Lik. classifiers is almost equal to or greater than 0.4, so that their results can be considered acceptable (as did not happen for the tests on the original data).

We can comment here in detail on the behaviour of the various classes for the tests with the 15×15 -pixel window (see Appendix C.2). The best classification results are obtained for the classes "houses", "trees" and "field 1". Indeed, for these classes, the percentages of both the user's accuracy and producer's accuracy remain quite high for all the classification algorithms (the lowest value is of 63.24% for the Prod. Acc. of the "houses" with the Min. Dist. classifier). Most of the pixels belonging to these classes have been correctly classified and few samples from other training areas have been erroneously assigned to the classes "houses", "trees" or "field 1". Hence, it seems that the co- and cross-polar nulls can be used to describe the targets associated with

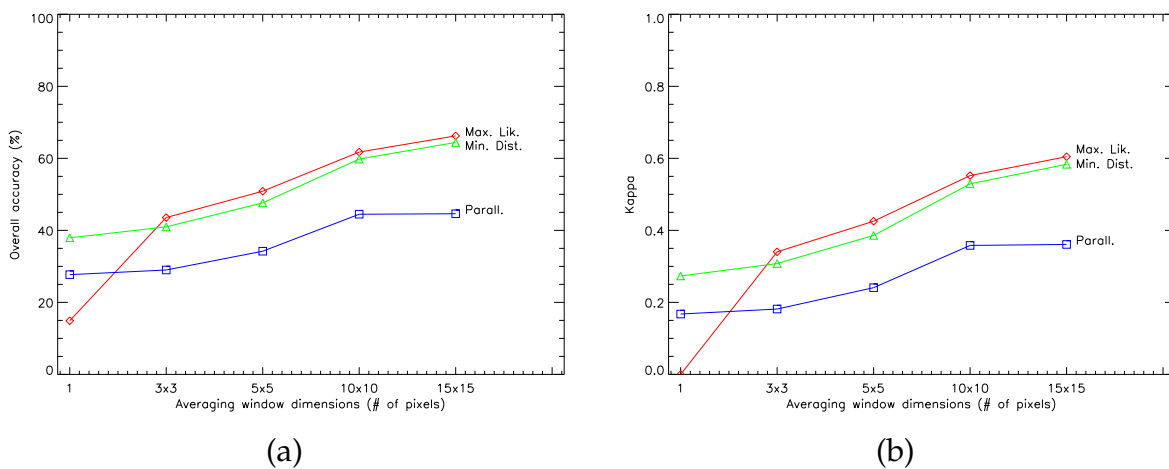


Figure 4.7: Accuracy estimation of the classification tests based on the co- and cross-polar nulls terms: (a) overall accuracy; (b) Kappa (October '99).

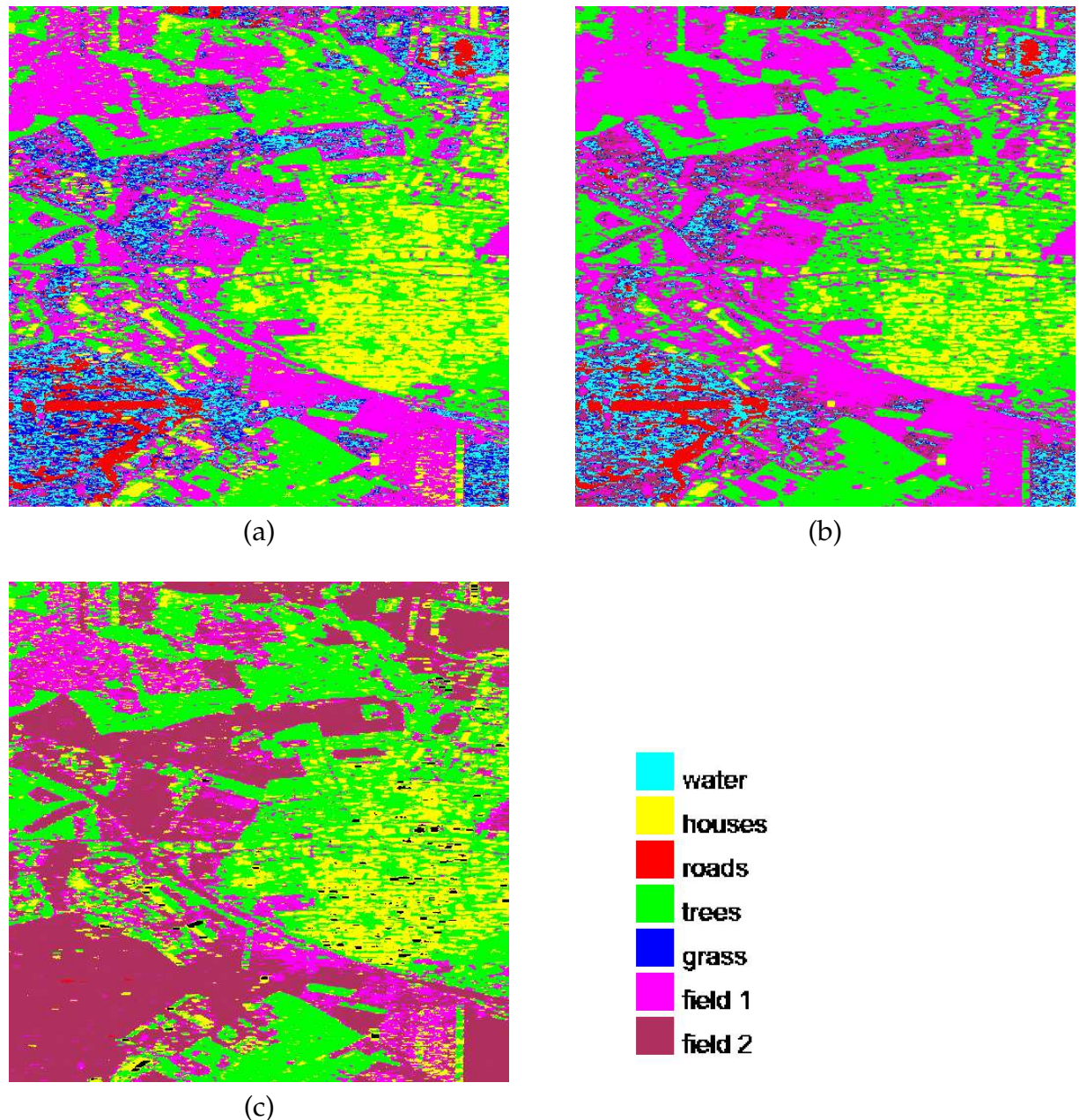


Figure 4.8: Classification maps based on the co- and cross-polar nulls terms (15×15 -pixel averaging window): (a) maximum likelihood; (b) minimum distance; (c) parallelepiped (October '99).

those ground cover types. On the contrary, more controversial is the classification of the “grass” and “field 2” classes, for whom the accuracy estimates remain low even in the considered best case of 15×15 -pixel averaging window. The class “roads”, finally, seems to represent a problem only for the Parall. classifier that gives a very low value, 3.65%, of producer’s accuracy.

For windows smaller than 15×15 pixels or for single-pixel based tests, the accuracy estimates drop rapidly and only the class “trees” shows user’s and producer’s accuracy values higher than 50%.

4.9 Parameters of the coherent target decomposition theorems

In Paragraph 2.5, we presented a review of TD theorems and stressed how these methods “intrinsically” represent a classification tool since they recognize and weight the contributions of different targets in a scene. For example, a colour composite image of the Krogager decomposition coefficients is already a classification image: the identified features are the three scattering mechanisms contemplated in the model and their weights are a way to assign the image pixels to each of them.

These methods have been used here as a preliminary step to the supervised classifications also carried out with the other polarimetric parameters. In particular, we studied [ACP02b] the three main coherent decomposition theorems: the one by Krogager, the Pauli one and that of Cameron. Since they are all coherent methods, they provide information on a pixel-level basis and refer to point-like scatterers. Notwithstanding their original point-like nature, it is again worth investigating how the significance of these decomposition theorems stretches over extended areas. Hence, for all of the TD methods, we repeated our tests with the three classification algorithms: firstly on the data directly derived through a given decomposition, and secondly after averaging the relevant parameters. Results are reported in Appendix C.3.

The first TD theorem under consideration is the SDH decomposition [Kro93], [KC95]. As seen on page 27, this approach yields the decomposition of the scattering matrix into three components, as if the scattering were due to a sphere, a diplane and a right- or left-wound helix. The relative weight of each contribution is determined by the k_i coefficients appearing in Equation (2.121); they are real quantities and provide three new pictures of the imaged scene. The classification tests have been performed only on these values provided as a three-layer input to the classifiers.

The overall accuracy estimates present values for the pixel based tests similar to those previously seen with the other polarimetric parameters. For Kappa, these are always near 0.2 for the parallelepiped classifier and 0.3 for the other two.

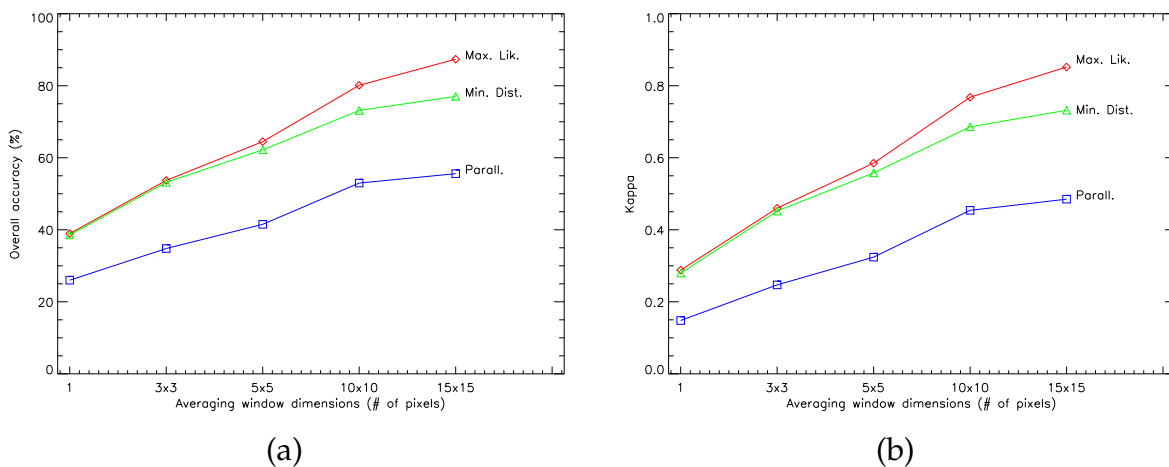


Figure 4.9: Accuracy estimation of the classification tests based on the three coefficients of the Krogager decomposition: (a) overall accuracy; (b) Kappa (October '99).

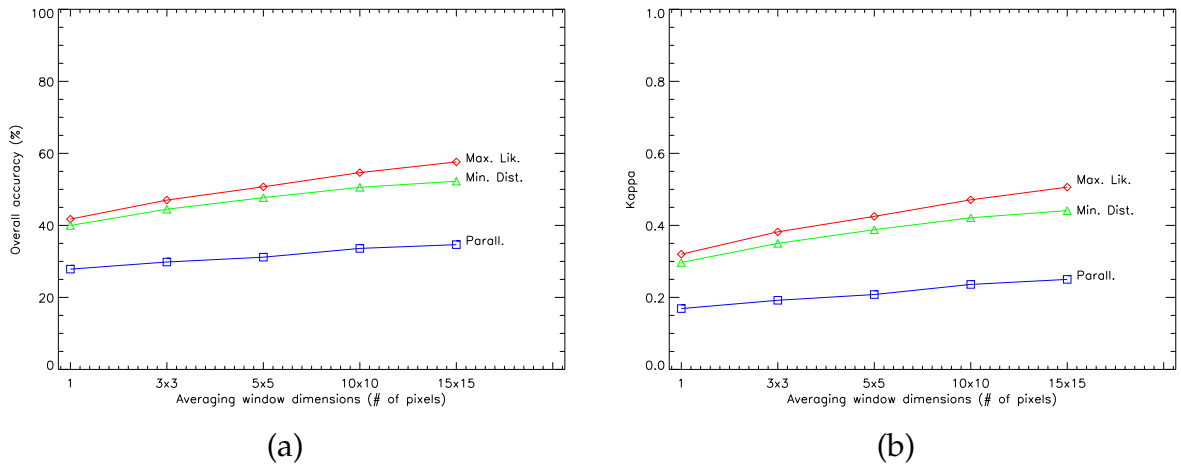


Figure 4.10: Accuracy estimation of the classification tests based on the three coefficients of the Pauli decomposition: (a) overall accuracy; (b) Kappa (October '99).

It is to be noted that the improvement of the accuracy with increasing dimensions of the averaging windows is now much faster than in the previous cases. Indeed, for the Min. Dist. and Max. Lik. classifiers the overall accuracy results are already acceptable ($K > 0.4$) for the 3×3 -pixel window and reaches values of the order of 0.75 for 15×15 -pixel window, which indicates an excellent classification performance. *These are the best results ever obtained with these two algorithms.* Although the parallelepiped classifier presents improved results too, it seems to provide basically the same accuracy percentages.

With reference to the largest averaging window, one obtains very good Us. Acc. and Pr. Acc. for all the classes with all three algorithms. Some limits are presented only by the Parall. classifier with the classes "water", "roads" and "grass". Indeed, this algorithm completely fails in recognizing the training pixels of the class "water" and classifies those of the "grass" only with an Us. Acc. of 6.33% and a Pr. Acc. of 0.46%.

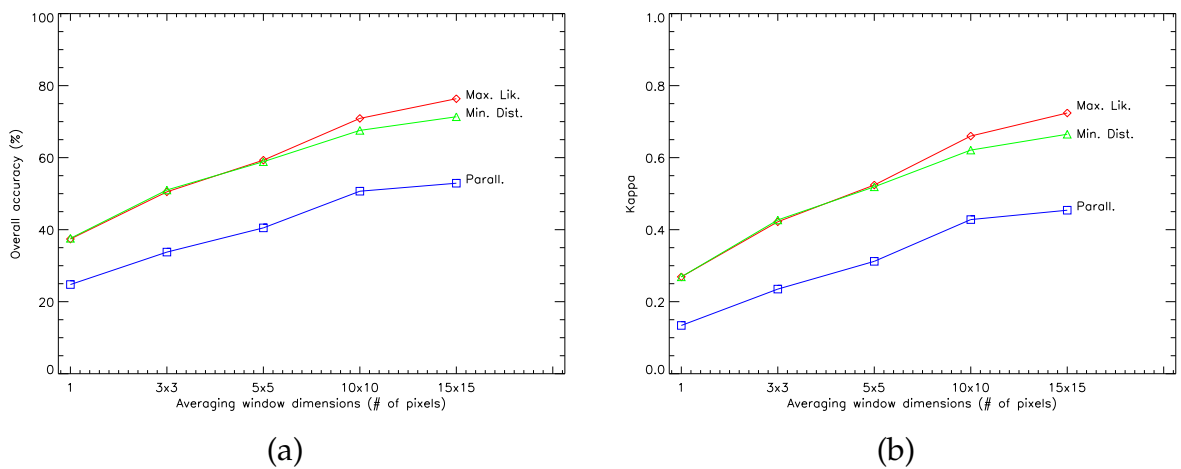


Figure 4.11: Accuracy estimation of the classification tests based on the norm of the two scattering vectors representing the Cameron decomposition terms: (a) overall accuracy; (b) Kappa (October '99).

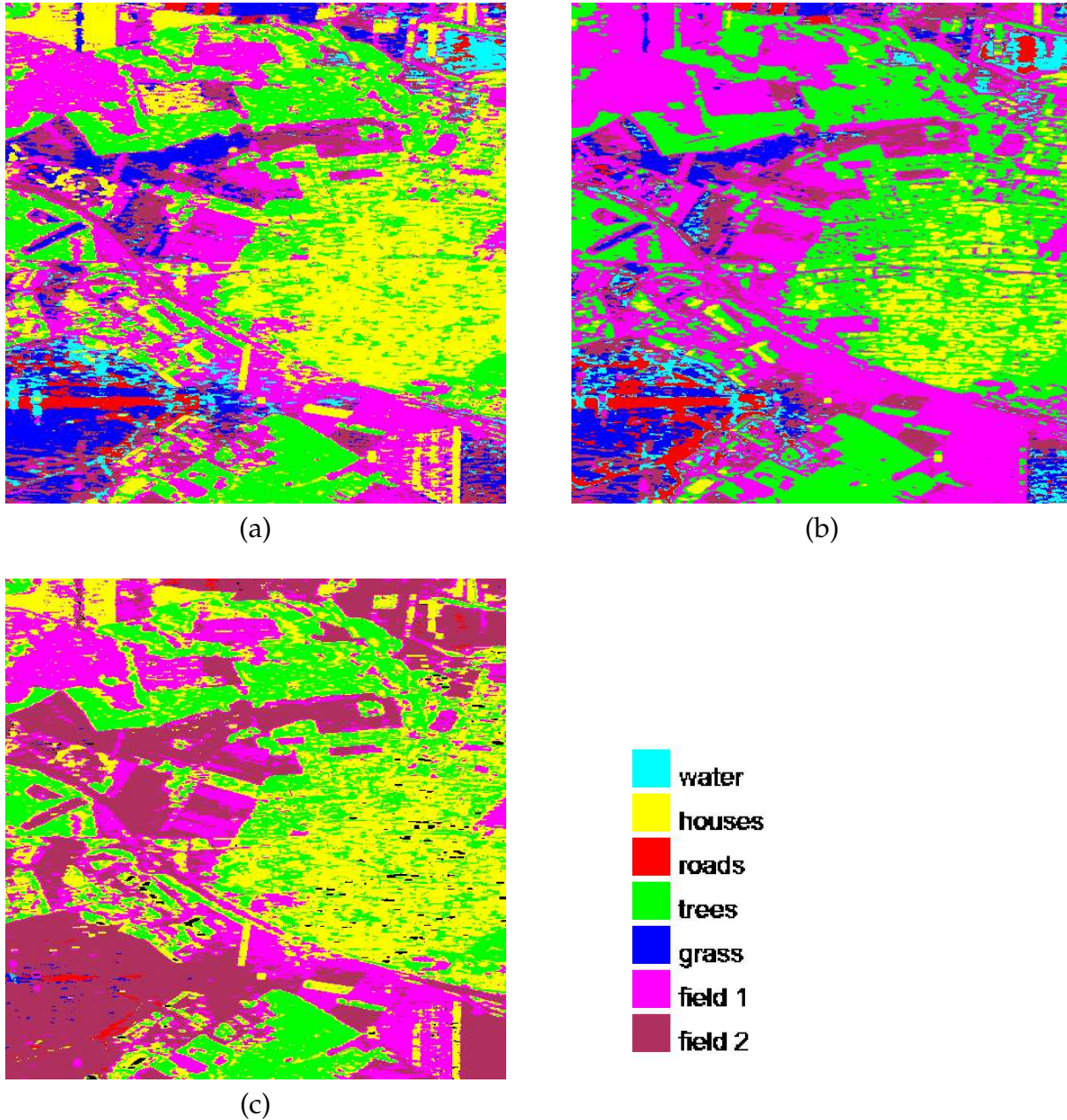


Figure 4.12: Classification maps based on the Krogager decomposition terms (15×15 -pixel averaging window): (a) maximum likelihood; (b) minimum distance; (c) parallelepiped (October '99).

The second TD method taken into account in our analysis is the Pauli decomposition. The tests performed on its characteristic parameters, the a , b and c complex coefficient appearing in (2.120), do not reach as good accuracy values as those of the Krogager decomposition. The Ov. Acc. of the parallelepiped classifier remains almost constant for all windows sizes and its values for the other algorithms do not differ significantly from those obtained by simply using the amplitudes of the three $[S]$ matrix elements. Hence, it seems that no meaningful improvement in terms of amount of information is provided by this TD theorem with respect to the original data (see Figure 4.10).

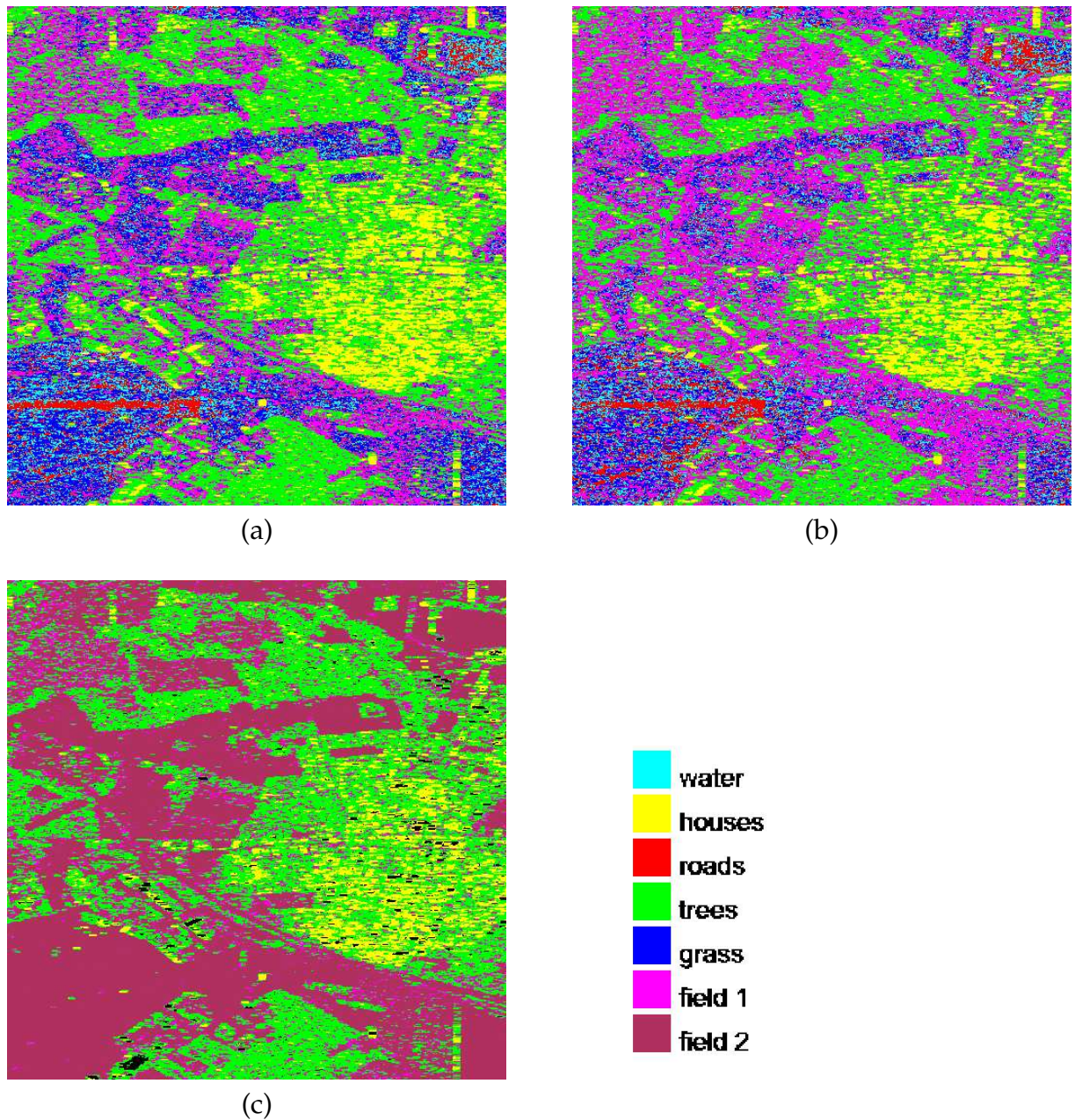


Figure 4.13: Classification maps based on the Pauli decomposition terms (15×15 -pixel averaging window): (a) maximum likelihood; (b) minimum distance; (c) parallelepiped (October '99).

The detail of the single classes tells us that the best results in terms of producer's and user's accuracy are those relative to the classes "houses" and "trees", whereas "grass", "water" and "roads" present much poorer values. Again, the parallelepiped algorithm fails to recognize the last three classes. As in the case of the tests directly performed on the $[S]$ matrix elements, one may suppose that the bad classification results for these classes are due to their low SNR that is not improved by the decomposition.

As a final example of the coherent TD theorems, we studied the Cameron decomposition [CL92], [CYL96]. As SAR data are calibrated in order to fulfill reciprocity constraints, the basic distinction among scatterers made by this method is based on their

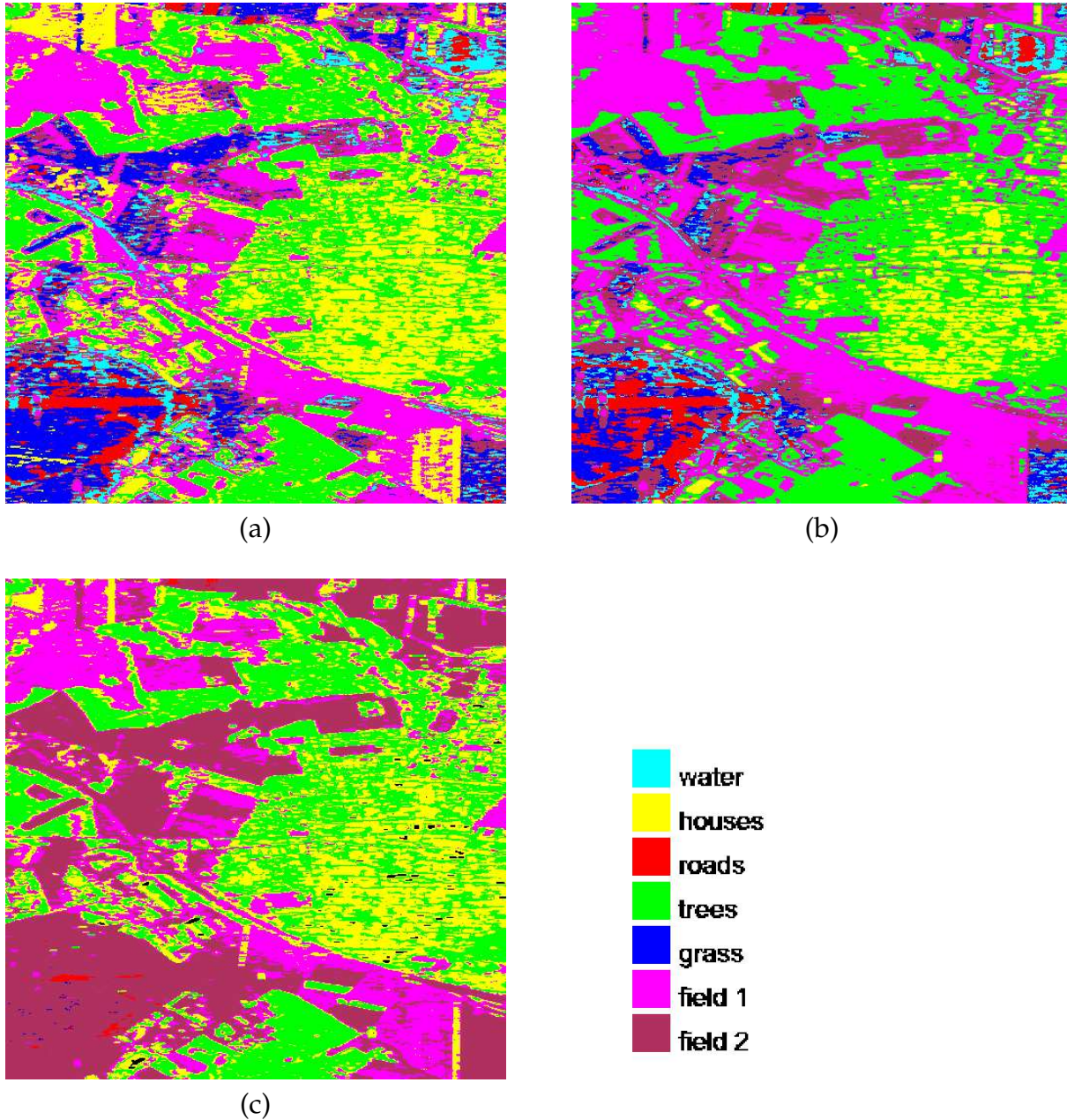


Figure 4.14: Classification maps based on the Cameron decomposition terms (15x15-pixel averaging window): (a) maximum likelihood; (b) minimum distance; (c) parallelepiped (October '99).

symmetry with respect to axes lying on a plane orthogonal to the radar line-of-sight. For this reason one has to perform only the decomposition (2.123) of the $[S]$ matrix into its most dominant and least dominant symmetric terms (henceforth *max sym* and *min sym*). The norm of the corresponding scattering vectors was then given as input to the classifiers.

It is evident from Figure 4.11 that the accuracy estimations now reach values comparable with those obtained with the Krogager decomposition. Their maxima are again obtained for the largest averaging window; the Ov. Acc. ranges from 52% for the Par- all. classifier to 76% for the Max. Lik. one. For this window size, one can note how

the maximum likelihood classifier yields good results even for those classes usually misclassified by the other algorithms, for instance “water” and “grass”. Indeed, the Us. Acc. remains above 50% in both cases, equal to 64% and 68% respectively. On the contrary, the parallelepiped classifier fails again to classify the test samples belonging to these two training areas. Finally, it is also interesting that the Max. Lik. and the Min. Dist. classifiers provide the same accuracy levels for the pixel-based tests and for those performed using the two smallest windows.

4.10 Entropy/ α parameters

The entropy parameter was discussed in Paragraph 3.3. It represents the capability of the diagonalized coherency matrix $[T_{(3)}]$ to distinguish among the different scattering mechanisms that contribute to the backscattered signal from a given resolution cell. As stated in that section, whilst the eigenvectors of $[T_{(3)}]$ each describe an independent scattering mechanism, its three eigenvalues (used to determine H) express their relative intensity and hence give a measure of the “complexity” of the interactions in a cell. Further information may then be obtained by means of the parameterization given in (3.13): the type of the identified mechanisms is related to the α angles and a general description of the given coherency matrix is related to the average $\bar{\alpha}$ value.

Properties of the scatterers may then be interpreted in terms of these parameters and their classification performed considering their distribution in the H/α space (see Figure 4.15). Since some physical limits exist for the variation of $\bar{\alpha}$ as a function of H , not all the H/α space represents real scatterers (i. e., not all the values of entropy and $\bar{\alpha}$ have a physical meaning). Hence, one can define curves limiting this space and, inside this physically feasible area, make a further distinction between eight classes of scattering mechanisms. These are clustered as follows [CP97]:

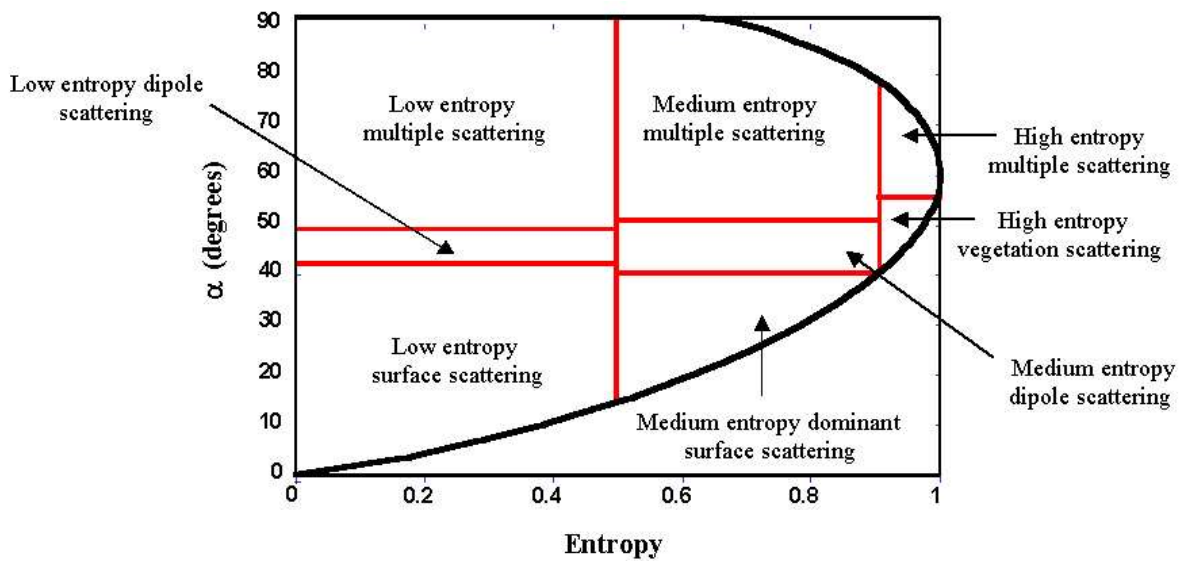


Figure 4.15: H/α plane and its division in sub-regions according to the scattering types (courtesy of I. Hajnsek).

Low entropy surface scattering. In this zone, low entropy scattering processes occur with $\bar{\alpha}$ values less than 42.5° . All surface single scattering phenomena should belong here: those within the geometrical optics limit, those treated by means of physical optics, Bragg surface scattering and specular scattering phenomena which do not involve 180° phase inversion between S_{hh} and S_{vv} . For instance, at L-band, water and very smooth terrain surfaces belong to this category.

Low entropy dipole scattering. This area corresponds to strongly correlated mechanisms having a large imbalance between S_{hh} and S_{vv} in amplitude. Isolated dipole scatterers, as well as vegetation having clearly oriented anisotropic scattering elements would appear in this zone.

Low entropy multiple scattering. Double or even-bounce scattering events are to be located here. This is the case for isolated dielectric and metallic dihedral scatterers.

Medium entropy dominant surface scattering. This zone presents a higher value of entropy due to increases in surface roughness and to canopy propagation effects. Hence, surfaces characterized by an increasing roughness/correlation length or surfaces covered by oblate spheroidal scatterers (such as certain types of leaves) would be located in this area.

Medium entropy dipole scattering. Moderate entropy with a dominant dipole scattering mechanism characterizes this zone that includes scattering from vegetated surfaces with anisotropic scatterers and moderate correlation for the orientation of the scatterers.

Medium entropy multiple scattering. Scattering phenomena contained in this region are those typically present in forested areas; in effect, double bounce mechanisms through the canopy increase the entropy. Also urban areas belong to this zone, as dense packing of localized scattering centres can generate moderate entropy with low order multiple scattering being dominant.

High entropy vegetation scattering. Scattering phenomena from forest canopies lies in this region as does the scattering from some types of vegetated surfaces with random highly anisotropic scattering elements.

High entropy multiple scattering. In this zone, double bounce mechanisms in a high entropy environment may still be distinguished. Good examples are forests or scattering from vegetation that has a well-developed branch and crown structure.

The proposed division of the H/α space may not only be directly applied to perform unsupervised classification but, as well, considered as a tool to check the accuracy of other classification techniques and their consistency. This is the strategy adopted in this work. Again, the three chosen supervised classification algorithms were used to perform tests with different sizes of the averaging window; in this way, a direct comparison with the other parameters is possible [ACP02b].

The values of H , $\bar{\alpha}$ and A are calculated after the averaging process, indeed, this is performed when evaluating the coherency matrix. As in the previous cases, the

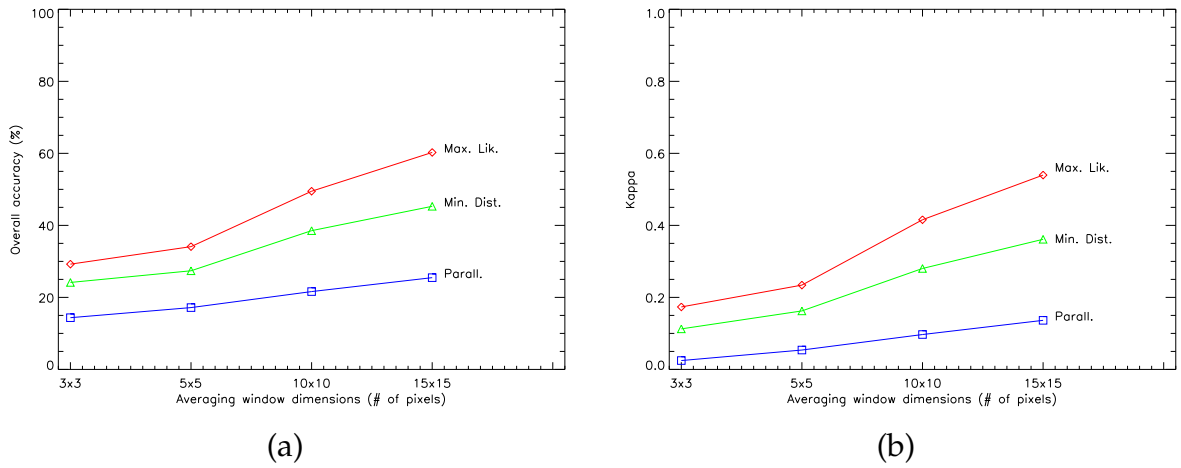


Figure 4.16: Accuracy estimation of the classification tests based on the H and $\bar{\alpha}$ parameters: (a) overall accuracy; (b) Kappa (October '99).

averaging windows have the following dimensions: 3×3 , 5×5 , 10×10 and 15×15 pixels. A first series of experiments is based only on the H and $\bar{\alpha}$ parameters, i. e., only these two have been given as input to the classifiers. The results of the three different methods in terms of Ov. Acc. and Kappa are illustrated in Figures 4.16 (a) and (b). A second series also takes into account the anisotropy A (hence, three parameters as input). The classification tests were repeated for all the cases and further graphs of the Ov. Acc. and Kappa were derived (see Figures 4.17 (a) and (b)). Tables summarizing the main results of the classification tests can be found in Appendix C.4.

In both series of tests, the level of accuracy remains relatively low. Because of this, in [SAC⁺00] the total backscattered power was used as temporary additional input for improving the segmentation of the H/α parameters.

The Ov. Acc. and the Kappa coefficient diagrams show again an increasing accuracy of the classification results ranging from the 3×3 to the 15×15 -pixel window. The two simplest classifiers, namely the Parall. and the Min. Dist., do not present remarkable

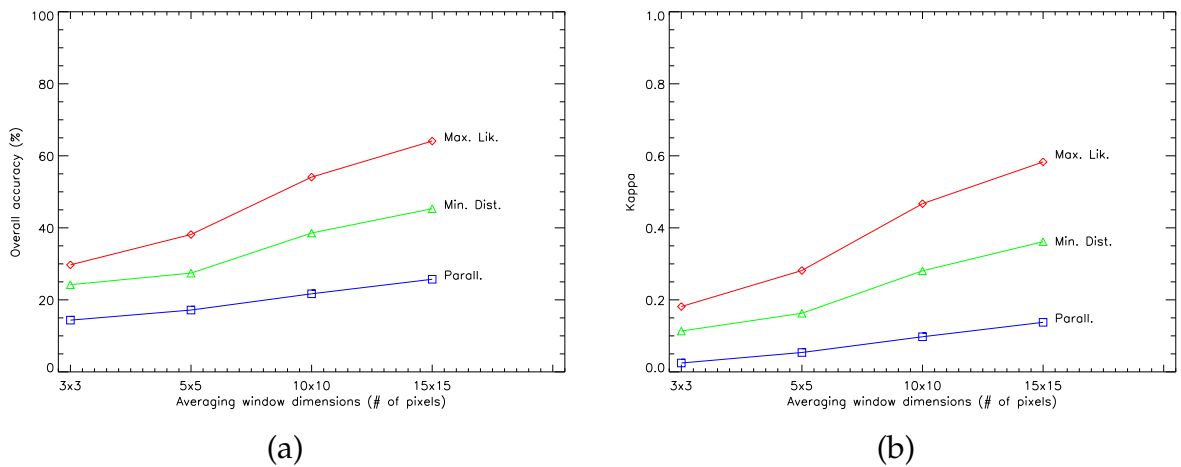


Figure 4.17: Accuracy estimation of the classification tests based on the H , $\bar{\alpha}$ and A parameters: (a) overall accuracy; (b) Kappa (October '99).

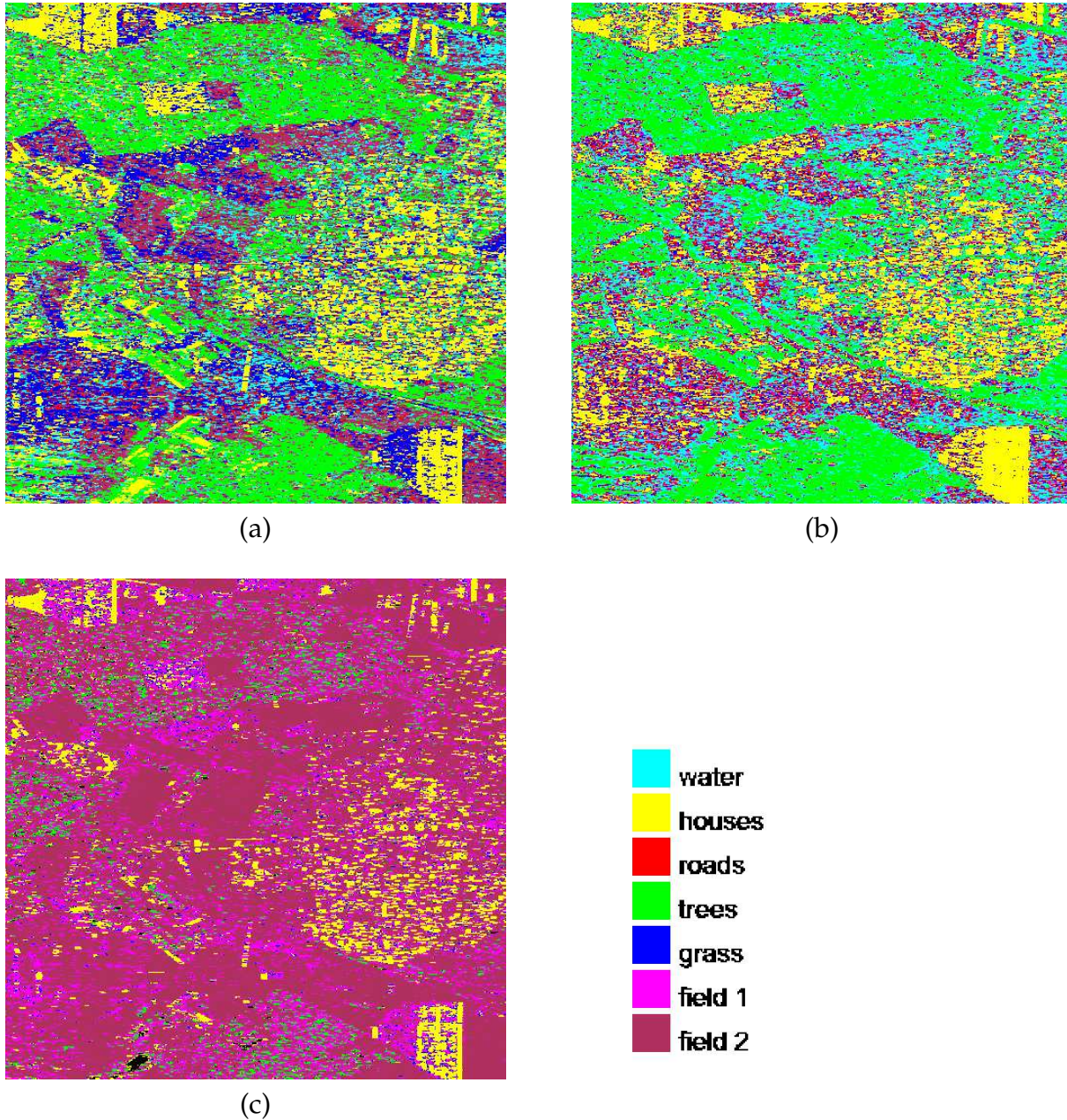


Figure 4.18: Classification maps based on the H and $\bar{\alpha}$ parameters (10×10 -pixel averaging window): (a) maximum likelihood; (b) minimum distance; (c) parallelepiped (October '99).

accuracy values. They are not sensitive to the additional anisotropy information: the values of the overall accuracy and of Kappa are not subject to significant variations. In particular, the Parall. algorithm provides similar results independently upon use of the anisotropy as input. Also the Max. Lik. appears to be not so effective as it was when applied to the SDH coefficients with averaging, even though an increase of accuracy of 10% has often occurred when adding anisotropy. Moreover, the Gaussian statistical hypothesis characterizing the Max. Lik. criteria is not satisfied by the polarimetric variables under study and, as stated before, represents a potential flaw in the use of this classification method.

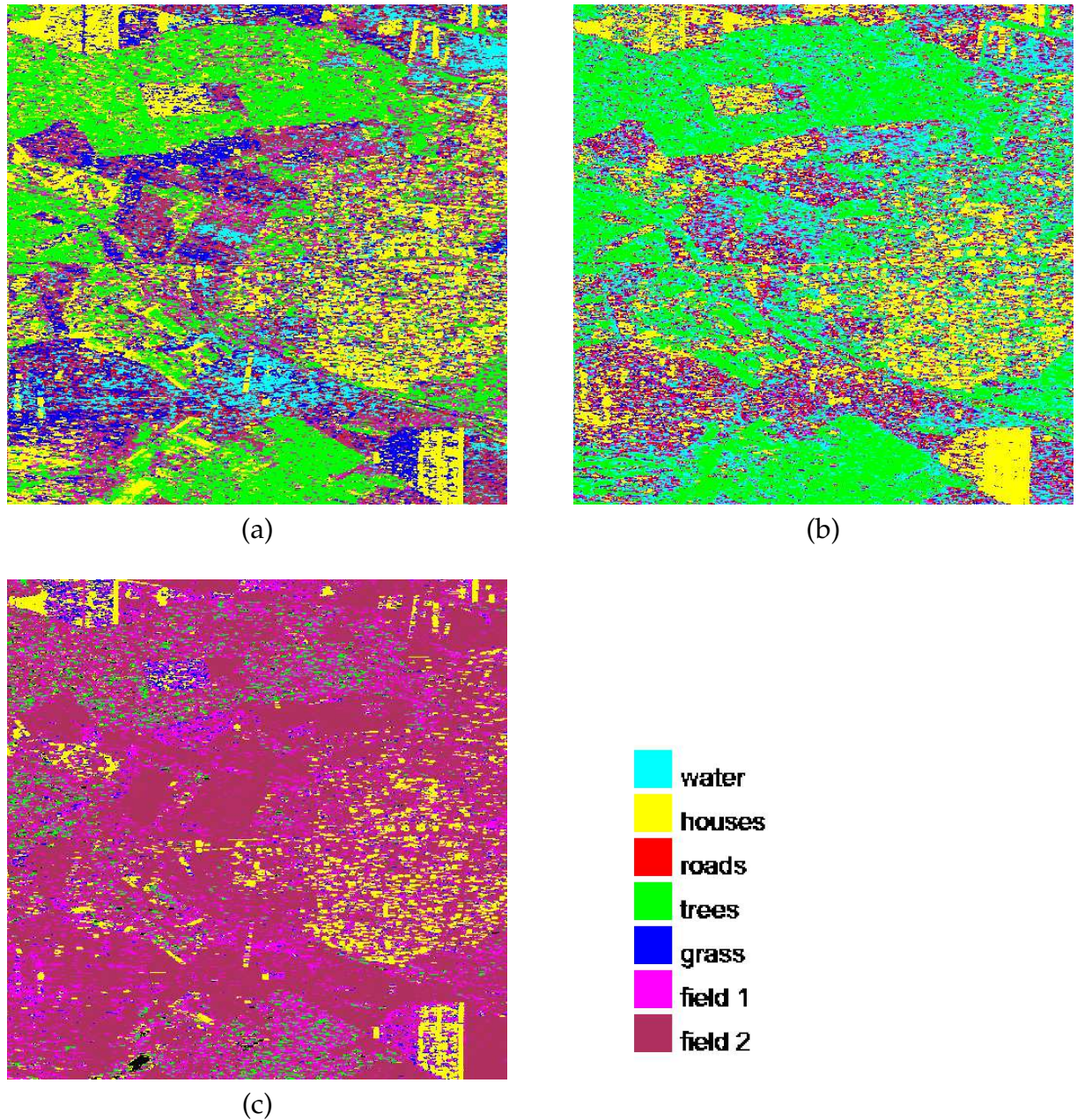


Figure 4.19: Classification maps based on the H , $\bar{\alpha}$ and A parameters (10×10 -pixel averaging window): (a) maximum likelihood; (b) minimum distance; (c) parallelepiped (October '99).

A visual analysis of the resulting classification maps also suggests some limitations of this method. The similar behaviour of the “water” and “roads” classes makes it impossible to distinguish them from each other. The urban area appears well defined, but cultivated fields are often assigned to “houses” or “water” classes. Different kinds of fields are not separable. Only the class “trees” shows good classification results and the measured values characterize it unambiguously.

4.11 Comparisons and conclusions

It is now possible to summarize the results discussed in the previous sections referring also to Table 4.3 in order to get a general overview over them. Since the tests were performed on a single data set, the considerations that will follow do not presume to have an absolute validity but should simply indicate a trend that is reasonable to assume valid for similar data and imaged scenes.

The first important observation is that *little improvement in our classification tests can be obtained using the incoherent polarimetric parameters derived from the original data rather than using directly these ones* [PAC⁺02], [ACP02b]. Indeed, the Ov. Acc. increases just slightly for the tests on the $H/\bar{\alpha}$ values with respect to those on the amplitude ones. A possible interpretation is the following: the entropy and anisotropy parameters are derived by the eigenvalues of the coherency matrix; no use is made of the corresponding eigenvectors. One may then suppose that part of the information originally contained in the data has been “neglected” leading to poorer, or poorer than expected, classification results. Moreover, $\bar{\alpha}$ is the only quantity that does not express an intensity.

Concerning the coherent parameters, only two of the decomposition methods, namely, the SDH and the Cameron decompositions, lead to significantly higher accuracy values, whereas the ratios of the [S] matrix elements [AC00] provide results significantly worse than all the other polarimetric parameters.

As a further note of caution, it should be reminded that the chosen algorithms implement quite general image classification methods and are not specifically intended for SAR data; hence, they are not the optimal tools for analyzing them. In general, the Max. Lik. classifier gives the best results (in terms of Ov. Acc. and Kappa coefficient); independently from the averaging windows dimensions, the values obtained are higher than in the other two cases. This may be attributed to the higher versatility of the second order statistic model of the Max. Lik. classifier in comparison with the first order statistics criteria adopted by the Parall. and Min. Dist. methods. Due to these considerations, the unsupervised segmentation proposed in [CP97] would be more appropriate for the incoherent parameters.

As expected, the choice of the training data set plays a relevant role: some of the selected ground coverage types always give rise to problems in the classification processes and bad accuracy results, whereas, for others, these are constantly acceptable.

Table 4.3: Accuracy estimates of all the classification tests relative to the 15×15 -pixel averaging window.

Class. alg. → Pol. parameters ↓	Maximum likelihood		Minimum distance		Parallelepiped	
	Ov. Acc. (%)	Kappa	Ov. Acc. (%)	Kappa	Ov. Acc. (%)	Kappa
Backscattered amplitude	57.03	0.5	50.96	0.43	33.88	0.24
Co- and cross-polar nulls	66.24	0.6	64.41	0.58	44.61	0.36
SDH coefficients	87.37	0.85	77.04	0.73	55.58	0.48
Pauli coefficients	57.61	0.51	52.27	0.44	34.65	0.25
Cameron terms	76.37	0.72	71.35	0.66	52.9	0.45
$H/\bar{\alpha}$	60.25	0.54	45.3	0.36	25.48	0.136
$H, \bar{\alpha}$ and A	64.1	0.58	45.31	0.36	25.71	0.137

In fact, in all the tests, the classes “houses”, “trees” and “field 1” were better recognized than the classes “roads”, “grass” and “water”. Hence, *the role of the analyst with a ground truth knowledge remains fundamental, in the sense that the selection of the training data and of the classification items affects the final results sometimes as deeply as the choice of the type of the inputs.*

Regarding the comparison among single-pixel and averaged areas classifications, we have shown that, *by averaging the values of the image pixels, the classification efficiency is, in general, enhanced. This could mean that the studied parameters refer to physical properties “spread” over neighbouring and somehow correlated pixels.* Indeed, the presence of “extended” parameter characteristics may have led to improved classification accuracy for increasing sizes of the averaging windows (at least in the limits of the 15×15 -pixel window as largest size). Another aspect to be taken into account, which influences the different results, is that the tests compare averages of both real and complex quantities.

It is worthwhile to stress that, to our knowledge, no systematic investigations similar to ours have been yet conducted on this subject.

5 Analysis of polarimetric parameters: interferometry

5.1 Overview

Polarimetry and interferometry seem to play distinct roles in radar remote sensing, leading also to their application to different tasks: polarimetric analysis makes it possible to separate different scattering mechanisms within a given resolution cell, whereas interferometric techniques allow for a topographical characterization of the scattering contributions. As an obvious consequence of these properties, one may try to use polarimetry and SAR interferometry for those cases when different scatterers are expected to occupy different positions. In particular, a topic actively investigated is the possibility to distinguish scatterers separated in height, and steps in this direction have been recently taken [CP98], [PRC99a], [PRC99b], [PC01], [IC01], [Sag00]. The interest in doing this is readily found when considering the various sources of decorrelation affecting two SAR images: a major cause is the volume scattering term, which is related to the height distribution of the effective scatterers above the chosen reference plane [ZV92], [BH98]. Hence, “resolving” the volume decorrelation and fixing the exact position of the scattering centres could also lead to an estimation of the height of the resulting distributed scatterers. Moreover, the exact determination of the volume scattering contribution is fundamental in DEM generation as well as in biomass estimation.

Due to all these reasons, the question of volume decorrelation is worth special attention. We present here a study on the potential of target decomposition methods combined with interferometry which is aimed at verifying if they can be used to reduce this effect and the problems connected to this approach. Given the differences among TD theorems, in particular among coherent and incoherent ones, we also investigate if different methods permit us to distinguish between volume scattering (that is, vegetated/forested areas) and coherent targets with a profile along their height (basically buildings and other man-made artifacts).

5.2 Theoretical aspects

In order to understand the phenomenon of decorrelation in SAR interferometry, it is helpful to provide more details about the expression of the interferometric coherence introduced in Equation (3.20).

5.2.1 Interferograms generation

Let us consider first a single SAR image and the geometry associated with it as given in Figure 5.1. Here, the primed coordinates are related to the target, while the unprimed ones refer to a reference point for the system response $h(x, R)$. With this geometry, the value of the image for a point on the ground at x' azimuth position and slant range R' can be expressed as [HUA95], [BH98]:

$$s(x, R) = \int \tilde{u}(\vec{r}') \exp(-j2kR') h(x - x', R - R') dV' + n(x, R). \quad (5.1)$$

In (5.1), $\vec{r}' = (x', y', z')$ and $dV' = dx' dy' dz'$, $\tilde{u}(\vec{r}')$ represents the three-dimensional complex terrain reflectivity (it will be referred to also as the *scattering object*), $h(x - x', R - R')$ and $n(x, R)$ are respectively the system response and noise, and \vec{k} the signal wavevector which results as function of the radar look angle θ :

$$\vec{k} = |\vec{k}|(0, \sin \theta, -\cos \theta). \quad (5.2)$$

The system response is usually modulated by rectangular filter functions of bandwidth W_R in range and W_x in azimuth, and hence has the form:

$$h(x, R) = \text{sinc}(W_x x) \text{sinc}(W_R R) = \frac{\sin(W_x x)}{W_x x} \frac{\sin(W_R R)}{W_R R}. \quad (5.3)$$

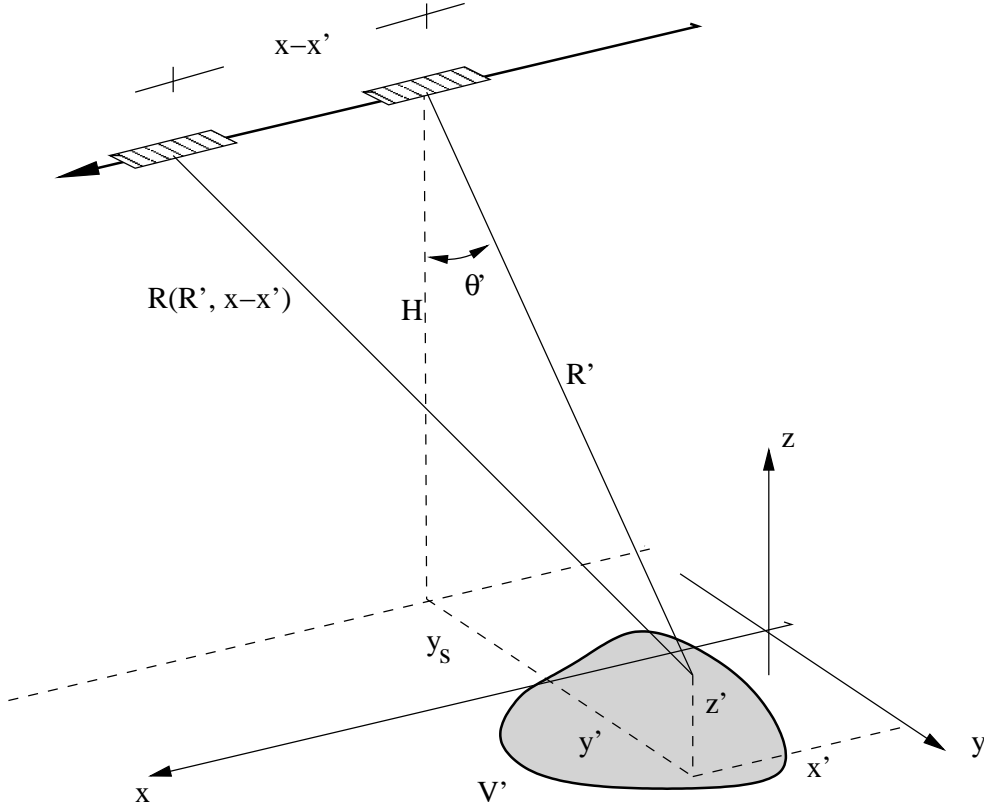


Figure 5.1: Range history $R(R', x - x')$ of a point scatterer belonging to an extended target.

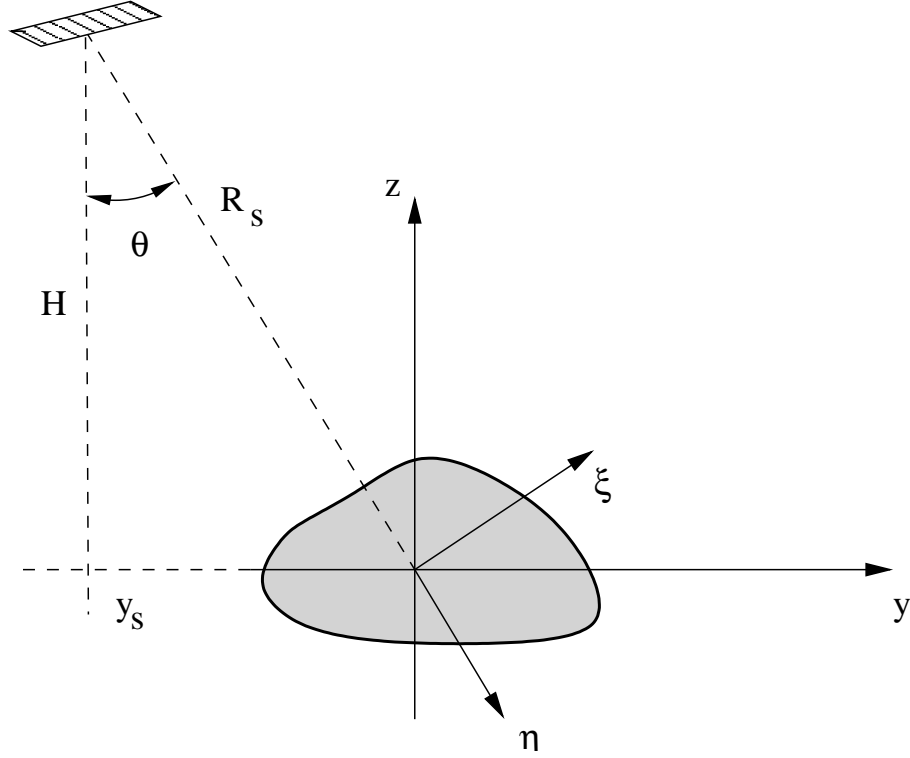


Figure 5.2: Range coordinate system for a fixed point in azimuth.

Now, let us further assume that the origin of the range coordinate in the SAR image has been set to:

$$R_s = \sqrt{H^2 + y_s^2} \quad (5.4)$$

so that we can define a new range coordinate η as:

$$\eta = R - R_s \quad (5.5)$$

and an axis ξ orthogonal to the η -axis directed as represented in Figure 5.2. In this new coordinate system, it is possible to derive the plane wave approximation of (5.1) as:

$$s(x, \eta) = \exp(-j2kR_s) \int \tilde{u}(\vec{r}') \exp(-j2\vec{k} \cdot \vec{r}') h(x - x', \eta - \eta') dV' + n(x, \eta). \quad (5.6)$$

When doing interferometry (see Figure 5.3), one works with two images characterized by different objects $\tilde{u}_1(\vec{r}_1)$ and $\tilde{u}_2(\vec{r}_2)$ which pass system responses $h_1(x, \eta)$ and $h_2(x, \eta)$ according to Equation (5.6). Due to the slightly different look angles, the (η, ξ) -coordinate systems of the images differ. However, the difference $\Delta\theta$ between the look angles is small enough such that an average angle θ_0 and a single (η, ξ) -coordinate system can be considered. Hence, only the exponential factor $\exp(-j2\vec{k} \cdot \vec{r}')$ in (5.6) is different in the two wave-vectors.

As the two SAR images may not have been acquired simultaneously, the scatterers may have changed between acquisitions (we will see later the possible causes of these changes) and the two complex reflectivities are connected by a cross-correlation function such that:

$$E[\tilde{u}_1(\vec{r}_1) \tilde{u}_2^*(\vec{r}_2)] = \sigma_{ve}(\vec{r}_1) \delta(\vec{r}_1 - \vec{r}_2), \quad (5.7)$$

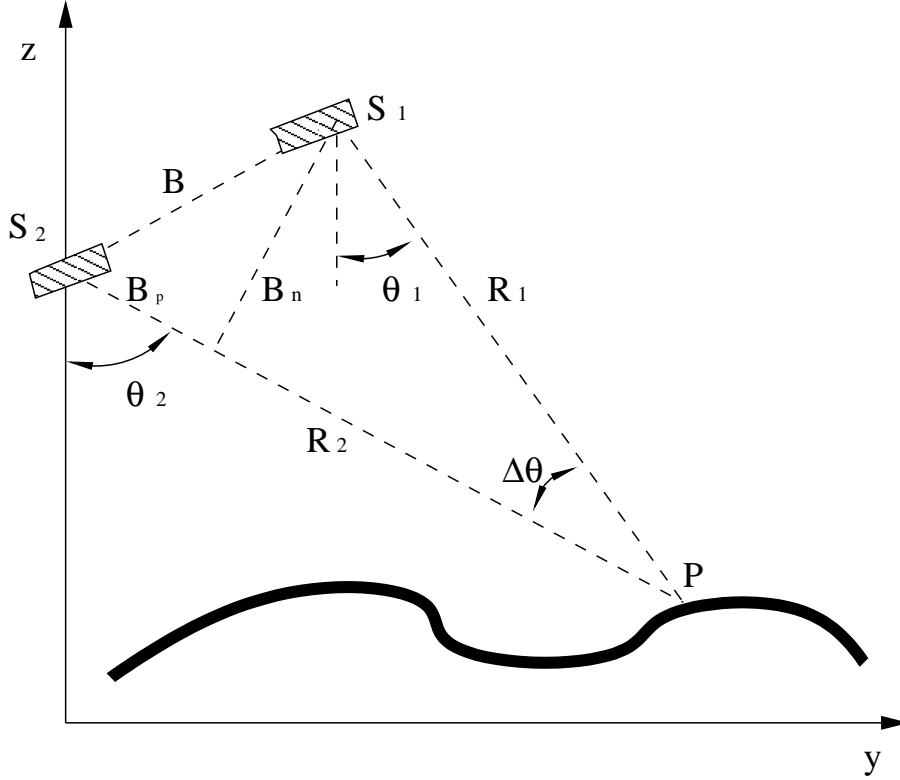


Figure 5.3: Front view of the interferometric data-take geometry.

where $E[\]$ stands for *expectation value* and $\sigma_{ve}(\vec{r})$ is the *volumetric backscatter coefficient* [BH98] of scatterers common to both images and expresses the amount of correlation of the two complex reflectivities. The coefficient $\sigma_{ve}(\vec{r})$ can be interpreted as the temporarily stable scattering contribution; scatterer contributions that have changed between observations average out in the expectation value.¹

Assuming mutually uncorrelated system noise $n_1(x, \eta)$ and $n_2(x, \eta)$ of intensity:

$$E[|n_1|^2] = N_1 \quad (5.8)$$

and

$$E[|n_2|^2] = N_2, \quad (5.9)$$

one may use the equations above to write the interferometric coherence as:

$$\gamma = |\gamma'| = \frac{|\int \sigma_{ve}(\vec{r}') h_1(x - x', \eta - \eta') h_2(x - x', \eta - \eta') \exp[-j2(\vec{k}_1 - \vec{k}_2) \cdot \vec{r}'] dV'|}{\sqrt{(S_1 + N_1)(S_2 + N_2)}} \quad (5.10)$$

and take the phase of the complex γ' as the expected interferometric phase.

S_1 and S_2 are the noise-free signal intensities of the two images and are equal to:

$$S_1 = \int \sigma_{v1}(\vec{r}') |h_1(x - x', \eta - \eta')|^2 dV', \quad (5.11)$$

¹This is true only for *random* changes of scatterers. Hence, this form of cross-correlation function is not applicable for objects that perform a rigid movement and whose scattering properties remain stable.

$$S_2 = \int \sigma_{v2}(\vec{r}') |h_2(x - x', \eta - \eta')|^2 dV', \quad (5.12)$$

where $\sigma_{v1}(\vec{r}')$ and $\sigma_{v2}(\vec{r}')$ represent the volumetric backscatter coefficients of the scattering objects and are a measure of their autocorrelation.

5.2.2 Decorrelation sources

According to [RM92] and [ZV92], the coherence can be written as the product of several contributions:

$$\gamma = \gamma_{SNR} \gamma_{temporal} \gamma_{spatial}. \quad (5.13)$$

γ_{SNR} represents the decorrelation due to additive noise, while $\gamma_{temporal}$ stands for temporal scene coherence and is defined as the ratio of temporarily stable scattering contributions to the total scattering intensity transferred to the SAR images (more details about these contributions and their analytical formulation can be found in [ZV92], [BH98] and [Pap99]).

The contribution deserving our attention in this chapter is $\gamma_{spatial}$, which describes the decorrelation caused by the different processing performed on the two SAR signals (in the sense that they have been differently “coupled” to the system responses). In turn, spatial decorrelation itself can be split into two terms relating to different scattering mechanisms, surface scattering and volume scattering, that is:

$$\gamma_{spatial} = \gamma_{sur} \gamma_{vol}. \quad (5.14)$$

This is possible under the assumption:

$$R^2 = x^2 + y^2 + z^2(x, y) \approx x^2 + y^2 \quad (5.15)$$

which, referring to Figure 5.1, implies the possibility of choosing the origin of the coordinates on the mean plane of the surface and far from the illuminated area. Hence, it holds: $x, y \gg z$ and the dependence of $h(x, \eta)$ from z can be neglected.

The characteristics of the targets on the ground and their differences (in size, shape, distribution and temporal stability) deeply influence the SAR image synthesis and the interferometric application [BH98]. Indeed, due to the high sensitivity to range variations of the phase term in the integral of (5.6), each scatterer in a resolution cell (meters) should be located with a precision of the order of a fraction of the wavelength (centimeters). This condition is hardly met for natural scenes that usually contain distributed targets. Also the expression of the volumetric backscatter coefficient depends completely on the nature of the imaged targets and two extreme situations are possible: point scatterers and Gaussian (or Rayleigh) scatterers.

The first case relates to ideal targets whose volumetric backscatter coefficient is of the type:

$$\sigma_{ve}(\vec{r}) = \sigma_0 \delta(\vec{r} - \vec{r}_0). \quad (5.16)$$

This means that the resolution cell may be treated as point-like at least concerning the determination of its position. Hence, the coherence is equal to 1 and the interferometric phase is exactly that which corresponds to the path difference from the two antennae to the target with no uncertainties in range. Such a case is realized, for instance, by “ad

hoc" artificial targets, the so-called *corner reflectors*, whose backscatter is so strong as to completely determine the value of $\sigma_{ve}(\vec{r})$ for that resolution cell since the contribution from surrounding natural targets is overcome. Backscattering from Gaussian scatterers is, on the contrary, due to several elementary random scatterers among which none provides a contribution clearly dominating the others.

Another aspect to be considered is the actual spatial distribution of the elementary scatterers, in particular, their eventual displacement in height. For example, the canopy layer of forests is constituted by randomly distributed scatterers, the leaves and the branches, with varying shape and orientation which are also subject to frequent, and random, changes in time. Backscattering from such targets usually yields very low coherence values and is referred to as *random volume* scattering. It is important to stress that the low coherence is due both to the vertical, almost continuous, structure of the target (for reasons that will be explained below) and to its low stationarity. For the case when only varying target heights affect the coherence but the elementary scatterers are stationary, discrete and limited in number, as those of walls or buildings, then it is helpful to introduce the new definition of *coherent volume* scattering [ACP02a], [AC03].

Coming back to Equation (5.14), one can consider the two contributions separately. The case of pure surface scattering is characterized by:

$$\sigma_{ve}(\vec{r}) = \sigma_{sur}(x, y) \delta(z - z_0), \quad (5.17)$$

that is, all scattering interactions are assumed to take place at a certain height $z = z_0$ and the degree of correlation depends on the phase variations of the scatterers on this plane. As we will see, it is possible to compensate the effect of the decorrelation due to changes in look angle of the sensors, by means of an adequate setting of the system responses.

Quite different is the scenario when volume scatterers are present. After compensating pure surface effects, $\gamma_{spatial}$ is determined by a volumetric backscatter coefficient with a profile in z and constant in x and y :

$$\sigma_{ve}(\vec{r}) = \sigma_{vol}(z). \quad (5.18)$$

Its characteristics change significantly depending on whether it represents coherent volume scatterers (buildings or other man-made artifacts) or a random volume (vegetated areas), though for both γ_{vol} has the form:

$$\gamma_{vol} = \frac{|\int \sigma_{vol}(z') \exp[-j2(k_{z',1} - k_{z',2})z'] dz'|}{\int \sigma_{vol}(z') dz'}, \quad (5.19)$$

where the components k_z are the projections onto the z -axis of the wavevectors. Indeed, in the case of coherent volume scatterers, a limited number of elementary scatterers can be found in each resolution cell or, at least, the number of multiple interactions is less than in a random volume so that the coherence tends to values nearer to 1 than in the second case.

5.2.3 Interferometric coherence enhancement

The reduction of the decorrelation effects of $\gamma_{spatial}$ follows different strategies according to the mechanisms originating γ_{sur} and γ_{vol} . Under the hypothesis of *pure surface*

scattering, the decorrelation is due only to the fact that the backscattered signals correspond to different bands of the ground reflectivity spectrum [PRGP94], [GGP⁺94]. This can be demonstrated starting from the approximated relation between the frequency f and the ground range wavenumber k_y :

$$k_y = 2 \frac{2\pi}{\lambda} \sin(\theta - \alpha) = \frac{4\pi f}{c} \sin(\theta - \alpha), \quad (5.20)$$

taking into account the two-way travel path and also a constant uniform slope of the terrain represented by α . The difference Δk_y , i. e., the variation of k_y generated by a slight change of the look angle $\Delta\theta$, is then:

$$\Delta k_y = \frac{4\pi f \Delta\theta}{c} \cos(\theta - \alpha). \quad (5.21)$$

Thus, in general, a look angle difference $\Delta\theta$ generates a shift and a stretch of the imaged terrain spectra. However, if the relative system bandwidth is small, the frequency f in (5.21) can be substituted by the central frequency f_0 and the stretch can be neglected, then the following equation holds:

$$\Delta k_y = \frac{4\pi f_0 \Delta\theta}{c} \cos(\theta - \alpha). \quad (5.22)$$

Finally, since the radar is not monochromatic (a certain bandwidth W centered around f_0 is always given), one may conclude that by changing the look angle of the SAR beam one gets a different band of the ground reflectivity spectrum. This difference is a source of decorrelation that affects $\gamma_{spatial}$ but, as was shown in [GGP⁺94], it can be overcome by means of tunable radars, i. e., systems whose processing filters can be tuned to the different centre frequencies (a technique known as *wavenumber shift filtering*):

$$h_2(x, \eta) = h_1(x, \eta) \exp(-j2\pi \Delta f \eta), \quad (5.23)$$

where:

$$\Delta f = -\frac{2B_n}{\lambda R_s \tan(\theta - \alpha)} \quad (5.24)$$

and B_n is the component of the baseline normal to the look direction [BH98]. Equation (5.24) does not relate to angular dependence of the scatterers, an assumption valid in this case.

A first method for resolving volume decorrelation by means of polarimetry was proposed by Cloude and Papathanassiou [CP98]. It consisted of associating a different scattering mechanism, and connected to that a scattering centre, to each scattering vector defined by the optimization of the interferometric coherence (see page 45). According to their expectations, the maximization constraints would act mainly on the volume term of $\gamma_{spatial}$ (in the hypothesis of reduced effects of temporal decorrelation). Moreover, in this way, the position in height of the scattering centres can also be defined. Thus this method should provide a first rough estimate of the height of extended targets.

In [CP98] and [Pap99], this result was suggested as a way to measure tree heights, assuming that the scattering centres so identified are situated almost at the top and at

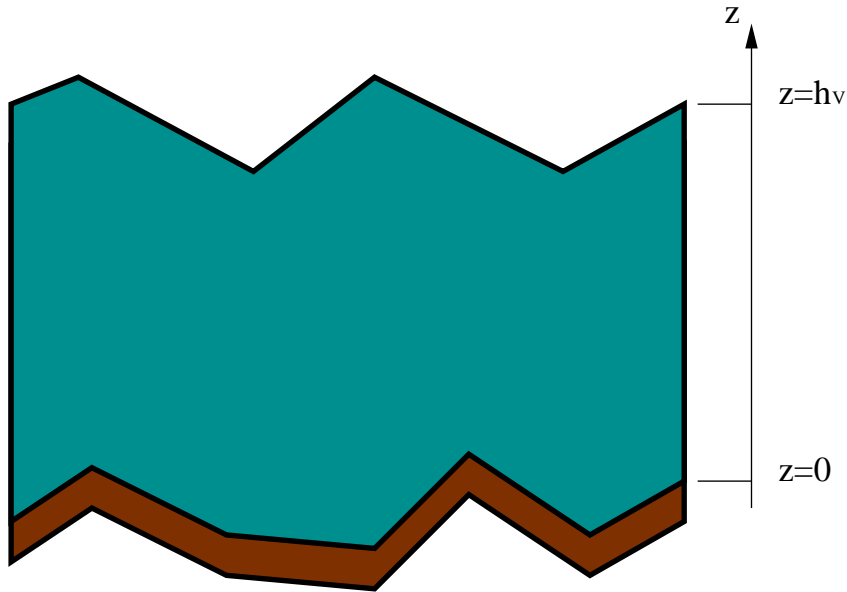


Figure 5.4: Schematic representation of the random volume over ground scattering model proposed in [PC01].

the base of the trees. Unfortunately, when applied to the estimation of forest heights, this direct approach presents limits that depend on the properties of the different scattering components. The main point is that, while scattering from a random volume (that of the branches and leaves layer) is unaffected by changes of polarization, the ground scattering is polarization-dependent but, since no polarization contains only one of these two contributions, it is not possible to completely separate them. As a result, the straightforward evaluation of their difference in height through their interferometric phase difference leads to underestimated values.

A different approach has been adopted specifically for the case of vegetated areas [PRC99a], [PRC99b], [PC01], [Sag00]. It is based on the use of scattering models connecting the interferometric measurements to some basic parameters characterizing the vegetation, such as the height of the canopies and foliage volume and its extinction coefficient. By means of these limited sets of parameters, simplified expressions of interferometric quantities (usually the coherence) can be derived; then, via minimization procedures of the difference between modelled and measured interferometric values, it is possible to invert the experimental measures and obtain an estimate of the chosen vegetation parameters. The main difficulty of this way of proceeding is the formulation of the models, which must be simple enough to allow the inversion but, at the same time, be able to properly describe the complexity of the imaged vegetation layer.

In [PRC99a], [PRC99b] and [PC01], an example of such a model is presented based on an interactions scenario which includes random volume as well as ground scattering [TS00]. It consists of a volume of randomly oriented scatterers above the ground. This is a good approximation for scattering at L-band. With the chosen model, one calculates the interferometric coherence taking into account direct backscattering from the ground and from the random volume; the contribution of multiple bounces is neglected. The parameters related to the vegetation layer are its thickness h_V , the scattering amplitude $m_V(\mathbf{w})$ for a given polarization \mathbf{w} of the randomly oriented scatterers,

and the volume extinction coefficient σ (in dB/m). Related to the ground beneath the vegetation are the topographic phase ϕ_0 and the scattering amplitude $m_G(\mathbf{w})$. Using again a vertical axis z with the origin on the ground surface and the same geometric parameters (average radar look angle θ_0 , range distance R , baseline B) introduced before, the complex interferometric coherence is written as [PC01]:

$$\gamma'(\mathbf{w}) = e^{j\phi_0} \frac{\gamma'_V + m(\mathbf{w})}{1 + m(\mathbf{w})}, \quad (5.25)$$

with $m(\mathbf{w})$ representing the effective ground-to-volume amplitude ratio:

$$m(\mathbf{w}) = \frac{m_G(\mathbf{w})}{m_V(\mathbf{w})} \exp\left(-\frac{2\sigma h_V}{\cos \theta_0}\right) \quad (5.26)$$

and γ'_V the complex coherence for the volume alone given by:

$$\gamma'_V = \frac{\int_0^{h_V} \exp\left(\frac{2\sigma z}{\cos \theta_0}\right) \exp(jk_z z) dz}{\int_0^{h_V} \exp\left(\frac{2\sigma z}{\cos \theta_0}\right) dz}. \quad (5.27)$$

k_z is the effective vertical interferometric wavenumber after spectral shift filtering and is equal to:

$$k_z = \frac{kB \cos \theta_0}{R \sin \theta_0}. \quad (5.28)$$

The volume extinction coefficient σ represent a mean extinction value of the vegetation and depends on the scatterers density and on their dielectric constant.

It is interesting to note that, due to (5.25), the position of the effective scattering centre is defined so that it lies above the ground at a height defined by the ground-to-volume amplitude ratio and by the attenuation length of the vegetation.

By adopting the same model of the vegetation and of the underlying ground, Sagués [Sag00] derived an alternative expression for $\gamma'(\mathbf{w})$ after spectral filtering:

$$\gamma'(\mathbf{w}) = \frac{e^{j\phi_0}}{K(\mathbf{w})} \left[\frac{e^{\chi h_V} - 1}{\chi} + m(\mathbf{w}) h_V \right], \quad (5.29)$$

with:

$$K(\mathbf{w}) = \left[\frac{e^{2\sigma \cos \theta_0 h_V} - 1}{2\sigma \cos \theta_0} + m(\mathbf{w}) h_V \right] \quad (5.30)$$

and

$$\chi = 2 \left[\sigma \cos \theta_0 \cos(\Delta\theta/2) - jk_0 \frac{\Delta\theta}{\sin \theta_0} \right], \quad (5.31)$$

where k_0 is the wavenumber corresponding to the central frequency f_0 .

To invert the models, the complex interferometric coherence of at least three different polarizations must be available so that one has a number of observables equal to the number of parameters involved. Hence, one must calculate the interferometric coherence using different polarizations. In this sense, a useful contribution could come from target decomposition theorems, especially if they could provide a way to better

define the ground-to-volume amplitude ratio or to distinguish volume scattering due to random volumes (for which the models were built) from scattering due to coherent targets extended in height.

The following sections contain a description of some TD methods analyzed and compared with the aim of establishing whether some of them could be helpful for such problems and, if this is not the case, for suggesting more appropriate fields of application.

5.3 Interferometric coherence analysis

In this section we address the analysis of the correlation properties of the scattering mechanisms contemplated in a series of decomposition theorems. We will describe at first their general characteristics and then we will go more deeply through the question of the volume decorrelation, its causes and its possible reduction [AC01], [ACK02], [ACP02a] and [AC03].

The study was conducted again with L-band data of the area of Oberpfaffenhofen, Germany, acquired by the E-SAR sensor of DLR during two different measurement campaigns (May '98 and October '99). Both sets are suitable for interferometry, with baselines of 15 m and 12 m respectively. For the coherence images, an averaging window of 6×12 pixel (in range and azimuth, respectively) was adopted.

5.3.1 General correlation properties

Let us start by analyzing the SDH decomposition [Kro93] and indicate its generic i th term as:

$$[\mathbf{S}]_i = \begin{bmatrix} S_{hh_i} & S_{hv_i} \\ S_{vh_i} & S_{vv_i} \end{bmatrix}, \quad (5.32)$$

where i refers each time to sphere, diplane or helix. With this technique, the interferometric coherence may be derived in two different ways: using the hh -elements of the three matrices and also by means of the corresponding scattering vectors. In the first case, for each scattering mechanism, one has to simply calculate [AC01]:

$$\gamma_i = \frac{|\langle S_{hh_i,1} S_{hh_i,2}^* \rangle|}{\sqrt{\langle S_{hh_i,1} S_{hh_i,1}^* \rangle \langle S_{hh_i,2} S_{hh_i,2}^* \rangle}}, \quad (5.33)$$

In Figures 5.5 (a), (b) and (c), the results relative to the data set of May '98 are represented; Figure 5.6 shows in more detail the interferometric coherence of the S_{hh} elements of the diplane-like matrix for the second data set.

When using the scattering vectors, Equation (3.34) can be applied directly and, for both images of the interferometric pair, one projects the original scattering vectors on the unitary vectors representing a given scattering mechanism. For example, for the first image of the pair and the i th term of its decomposition:

$$\mu_{1_i} = \mathbf{w}_{1_i}^\dagger \mathbf{k}_1, \quad (5.34)$$

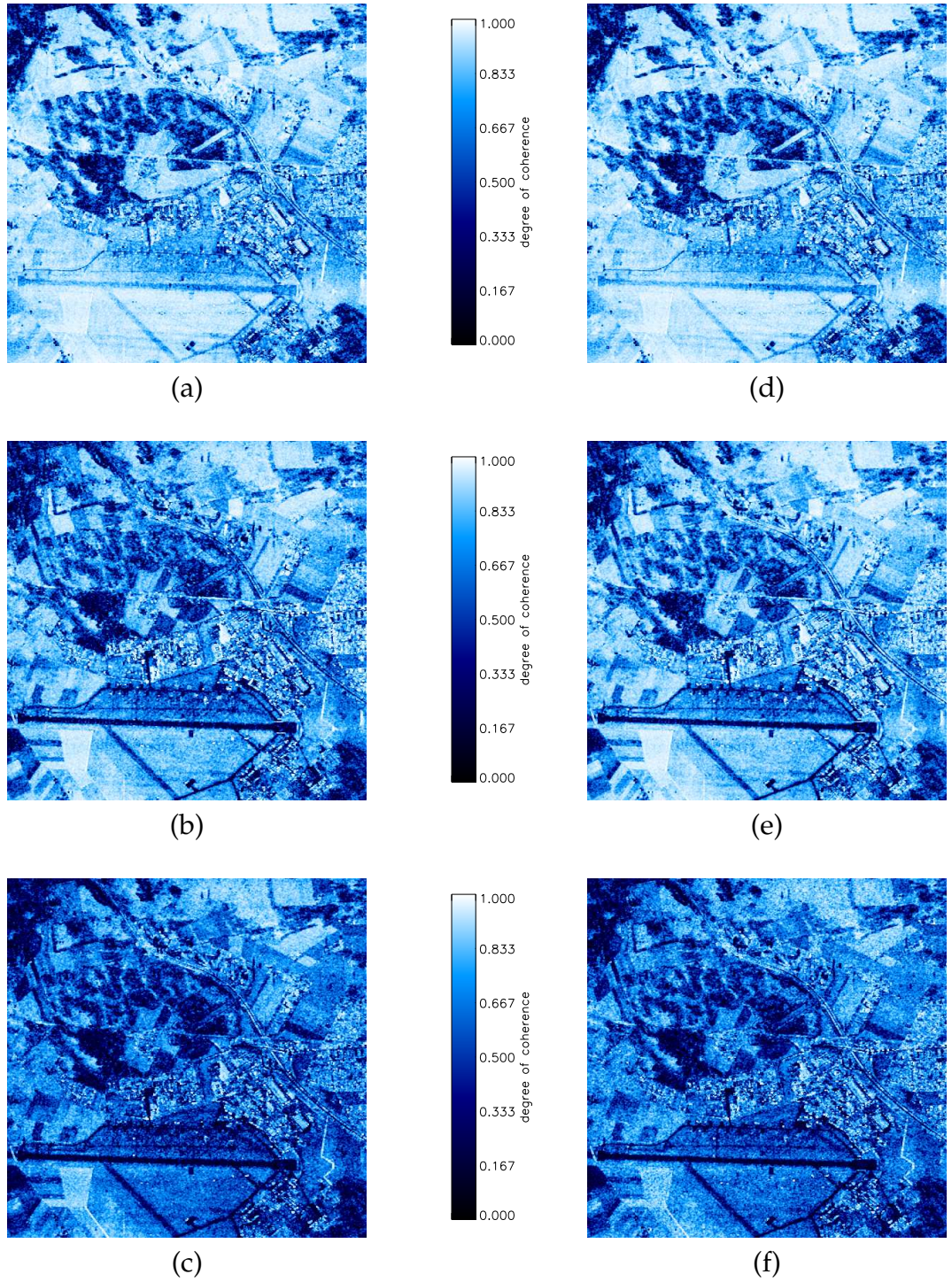


Figure 5.5: Interferometric coherence derived from: (a) the S_{hh} elements of the sphere term; (b) the S_{hh} elements of the diplane term; (c) the S_{hh} elements of the helix term; (d) the unitary polarization vectors representing the sphere term; (e) the unitary polarization vectors representing the diplane term; (f) the unitary polarization vectors representing the helix term (May '98; baseline: 15 m).

where:

$$\mathbf{w}_{1_i} = \frac{\mathbf{k}_{1_i}}{\|\mathbf{k}_{1_i}\|} \quad (5.35)$$

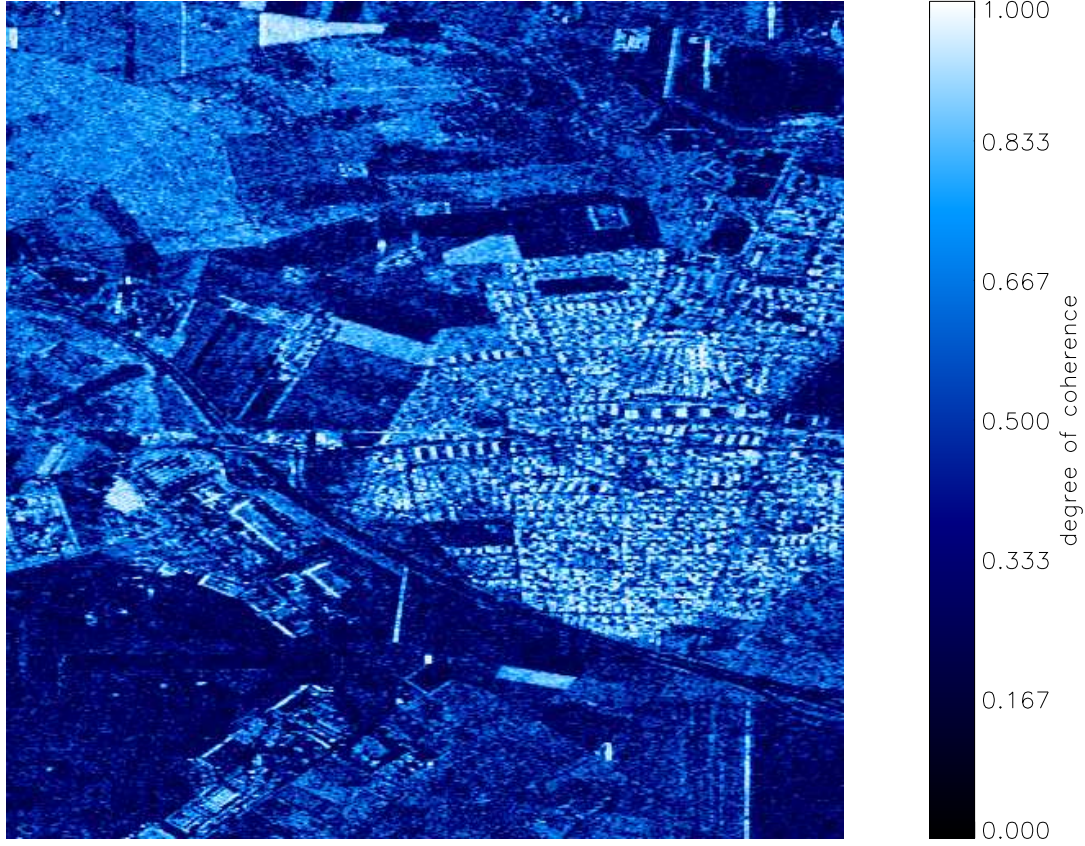


Figure 5.6: Interferometric coherence derived from the S_{hh} elements of the diplane term (October '99; baseline: 12 m).

and k_{1_i} is calculated using the Pauli basis:

$$k_{1_i} = \frac{1}{\sqrt{2}} \begin{bmatrix} S_{hh_{i,1}} + S_{vv_{i,1}} \\ S_{hh_{i,1}} - S_{vv_{i,1}} \\ 2S_{hv_{i,1}} \end{bmatrix}. \quad (5.36)$$

As stated before, the final results do not depend on the chosen basis. Of course, the constraint (3.39) on the phase of the w vectors of the two images corresponding to the same scattering mechanism must be taken into account.

As a first comment, it should be noted in the images and graphs reported here that there are some differences between the two series of coherence images, one based on the hh -elements and the other on the coefficients of the unitary component matrices. The latter should be preferred, since they seem to be less sensitive to noise effects than the hh -elements alone.

Considering the data as a whole, one sees that the three scattering mechanisms present different correlation properties and that, in general, a higher correlation characterizes the sphere-like component with respect to the other terms of the decomposition and also to the corresponding non-decomposed data. This can be easily seen in the graphs of Figure 5.9 that report the histograms of the coherence in the various cases.

The higher correlation of the sphere-like terms is particularly evident in the flat area by the runway, but it is present also in the forested areas. Here, assuming the behaviour of the canopies to resemble that of a random volume, the variation of the

coherence among the three images may indicate the presence of at least two contributions due to ground scattering [PRC99a], [PRC99b], [PC01]. The degree of coherence of the diplane-like terms improves in the village and in a small and isolated forest stand directly to the right of the airfield (see Figure 5.6). In both cases it is again the reduced effect of the volume decorrelation which explains this result. Indeed, in urban areas, structures such as flat surfaces and walls are often present and they behave almost like ideal double bounce scatterers characterized by coherence values almost equal to 1. Generally, in the presence of man-made artifacts, the contribution of scattering from isolated points at different heights decreases in comparison with that of mechanisms that better resemble point scatterers. Quite interesting is also the scenario for the isolated group of trees: they cause a double bounce between the bare field around them and their trunks, hence another strong contribution of ground scattering with a well-defined mechanism.

The second TD method considered is that based on the Pauli matrices [ACK02]. In Equation (2.120), the three terms of the decomposition will be indicated as a , b and c or, respectively, as first, second and third term. Also in this case the three scattering mechanisms show different correlation properties, with a (corresponding to the sphere-like term of the SDH decomposition) having the highest degree of coherence (see Figures 5.7 (a), (b) and (c)). This depends again on the stronger backscattered signals from the ground. In the forested areas of the scene, assuming again that the canopies resemble a random volume, it is possible to observe variations of the coherence among the three images, suggesting different contributions of the scattering from the ground beneath the canopies [PRC99a], [PRC99b], [PC01].

The behaviour of the overall coherence histograms shows only one relevant difference between the two TD methods: the third terms of the Pauli decomposition have a higher correlation degree than the helix-like terms of the Krogager one. Both elements of the two decompositions are representative of depolarization processes occurring with the scattering but, as they do not give similar responses, they seem to be able to distinguish different depolarization mechanisms.

We studied, as last example of coherent TD methods, the Cameron decomposition [CL92], [CYL96]. In fact, as SAR data are calibrated in order to fulfill reciprocity constraints, the basic distinction among scatterers is based on their symmetry with respect to the axes lying on a plane orthogonal to the radar line-of-sight. This means that we had only to perform the decomposition (2.123) of the $[S]$ matrix into its most dominant and least dominant symmetric terms (max sym and min sym). Another point to remember is that, according to the theory, these two terms are orthogonal.

The interferometric coherences of the two components present aspects which are quite original with respect to those previously seen. Let us analyze Figures 5.7 (d) and (e) and Figure 5.9 (d); no other technique leads to such a separation of the coherence values among the various terms: the correlation of the max sym term is higher than any of the decompositions terms already considered, while it is also notable the low backscattered intensity that leads the min sym component to have a very low coherence. Moreover, this enhanced separation characterizes the data as a whole, regardless of the particular homogeneous subsets of land coverages.

For a better understanding of the results presented to now, we compared them with a series of images obtained from the optimal polarizations which maximize the inter-

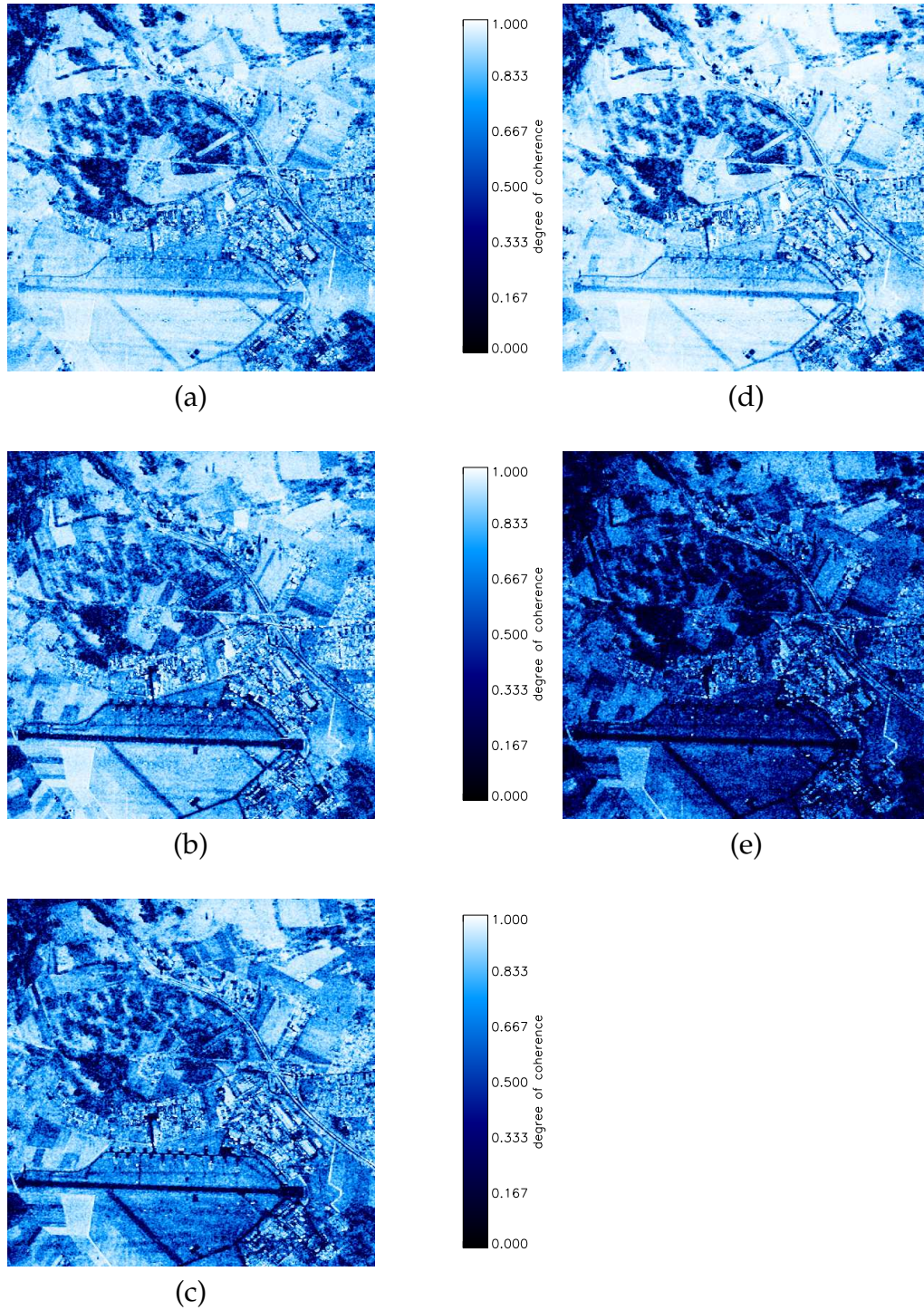


Figure 5.7: Interferometric coherence derived from: (a) the 1st Pauli term; (b) the 2nd Pauli term; (c) the 3rd term; (d) the scattering vectors of Cameron most dominant symmetric term; (e) the scattering vectors of Cameron least dominant symmetric term (May '98; baseline: 15 m).

ferometric coherence [CP98], [Pap99]. These polarizations are no longer related to a coherent decomposition as the coherence optimization does not operate on the $[S]$ matrix. For obtaining these images we used an averaging window of 6×12 pixels; hence,

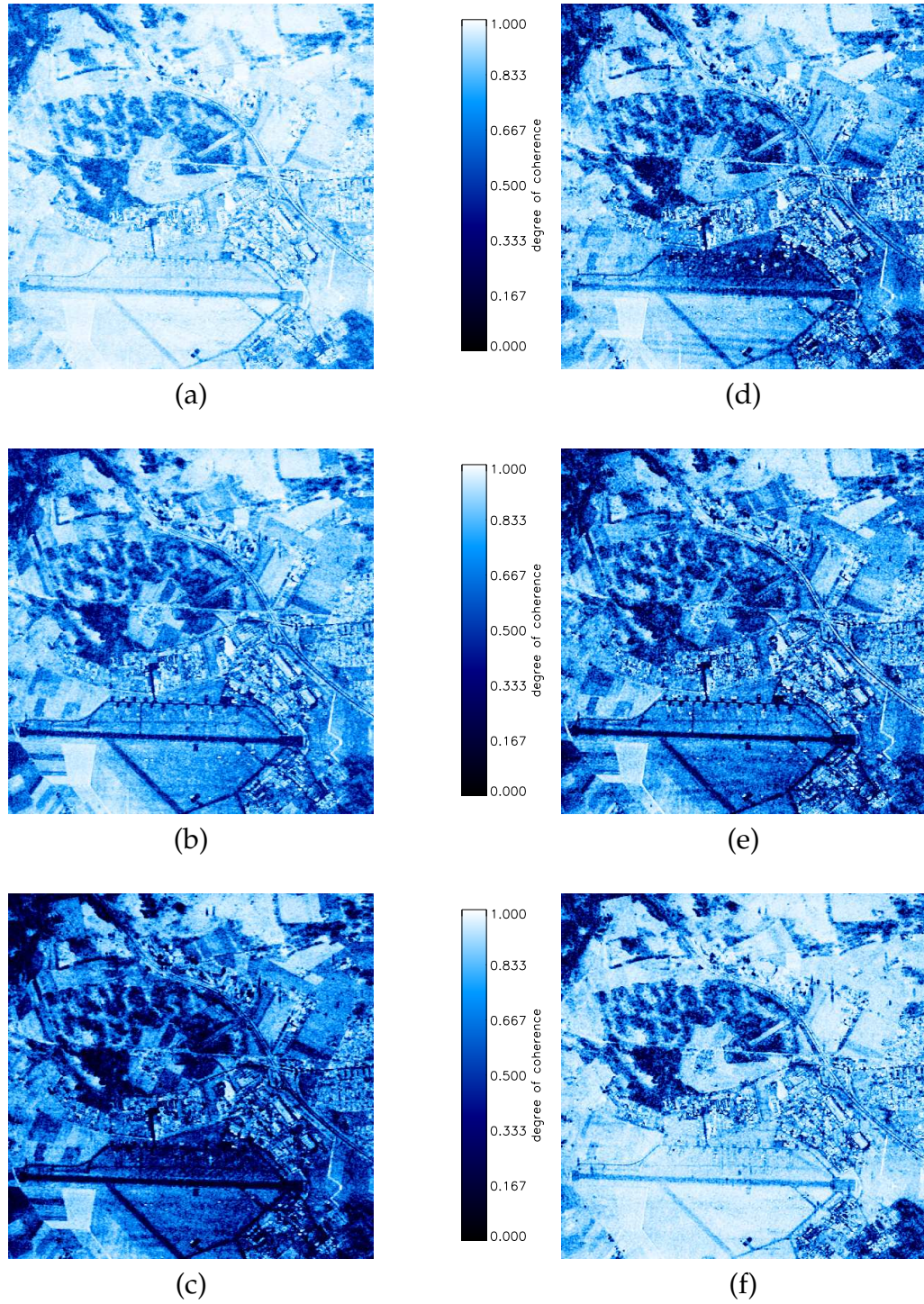


Figure 5.8: Interferometric coherence derived from: (a) the 1st optimal value; (b) the 2nd optimal value; (c) the 3rd optimal value; (d) the original S_{hh} elements; (e) the original S_{hv} elements; (f) the original S_{vv} elements (May '98; baseline: 15 m).

the results are comparable with the previous coherent ones.

When considering the actual improvement of the coherence, one sees in Figure 5.8 that only the first optimal polarizations are highly correlated. The other two polarization pairs present a degree of coherence comparable to that of the terms of the previous

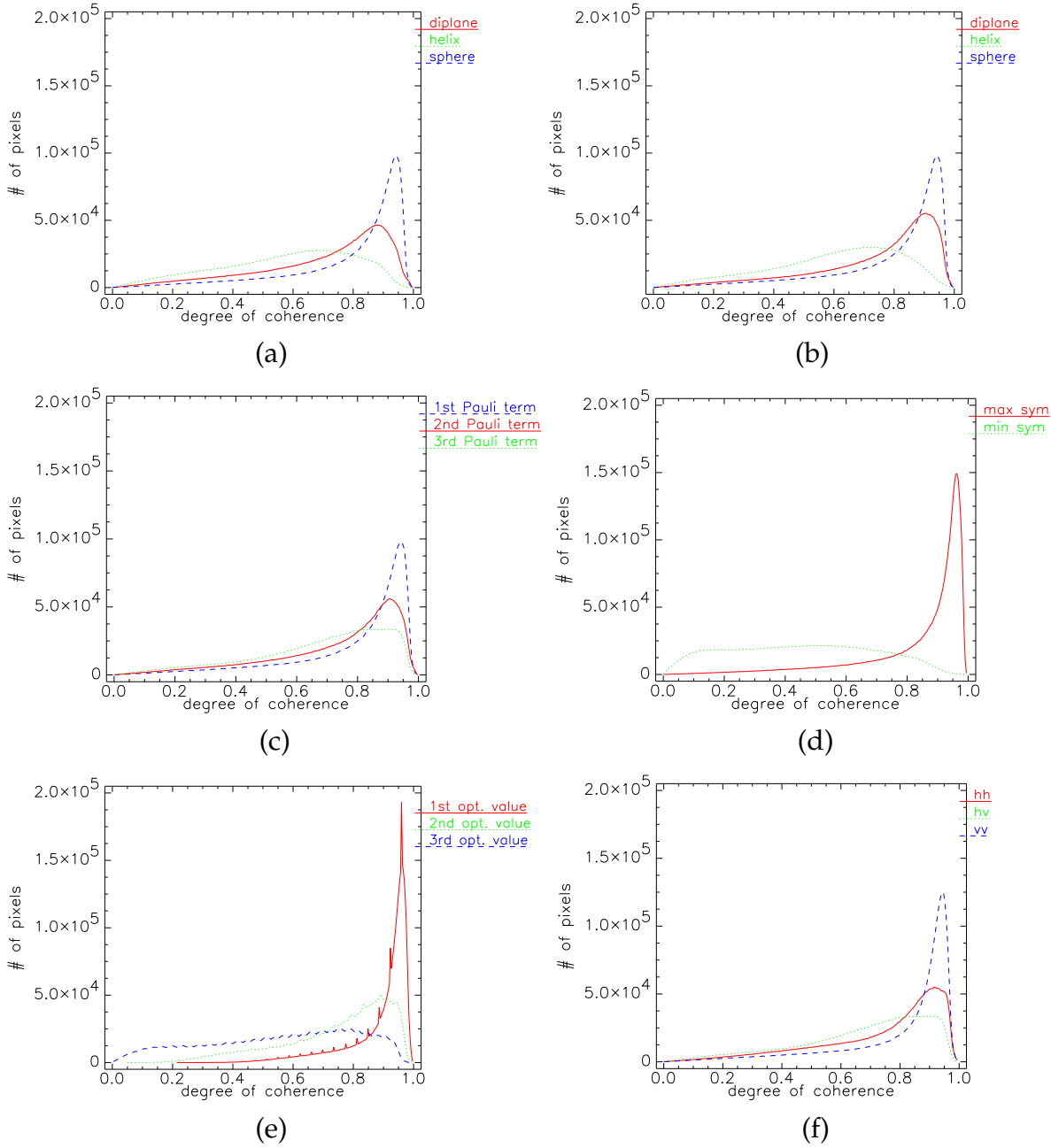


Figure 5.9: Histograms of the interferometric coherence of the whole area derived from: (a) the S_{hh} of the SDH decomposition terms; (b) the scattering vectors of the SDH decomposition terms; (c) the Pauli decomposition coefficients; (d) the scattering vectors of the Cameron decomposition terms; (e) the optimal polarizations; (f) the original polarimetric data (May '98; baseline: 15 m).

TD techniques.

The optimized coherence images provide a valuable comparison with the others, in particular when trying to estimate how well a coherent decomposition theorem is able to identify and separate targets with given deterministic properties, i. e., to distinguish those targets with a relatively high degree of coherence but whose simultaneous presence in the very same resolution cell leads to a reduction of its total value. More-

over, they should also be able to describe distributed targets by finding their “best representation” as ideal point scatterers. This property of the optimization method distinguishes it from the coherent ones whose application to distributed targets is still controversial. Due to these facts, one should expect similar behaviours of the coherent and incoherent methods in presence of deterministic scatterers whereas they should behave differently when dealing with partial ones. Practically this can be seen at the pixel level by comparing the optimal coherences to those relative to the various mechanisms of another method and seeing also when they correspond to each other.

Remarking again that targets with symmetry characteristics are also the most coherent, at least according to the results obtained with the Cameron decomposition, it seems conceivable to suppose that the first optimal polarization always identifies those targets having this kind of property.

Some coherence images relative to the original acquired data have also been included for comparison; they are reported in Figures 5.8 (d), (e) and (f). The main information that can be retrieved from them regards the predominance of Bragg or Fresnel scattering from the ground [CM91], [BW85], [UMF82]. The imbalance in backscattered intensity between the hh - and vv -channels yields also variations of the coherence values, so that a correlation of the S_{hh} elements higher than those of S_{vv} means a prevalence of Fresnel type scattering, typical of almost flat surfaces, whereas the opposite case is verified for scattering from rough surfaces described by the Bragg model.

5.3.2 Volume decorrelation

As is well known, buildings, houses and other constructions cause volume decorrelation just as trees do, but while for random volumes some models for the interferometric coherence are given [TMMvZ96], [TS00], [PC01], to our knowledge, none has been presented for “coherent” extended targets. In fact, due to their deep intrinsic differences, urban areas and forests lead to decorrelation effects having original characteristics each and, hence, require different coherence models. However, even when precise models are not available, it is interesting to see whether these differences can at least be enhanced and recognized by means of TD theorems. Let us consider again the correlation properties of the terms in each decomposition procedure, limiting our analysis to forested and urban areas (we selected areas whose expanse, in terms of number of pixels, is almost identical).

For each mechanism of the various methods, there is evidence of different behaviour of the coherence in forests and towns; more in detail, the decompositions show that there exist different sources of volume decorrelation and that, for reasons we will explain later on, this can be better resolved when it is due to targets resembling ideal point scatterers. Comparing Figures 5.10 and 5.11 it is evident that the urban area has a much higher coherence than the forest. In both cases, no meaningful improvement seems to be given by the Krogager and Pauli decompositions in general and only the max sym Cameron terms and the first optimal polarizations show an enhanced coherence [ACP02a], [AC03].

Regarding the coherence distributions, one may note this: for the forest, the histograms of the hh , hv and vv -channels are basically identical and so are also those of

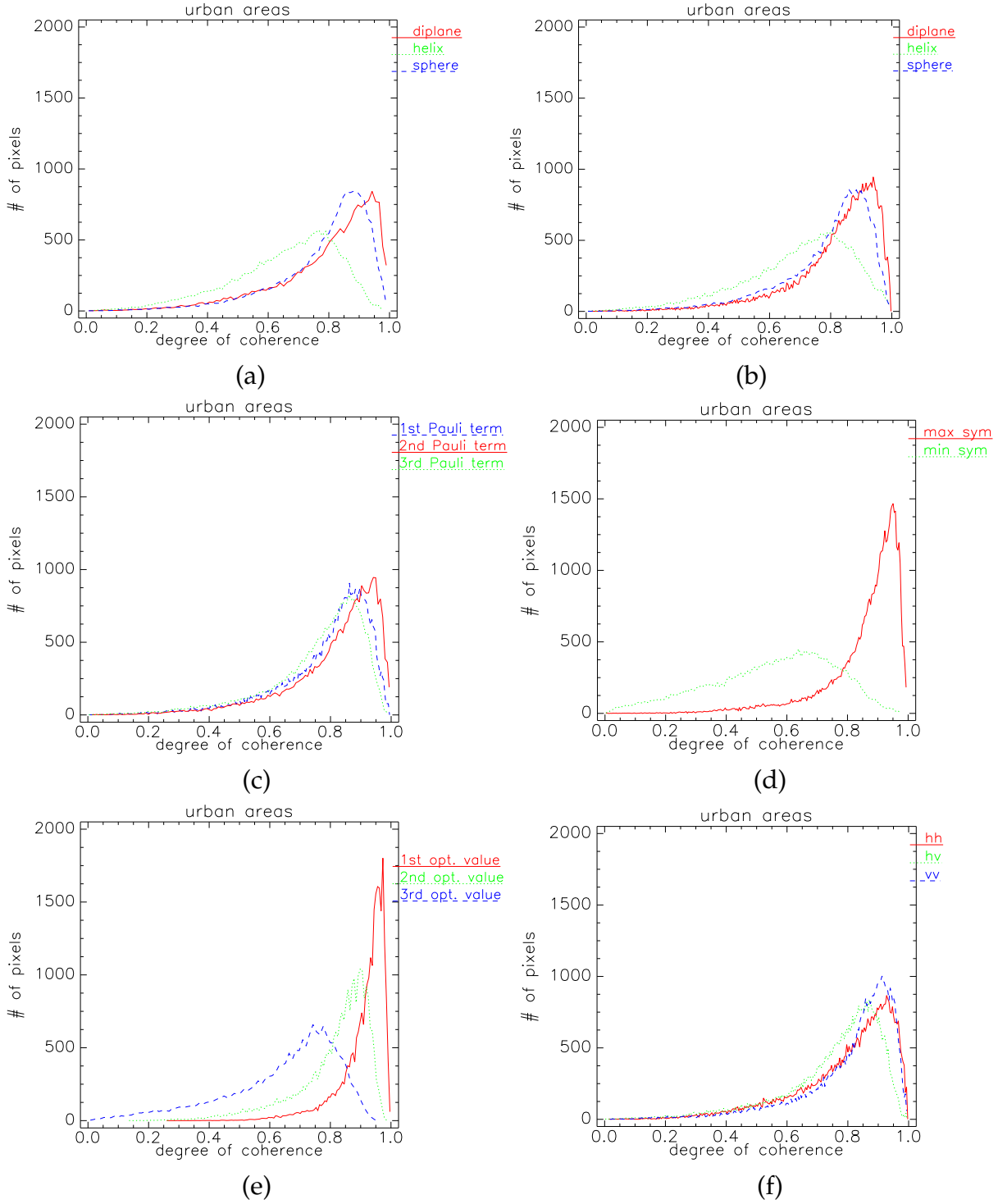


Figure 5.10: Histograms of the interferometric coherence for urban areas derived from: (a) the S_{hh} of the SDH decomposition terms; (b) the scattering vectors of the SDH decomposition terms; (c) the Pauli decomposition coefficients; (d) the scattering vectors of the Cameron decomposition terms; (e) the optimal polarizations; (f) the original polarimetric data (May '98; baseline: 15 m).

the Pauli terms. The corresponding histograms for the town data present shapes where only small differences among the decomposition terms are recognizable. In general,

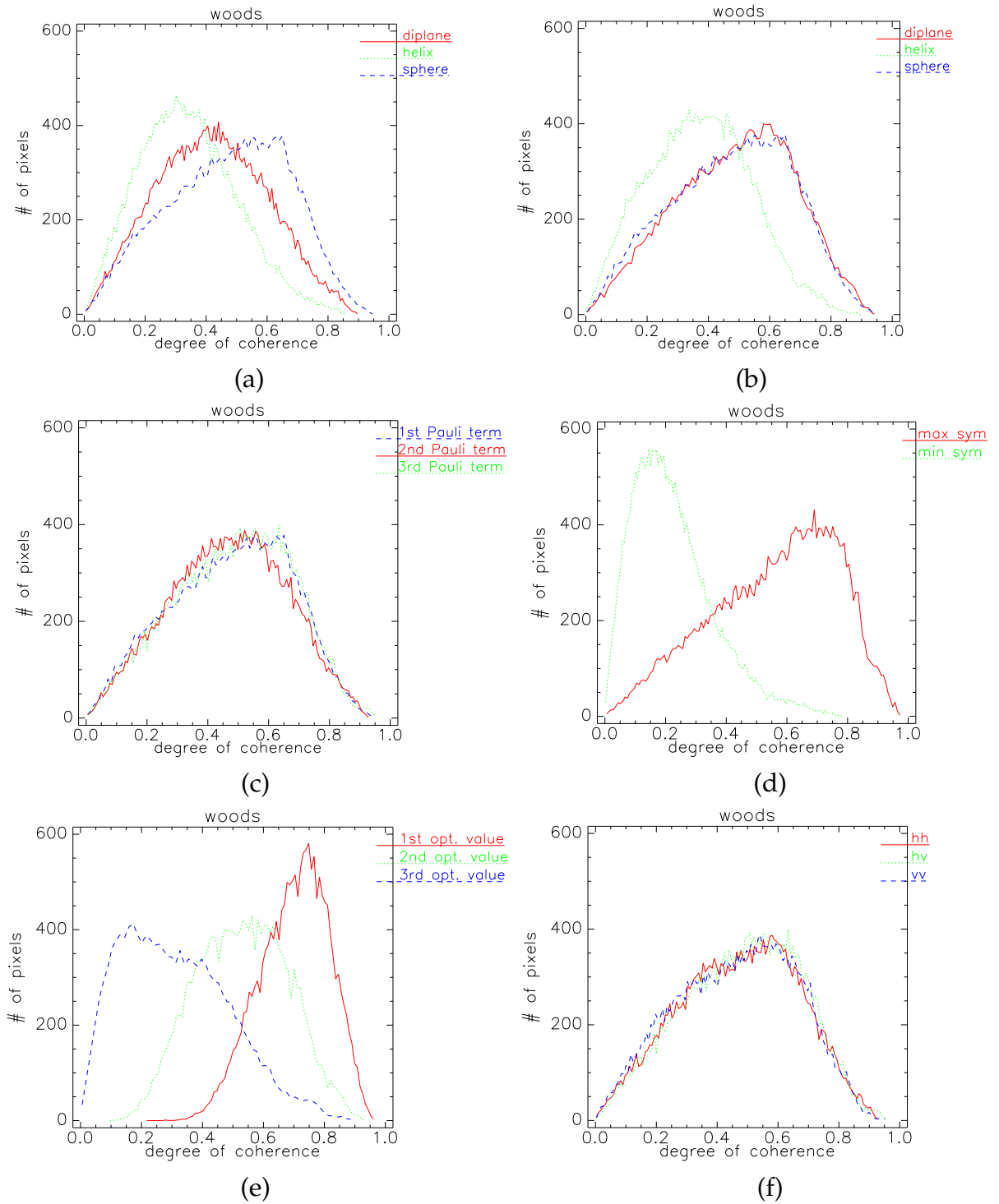


Figure 5.11: Histograms of the interferometric coherence for forested areas derived from: (a) the S_{hh} of the SDH decomposition terms; (b) the scattering vectors of the SDH decomposition terms; (c) the Pauli decomposition coefficients; (d) the scattering vectors of the Cameron decomposition terms; (e) the optimal polarizations; (f) the original polarimetric data (May '98; baseline: 15 m).

this can be explained assuming decorrelation mechanisms that are polarization independent; in this case, indeed, similar values of the coherence, distributed in the same

way, should be expected. On the contrary, if a scattering mechanism depends on the polarization of the incident wave, so does its correlation and the question is then to find which polarization puts into evidence this dependence most clearly. According to the graphs, only the Pauli decomposition partly fails in doing this; all the other methods lead to coherence distributions with an original behaviour for each term. In particular, the curves of the Cameron decomposition terms and of the optimal polarizations are clearly distinguished but their shape does not have not a special meaning.

The point of the shape of the correlation distributions is also worth attention and some comments about it would be better understood by looking at the graphs of the urban areas. In an ideal case, given a single point scatterer for each resolution cell of a scene, the coherence would always be 1 and its distribution simply a δ -distribution centered there. The more the targets differ from point scatterers the wider is the spread of the coherence distribution to values lower than 1.

When more than one target is present in each resolution cell, the question is which is dominant and how do they combine together to return a single backscattered intensity for a pixel. Due to mutual interactions and differences among the responses, the coherence will be lower than 1 even in the presence of point scatterers if these are vertically distributed. Only in the case of orthogonal (i. e., completely independent) scattering mechanisms, is it possible to recover the individual responses separately by selecting the appropriate polarizations and obtain again coherence values equal to 1. As TD theorems perform this separation, one should expect that, for a resolution cell containing the very same targets of the decomposition model, the coherence of each term would be 1 or close to 1 depending on the orthogonality of the mechanisms. Hence, the shape of the coherence histograms of the various terms will also tend to a δ -distribution centered at 1. In principle, this could represent a measure of the correctness of the adopted model: the departure of the coherence histogram from a δ -distribution should reveal how well a certain theoretical model explains the actual targets present in the scene. This is why we anticipated that coherent decompositions seem to better resolve volume decorrelation when it is due to targets resembling ideal point scatterers (as it happens in urban areas) than in the presence of random volume structures (forests). Indeed, in both situations the experimental results indicate the presence of several scattering mechanisms (as in the forested areas where different contributions from the ground are evident), but for the town data the histograms of the coherent decompositions resemble those of the optimal polarizations and tend to $\delta(x - 1)$, whereas this trend is not observed for the forest data.

5.4 Interferometric phase analysis

As demonstrated, the method adopted in [CP98] and [Pap99] to resolve volume decorrelation by means of the optimal polarizations shows some limits when dealing with random volumes (that is, the case of scattering from vegetated areas). The underestimation of the tree heights with this technique is due to the fact that the orthogonal scattering mechanisms refer to scattering centres placed not exactly at the basis and on the top of the trees. It is then interesting to investigate other polarizations and see if better results can be obtained. Hence, we evaluated the expectation value of the in-

terferometric phases of our data in all of the considered cases of TD methods. This analysis was conducted on a basic level, directly considering the interferograms and their differences without retrieving from them the corresponding height values.

Let us start by considering again the SDH decomposition. Since it is not derived from a basis of matrices (as, for example, the Pauli ones), the resulting terms are not mutually orthogonal; nevertheless, at least one matrix of the Krogager decomposition is orthogonal to the other two, so that one may assume the corresponding scattering mechanisms to be statistically independent and one can also check if their distinction via the chosen decomposition corresponds to their separation in height. Again, one can proceed either using the S_{hh} elements of the matrices of the decomposition or their unitary polarization vectors.

Firstly, we refer to the sphere and diplane-like matrices because they are the terms giving the strongest backscattered power contribution and because the scattering mechanisms they represent are more easily associated to real targets in the scene. The interferometric phases relative to the S_{hh} elements of the two terms are represented in Figures 5.12 (a) and (b), whereas in (c) their difference is shown. Looking at the images, one sees that the phase difference is not applicable in a straightforward way for evaluating tree heights: the areas covered with woods do not show any clear variation in this quantity. Though some part of the forests do present interferometric phase differences between the two mechanisms, they cannot be identified yet as homogeneous and well-defined areas. Another aspect to be considered is the position of the phase centres corresponding to the two mechanisms. Even when they are correctly identified and separated, the question as to where they are placed with respect to the real trees remains. Single bounce phenomena, such as those expressed via the sphere-like matrix, can occur not only on the ground but sometimes on the trunk of the imaged tree. Uncertainties are also bound to double bounces; for these, in particular, it is not possible to predict where the scattering centres will be even when related to a ground-trunk double bounce, that is, almost the “optimal” scenario. Moreover, the decorrelation due to random volume, being polarization independent, acts in the same way for the two mechanisms and its influence cannot be used as a further “discriminator” for the phase centres [PC01].

Similar results were obtained using the sphere and helix terms, leading to the same conclusions for this other pair of orthogonal mechanisms.

Some more information was obtained from the unitary polarization vectors (see Figure 5.13); in particular, we report here the example of the sphere and the helix terms. The use of these quantities permits us to estimate some phase differences in the area of the forest as well as on the runway of the airfield. One may anticipate the hypothesis of a separation of the scattering centres: the sphere-like mechanism (single bounce) present mainly on the ground and the depolarization effects, described by the helix term, basically related to the canopies and hence placed at a variable height below the top of the trees. A controversial point is then the interpretation of the same phase difference on the runway, since no separation in height of the scattering centres could have originated it in this case. An explanation may be found in the different amount of noise of the two contributions: as put in evidence also by the coherence images previously analyzed, a different “partition” of the noise between the terms of

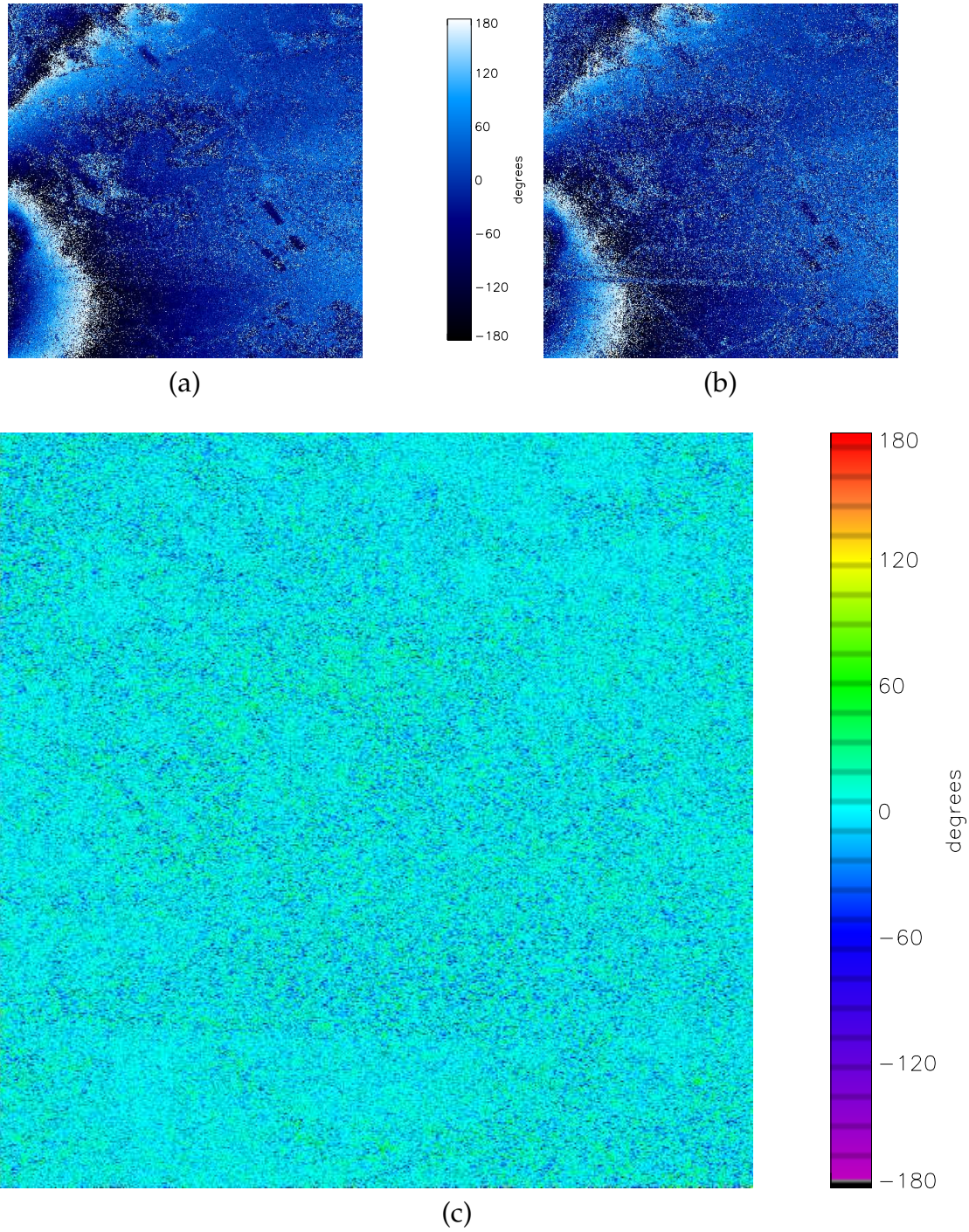


Figure 5.12: Interferometric phases of: (a) the S_{hh} elements of the sphere term; (b) the S_{hh} elements of the diplane term. (c) Difference of the two interferometric phases (May '98, baseline: 15 m).

the decomposition may be supposed, leading also to separated phase centres (or phase displacements between the mechanisms).

Due to the substantial similarity of the Krogager and the Pauli decompositions, the study of the phase differences between the terms of this other TD method does not lead to new significant results (see Figure 5.14). Again, the areas where more con-

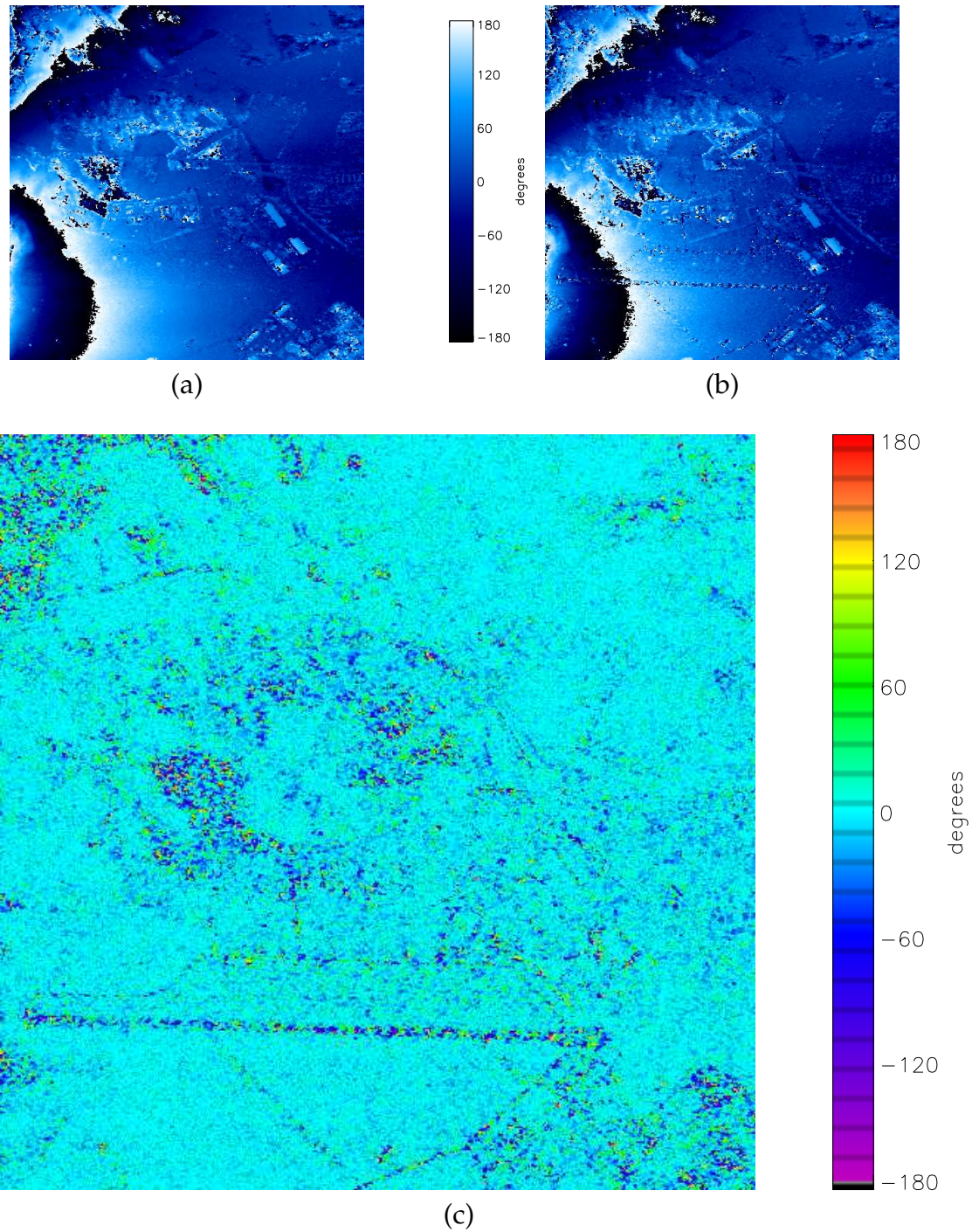


Figure 5.13: Interferometric phases of: (a) the unitary polarization vectors representing the sphere term; (b) the unitary polarization vectors representing the helix term. (c) Difference of the two interferometric phases (May '98, baseline: 15 m).

sistent phase differences may be observed are the runway and the forest. Hence, the considerations made regarding the SDH terms can be repeated.

Also the results relative to the Cameron decomposition terms and to the optimal polarizations give rise to an interferometric phase difference on the airfield runway and in the forest, as can be seen in Figures 5.15 and 5.16. For the runway, the phase

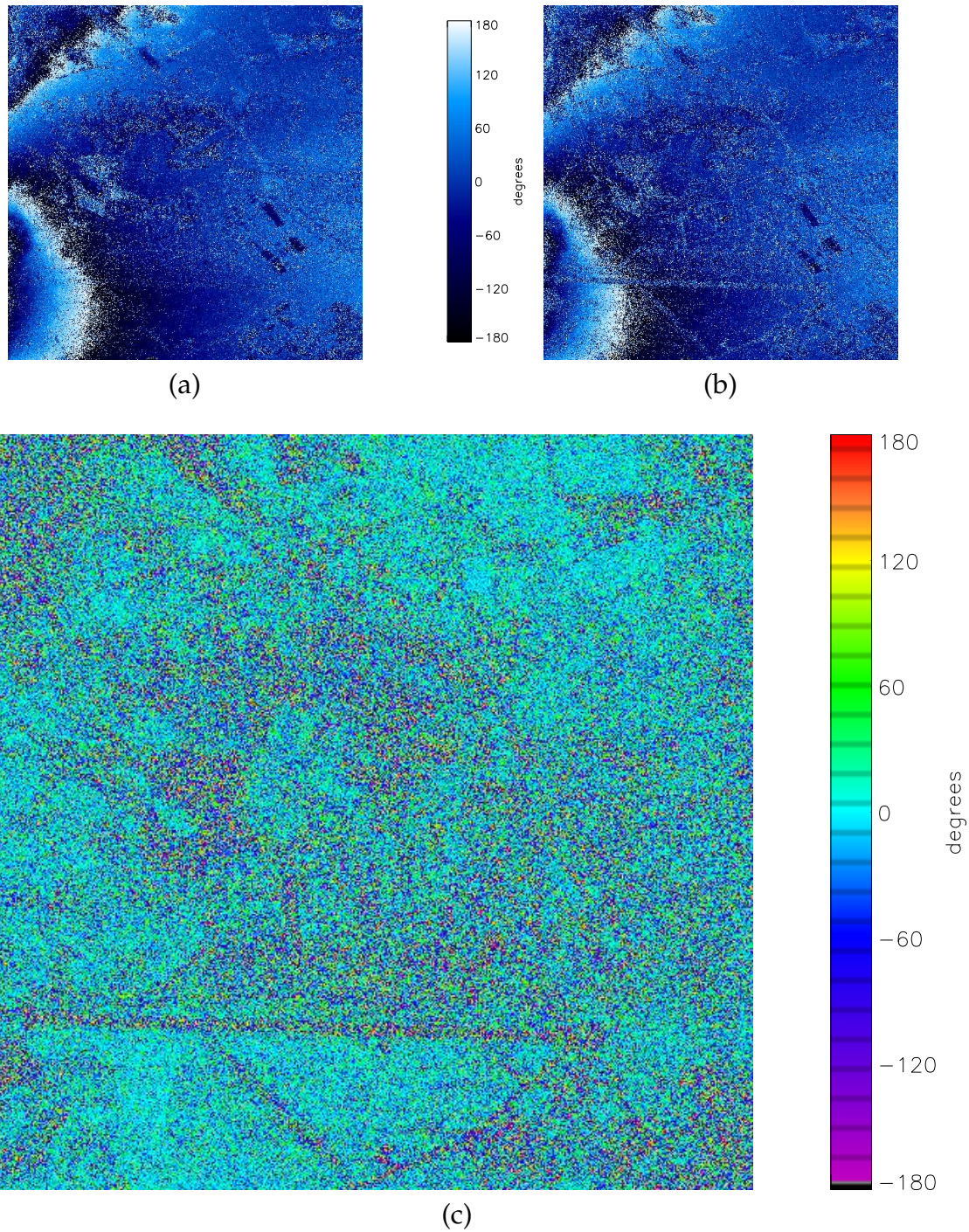


Figure 5.14: Interferometric phases of: (a) the 1st Pauli term; (b) the 2nd Pauli term. (c) Difference of the two interferometric phases (May '98, baseline: 15 m).

difference cannot be interpreted in terms of a difference in the height of the scatterers. Hence, it seems that it represents only a polarimetric (not a geometric) property of the observed scatterers.

The phase difference measured in the forested areas, though representing height variations of the phase centres, is affected by “purely” polarimetric properties as well and, in fact, the runway results may be considered a confirmation of this fact. Due

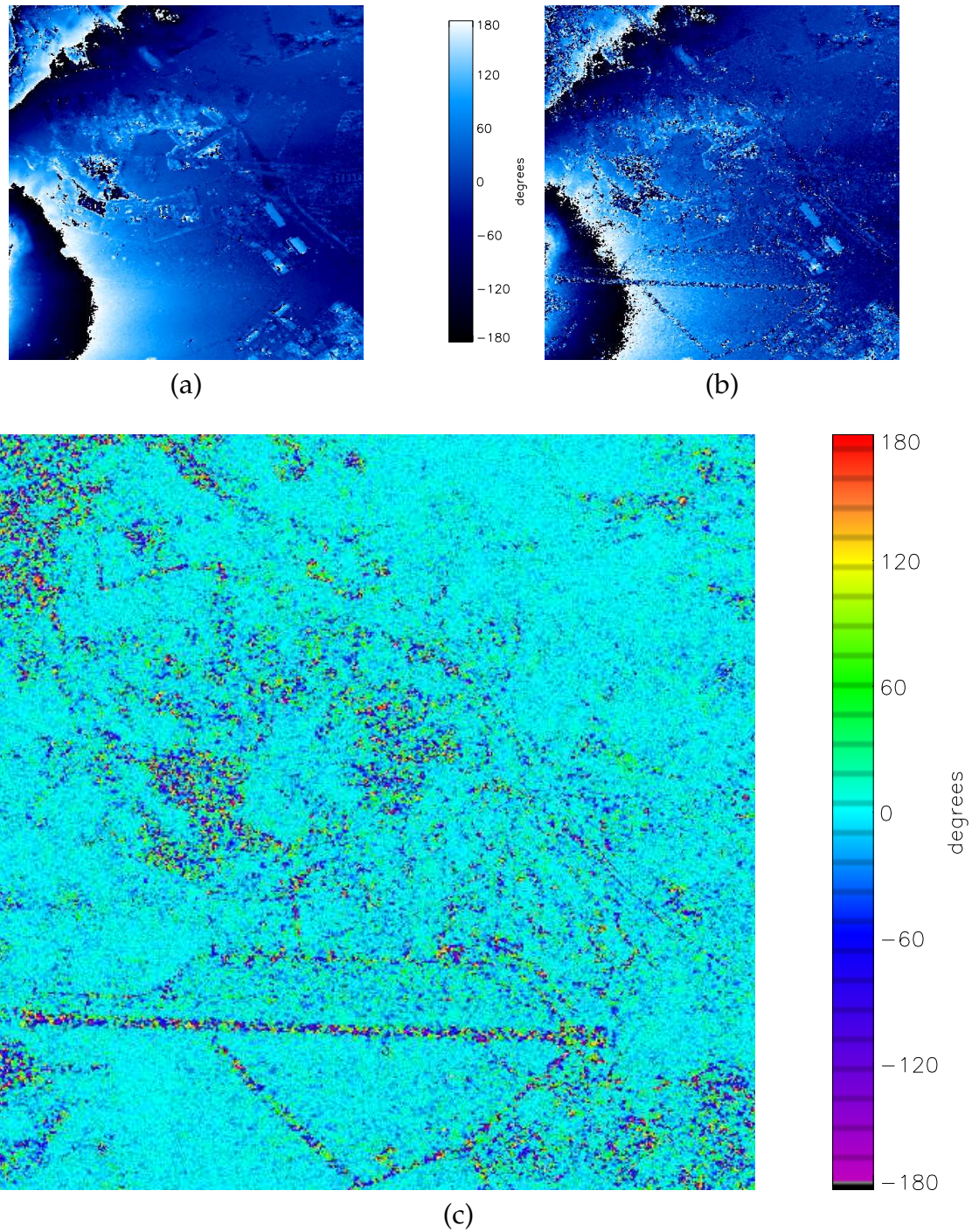


Figure 5.15: Interferometric phases of: (a) the scattering vectors of Cameron most dominant symmetric term; (b) the scattering vectors of Cameron least dominant symmetric term. (c) Difference of the two interferometric phases (May '98, baseline: 15 m).

to these considerations, again, the observed interferometric phase differences cannot be used in a straightforward manner to discriminate the phase centres in vegetated areas and it stresses the limits of the direct application of decomposition (coherent or incoherent) methods for tree height estimation.

In summary, our analysis does not reveal structured phase differences to be phys-

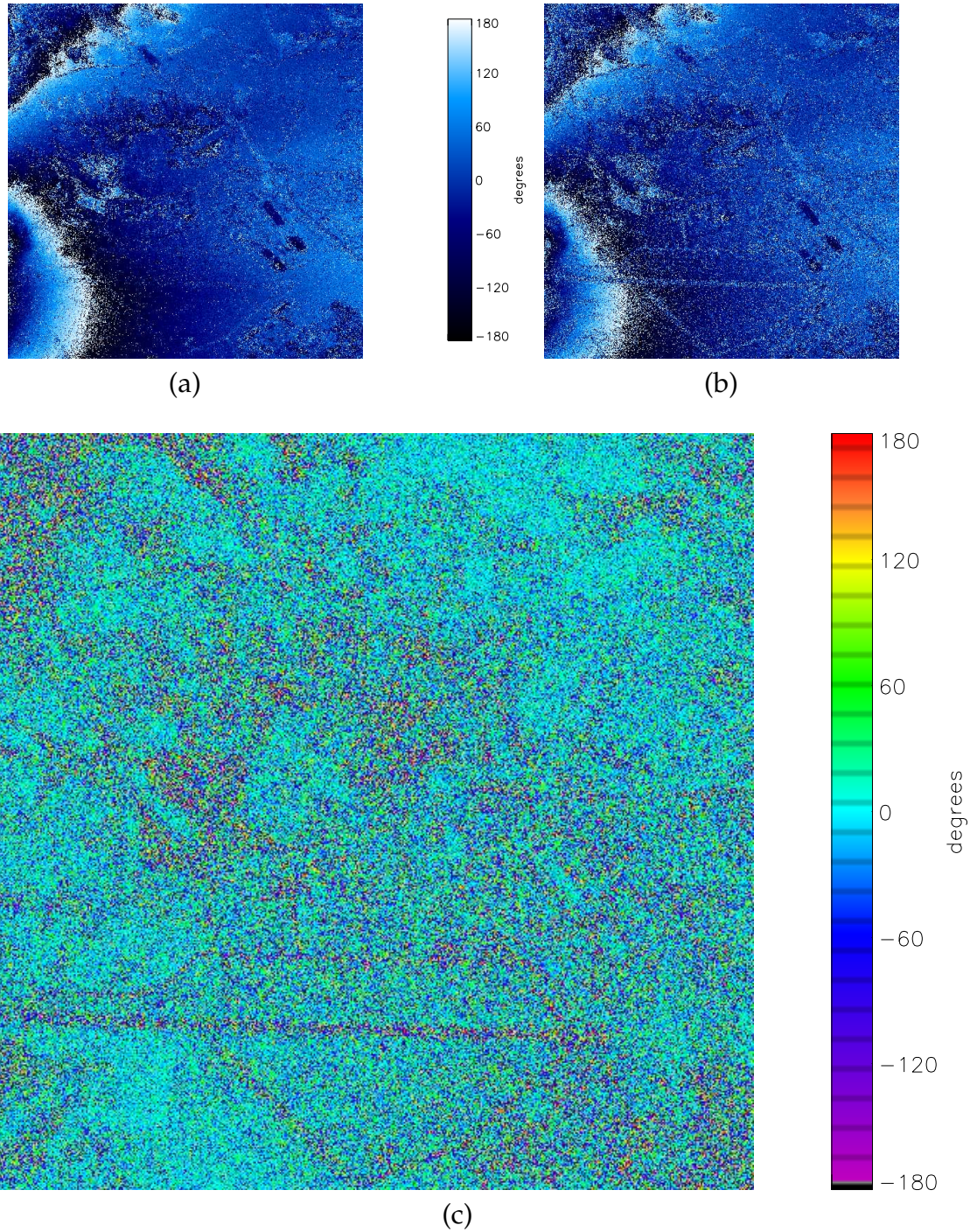


Figure 5.16: Interferometric phases of: (a) the 1st optimal value; (b) the 2nd optimal value. (c) Difference of the two interferometric phases (May '98, baseline: 15 m).

ically meaningful. That is, the role played by geometric considerations seems to be limited. Nevertheless, it puts in evidence other effects, mainly due to the polarimetric properties of the scatterers, which may be the subject of further, specifically dedicated, investigations.

5.5 Final considerations

In this chapter we described the interferometric properties of polarizations derived after applying TD methods, namely the Krogager decomposition, the Pauli one and that of Cameron as coherent methods and the optimal polarizations as example of incoherent methods.

Among the coherent theorems, one should note the use, for the very first time, of the Cameron decomposition terms for interferometry. As demonstrated, the interferometric coherence of its two components presents aspects which are quite original; no other technique leads to such a separation of the coherence values among the various terms: the correlation of the max sym term is higher than any of the other decompositions terms considered, while it is also notable that the low backscattered intensity leads the min sym component to have a very low coherence. Moreover, this enhanced separation characterizes the data as a whole, regardless of the particular homogeneous subsets of land coverages.

Two topics in particular were investigated: the capability of these methods to resolve volume decorrelation and to find the exact position of the scattering centres in order to estimate the height of distributed scatterers; the distinction between volume scattering due to random volumes (that is, vegetated areas) and coherent targets with extension in height (mainly buildings and other man-made artifacts).

We have seen that the scattering mechanisms associated with the various TD methods present different correlation properties and that, in general, these are strongly influenced by the actual amount of backscattered signal attributed to the given mechanism after the decomposition, as well as by its SNR [AC01], [ACK02].

As already known from the literature, at least for the optimal polarizations, the distinction among the scattering mechanisms does not allow a precise separation in height of the scattering centres in the presence of random volumes [PC01]. Hence, an estimation of tree height is not possible via a direct measure of the interferometric phase differences among scattering mechanisms. We verified this for the optimal polarizations and also extended the analysis to the coherent cases obtaining similar results.

For the Krogager and the Pauli decompositions, the study of the phase differences between the terms did not lead to significant results. The areas where more consistent phase differences may be observed are the forest and the runway. Also the results relative to the Cameron decomposition terms, though more evident, give rise to an interferometric phase difference mainly in the forest and on the airfield runway. In the first case, the characteristics of random volume scattering do not allow the separation of the phase centres and the estimation of the volume extension. For the runway, the phase difference cannot be interpreted in terms of a difference in the height of the scatterers. Hence, it seems that it represents only a polarimetric (not a geometric) property of the observed scatterers.

These investigations do not reveal structured phase differences to be physically meaningful. These considerations arise a hitherto important question posed to us by the scientific community before the study was undertaken, namely, how the polarimetric properties of the decomposition terms are related to the interferometric phase differences between them. A subject to be, in our opinion, further investigated.

The results concerning the distinction between random volume scattering and the newly defined coherent volume scattering were more promising [ACP02a], [AC03]. *For each mechanism of the various methods, there was evidence of different behaviour of the coherence in forests and towns; more precisely, the decompositions confirmed that different sources of volume decorrelation exist and we explained why this can be better resolved when it is due to targets resembling ideal point scatterers. Moreover, we showed that coherent and incoherent TD methods provide similar results in the presence of coherent volume scattering and that their behaviour differs increasingly with random volume scattering. This property could be used as a further source of information in classification processes and should also be taken into account when estimating the height of coherent extended targets (like buildings), since the theoretical limits to height estimation of random volumes are no longer valid.*

6 Conclusions

This work started from the observation that a variety of representations of polarimetric data exist and that, in the scientific community, a sort of “competition” is more or less evidently present among them. This situation depends, in part, on the fact that different polarimetric representations have been developed for pursuing specific tasks and have hence been “ad hoc” fitted to the proposed goal. Thus we decided that rather than adopting just one method for a precise scope, that we should consider them all and compare them in the most extensive way. This systematic approach was intended to verify if substantial differences exist among the various polarimetric observables in terms of amount of information they can provide.

The research was then divided into two main parts: a direct analysis of the main parameters derived from polarimetric SAR data, and a study on those quantities that are also suitable to interferometric applications.

In Chapter 4, the first part of this study was reported. We compared a set of polarimetric quantities by means of measures of classification accuracy. A first observation was that *little improvement of the classification tests is obtained using some of the more “refined” polarimetric parameters derived from the original data rather than using directly these ones* [PAC⁺02], [ACP02b]. Only the ratios of the [S] matrix elements provide results significantly worse than the other polarimetric parameters [AC00]. Another important conclusion is related to the comparison among single-pixel and averaged-area classifications; we showed that, *by averaging the values of the image pixels, the classification efficiency is, in general, enhanced*. This could mean that the parameters under study refer to physical properties “spread” over neighbor pixels and correlated. Indeed, the presence of “extended” parameter characteristics may have led to improved classification accuracy for increasing sizes of the averaging windows. This is partly in contradiction to the theoretical expectation that some quantities should be related only to point-like scatterers.

In general, better classification results are normally available with optical images since the chosen classification algorithms were originally developed for this kind of data. Hence, although valuable results could still be obtained with some of the parameters under study, the use of classification techniques specifically suited for polarimetric SAR data, like the unsupervised segmentation proposed in [CP97] for the incoherent parameters, would be more appropriate.

The second part of our research dealt with the interferometric applications of some of the polarimetric parameters considered. Chapter 5 described the theoretical aspects of the subject and the results of our investigations that again consisted mainly of a comparison between coherent and incoherent parameters.

When deriving the interferometric coherence images, we saw that *the polarimetric parameters studied give different results and can provide original insights into the degree of coherence of the various scattering mechanisms present in a resolution cell* [AC01], [ACK02].

A topic of particular interest was the study of the effects of volume decorrelation on the interferometric images. In this context, we introduced the concept of *coherent volume scattering* [ACP02a], [AC03] in contrast with the random volume one, for the case when only varying target heights affects the coherence but the elementary scatterers are stationary and not randomly distributed. This is the case, for example, for walls, buildings and other man-made artifacts. An important point is the identification of the scattering mechanisms present in each resolution cell. This point relates the acquired data directly to the physics of the scattering interactions and immediately provides information about the observed scatterers. Our observations seem to confirm *the capability of coherent decomposition theorems in distinguishing volume decorrelation due to random volumes (that is, tree foliage) from that which is due to height distribution of coherent scatterers (as with man-made artifacts)*.

A part of Chapter 5 was dedicated to the analysis of the phase difference between interferograms of different decomposition terms. The capability of the target decomposition theorems to distinguish phase centres associated with separated targets was then studied referring, in particular, to height estimation of trees and buildings. This topic was only briefly addressed and studied in this work, but we were able to confirm the theoretical expectation that *it is not possible to discriminate the phase centres in vegetated areas since decorrelation due to random volume is polarization independent* [PC01]. Hence, also with coherent TDs, tree height determination is not possible by a straightforward inversion of the difference in interferometric phases. On the contrary, the use of these techniques for coherent volume scattering resolution and height estimation is more promising and, therefore, suggested as a topic for further investigation.

A Relationships among polarization geometrical parameters

Let us show how Equations (2.31) and (2.32) are derived in [BW85], in the most general case of elliptic polarization and starting from an EM wave written as (2.23), i. e.:

$$\vec{E} = (E_h^2 + E_v^2)^{1/2} [\cos \alpha e^{j\delta_h} \hat{h} + \sin \alpha e^{j\delta_v} \hat{v}] \cdot \exp j(\omega t - \vec{k} \cdot \vec{r}). \quad (\text{A.1})$$

Writing for simplicity:

$$a_1 = (E_h^2 + E_v^2)^{1/2} \cos \alpha, \quad (\text{A.2})$$

$$a_2 = (E_h^2 + E_v^2)^{1/2} \sin \alpha \quad (\text{A.3})$$

and

$$\tau = \omega t - \vec{k} \cdot \vec{r}, \quad (\text{A.4})$$

one can derive the real part of the components of \vec{E} as:

$$\begin{cases} E_h = a_1 \cos(\tau + \delta_h) \\ E_v = a_2 \cos(\tau + \delta_v). \end{cases} \quad (\text{A.5})$$

In general, the axes of the ellipse are not in the \hat{h} and \hat{v} directions. Let us reconsider Figure 2.3 and let $(0, \hat{x}, \hat{y})$ be a new reference system with the axes along the axes of the ellipse so that ψ ($0 \leq \psi < \pi$) is the angle between \hat{h} and the direction \hat{x} of the major axis. Then the components E_x and E_y are related to E_h and E_v by:

$$\begin{cases} E_x = E_h \cos \psi + E_v \sin \psi \\ E_y = -E_h \sin \psi + E_v \cos \psi. \end{cases} \quad (\text{A.6})$$

If $2a$ and $2b$ ($a \geq b$) are the lengths of the axes of the ellipse, the equation of the ellipse in the new reference system is:

$$\begin{cases} E_x = a \cos(\tau + \delta_0) \\ E_y = \pm b \sin(\tau + \delta_0), \end{cases} \quad (\text{A.7})$$

indicating that the relative phase δ of the two orthogonal components is now expressed by:

$$\delta = \pi/2 + \delta_0. \quad (\text{A.8})$$

The two signs in (A.7) distinguish the two possible directions in which the end point of the electric vector may describe the ellipse.

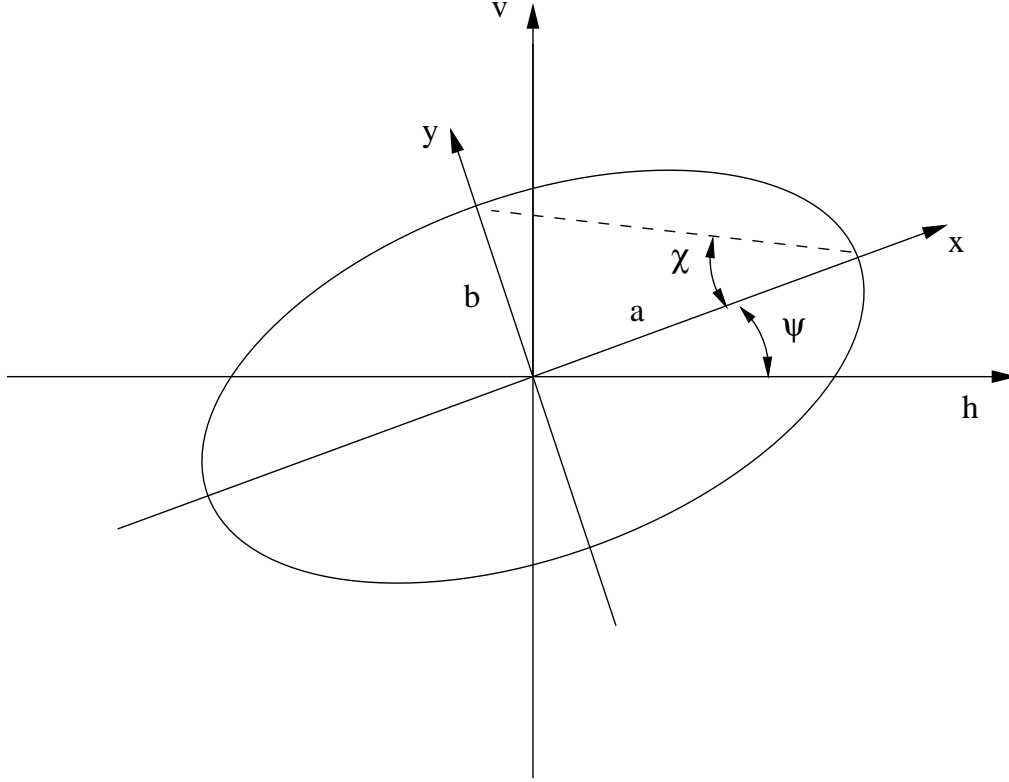


Figure A.1: Polarization ellipse.

To determine a and b we compare (A.6) and (A.7) and use (A.5):

$$\begin{cases} a(\cos \tau \cos \delta_0 - \sin \tau \sin \delta_0) = \\ = a_1 \cos(\tau + \delta_h) \cos \psi + a_2 \cos(\tau + \delta_v) \sin \psi = \\ = a_1(\cos \tau \cos \delta_h - \sin \tau \sin \delta_h) \cos \psi + a_2(\cos \tau \cos \delta_v - \sin \tau \sin \delta_v) \sin \psi \\ \pm b(\sin \tau \cos \delta_0 + \cos \tau \sin \delta_0) = \\ = -a_1 \cos(\tau + \delta_h) \sin \psi + a_2 \cos(\tau + \delta_v) \cos \psi = \\ = -a_1(\cos \tau \cos \delta_h - \sin \tau \sin \delta_h) \sin \psi + a_2(\cos \tau \cos \delta_v - \sin \tau \sin \delta_v) \cos \psi. \end{cases} \quad (\text{A.9})$$

Next we equate the coefficients of $\cos \tau$ and $\sin \tau$:

$$a \cos \delta_0 = a_1 \cos \delta_h \cos \psi + a_2 \cos \delta_v \sin \psi \quad (\text{A.10})$$

$$a \sin \delta_0 = a_1 \sin \delta_h \cos \psi + a_2 \sin \delta_v \sin \psi \quad (\text{A.11})$$

$$\pm b \cos \delta_0 = a_1 \sin \delta_h \sin \psi - a_2 \sin \delta_v \cos \psi \quad (\text{A.12})$$

$$\pm b \sin \delta_0 = -a_1 \cos \delta_h \sin \psi + a_2 \cos \delta_v \cos \psi. \quad (\text{A.13})$$

By squaring and adding the two terms with a and the two terms with b we obtain:

$$a^2 = a_1^2 \cos^2 \psi + a_2^2 \sin^2 \psi + 2a_1 a_2 \cos \psi \sin \psi \cos \delta \quad (\text{A.14})$$

$$b^2 = a_1^2 \sin^2 \psi + a_2^2 \cos^2 \psi - 2a_1 a_2 \cos \psi \sin \psi \cos \delta. \quad (\text{A.15})$$

Hence:

$$a^2 + b^2 = a_1^2 + a_2^2. \quad (\text{A.16})$$

Next we multiply (A.10) by (A.12), (A.11) by (A.13) and add. This gives:

$$\mp ab = a_1 a_2 \sin \delta. \quad (\text{A.17})$$

Further on, dividing (A.12) by (A.10) and (A.13) by (A.11) we obtain:

$$\begin{aligned} \pm \frac{b}{a} &= \frac{a_1 \sin \delta_h \sin \psi - a_2 \sin \delta_v \cos \psi}{a_1 \cos \delta_h \cos \psi + a_2 \cos \delta_v \sin \psi} = \\ &= \frac{-a_1 \cos \delta_h \sin \psi + a_2 \cos \delta_v \cos \psi}{a_1 \sin \delta_h \cos \psi + a_2 \sin \delta_v \sin \psi}, \end{aligned} \quad (\text{A.18})$$

and, leaving aside $\pm b/a$, multiplying both the remaining terms by the product of the two denominators and adding and subtracting the angles, these relations give the following equation for ψ :

$$(a_1^2 - a_2^2) \sin 2\psi = 2a_1 a_2 \cos \delta \cos 2\psi. \quad (\text{A.19})$$

Considering now the angle α ($0 \leq \alpha \leq \pi/2$), such that:

$$\frac{a_2}{a_1} = \tan \alpha, \quad (\text{A.20})$$

Equation (A.19) then becomes:

$$\tan 2\psi = \frac{2a_1 a_2}{a_1^2 - a_2^2} \cos \delta = \frac{2 \tan \alpha}{1 - \tan^2 \alpha} \cos \delta, \quad (\text{A.21})$$

i. e.:

$$\tan 2\psi = \tan 2\alpha \cos \delta. \quad (\text{A.22})$$

Now, from (A.16) and (A.17) we also have:

$$\mp \frac{2ab}{a^2 + b^2} = \frac{2a_1 a_2}{a_1^2 + a_2^2} \sin \delta = \frac{2 \tan \alpha}{1 + \tan^2 \alpha} \sin \delta = \sin 2\alpha \sin \delta. \quad (\text{A.23})$$

Let χ ($-\pi/4 \leq \chi \leq +\pi/4$) be another auxiliary angle, such that:

$$\tan \chi = \mp \frac{b}{a}. \quad (\text{A.24})$$

The numerical value of $\tan \chi$ represents the ratio of the axes of the ellipse and the sign of χ distinguishes the two directions in which the ellipse may be described. Equation (A.23) may then be rewritten in the form:

$$\sin 2\chi = \sin 2\alpha \sin \delta. \quad (\text{A.25})$$

B Target decomposition theorems

B.1 Krogager decomposition

The following details about the Krogager decomposition method are taken from [Kro93] and [KC95].

Due to reciprocity, in monostatic configurations, the matrix $[\mathbf{S}]$ has the form:

$$[\mathbf{S}] = \begin{bmatrix} a+b & c \\ c & a-b \end{bmatrix} \quad (\text{B.1})$$

(see the general expression (2.120)).

According to Krogager, after mathematical manipulations of the complex elements a , b and c , $[\mathbf{S}]$ can be decomposed as shown in (2.121):

$$[\mathbf{S}] = k_s[\mathbf{S}]_{sphere} + e^{j(\phi_b - \phi_a)}(k_d[\mathbf{S}]_{diplane} + k_h[\mathbf{S}]_{helix}), \quad (\text{B.2})$$

assuming phase-normalization with respect to a .

k_s , k_d and k_h are real quantities whose values are given by:

$$k_s = |a|, \quad (\text{B.3})$$

$$k_d = |b|\sqrt{(1 - |\text{Im}\{d\}|)^2 + (\text{Re}\{d\})^2}, \quad (\text{B.4})$$

$$k_h = 2|\text{Im}\{d\}||b|, \quad (\text{B.5})$$

where:

$$d = \frac{c}{b}, \quad (\text{B.6})$$

while the matrices expressing scattering from a sphere, a diplane and a right- or left-wound helix have the form:

$$[\mathbf{S}]_{sphere} = \begin{bmatrix} 1 & 0 \\ 0 & 1 \end{bmatrix}, \quad (\text{B.7})$$

$$[\mathbf{S}]_{diplane} = \begin{bmatrix} \cos 2\theta & \sin 2\theta \\ \sin 2\theta & -\cos 2\theta \end{bmatrix}, \quad (\text{B.8})$$

with:

$$\tan 2\theta = \frac{\text{Re}\{d\}}{1 - |\text{Im}\{d\}|}, \quad (\text{B.9})$$

and

$$[\mathbf{S}]_{helix} = \frac{1}{2} \begin{bmatrix} 1 & \pm j \\ \pm j & -1 \end{bmatrix}. \quad (\text{B.10})$$

The sense of the helix component (the sign of j) is chosen according to $\text{sign}(\phi_d) = \text{sign}(\phi_c - \phi_b)$.

However, this representation does not have the desired roll-invariant property, which means that the parameters calculated in this way are not all independent of the orientation angle around the line of sight.

To avoid this problem, one can adopt a slightly different model, namely [KC95]:

$$\begin{aligned} [\mathbf{S}] &= e^{j\phi} \{ e^{j\phi_s} k_s [\mathbf{S}]_{\text{sphere}} + k_d [\mathbf{S}]_{\text{diplane}(\theta)} + k_h [\mathbf{S}]_{\text{helix}(\theta)} \} = \\ &= e^{j\phi} \left\{ e^{j\phi_s} k_s \begin{bmatrix} 1 & 0 \\ 0 & 1 \end{bmatrix} + k_d \begin{bmatrix} \cos 2\theta & \sin 2\theta \\ \sin 2\theta & -\cos 2\theta \end{bmatrix} + k_h \frac{e^{\mp j2\theta}}{2} \begin{bmatrix} 1 & \pm j \\ \pm j & -1 \end{bmatrix} \right\}, \end{aligned} \quad (\text{B.11})$$

where both the diplane and the helix are considered rotated by an angle θ , and express it (considering only a right-wound helix) in terms of the right-left circular polarization basis:

$$\begin{aligned} [\mathbf{S}_C] &= e^{j\phi} \left\{ e^{j\phi_s} k_s \begin{bmatrix} 0 & j \\ j & 0 \end{bmatrix} + k_d \begin{bmatrix} e^{j2\theta} & 0 \\ 0 & -e^{-j2\theta} \end{bmatrix} + k_h \begin{bmatrix} e^{j2\theta} & 0 \\ 0 & 0 \end{bmatrix} \right\} = \\ &= e^{j\phi} \begin{bmatrix} (k_d + k_h)e^{j2\theta} & jk_s e^{j\phi_s} \\ jk_s e^{j\phi_s} & -k_d e^{-j2\theta} \end{bmatrix}. \end{aligned} \quad (\text{B.12})$$

Let us now consider a general symmetric (i. e., having $S_{RL} = S_{LR}$) scattering matrix in this basis:

$$[\mathbf{S}_C] = \begin{bmatrix} S_{RR} & S_{RL} \\ S_{RL} & S_{LL} \end{bmatrix} = \begin{bmatrix} |S_{RR}|e^{j\phi_{RR}} & |S_{RL}|e^{j\phi_{RL}} \\ |S_{RL}|e^{j\phi_{RL}} & -|S_{LL}|e^{j(\phi_{LL}-\pi)} \end{bmatrix} \quad (\text{B.13})$$

and define:

$$\phi_1 = \phi_{RR} + \phi_{LL} - \pi, \quad (\text{B.14})$$

$$\phi_2 = \phi_{RR} - \phi_{LL} + \pi, \quad (\text{B.15})$$

which inserted in (B.13) yield:

$$[\mathbf{S}_C] = e^{j\frac{1}{2}\phi_1} \begin{bmatrix} |S_{RR}|e^{j\frac{1}{2}\phi_2} & |S_{RL}|e^{j(\phi_{RL}-\frac{1}{2}\phi_1)} \\ |S_{RL}|e^{j(\phi_{RL}-\frac{1}{2}\phi_1)} & -|S_{LL}|e^{-j\frac{1}{2}\phi_2} \end{bmatrix}. \quad (\text{B.16})$$

Now, if $|S_{RR}| > |S_{LL}|$, we may write:

$$[\mathbf{S}_C] = e^{j\frac{1}{2}\phi_1} \begin{bmatrix} [(|S_{RR}| - |S_{LL}|) + |S_{LL}|]e^{j\frac{1}{2}\phi_2} & |S_{RL}|e^{j(\phi_{RL}-\frac{1}{2}\phi_1)} \\ |S_{RL}|e^{j(\phi_{RL}-\frac{1}{2}\phi_1)} & -|S_{LL}|e^{-j\frac{1}{2}\phi_2} \end{bmatrix}, \quad (\text{B.17})$$

that, compared with (B.12), yields:

$$k_s = |S_{RL}|, \quad (\text{B.18})$$

$$k_d^+ = |S_{LL}|, \quad (\text{B.19})$$

$$k_h^+ = |S_{RR}| - |S_{LL}|. \quad (\text{B.20})$$

Similarly, if $|S_{LL}| > |S_{RR}|$, one can compare (B.17) with the analogue of (B.12) written for a left helix and derive:

$$k_d^- = |S_{RR}|, \quad (\text{B.21})$$

$$k_h^- = |S_{LL}| - |S_{RR}|. \quad (\text{B.22})$$

The angles defined in (B.12) can be obtained as well, by comparison, as:

$$\phi = \frac{1}{2}(\phi_{RR} + \phi_{LL} - \pi), \quad (\text{B.23})$$

$$\theta = \frac{1}{4}(\phi_{RR} - \phi_{LL} + \pi), \quad (\text{B.24})$$

$$\phi_s = \phi_{RL} - \frac{1}{2}(\phi_{RR} + \phi_{LL}). \quad (\text{B.25})$$

All the parameters so calculated have the desired orientation independence, so that, in general, one has to simply perform a change of basis to RL-circular in order to derive them.

B.2 Cameron decomposition

The decomposition method proposed by Cameron [CL92], [CYL96] is based on the repeated extraction of the basic properties of the scatterers, like reciprocity and symmetry, by means of projections of the measured scattering vectors onto the relative subspaces or subsets of reciprocal, symmetric, etc., scattering vectors. Indeed, in the general case of bistatic configurations, the reciprocity constraint is not given and the most basic property possessed by a scatterer which can be derived from its $[\mathbf{S}]$ matrix is just its tendency to be approximately reciprocal. Moreover, even in the monostatic case reciprocity is sometimes violated, due to propagation effects or interactions with special materials (for example, materials whose interaction with the EM field is non-linear).

When considering the space of the scattering vectors (expressing them in the lexicographic basis so that $\mathbf{k}_{(4)L}$ represents $[\mathbf{S}]$), those corresponding to reciprocal targets occupy the subspace $V_{rec} \subset \mathbb{C}^4$ generated by the projection matrix $[\mathbf{P}_{rec}]$,

$$[\mathbf{P}_{rec}] = \begin{bmatrix} 1 & 0 & 0 & 0 \\ 0 & 1/2 & 1/2 & 0 \\ 0 & 1/2 & 1/2 & 0 \\ 0 & 0 & 0 & 1 \end{bmatrix}. \quad (\text{B.26})$$

Any scattering matrix can be uniquely decomposed into two components orthogonal in \mathbb{C}^4 , \mathbf{k}_{rec} and $\mathbf{k}_{non-rec}$, with: $\mathbf{k}_{rec} \in V_{rec}$ and $\mathbf{k}_{non-rec} \in V_{non-rec}$ ($V_{non-rec}$ is the subspace of \mathbb{C}^4 which is orthogonal to V_{rec}).

The decomposition is then given by:

$$\mathbf{k}_{(4)L} = \mathbf{k}_{rec} + \mathbf{k}_{non-rec}, \quad (\text{B.27})$$

with:

$$\mathbf{k}_{rec} = [\mathbf{P}_{rec}] \mathbf{k}_{(4)L}, \quad (\text{B.28})$$

$$\mathbf{k}_{non-rec} = ([\mathbf{I}] - [\mathbf{P}_{rec}]) \mathbf{k}_{(4)L}. \quad (\text{B.29})$$

The degree to which a scattering matrix obeys reciprocity can be measured by comparing the magnitude of the two components, \mathbf{k}_{rec} and $\mathbf{k}_{non-rec}$. This measure is given by the parameter θ_{rec} , which is the angle between the scattering vector and the subspace V_{rec} of the vectors corresponding to reciprocal scattering matrices:

$$\theta_{rec} = \arccos \left\| [\mathbf{P}_{rec}] \hat{\mathbf{k}}_{(4)L} \right\|, \quad 0 \leq \theta_{rec} \leq \frac{\pi}{2}, \quad (\text{B.30})$$

where:

$$\hat{\mathbf{k}}_{(4)L} = \frac{\mathbf{k}_{(4)L}}{\|\mathbf{k}_{(4)L}\|}. \quad (\text{B.31})$$

Scattering matrices with $\theta_{rec} = 0$ correspond to scatterers which strictly obey the reciprocity principle whereas scattering matrices with $\theta_{rec} = \pi/2$ lie entirely in the complement of V_{rec} and thus violate the reciprocity principle.

A reciprocal scattering matrix can be further decomposed into components related to most dominant symmetric and least dominant symmetric scatterers (intended here as scatterers having an axis of symmetry in the plane orthogonal to the radar line-of-sight). This division, unfortunately, does not define two orthogonal subspaces of V_{rec} , since both components belong to the subset W_{sym} of the symmetric scattering vectors, which is simply a subset of V_{rec} .

To effect this separation, one uses the three reciprocal matrices (normalized) of the Pauli set:

$$[\mathbf{S}_a] = \frac{1}{\sqrt{2}} \begin{bmatrix} 1 & 0 \\ 0 & 1 \end{bmatrix}, \quad (\text{B.32})$$

$$[\mathbf{S}_b] = \frac{1}{\sqrt{2}} \begin{bmatrix} 1 & 0 \\ 0 & -1 \end{bmatrix}, \quad (\text{B.33})$$

$$[\mathbf{S}_c] = \frac{1}{\sqrt{2}} \begin{bmatrix} 0 & 1 \\ 1 & 0 \end{bmatrix} \quad (\text{B.34})$$

and their corresponding scattering vectors \mathbf{k}_a , \mathbf{k}_b and \mathbf{k}_c . Since for a generic $\mathbf{k}_{rec} \in V_{rec}$ it holds:

$$\mathbf{k}_{rec} = \alpha \mathbf{k}_a + \beta \mathbf{k}_b + \gamma \mathbf{k}_c, \quad (\text{B.35})$$

being $\alpha, \beta, \gamma \in \mathbb{C}$, it is then possible to write:

$$\mathbf{k}_{rec} = [\mathbf{P}_{sym}] \mathbf{k}_{rec} + ([\mathbf{I}] - [\mathbf{P}_{sym}]) \mathbf{k}_{rec} = \mathbf{k}_{sym}^{max} + \mathbf{k}_{sym}^{min}, \quad (\text{B.36})$$

defining $[\mathbf{P}_{sym}]$ as:

$$\mathbf{k}_{sym}^{max} = [\mathbf{P}_{sym}] \mathbf{k}_{rec} = \langle \mathbf{k}_{rec} | \mathbf{k}_a \rangle \mathbf{k}_a + \langle \mathbf{k}_{rec} | \mathbf{k}' \rangle \mathbf{k}', \quad (\text{B.37})$$

with:

$$\mathbf{k}' = \cos \theta \mathbf{k}_b + \sin \theta \mathbf{k}_c. \quad (\text{B.38})$$

In the equation above, θ is chosen such that $|\langle \mathbf{k}_{rec} | \mathbf{k}' \rangle|$ is a maximum. Within these hypotheses, it is guaranteed that \mathbf{k}_{sym}^{max} is the largest symmetric component that can be extracted from \mathbf{k}_{rec} . As anticipated, both the most dominant and the least dominant symmetric components belong to W_{sym} and it can be proven that they are orthogonal.

$[\mathbf{P}_{sym}]$ is defined by introducing \mathbf{k}' given by (B.38), with θ satisfying:

$$\theta = \frac{1}{2}\chi, \quad (\text{B.39})$$

where:

$$\sin \chi = \frac{\beta\gamma^* + \beta^*\gamma}{\sqrt{(\beta\gamma^* + \beta^*\gamma)^2 + (|\beta|^2 - |\gamma|^2)^2}} \quad (\text{B.40})$$

and

$$\cos \chi = \frac{|\beta|^2 - |\gamma|^2}{\sqrt{(\beta\gamma^* + \beta^*\gamma)^2 + (|\beta|^2 - |\gamma|^2)^2}}. \quad (\text{B.41})$$

Again, the degree to which \mathbf{k}_{rec} deviates from belonging to the subset W_{sym} of the symmetric scattering vectors is measured by the angle τ :

$$\tau = \arccos \left| \frac{\langle \mathbf{k}_{rec} | [\mathbf{P}_{sym}] \mathbf{k}_{rec} \rangle}{\|\mathbf{k}_{rec}\| \cdot \|[\mathbf{P}_{sym}] \mathbf{k}_{rec}\|} \right|, \quad 0 \leq \tau \leq \frac{\pi}{4}. \quad (\text{B.42})$$

If $\tau = 0$ then $\mathbf{k}_{rec} \in W_{sym}$. The maximum asymmetry condition, $\tau = \frac{\pi}{4}$ occurs, on the contrary, if and only if \mathbf{k}_{rec} is the scattering vector of a left or right helix.

Equation (B.30) may be generalized in order to compare an arbitrary scattering matrix $[\mathbf{S}]$ with a given test one $[\mathbf{S}_{test}]$. As reported in [CYL96], it is in fact possible to define a metric which compares normalized scattering matrices belonging to W_{sym} . Such a metric is independent of the overall relative phases of the scattering matrices and independent of the orientations (rotations about the line-of-sight axis) of the scatterers represented. In this way, one can iteratively split a scattering matrix into several components by evaluating its properties (reciprocity, symmetry) and comparing it with typical ones (such as helices, diplanes, dipoles, etc.)

C Classification results

The classification tests discussed in Chapter 4 lead to numerical estimates of their accuracy expressed in different forms (confusion matrices, error measures, etc.). For sake of compactness, we report here only the main results of those performed on the data set of October '99 in terms of producer's and user's accuracy and of omission and commission errors.

We choose for the tests on the coherent parameters the measures relative to the single-pixel basis and to the largest window. For those on the incoherent parameters (entropy, α and anisotropy), the measures concerning the 3×3 -pixel averaging window have been given as smallest size case.

C.1 Backscattered wave amplitude

[S] matrix elements (single-pixel basis) - Max. Lik. classification test:

- Overall accuracy = (62243/150262) 41.42%
- Kappa coefficient = 0.316

Table C.1: Pr. Acc. and Us. Acc. estimates relative to the Max. Lik. classification test performed on the the three [S] matrix elements (single-pixel basis).

Class	Pr. Acc. (%)	Us. Acc. (%)	Pr. Acc. (pixels)	Us. Acc. (pixels)
water	21.34	29.75	4774/22374	4774/16048
houses	28.71	84.87	6744/23492	6744/7946
roads	78.70	34.89	15411/19582	15411/44170
trees	76.07	57.72	17164/22562	17164/29737
grass	10.54	22.75	1875/17784	1875/8242
field 1	45.28	43.46	11942/26372	11942/27476
field 2	23.94	26.03	4333/18096	4333/16643

Table C.2: Commission and omission error estimates relative to the Max. Lik. classification test performed the three [S] matrix elements (single-pixel basis).

Class	Comm. (%)	Om. (%)	Comm. (pixels)	Om. (pixels)
water	70.25	78.66	11274/22374	17600/22374
houses	15.13	71.29	1202/23492	16748/23492
roads	65.11	21.30	28759/19582	4171/19582
trees	42.28	23.93	12573/22562	5398/22562
grass	77.25	89.46	6367/17784	15909/17784
field 1	56.54	54.72	15534/26372	14430/26372
field 2	73.97	76.06	12310/18096	13763/18096

[S] matrix elements (single-pixel basis) - Min. Dist. classification test:

- Overall accuracy = (56676/150262) 37.72%
- Kappa coefficient = 0.27

Table C.3: Pr. Acc. and Us. Acc. estimates relative to the Min. Dist. classification test performed on the the three [S] matrix elements (single-pixel basis).

Class	Pr. Acc. (%)	Us. Acc. (%)	Pr. Acc. (pixels)	Us. Acc. (pixels)
water	14.84	28.54	3320/22374	3320/11631
houses	35.26	73.03	8284/23492	8284/11343
roads	67.96	33.84	13307/19582	13307/39323
trees	58.67	53.43	13237/22562	13237/24776
grass	15.45	20.80	2748/17784	2748/13212
field 1	50.07	35.50	13205/26372	13205/37196
field 2	14.23	20.15	2575/18096	2575/12781

Table C.4: Commission and omission error estimates relative to the Min. Dist. classification test performed the three [S] matrix elements (single-pixel basis).

Class	Comm. (%)	Om. (%)	Comm. (pixels)	Om. (pixels)
water	71.46	85.16	8311/22374	19054/22374
houses	26.97	64.74	3059/23492	15208/23492
roads	66.16	32.04	26016/19582	6275/19582
trees	46.57	41.33	11539/22562	9325/22562
grass	79.20	84.55	10464/17784	15036/17784
field 1	64.50	49.93	23991/26372	13167/26372
field 2	79.85	85.77	10206/18096	15521/18096

[S] matrix elements (single-pixel basis) - Parall. classification test:

- Overall accuracy = (41626/150262) 27.7%
- Kappa coefficient = 0.168

Table C.5: Pr. Acc. and Us. Acc. estimates relative to the Parall. classification test performed on the the three [S] matrix elements (single-pixel basis).

Class	Pr. Acc. (%)	Us. Acc. (%)	Pr. Acc. (pixels)	Us. Acc. (pixels)
water	0.00	0.00	0/22374	0/0
houses	19.46	89.42	4571/23492	4571/5112
roads	0.00	0.00	0/19582	0/0
trees	64.84	59.59	14629/22562	14629/24548
grass	0.00	0.00	0/17784	0/0
field 1	17.87	30.12	4712/26372	4712/15644
field 2	97.89	17.04	17714/18096	17714/103952

Table C.6: Commission and omission error estimates relative to the Parall. classification test performed the three [S] matrix elements (single-pixel basis).

Class	Comm. (%)	Om. (%)	Comm. (pixels)	Om. (pixels)
water	0.00	100.00	0/22374	22374/22374
houses	10.58	80.54	541/23492	18921/23492
roads	0.00	100.00	0/19582	19582/19582
trees	40.41	35.16	9919/22562	7933/22562
grass	0.00	100.00	0/17784	17784/17784
field 1	69.88	82.13	10932/26372	21660/26372
field 2	82.96	2.11	86238/18096	382/18096

[S] matrix elements (15×15 -pixel averaging window) - Max. Lik. classification test:

- Overall accuracy = (85689/150262) 57.03%
- Kappa coefficient = 0.5

Table C.7: Pr. Acc. and Us. Acc. estimates relative to the Max. Lik. classification test performed on the the three [S] matrix elements (15×15 -pixel averaging window).

Class	Pr. Acc. (%)	Us. Acc. (%)	Pr. Acc. (pixels)	Us. Acc. (pixels)
water	49.62	52.77	11101/22374	11101/21035
houses	64.02	91.96	15039/23492	15039/16354
roads	80.07	52.82	15680/19582	15680/29687
trees	86.83	67.88	19591/22562	19591/28860
grass	47.75	35.02	8491/17784	8491/24246
field 1	42.55	62.25	11222/26372	11222/18027
field 2	25.23	37.87	4565/18096	4565/12053

Table C.8: Commission and omission error estimates relative to the Max. Lik. classification test performed the three [S] matrix elements (15×15 -pixel averaging window).

Class	Comm. (%)	Om. (%)	Comm. (pixels)	Om. (pixels)
water	47.23	50.38	9934/22374	11273/22374
houses	8.04	35.98	1315/23492	8453/23492
roads	47.18	19.93	14007/19582	3902/19582
trees	32.12	13.17	9269/22562	2971/22562
grass	64.98	52.25	15755/17784	9293/17784
field 1	37.75	57.45	6805/26372	15150/26372
field 2	62.13	74.77	7488/18096	13531/18096

[S] matrix elements (15×15 -pixel averaging window) - Min. Dist. classification test:

- Overall accuracy = $(76552/150262)$ 50.96%
- Kappa coefficient = 0.43

Table C.9: Pr. Acc. and Us. Acc. estimates relative to the Min. Dist. classification test performed on the the three [S] matrix elements (15×15 -pixel averaging window).

Class	Pr. Acc. (%)	Us. Acc. (%)	Pr. Acc. (pixels)	Us. Acc. (pixels)
water	39.73	44.57	8890/22374	8890/19944
houses	59.26	93.32	13921/23492	13921/14918
roads	76.21	45.73	14924/19582	14924/32638
trees	76.42	65.08	17243/22562	17243/26497
grass	23.00	26.72	4090/17784	4090/15308
field 1	50.44	46.59	13301/26372	13301/28550
field 2	23.12	33.71	4183/18096	4183/12407

Table C.10: Commission and omission error estimates relative to the Min. Dist. classification test performed the three [S] matrix elements (15×15 -pixel averaging window).

Class	Comm. (%)	Om. (%)	Comm. (pixels)	Om. (pixels)
water	55.43	60.27	11054/22374	13484/22374
houses	6.68	40.74	997/23492	9571/23492
roads	54.27	23.79	17714/19582	4658/19582
trees	34.92	23.58	9254/22562	5319/22562
grass	73.28	77.00	11218/17784	13694/17784
field 1	53.41	49.56	15249/26372	13071/26372
field 2	66.29	76.88	8224/18096	13913/18096

[S] matrix elements (15×15 -pixel averaging window) - Parall. classification test:

- Overall accuracy = (50912/150262) 33.88%
- Kappa coefficient = 0.24

Table C.11: Pr. Acc. and Us. Acc. estimates relative to the Parall. classification test performed on the the three [S] matrix elements (15×15 -pixel averaging window).

Class	Pr. Acc. (%)	Us. Acc. (%)	Pr. Acc. (pixels)	Us. Acc. (pixels)
water	0.00	0.00	0/22374	0/0
houses	48.55	98.75	11406/23492	11406/11550
roads	0.00	0.00	0/19582	0/0
trees	85.42	64.13	19272/22562	19272/30051
grass	0.00	0.00	0/17784	0/0
field 1	9.75	44.28	2572/26372	2572/5809
field 2	97.60	17.35	17662/18096	17662/101804

Table C.12: Commission and omission error estimates relative to the Parall. classification test performed the three [S] matrix elements (15×15 -pixel averaging window).

Class	Comm. (%)	Om. (%)	Comm. (pixels)	Om. (pixels)
water	0.00	100.00	0/22374	22374/22374
houses	1.25	51.45	144/23492	12086/23492
roads	0.00	100.00	0/19582	19582/19582
trees	35.87	14.58	10779/22562	3290/22562
grass	0.00	100.00	0/17784	17784/17784
field 1	55.72	90.25	3237/26372	23800/26372
field 2	82.65	2.40	84142/18096	434/18096

C.2 Characteristic polarizations

[S] matrix co- and cross-polar nulls (single-pixel basis) - Max. Lik. classification test:

- Overall accuracy = (22374/150262) 14.9%
- Kappa coefficient = 0

Table C.13: Pr. Acc. and Us. Acc. estimates relative to the Max. Lik. classification test performed on the [S] matrix co- and cross-polar nulls (single-pixel basis).

Class	Pr. Acc. (%)	Us. Acc. (%)	Pr. Acc. (pixels)	Us. Acc. (pixels)
water	100.00	14.89	22374/22374	22374/150262
houses	0.00	0.00	0/23492	0/0
roads	0.00	0.00	0/19582	0/0
trees	0.00	0.00	0/22562	0/0
grass	0.00	0.00	0/17784	0/0
field 1	0.00	0.00	0/26372	0/0
field 2	0.00	0.00	0/18096	0/0

Table C.14: Commission and omission error estimates relative to the Max. Lik. classification test performed on the [S] matrix co- and cross-polar nulls (single-pixel basis).

Class	Comm. (%)	Om. (%)	Comm. (pixels)	Om. (pixels)
water	85.11	0.00	127888/22374	0/22374
houses	0.00	100.00	0/23492	23492/23492
roads	0.00	100.00	0/19582	19582/19582
trees	0.00	100.00	0/22562	22562/22562
grass	0.00	100.00	0/17784	17784/17784
field 1	0.00	100.00	0/26372	26372/26372
field 2	0.00	100.00	0/18096	18096/18096

[S] matrix co- and cross-polar nulls (single-pixel basis) - Min. Dist. classification test:

- Overall accuracy = (56996/150262) 37.93%
- Kappa coefficient = 0.273

Table C.15: Pr. Acc. and Us. Acc. estimates relative to the Min. Dist. classification test performed on the [S] matrix co- and cross-polar nulls (single-pixel basis).

Class	Pr. Acc. (%)	Us. Acc. (%)	Pr. Acc. (pixels)	Us. Acc. (pixels)
water	9.21	25.20	2061/22374	2061/8180
houses	34.64	70.12	8137/23492	8137/11604
roads	67.66	33.72	13249/19582	13249/39291
trees	58.50	54.12	13198/22562	13198/24385
grass	17.00	21.30	3023/17784	3023/14194
field 1	53.93	37.48	14223/26372	14223/37946
field 2	17.16	21.18	3105/18096	3105/14662

Table C.16: Commission and omission error estimates relative to the Min. Dist. classification test performed on the [S] matrix co- and cross-polar nulls (single-pixel basis).

Class	Comm. (%)	Om. (%)	Comm. (pixels)	Om. (pixels)
water	74.80	90.79	6119/22374	20313/22374
houses	29.88	65.36	3467/23492	15355/23492
roads	66.28	32.34	26042/19582	6333/19582
trees	45.88	41.50	11187/22562	9364/22562
grass	78.70	83.00	11171/17784	14761/17784
field 1	62.52	46.07	23723/26372	12149/26372
field 2	78.82	82.84	11557/18096	14991/18096

[S] matrix co- and cross-polar nulls (single-pixel basis) - Parall. classification test:

- Overall accuracy = (38098/150262) 25.35%
- Kappa coefficient = 0.14

Table C.17: Pr. Acc. and Us. Acc. estimates relative to the Parall. classification test performed on the [S] matrix co- and cross-polar nulls (single-pixel basis).

Class	Pr. Acc. (%)	Us. Acc. (%)	Pr. Acc. (pixels)	Us. Acc. (pixels)
water	0.00	0.00	0/22374	0/0
houses	19.00	89.58	4464/23492	4464/4983
roads	0.00	0.00	0/19582	0/0
trees	51.79	55.54	11684/22562	11684/21037
grass	0.00	0.00	0/17784	0/0
field 1	16.06	24.30	4236/26372	4236/17430
field 2	97.89	16.71	17714/18096	17714/106039

Table C.18: Commission and omission error estimates relative to the Parall. classification test performed on the [S] matrix co- and cross-polar nulls (single-pixel basis).

Class	Comm. (%)	Om. (%)	Comm. (pixels)	Om. (pixels)
water	0.00	100.00	0/22374	22374/22374
houses	10.42	81.00	519/23492	19028/23492
roads	0.00	100.00	0/19582	19582/19582
trees	44.46	48.21	9353/22562	10878/22562
grass	0.00	100.00	0/17784	17784/17784
field 1	75.70	83.94	13194/26372	22136/26372
field 2	83.29	2.11	88325/18096	382/18096

[S] matrix co- and cross-polar nulls (15×15 -pixel averaging window) - Max. Lik. classification test:

- Overall accuracy = (99530/150262) 66.24%
- Kappa coefficient = 0.6

Table C.19: Pr. Acc. and Us. Acc. estimates relative to the Max. Lik. classification test performed on the [S] matrix co- and cross-polar nulls (15×15 -pixel averaging window).

Class	Pr. Acc. (%)	Us. Acc. (%)	Pr. Acc. (pixels)	Us. Acc. (pixels)
water	46.67	37.18	10443/22374	10443/28087
houses	75.02	96.59	17624/23492	17624/18246
roads	88.33	68.83	17296/19582	17296/25130
trees	97.88	78.97	22083/22562	22083/27964
grass	36.38	39.47	6470/17784	6470/16393
field 1	83.50	86.65	22020/26372	22020/25413
field 2	19.86	39.81	3594/18096	3594/9029

Table C.20: Commission and omission error estimates relative to the Max. Lik. classification test performed on the [S] matrix co- and cross-polar nulls (15×15 -pixel averaging window).

Class	Comm. (%)	Om. (%)	Comm. (pixels)	Om. (pixels)
water	62.82	53.33	17644/22374	11931/22374
houses	3.41	24.98	622/23492	5868/23492
roads	31.17	11.67	7834/19582	2286/19582
trees	21.03	2.12	5881/22562	479/22562
grass	60.53	63.62	9923/17784	11314/17784
field 1	13.35	16.50	3393/26372	4352/26372
field 2	60.19	80.14	5435/18096	14502/18096

[S] matrix co- and cross-polar nulls (15×15 -pixel averaging window) - Min. Dist. classification test:

- Overall accuracy = (96782/150262) 64.41%
- Kappa coefficient = 0.58

Table C.21: Pr. Acc. and Us. Acc. estimates relative to the Min. Dist. classification test performed on the [S] matrix co- and cross-polar nulls (15×15 -pixel averaging window).

Class	Pr. Acc. (%)	Us. Acc. (%)	Pr. Acc. (pixels)	Us. Acc. (pixels)
water	42.06	38.95	9411/22374	9411/24162
houses	63.24	99.93	14856/23492	14856/14866
roads	88.48	71.39	17326/19582	17326/24271
trees	99.18	72.12	22378/22562	22378/31030
grass	18.32	31.86	3258/17784	3258/10226
field 1	84.80	86.03	22364/26372	22364/25997
field 2	39.73	36.47	7189/18096	7189/19710

Table C.22: Commission and omission error estimates relative to the Min. Dist. classification test performed on the [S] matrix co- and cross-polar nulls (15×15 -pixel averaging window).

Class	Comm. (%)	Om. (%)	Comm. (pixels)	Om. (pixels)
water	61.05	57.94	14751/22374	12963/22374
houses	0.07	36.76	10/23492	8636/23492
roads	28.61	11.52	6945/19582	2256/19582
trees	27.88	0.82	8652/22562	184/22562
grass	68.14	81.68	6968/17784	14526/17784
field 1	13.97	15.20	3633/26372	4008/26372
field 2	63.53	60.27	12521/18096	10907/18096

[S] matrix co- and cross-polar nulls (15×15 -pixel averaging window) - Parall. classification test:

- Overall accuracy = (67039/150262) 44.61%
- Kappa coefficient = 0.36

Table C.23: Pr. Acc. and Us. Acc. estimates relative to the Parall. classification test performed on the [S] matrix co- and cross-polar nulls (15×15 -pixel averaging window).

Class	Pr. Acc. (%)	Us. Acc. (%)	Pr. Acc. (pixels)	Us. Acc. (pixels)
water	0.00	0.00	0/22374	0/0
houses	68.49	93.41	16089/23492	16089/17224
roads	3.65	100.00	715/19582	715/715
trees	97.75	77.72	22055/22562	22055/28379
grass	0.00	0.00	0/17784	0/0
field 1	40.06	95.43	10565/26372	10565/11071
field 2	97.34	19.20	17615/18096	17615/91732

Table C.24: Commission and omission error estimates relative to the Parall. classification test performed on the [S] matrix co- and cross-polar nulls (15×15 -pixel averaging window).

Class	Comm. (%)	Om. (%)	Comm. (pixels)	Om. (pixels)
water	0.00	100.00	0/22374	22374/22374
houses	6.59	31.51	1135/23492	7403/23492
roads	0.00	96.35	0/19582	18867/19582
trees	22.28	2.25	6324/22562	507/22562
grass	0.00	100.00	0/17784	17784/17784
field 1	4.57	59.94	506/26372	15807/26372
field 2	80.80	2.66	74117/18096	481/18096

C.3 Parameters of the coherent target decomposition theorems

SDH decomposition terms (single-pixel basis) - Max. Lik. classification test:

- Overall accuracy = (58544/150262) 38.96%
- Kappa coefficient = 0.29

Table C.25: Pr. Acc. and Us. Acc. estimates relative to the Max. Lik. classification test performed on the SDH decomposition terms (single-pixel basis).

Class	Pr. Acc. (%)	Us. Acc. (%)	Pr. Acc. (pixels)	Us. Acc. (pixels)
water	16.65	26.39	3726/22374	3726/14117
houses	26.89	83.92	6316/23492	6316/7526
roads	73.66	32.61	14425/19582	14425/44238
trees	72.02	54.04	16249/22562	16249/30071
grass	26.15	26.24	4650/17784	4650/17719
field 1	40.53	41.51	10689/26372	10689/25751
field 2	13.75	22.96	2489/18096	2489/10840

Table C.26: Commission and omission error estimates relative to the Max. Lik. classification test performed on the SDH decomposition terms (single-pixel basis).

Class	Comm. (%)	Om. (%)	Comm. (pixels)	Om. (pixels)
water	73.61	83.35	10391/22374	18648/22374
houses	16.08	73.11	1210/23492	17176/23492
roads	67.39	26.34	29813/19582	5157/19582
trees	45.96	27.98	13822/22562	6313/22562
grass	73.76	73.85	13069/17784	13134/17784
field 1	58.49	59.47	15062/26372	15683/26372
field 2	77.04	86.25	8351/18096	15607/18096

SDH decomposition terms (single-pixel basis) - Min. Dist. classification test:

- Overall accuracy = (57938/150262) 38.56%
- Kappa coefficient = 0.28

Table C.27: Pr. Acc. and Us. Acc. estimates relative to the Min. Dist. classification test performed on the SDH decomposition terms (single-pixel basis).

Class	Pr. Acc. (%)	Us. Acc. (%)	Pr. Acc. (pixels)	Us. Acc. (pixels)
water	20.15	26.45	4508/22374	4508/17046
houses	34.68	71.80	8147/23492	8147/11347
roads	61.77	34.11	12095/19582	12095/35462
trees	59.26	54.66	13371/22562	13371/24460
grass	26.64	26.06	4737/17784	4737/18176
field 1	50.24	37.05	13250/26372	13250/35764
field 2	10.11	22.86	1830/18096	1830/8007

Table C.28: Commission and omission error estimates relative to the Min. Dist. classification test performed on the SDH decomposition terms (single-pixel basis).

Class	Comm. (%)	Om. (%)	Comm. (pixels)	Om. (pixels)
water	73.55	79.85	12538/22374	17866/22374
houses	28.20	65.32	3200/23492	15345/23492
roads	65.89	38.23	23367/19582	7487/19582
trees	45.34	40.74	11089/22562	9191/22562
grass	73.94	73.36	13439/17784	13047/17784
field 1	62.95	49.76	22514/26372	13122/26372
field 2	77.14	89.89	6177/18096	16266/18096

SDH decomposition terms (single-pixel basis) - Parall. classification test:

- Overall accuracy = (39074/150262) 26%
- Kappa coefficient = 0.15

Table C.29: Pr. Acc. and Us. Acc. estimates relative to the Parall. classification test performed on the SDH decomposition terms (single-pixel basis).

Class	Pr. Acc. (%)	Us. Acc. (%)	Pr. Acc. (pixels)	Us. Acc. (pixels)
water	0.00	0.00	0/22374	0/0
houses	18.50	87.35	4345/23492	4345/4974
roads	0.00	0.00	0/19582	0/0
trees	55.61	56.04	12546/22562	12546/22389
grass	0.00	0.00	0/17784	0/0
field 1	17.44	26.69	4599/26372	4599/17230
field 2	97.17	16.82	17584/18096	17584/104517

Table C.30: Commission and omission error estimates relative to the Parall. classification test performed on the SDH decomposition terms (single-pixel basis).

Class	Comm. (%)	Om. (%)	Comm. (pixels)	Om. (pixels)
water	0.00	100.00	0/22374	22374/22374
houses	12.65	81.50	629/23492	19147/23492
roads	0.00	100.00	0/19582	19582/19582
trees	43.96	44.39	9843/22562	10016/22562
grass	0.00	100.00	0/17784	17784/17784
field 1	73.31	82.56	12631/26372	21773/26372
field 2	83.18	2.83	86933/18096	512/18096

SDH decomposition terms (15×15-pixel averaging window) - Max. Lik. classification test:

- Overall accuracy = (131279/150262) 87.37%
- Kappa coefficient = 0.85

Table C.31: Pr. Acc. and Us. Acc. estimates relative to the Max. Lik. classification test performed on the SDH decomposition terms (15×15-pixel averaging window).

Class	Pr. Acc. (%)	Us. Acc. (%)	Pr. Acc. (pixels)	Us. Acc. (pixels)
water	74.02	82.24	16562/22374	16562/20139
houses	90.80	98.37	21330/23492	21330/21683
roads	87.05	78.18	17046/19582	17046/21804
trees	99.41	91.21	22429/22562	22429/24591
grass	87.34	83.53	15532/17784	15532/18594
field 1	88.18	94.80	23255/26372	23255/24531
field 2	83.58	79.94	15125/18096	15125/18920

Table C.32: Commission and omission error estimates relative to the Max. Lik. classification test performed on the SDH decomposition terms (15×15-pixel averaging window).

Class	Comm. (%)	Om. (%)	Comm. (pixels)	Om. (pixels)
water	17.76	25.98	3577/22374	5812/22374
houses	1.63	9.20	353/23492	2162/23492
roads	21.82	12.95	4758/19582	2536/19582
trees	8.79	0.59	2162/22562	133/22562
grass	16.47	12.66	3062/17784	2252/17784
field 1	5.20	11.82	1276/26372	3117/26372
field 2	20.06	16.42	3795/18096	2971/18096

SDH decomposition terms (15×15 -pixel averaging window) - Min. Dist. classification test:

- Overall accuracy = $(115760/150262)$ 77.04%
- Kappa coefficient = 0.73

Table C.33: Pr. Acc. and Us. Acc. estimates relative to the Min. Dist. classification test performed on the SDH decomposition terms (15×15 -pixel averaging window).

Class	Pr. Acc. (%)	Us. Acc. (%)	Pr. Acc. (pixels)	Us. Acc. (pixels)
water	55.55	70.02	12428/22374	12428/17749
houses	64.03	100.00	15042/23492	15042/15042
roads	88.33	70.78	17297/19582	17297/24438
trees	100.00	72.76	22562/22562	22562/31008
grass	74.58	79.73	13263/17784	13263/16635
field 1	86.25	93.04	22745/26372	22745/24446
field 2	68.65	59.32	12423/18096	12423/20944

Table C.34: Commission and omission error estimates relative to the Min. Dist. classification test performed on the SDH decomposition terms (15×15 -pixel averaging window).

Class	Comm. (%)	Om. (%)	Comm. (pixels)	Om. (pixels)
water	29.98	44.45	5321/22374	9946/22374
houses	0.00	35.97	0/23492	8450/23492
roads	29.22	11.67	7141/19582	2285/19582
trees	27.24	0.00	8446/22562	0/22562
grass	20.27	25.42	3372/17784	4521/17784
field 1	6.96	13.75	1701/26372	3627/26372
field 2	40.68	31.35	8521/18096	5673/18096

SDH decomposition terms (15×15 -pixel averaging window) - Parall. classification test:

- Overall accuracy = $(115760/150262)$ 55.58%
- Kappa coefficient = 0.48

Table C.35: Pr. Acc. and Us. Acc. estimates relative to the Parall. classification test performed on the SDH decomposition terms (15×15 -pixel averaging window).

Class	Pr. Acc. (%)	Us. Acc. (%)	Pr. Acc. (pixels)	Us. Acc. (pixels)
water	0.00	0.00	0/22374	0/0
houses	81.04	96.10	19038/23492	19038/19811
roads	23.34	83.12	4571/19582	4571/5499
trees	99.16	86.75	22373/22562	22373/25791
grass	0.46	6.33	81/17784	81/1279
field 1	74.73	92.16	19707/26372	19707/21384
field 2	98.10	23.52	17752/18096	17752/75462

Table C.36: Commission and omission error estimates relative to the Parall. classification test performed on the SDH decomposition terms (15×15 -pixel averaging window).

Class	Comm. (%)	Om. (%)	Comm. (pixels)	Om. (pixels)
water	0.00	100.00	0/22374	22374/22374
houses	3.90	18.96	773/23492	4454/23492
roads	16.88	76.66	928/19582	15011/19582
trees	13.25	0.84	3418/22562	189/22562
grass	93.67	99.54	1198/17784	17703/17784
field 1	7.84	25.27	1677/26372	6665/26372
field 2	76.48	1.90	57710/18096	344/18096

Pauli decomposition terms (single-pixel averaging window) - Max. Lik. classification test:

- Overall accuracy = (62713/150262) 41.74%
- Kappa coefficient = 0.32

Table C.37: Pr. Acc. and Us. Acc. estimates relative to the Max. Lik. classification test performed on the Pauli decomposition terms (single-pixel basis).

Class	Pr. Acc. (%)	Us. Acc. (%)	Pr. Acc. (pixels)	Us. Acc. (pixels)
water	20.35	30.60	4554/22374	4554/14883
houses	28.72	85.70	6746/23492	6746/7872
roads	74.13	34.94	14516/19582	14516/41546
trees	76.37	57.47	17230/22562	17230/29981
grass	25.67	27.31	4565/17784	4565/16716
field 1	43.13	44.71	11375/26372	11375/25441
field 2	20.60	26.96	3727/18096	3727/13823

Table C.38: Commission and omission error estimates relative to the Max. Lik. classification test performed on the Pauli decomposition terms (single-pixel basis).

Class	Comm. (%)	Om. (%)	Comm. (pixels)	Om. (pixels)
water	69.40	79.65	10329/22374	17820/22374
houses	14.30	71.28	1126/23492	16746/23492
roads	65.06	25.87	27030/19582	5066/19582
trees	42.53	23.63	12751/22562	5332/22562
grass	72.69	74.33	12151/17784	13219/17784
field 1	55.29	56.87	14066/26372	14997/26372
field 2	73.04	79.40	10096/18096	14369/18096

Pauli decomposition terms (single-pixel averaging window) - Min. Dist. classification test:

- Overall accuracy = (60071/150262) 39.98%
- Kappa coefficient = 0.3

Table C.39: Pr. Acc. and Us. Acc. estimates relative to the Min. Dist. classification test performed on the Pauli decomposition terms (single-pixel basis).

Class	Pr. Acc. (%)	Us. Acc. (%)	Pr. Acc. (pixels)	Us. Acc. (pixels)
water	22.64	29.28	5065/22374	5065/17296
houses	35.82	75.85	8416/23492	8416/11096
roads	61.02	34.53	11948/19582	11948/34600
trees	62.88	58.24	14188/22562	14188/24363
grass	28.73	25.98	5109/17784	5109/19668
field 1	51.93	37.96	13696/26372	13696/36078
field 2	9.11	23.03	1649/18096	1649/7161

Table C.40: Commission and omission error estimates relative to the Min. Dist. classification test performed on the Pauli decomposition terms (single-pixel basis).

Class	Comm. (%)	Om. (%)	Comm. (pixels)	Om. (pixels)
water	70.72	77.36	12231/22374	17309/22374
houses	24.15	64.18	2680/23492	15076/23492
roads	65.47	38.98	22652/19582	7634/19582
trees	41.76	37.12	10175/22562	8374/22562
grass	74.02	71.27	14559/17784	12675/17784
field 1	62.04	48.07	22382/26372	12676/26372
field 2	76.97	90.89	5512/18096	16447/18096

Pauli decomposition terms (single-pixel averaging window) - Parall. classification test:

- Overall accuracy = (41848/150262) 27.85%
- Kappa coefficient = 0.17

Table C.41: Pr. Acc. and Us. Acc. estimates relative to the Parall. classification test performed on the Pauli decomposition terms (single-pixel basis).

Class	Pr. Acc. (%)	Us. Acc. (%)	Pr. Acc. (pixels)	Us. Acc. (pixels)
water	0.00	0.00	0/22374	0/0
houses	19.59	89.74	4602/23492	4602/5128
roads	0.00	0.00	0/19582	0/0
trees	64.83	59.55	14626/22562	14626/24560
grass	0.00	0.00	0/17784	0/0
field 1	18.75	30.78	4944/26372	4944/16062
field 2	97.68	17.09	17676/18096	17676/103419

Table C.42: Commission and omission error estimates relative to the Parall. classification test performed on the Pauli decomposition terms (single-pixel basis).

Class	Comm. (%)	Om. (%)	Comm. (pixels)	Om. (pixels)
water	0.00	100.00	0/22374	22374/22374
houses	10.26	80.41	526/23492	18890/23492
roads	0.00	100.00	0/19582	19582/19582
trees	40.45	35.17	9934/22562	7936/22562
grass	0.00	100.00	0/17784	17784/17784
field 1	69.22	81.25	11118/26372	21428/26372
field 2	82.91	2.32	85743/18096	420/18096

Pauli decomposition terms (15×15-pixel averaging window) - Max. Lik. classification test:

- Overall accuracy = (86562/150262) 57.61%
- Kappa coefficient = 0.51

Table C.43: Pr. Acc. and Us. Acc. estimates relative to the Max. Lik. classification test performed on the Pauli decomposition terms (15×15-pixel averaging window).

Class	Pr. Acc. (%)	Us. Acc. (%)	Pr. Acc. (pixels)	Us. Acc. (pixels)
water	45.58	44.94	10199/22374	10199/22694
houses	66.96	93.14	15731/23492	15731/16889
roads	77.11	56.32	15099/19582	15099/26811
trees	87.64	69.98	19773/22562	19773/28257
grass	51.46	37.08	9151/17784	9151/24676
field 1	44.92	64.21	11847/26372	11847/18451
field 2	26.32	38.14	4762/18096	4762/12484

Table C.44: Commission and omission error estimates relative to the Max. Lik. classification test performed on the Pauli decomposition terms (15×15-pixel averaging window).

Class	Comm. (%)	Om. (%)	Comm. (pixels)	Om. (pixels)
water	55.06	54.42	12495/22374	12175/22374
houses	6.86	33.04	1158/23492	7761/23492
roads	43.68	22.89	11712/19582	4483/19582
trees	30.02	12.36	8484/22562	2789/22562
grass	62.92	48.54	15525/17784	8633/17784
field 1	35.79	55.08	6604/26372	14525/26372
field 2	61.86	73.68	7722/18096	13334/18096

Pauli decomposition terms (15×15 -pixel averaging window) - Min. Dist. classification test:

- Overall accuracy = $(78537/150262)$ 52.27%
- Kappa coefficient = 0.44

Table C.45: Pr. Acc. and Us. Acc. estimates relative to the Min. Dist. classification test performed on the Pauli decomposition terms (15×15 -pixel averaging window).

Class	Pr. Acc. (%)	Us. Acc. (%)	Pr. Acc. (pixels)	Us. Acc. (pixels)
water	33.04	33.87	7392/22374	7392/21827
houses	59.97	97.53	14087/23492	14087/14444
roads	73.39	48.51	14371/19582	14371/29627
trees	81.78	67.67	18451/22562	18451/27267
grass	34.46	34.75	6128/17784	6128/17637
field 1	53.78	50.66	14182/26372	14182/27996
field 2	21.70	34.25	3926/18096	3926/11464

Table C.46: Commission and omission error estimates relative to the Min. Dist. classification test performed on the Pauli decomposition terms (15×15 -pixel averaging window).

Class	Comm. (%)	Om. (%)	Comm. (pixels)	Om. (pixels)
water	66.13	66.96	14435/22374	14982/22374
houses	2.47	40.03	357/23492	9405/23492
roads	51.49	26.61	15256/19582	5211/19582
trees	32.33	18.22	8816/22562	4111/22562
grass	65.25	65.54	11509/17784	11656/17784
field 1	49.34	46.22	13814/26372	12190/26372
field 2	65.75	78.30	7538/18096	14170/18096

Pauli decomposition terms (15×15 -pixel averaging window) - Parall. classification test:

- Overall accuracy = (52069/150262) 34.65%
- Kappa coefficient = 0.25

Table C.47: Pr. Acc. and Us. Acc. estimates relative to the Parall. classification test performed on the Pauli decomposition terms (15×15 -pixel averaging window).

Class	Pr. Acc. (%)	Us. Acc. (%)	Pr. Acc. (pixels)	Us. Acc. (pixels)
water	0.00	0.00	0/22374	0/0
houses	52.84	97.96	12414/23492	12414/12673
roads	0.00	0.00	0/19582	0/0
trees	85.94	66.60	19390/22562	19390/29112
grass	0.00	0.00	0/17784	0/0
field 1	9.86	47.33	2601/26372	2601/5496
field 2	97.61	17.34	17664/18096	17664/101871

Table C.48: Commission and omission error estimates relative to the Parall. classification test performed on the Pauli decomposition terms (15×15 -pixel averaging window).

Class	Comm. (%)	Om. (%)	Comm. (pixels)	Om. (pixels)
water	0.00	100.00	0/22374	22374/22374
houses	2.04	47.16	259/23492	11078/23492
roads	0.00	100.00	0/19582	19582/19582
trees	33.40	14.06	9722/22562	3172/22562
grass	0.00	100.00	0/17784	17784/17784
field 1	52.67	90.14	2895/26372	23771/26372
field 2	82.66	2.39	84207/18096	432/18096

Cameron decomposition terms (single-pixel averaging window) - Max. Lik. classification test:

- Overall accuracy = (56193/150262) 37.4%
- Kappa coefficient = 0.27

Table C.49: Pr. Acc. and Us. Acc. estimates relative to the Max. Lik. classification test performed on the Cameron decomposition terms (single-pixel basis).

Class	Pr. Acc. (%)	Us. Acc. (%)	Pr. Acc. (pixels)	Us. Acc. (pixels)
water	16.21	25.05	3627/22374	3627/14481
houses	25.83	82.39	6068/23492	6068/7365
roads	76.58	31.23	14995/19582	14995/48010
trees	69.24	52.82	15622/22562	15622/29577
grass	24.70	22.55	4392/17784	4392/19474
field 1	40.61	38.93	10710/26372	10710/27509
field 2	4.30	20.25	779/18096	779/3846

Table C.50: Commission and omission error estimates relative to the Max. Lik. classification test performed on the Cameron decomposition terms (single-pixel basis).

Class	Comm. (%)	Om. (%)	Comm. (pixels)	Om. (pixels)
water	74.95	83.79	10854/22374	18747/22374
houses	17.61	74.17	1297/23492	17424/23492
roads	68.77	23.42	33015/19582	4587/19582
trees	47.18	30.76	13955/22562	6940/22562
grass	77.45	75.30	15082/17784	13392/17784
field 1	61.07	59.39	16799/26372	15662/26372
field 2	79.75	95.70	3067/18096	17317/18096

Cameron decomposition terms (single-pixel averaging window) - Min. Dist. classification test:

- Overall accuracy = 56502/150262) 37.60%
- Kappa coefficient = 0.27

Table C.51: Pr. Acc. and Us. Acc. estimates relative to the Min. Dist. classification test performed on the Cameron decomposition terms (single-pixel basis).

Class	Pr. Acc. (%)	Us. Acc. (%)	Pr. Acc. (pixels)	Us. Acc. (pixels)
water	14.89	26.34	3332/22374	3332/12651
houses	34.27	69.60	8050/23492	8050/11566
roads	65.65	33.80	12856/19582	12856/38034
trees	56.98	52.86	12855/22562	12855/24318
grass	20.14	23.44	3581/17784	3581/15275
field 1	52.65	36.30	13886/26372	13886/38251
field 2	10.73	19.10	1942/18096	1942/10167

Table C.52: Commission and omission error estimates relative to the Min. Dist. classification test performed on the Cameron decomposition terms (single-pixel basis).

Class	Comm. (%)	Om. (%)	Comm. (pixels)	Om. (pixels)
water	73.66	85.11	9319/22374	19042/22374
houses	30.40	65.73	3516/23492	15442/23492
roads	66.20	34.35	25178/19582	6726/19582
trees	47.14	43.02	11463/22562	9707/22562
grass	76.56	79.86	11694/17784	14203/17784
field 1	63.70	47.35	24365/26372	12486/26372
field 2	80.90	89.27	8225/18096	16154/18096

Cameron decomposition terms (single-pixel averaging window) - Parall. classification test:

- Overall accuracy = (37208/150262) 24.76%
- Kappa coefficient = 0.13

Table C.53: Pr. Acc. and Us. Acc. estimates relative to the Parall. classification test performed on the Cameron decomposition terms (single-pixel basis).

Class	Pr. Acc. (%)	Us. Acc. (%)	Pr. Acc. (pixels)	Us. Acc. (pixels)
water	0.00	0.00	0/22374	0/0
houses	17.98	92.03	4225/23492	4225/4591
roads	0.00	0.00	0/19582	0/0
trees	50.50	55.84	11394/22562	11394/20404
grass	0.00	0.00	0/17784	0/0
field 1	14.22	22.05	3750/26372	3750/17008
field 2	98.58	16.56	17839/18096	17839/107703

Table C.54: Commission and omission error estimates relative to the Parall. classification test performed on the Cameron decomposition terms (single-pixel basis).

Class	Comm. (%)	Om. (%)	Comm. (pixels)	Om. (pixels)
water	0.00	100.00	0/22374	22374/22374
houses	7.97	82.02	366/23492	19267/23492
roads	0.00	100.00	0/19582	19582/19582
trees	44.16	49.50	9010/22562	11168/22562
grass	0.00	100.00	0/17784	17784/17784
field 1	77.95	85.78	13258/26372	22622/26372
field 2	83.44	1.42	89864/18096	257/18096

Cameron decomposition terms (15×15 -pixel averaging window) - Max. Lik. classification test:

- Overall accuracy = $(114752/150262)$ 76.37%
- Kappa coefficient = 0.72

Table C.55: Pr. Acc. and Us. Acc. estimates relative to the Max. Lik. classification test performed on the Cameron decomposition terms (15×15 -pixel averaging window).

Class	Pr. Acc. (%)	Us. Acc. (%)	Pr. Acc. (pixels)	Us. Acc. (pixels)
water	53.02	64.33	11863/22374	11863/18442
houses	76.85	96.16	18054/23492	18054/18775
roads	88.58	73.41	17345/19582	17345/23626
trees	98.43	80.33	22207/22562	22207/27645
grass	79.91	68.26	14211/17784	14211/20819
field 1	85.02	90.92	22421/26372	22421/24661
field 2	47.81	53.09	8651/18096	8651/16294

Table C.56: Commission and omission error estimates relative to the Max. Lik. classification test performed on the Cameron decomposition terms (15×15 -pixel averaging window).

Class	Comm. (%)	Om. (%)	Comm. (pixels)	Om. (pixels)
water	35.67	46.98	6579/22374	10511/22374
houses	3.84	23.15	721/23492	5438/23492
roads	26.59	11.42	6281/19582	2237/19582
trees	19.67	1.57	5438/22562	355/22562
grass	31.74	20.09	6608/17784	3573/17784
field 1	9.08	14.98	2240/26372	3951/26372
field 2	46.91	52.19	7643/18096	9445/18096

Cameron decomposition terms (15×15 -pixel averaging window) - Min. Dist. classification test:

- Overall accuracy = $(107212/150262)$ 71.35%
- Kappa coefficient = 0.66

Table C.57: Pr. Acc. and Us. Acc. estimates relative to the Min. Dist. classification test performed on the Cameron decomposition terms (15×15 -pixel averaging window).

Class	Pr. Acc. (%)	Us. Acc. (%)	Pr. Acc. (pixels)	Us. Acc. (pixels)
water	43.62	65.13	9760/22374	9760/14986
houses	63.06	100.00	14814/23492	14814/14814
roads	89.08	69.41	17444/19582	17444/25132
trees	100.00	72.23	22562/22562	22562/31237
grass	56.92	63.44	10122/17784	10122/15955
field 1	85.83	91.34	22636/26372	22636/24783
field 2	54.56	42.28	9874/18096	9874/23355

Table C.58: Commission and omission error estimates relative to the Min. Dist. classification test performed on the Cameron decomposition terms (15×15 -pixel averaging window).

Class	Comm. (%)	Om. (%)	Comm. (pixels)	Om. (pixels)
water	34.87	56.38	5226/22374	12614/22374
houses	0.00	36.94	0/23492	8678/23492
roads	30.59	10.92	7688/19582	2138/19582
trees	27.77	0.00	8675/22562	0/22562
grass	36.56	43.08	5833/17784	7662/17784
field 1	8.66	14.17	2147/26372	3736/26372
field 2	57.72	45.44	13481/18096	8222/18096

Cameron decomposition terms (15×15 -pixel averaging window) - Parall. classification test:

- Overall accuracy = (79486/150262) 52.9%
- Kappa coefficient = 0.45

Table C.59: Pr. Acc. and Us. Acc. estimates relative to the Parall. classification test performed on the Cameron decomposition terms (15×15 -pixel averaging window).

Class	Pr. Acc. (%)	Us. Acc. (%)	Pr. Acc. (pixels)	Us. Acc. (pixels)
water	0.00	0.00	0/22374	0/0
houses	71.72	98.83	16849/23492	16849/17048
roads	20.02	99.97	3920/19582	3920/3921
trees	99.53	79.02	22457/22562	22457/28419
grass	0.00	0.00	0/17784	0/58
field 1	70.14	95.54	18498/26372	18498/19361
field 2	98.15	21.99	17762/18096	17762/80774

Table C.60: Commission and omission error estimates relative to the Parall. classification test performed on the Cameron decomposition terms (15×15 -pixel averaging window).

Class	Comm. (%)	Om. (%)	Comm. (pixels)	Om. (pixels)
water	0.00	100.00	0/22374	22374/22374
houses	1.17	28.28	199/23492	6643/23492
roads	0.03	79.98	1/19582	15662/19582
trees	20.98	0.47	5962/22562	105/22562
grass	100.00	100.00	58/17784	17784/17784
field 1	4.46	29.86	863/26372	7874/26372
field 2	78.01	1.85	63012/18096	334/18096

C.4 Entropy/ α parameters

H and $\bar{\alpha}$ (3×3 -pixel averaging window) - Max. Lik. classification test:

- Overall accuracy = (43921/150262) 29.23%
- Kappa coefficient = 0.17

Table C.61: Pr. Acc. and Us. Acc. estimates relative to the Max. Lik. classification test performed on the H and $\bar{\alpha}$ parameters (3×3 -pixel averaging window).

Class	Pr. Acc. (%)	Us. Acc. (%)	Pr. Acc. (pixels)	Us. Acc. (pixels)
water	72.72	22.56	16271/22374	16271/72108
houses	31.52	47.84	7404/23492	7404/15475
roads	2.29	14.52	448/19582	448/3085
trees	65.03	48.93	14672/22562	14672/29985
grass	12.43	18.11	2210/17784	2210/12205
field 1	0.03	33.33	8/26372	8/24
field 2	16.07	16.73	2908/18096	2908/17380

Table C.62: Commission and omission error estimates relative to the Max. Lik. classification test performed on the H and $\bar{\alpha}$ parameters (3×3 -pixel averaging window).

Class	Comm. (%)	Om. (%)	Comm. (pixels)	Om. (pixels)
water	77.44	27.28	55837/22374	6103/22374
houses	52.16	68.48	8071/23492	16088/23492
roads	85.48	97.71	2637/19582	19134/19582
trees	51.07	34.97	15313/22562	7890/22562
grass	81.89	87.57	9995/17784	15574/17784
field 1	66.67	99.97	16/26372	26364/26372
field 2	83.27	83.93	14472/18096	15188/18096

H and $\bar{\alpha}$ (3×3 -pixel averaging window) - Min. Dist. classification test:

- Overall accuracy = (36284/150262) 24.15%
- Kappa coefficient = 0.11

Table C.63: Pr. Acc. and Us. Acc. estimates relative to the Min. Dist. classification test performed on the H and $\bar{\alpha}$ parameters (3×3 -pixel averaging window).

Class	Pr. Acc. (%)	Us. Acc. (%)	Pr. Acc. (pixels)	Us. Acc. (pixels)
water	50.14	19.21	11219/22374	11219/58401
houses	4.43	11.04	1040/23492	1040/9423
roads	1.68	17.80	328/19582	328/1843
trees	73.02	43.08	16474/22562	16474/38237
grass	0.75	14.10	133/17784	133/943
field 1	7.90	19.97	2084/26372	2084/10435
field 2	27.66	16.16	5006/18096	5006/30980

Table C.64: Commission and omission error estimates relative to the Min. Dist. classification test performed on the H and $\bar{\alpha}$ parameters (3×3 -pixel averaging window).

Class	Comm. (%)	Om. (%)	Comm. (pixels)	Om. (pixels)
water	80.79	49.86	47182/22374	11155/22374
houses	88.96	95.57	8383/23492	22452/23492
roads	82.20	98.32	1515/19582	19254/19582
trees	56.92	26.98	21763/22562	6088/22562
grass	85.90	99.25	810/17784	17651/17784
field 1	80.03	92.10	8351/26372	24288/26372
field 2	83.84	72.34	25974/18096	13090/18096

H and $\bar{\alpha}$ (3×3 -pixel averaging window) - Parall. classification test:

- Overall accuracy = (21587/150262) 14.37%
- Kappa coefficient = 0.025

Table C.65: Pr. Acc. and Us. Acc. estimates relative to the Parall. classification test performed on the H and $\bar{\alpha}$ parameters (3×3 -pixel averaging window).

Class	Pr. Acc. (%)	Us. Acc. (%)	Pr. Acc. (pixels)	Us. Acc. (pixels)
water	0.00	0.00	0/22374	0/0
houses	9.55	97.10	2243/23492	2243/2310
roads	0.00	0.00	0/19582	0/0
trees	4.96	64.09	1119/22562	1119/1746
grass	0.51	7.34	90/17784	90/1226
field 1	0.79	10.11	209/26372	209/2067
field 2	99.06	12.55	17926/18096	17926/142884

Table C.66: Commission and omission error estimates relative to the Parall. classification test performed on the H and $\bar{\alpha}$ parameters (3×3 -pixel averaging window).

Class	Comm. (%)	Om. (%)	Comm. (pixels)	Om. (pixels)
water	0.00	100.00	0/22374	22374/22374
houses	2.90	90.45	67/23492	21249/23492
roads	0.00	100.00	0/19582	19582/19582
trees	35.91	95.04	627/22562	21443/22562
grass	92.66	99.49	1136/17784	17694/17784
field 1	89.89	99.21	1858/26372	26163/26372
field 2	87.45	0.94	124958/18096	170/18096

H and $\bar{\alpha}$ (15×15 -pixel averaging window) - Max. Lik. classification test:

- Overall accuracy = (90539/150262) 60.25%
- Kappa coefficient = 0.54

Table C.67: Pr. Acc. and Us. Acc. estimates relative to the Max. Lik. classification test performed on the H and $\bar{\alpha}$ parameters (15×15 -pixel averaging window).

Class	Pr. Acc. (%)	Us. Acc. (%)	Pr. Acc. (pixels)	Us. Acc. (pixels)
water	70.46	67.88	15765/22374	15765/23224
houses	67.99	89.97	15972/23492	15972/17752
roads	36.77	34.78	7200/19582	7200/20702
trees	93.37	91.97	21067/22562	21067/22906
grass	71.51	48.68	12717/17784	12717/26122
field 1	12.08	60.73	3187/26372	3187/5248
field 2	80.85	42.65	14631/18096	14631/34308

Table C.68: Commission and omission error estimates relative to the Max. Lik. classification test performed on the H and $\bar{\alpha}$ parameters (15×15 -pixel averaging window).

Class	Comm. (%)	Om. (%)	Comm. (pixels)	Om. (pixels)
water	32.12	29.54	7459/22374	6609/22374
houses	10.03	32.01	1780/23492	7520/23492
roads	65.22	63.23	13502/19582	12382/19582
trees	8.03	6.63	1839/22562	1495/22562
grass	51.32	28.49	13405/17784	5067/17784
field 1	39.27	87.92	2061/26372	23185/26372
field 2	57.35	19.15	19677/18096	3465/18096

H and $\bar{\alpha}$ (15×15 -pixel averaging window) - Min. Dist. classification test:

- Overall accuracy = (68067/150262) 45.3%
- Kappa coefficient = 0.36

Table C.69: Pr. Acc. and Us. Acc. estimates relative to the Min. Dist. classification test performed on the H and $\bar{\alpha}$ parameters (15×15 -pixel averaging window).

Class	Pr. Acc. (%)	Us. Acc. (%)	Pr. Acc. (pixels)	Us. Acc. (pixels)
water	58.86	35.29	13170/22374	13170/37319
houses	57.00	66.34	13391/23492	13391/20184
roads	30.61	25.59	5995/19582	5995/23431
trees	90.05	89.11	20318/22562	20318/22801
grass	47.79	39.33	8499/17784	8499/21607
field 1	14.78	26.02	3897/26372	3897/14975
field 2	15.46	28.12	2797/18096	2797/9945

Table C.70: Commission and omission error estimates relative to the Min. Dist. classification test performed on the H and $\bar{\alpha}$ parameters (15×15 -pixel averaging window).

Class	Comm. (%)	Om. (%)	Comm. (pixels)	Om. (pixels)
water	64.71	41.14	24149/22374	9204/22374
houses	33.66	43.00	6793/23492	10101/23492
roads	74.41	69.39	17436/19582	13587/19582
trees	10.89	9.95	2483/22562	2244/22562
grass	60.67	52.21	13108/17784	9285/17784
field 1	73.98	85.22	11078/26372	22475/26372
field 2	71.88	84.54	7148/18096	15299/18096

H and $\bar{\alpha}$ (15×15 -pixel averaging window) - Parall. classification test:

- Overall accuracy = (38289/150262) 25.48%
- Kappa coefficient = 0.136

Table C.71: Pr. Acc. and Us. Acc. estimates relative to the Parall. classification test performed on the H and $\bar{\alpha}$ parameters (15×15 -pixel averaging window).

Class	Pr. Acc. (%)	Us. Acc. (%)	Pr. Acc. (pixels)	Us. Acc. (pixels)
water	0.00	0.00	0/22374	0/0
houses	47.54	95.91	11167/23492	11167/11643
roads	0.00	0.00	0/19582	0/0
trees	32.47	99.84	7326/22562	7326/7338
grass	0.50	5.05	89/17784	89/1762
field 1	6.59	5.03	1737/26372	1737/34560
field 2	99.30	18.95	17970/18096	17970/94844

Table C.72: Commission and omission error estimates relative to the Parall. classification test performed on the H and $\bar{\alpha}$ parameters (15×15 -pixel averaging window).

Class	Comm. (%)	Om. (%)	Comm. (pixels)	Om. (pixels)
water	0.00	100.00	0/22374	22374/22374
houses	4.09	52.46	476/23492	12325/23492
roads	0.00	100.00	0/19582	19582/19582
trees	0.16	67.53	12/22562	15236/22562
grass	94.95	99.50	1673/17784	17695/17784
field 1	94.97	93.41	32823/26372	24635/26372
field 2	81.05	0.70	76874/18096	126/18096

H , $\bar{\alpha}$ and A (3×3 -pixel averaging window) - Max. Lik. classification test:

- Overall accuracy = (44656/150262) 29.72%
- Kappa coefficient = 0.18

Table C.73: Pr. Acc. and Us. Acc. estimates relative to the Max. Lik. classification test performed on the H , $\bar{\alpha}$ and A parameters (3×3 -pixel averaging window).

Class	Pr. Acc. (%)	Us. Acc. (%)	Pr. Acc. (pixels)	Us. Acc. (pixels)
water	64.24	23.78	14374/22374	14374/60450
houses	31.53	53.90	7408/23492	7408/13745
roads	5.18	17.41	1014/19582	1014/5825
trees	64.60	47.96	14574/22562	14574/30386
grass	17.04	18.68	3030/17784	3030/16224
field 1	0.33	22.37	87/26372	87/389
field 2	23.04	17.94	4169/18096	4169/23243

Table C.74: Commission and omission error estimates relative to the Max. Lik. classification test performed on the H , $\bar{\alpha}$ and A parameters (3×3 -pixel averaging window).

Class	Comm. (%)	Om. (%)	Comm. (pixels)	Om. (pixels)
water	76.22	35.76	46076/22374	8000/22374
houses	46.10	68.47	6337/23492	16084/23492
roads	82.59	94.82	4811/19582	18568/19582
trees	52.04	35.40	15812/22562	7988/22562
grass	81.32	82.96	13194/17784	14754/17784
field 1	77.63	99.67	302/26372	26285/26372
field 2	82.06	76.96	19074/18096	13927/18096

H , $\bar{\alpha}$ and A (3×3 -pixel averaging window) - Min. Dist. classification test:

- Overall accuracy = (36388/150262) 24.22%
- Kappa coefficient = 0.11

Table C.75: Pr. Acc. and Us. Acc. estimates relative to the Min. Dist. classification test performed on the H , $\bar{\alpha}$ and A parameters (3×3 -pixel averaging window).

Class	Pr. Acc. (%)	Us. Acc. (%)	Pr. Acc. (pixels)	Us. Acc. (pixels)
water	50.27	19.31	11248/22374	11248/58252
houses	4.40	11.18	1034/23492	1034/9246
roads	1.86	18.32	364/19582	364/1987
trees	73.02	43.08	16474/22562	16474/38237
grass	0.98	15.73	174/17784	174/1106
field 1	7.92	19.98	2088/26372	2088/10451
field 2	27.66	16.16	5006/18096	5006/30983

Table C.76: Commission and omission error estimates relative to the Min. Dist. classification test performed on the H , $\bar{\alpha}$ and A parameters (3×3 -pixel averaging window).

Class	Comm. (%)	Om. (%)	Comm. (pixels)	Om. (pixels)
water	80.69	49.73	47004/22374	11126/22374
houses	88.82	95.60	8212/23492	22458/23492
roads	81.68	98.14	1623/19582	19218/19582
trees	56.92	26.98	21763/22562	6088/22562
grass	84.27	99.02	932/17784	17610/17784
field 1	80.02	92.08	8363/26372	24284/26372
field 2	83.84	72.34	25977/18096	13090/18096

H , $\bar{\alpha}$ and A (3×3 -pixel averaging window) - Parall. classification test:

- Overall accuracy = (21587/150262) 14.37%
- Kappa coefficient = 0.025

Table C.77: Pr. Acc. and Us. Acc. estimates relative to the Parall. classification test performed on the H , $\bar{\alpha}$ and A parameters (3×3 -pixel averaging window).

Class	Pr. Acc. (%)	Us. Acc. (%)	Pr. Acc. (pixels)	Us. Acc. (pixels)
water	0.00	0.00	0/22374	0/0
houses	9.55	97.10	2243/23492	2243/2310
roads	0.00	0.00	0/19582	0/0
trees	4.96	64.09	1119/22562	1119/1746
grass	0.51	7.34	90/17784	90/1226
field 1	0.79	10.11	209/26372	209/2067
field 2	99.06	12.55	17926/18096	17926/142884

Table C.78: Commission and omission error estimates relative to the Parall. classification test performed on the H , $\bar{\alpha}$ and A parameters (3×3 -pixel averaging window).

Class	Comm. (%)	Om. (%)	Comm. (pixels)	Om. (pixels)
water	0.00	100.00	0/22374	22374/22374
houses	2.90	90.45	67/23492	21249/23492
roads	0.00	100.00	0/19582	19582/19582
trees	35.91	95.04	627/22562	21443/22562
grass	92.66	99.49	1136/17784	17694/17784
field 1	89.89	99.21	1858/26372	26163/26372
field 2	87.45	0.94	124958/18096	170/18096

H , $\bar{\alpha}$ and A (15×15 -pixel averaging window) - Max. Lik. classification test:

- Overall accuracy = (96312/150262) 64.1%
- Kappa coefficient = 0.58

Table C.79: Pr. Acc. and Us. Acc. estimates relative to the Max. Lik. classification test performed on the H , $\bar{\alpha}$ and A parameters (15×15 -pixel averaging window).

Class	Pr. Acc. (%)	Us. Acc. (%)	Pr. Acc. (pixels)	Us. Acc. (pixels)
water	83.36	65.99	18650/22374	18650/28263
houses	71.08	88.85	16698/23492	16698/18794
roads	39.25	37.03	7686/19582	7686/20755
trees	97.53	96.90	22005/22562	22005/22709
grass	64.08	51.57	11396/17784	11396/22100
field 1	21.55	67.59	5682/26372	5682/8407
field 2	78.44	48.56	14195/18096	14195/29234

Table C.80: Commission and omission error estimates relative to the Max. Lik. classification test performed on the H , $\bar{\alpha}$ and A parameters (15×15 -pixel averaging window).

Class	Comm. (%)	Om. (%)	Comm. (pixels)	Om. (pixels)
water	34.01	16.64	9613/22374	3724/22374
houses	11.15	28.92	2096/23492	6794/23492
roads	62.97	60.75	13069/19582	11896/19582
trees	3.10	2.47	704/22562	557/22562
grass	48.43	35.92	10704/17784	6388/17784
field 1	32.41	78.45	2725/26372	20690/26372
field 2	51.44	21.56	15039/18096	3901/18096

H , $\bar{\alpha}$ and A (15×15 -pixel averaging window) - Min. Dist. classification test:

- Overall accuracy = (68086/150262) 45.31%
- Kappa coefficient = 0.36

Table C.81: Pr. Acc. and Us. Acc. estimates relative to the Min. Dist. classification test performed on the H , $\bar{\alpha}$ and A parameters (15×15 -pixel averaging window).

Class	Pr. Acc. (%)	Us. Acc. (%)	Pr. Acc. (pixels)	Us. Acc. (pixels)
water	58.92	35.34	13182/22374	13182/37305
houses	57.00	66.34	13391/23492	13391/20184
roads	30.60	25.57	5992/19582	5992/23431
trees	90.06	89.12	20319/22562	20319/22800
grass	47.79	39.33	8499/17784	8499/21608
field 1	14.78	26.04	3898/26372	3898/14972
field 2	15.50	28.16	2805/18096	2805/9962

Table C.82: Commission and omission error estimates relative to the Min. Dist. classification test performed on the H , $\bar{\alpha}$ and A parameters (15×15 -pixel averaging window).

Class	Comm. (%)	Om. (%)	Comm. (pixels)	Om. (pixels)
water	64.66	41.08	24123/22374	9192/22374
houses	33.66	43.00	6793/23492	10101/23492
roads	74.43	69.40	17439/19582	13590/19582
trees	10.88	9.94	2481/22562	2243/22562
grass	60.67	52.21	13109/17784	9285/17784
field 1	73.96	85.22	11074/26372	22474/26372
field 2	71.84	84.50	7157/18096	15291/18096

H , $\bar{\alpha}$ and A (15×15 -pixel averaging window) - Parall. classification test:

- Overall accuracy = (38637/150262) 25.71%
- Kappa coefficient = 0.137

Table C.83: Pr. Acc. and Us. Acc. estimates relative to the Parall. classification test performed on the H , $\bar{\alpha}$ and A parameters (15×15 -pixel averaging window).

Class	Pr. Acc. (%)	Us. Acc. (%)	Pr. Acc. (pixels)	Us. Acc. (pixels)
water	0.00	0.00	0/22374	0/0
houses	47.59	92.55	11179/23492	11179/12079
roads	0.00	0.00	0/19582	0/0
trees	32.40	99.84	7310/22562	7310/7322
grass	2.40	15.97	427/17784	427/2673
field 1	6.67	4.62	1758/26372	1758/38048
field 2	99.27	19.95	17963/18096	17963/90025

Table C.84: Commission and omission error estimates relative to the Parall. classification test performed on the H , $\bar{\alpha}$ and A parameters (15×15 -pixel averaging window).

Class	Comm. (%)	Om. (%)	Comm. (pixels)	Om. (pixels)
water	0.00	100.00	0/22374	22374/22374
houses	7.45	52.41	900/23492	12313/23492
roads	0.00	100.00	0/19582	19582/19582
trees	0.16	67.60	12/22562	15252/22562
grass	84.03	97.60	2246/17784	17357/17784
field 1	95.38	93.33	36290/26372	24614/26372
field 2	80.05	0.73	72062/18096	133/18096

Bibliography

- [AB77] R. M. A. Azzam and N. M. Bashara. “*Ellipsometry and polarized light*”. North-Holland, Amsterdam, the Netherlands, 1977.
- [AB89] A. P. Agrawal and W-M. Boerner. “Redevelopment of Kennaugh’s target characteristic polarization state theory using polarization transformation ratio formalism for the coherent case”. *IEEE Transactions on Geoscience and Remote Sensing*, vol. 27 (1): pages 2–14, January 1989.
- [AC00] V. Alberga and M. Chandra. “Analysis of amplitude ratios in SAR polarimetry”. In *Kleinheubacher Berichte 2000*, pages 527–534, Kleinheubach, Germany, 25 - 29 September 2000.
- [AC01] V. Alberga and M. Chandra. “Combined application of target decomposition methods and polarimetric SAR interferometry: some preliminary results”. In *Proceedings of SPIE - SAR Image Analysis, Modeling, and Techniques IV*, volume 4543, pages 140–150, Toulouse, France, 17 - 18 September 2001.
- [AC03] V. Alberga and M. Chandra. “Volume decorrelation resolution in polarimetric SAR interferometry”. *Electronic Letters*, vol. 39 (3): pages 314–315, February 2003.
- [ACK02] V. Alberga, M. Chandra, and E. Krogager. “A comparison of target decomposition theorems in SAR interferometry applications”. In *Proceedings of URSI-F Open Symposium on Propagation and Remote Sensing 2002*, Garmisch-Partenkirchen, Germany, 12 - 15 February 2002. Proceedings available only on CD.
- [ACP02a] V. Alberga, M. Chandra, and K. P. Papathanassiou. “An analysis of volume decorrelation in polarimetric SAR interferometry”. In *Proceedings of EUSAR 2002*, pages 613–616, Cologne, Germany, 4 - 6 June 2002.
- [ACP02b] V. Alberga, M. Chandra, and L. Pipia. “Supervised classification of coherent and incoherent polarimetric SAR observables: comparison and accuracy assessments”. In *Proceedings of SPIE - SAR Image Analysis, Modeling, and Techniques V*, volume 4883, pages 181–191, Agia Pelagia, Crete, Greece, 23 - 24 September 2002.
- [Alb98] V. Alberga. “Utilizzo di dati SAR per lo studio di aree a rischio ambientale” (in Italian). Master’s thesis, University of Bari, Italy, July 1998.

- [BEACM81] W-M. Boerner, M. B. El-Arini, C-Y. Chan, and P. M. Mastoris. "Polarization dependence in electromagnetic inverse problems". *IEEE Transactions on Antennas and Propagation*, vol. AP-29 (2): pages 262–271, March 1981.
- [BH98] R. Bamler and P. Hartl. "Synthetic aperture radar interferometry". *Inverse Problems*, vol. 14: pages R1–R54, 1998.
- [BSA⁺99] P. Blonda, G. Satalino, V. Alberga, J. Wasowski, M. Parise, M-T. Chiaradia, R. Viggiano, and M. Pappalepore. "Soft computing techniques for data classification in a landslide-prone area of Italy". In *Proceedings of IGARSS '99*, pages 1600–1602, Hamburg, Germany, 28 June - 2 July 1999.
- [BW85] M. Born and E. Wolf. "*Principles of optics*". Pergamon Press, New York, USA, sixth edition, 1985.
- [BYXY91] W-M. Boerner, W-L. Yan, A-Q. Xi, and Y. Yamaguchi. "On the basic principles of radar polarimetry: the target characteristic polarization state theory of Kennaugh, Huynen's polarization fork concept and its extension to the partially polarized case". *Proceedings of the IEEE*, vol. 79 (10): pages 1538–1550, October 1991.
- [CFLSS99] S. R. Cloude, J. Fortuny, J. M. Lopez-Sanchez, and A. J. Sieber. "Wide-band polarimetric radar inversion studies for vegetation layers". *IEEE Transactions on Geoscience and Remote Sensing*, vol. 37 (5): pages 2430–2441, September 1999.
- [CL90] W. L. Cameron and L. K. Leung. "Feature motivated polarization scattering matrix decomposition". In *Proceedings of the IEEE International Radar Conference*, pages 549–557, Arlington, Virginia, USA, 7 - 10 May 1990.
- [CL92] W. L. Cameron and L. K. Leung. "Identification of elemental polarimetric scatterer responses in high-resolution ISAR and SAR signature measurements". In *Proceedings of JIPR '92*, pages 196–212, Nantes, France, 8 - 10 September 1992.
- [Clo83] S. R. Cloude. "Polarimetric techniques in radar signal processing". *Microwave Journal*, vol. 26 (7): pages 119–127, July 1983.
- [Clo86] S. R. Cloude. "Group theory and polarization algebra". *Optik*, vol. 75 (1): pages 26–36, December 1986.
- [Clo92] S. R. Cloude. "Uniqueness of target decomposition theorems in radar polarimetry", pages 267–296. In *NATO-ASI C [eae92]*, 1992. Proceedings of the NATO-ARW, Bad Windsheim, West Germany, 18 - 24 September 1988.
- [CM91] J. C. Curlander and R. N. McDonough. "*Synthetic aperture radar - Systems and signal processing*". John Wiley & Sons, New York, USA, 1991.
- [Con91] R. G. Congalton. "A review of assessing the accuracy of classification of remotely sensed data". *Remote Sensing of Environment*, vol. 37: pages 35–46, 1991.

- [Cop60] J. R. Copeland. "Radar target classification by polarization properties". *Proceedings of the IRE*, vol. 48 (7): pages 1290–1296, 1960.
- [CP96] S. R. Cloude and E. Pottier. "A review of target decomposition theorems in radar polarimetry". *IEEE Transactions on Geoscience and Remote Sensing*, vol. 34 (2): pages 498–518, March 1996.
- [CP97] S. R. Cloude and E. Pottier. "An entropy based classification scheme for land application of polarimetric SAR". *IEEE Transactions on Geoscience and Remote Sensing*, vol. 35 (1): pages 68–78, January 1997.
- [CP98] S. R. Cloude and K. P. Papathanassiou. "Polarimetric SAR interferometry". *IEEE Transactions on Geoscience and Remote Sensing*, vol. 36 (5): pages 1551–1565, September 1998.
- [CYL96] W. L. Cameron, N. N. Youssef, and L. K. Leung. "Simulated polarimetric signatures of primitive geometrical shapes". *IEEE Transactions on Geoscience and Remote Sensing*, vol. 34 (3): pages 793–803, May 1996.
- [Des51] G. A. Deschamps. "Geometrical representation of the polarization plane electromagnetic wave". *Proceedings of the IRE*, vol. 39 (5): pages 540–544, 1951.
- [DvZE95] P. C. Dubois, J. J. van Zyl, and T. Engman. "Measuring soil moisture with imaging radar". *IEEE Transactions on Geoscience and Remote Sensing*, vol. 33 (4): pages 915–926, July 1995.
- [eae85] W-M. Boerner et al. (eds.). "*Inverse methods in electromagnetic imaging*". NATO-ASI C. D. Reidel Publishing Company, Dordrecht, the Netherlands, 1985. Proceedings of the NATO-ARW, Bad Windsheim, West Germany, 18 - 24 September 1983.
- [eae92] W-M. Boerner et al. (eds.). "*Direct and inverse methods in radar polarimetry*". NATO-ASI C. Kluwer Academic Publishers, Dordrecht, the Netherlands, 1992. Proceedings of the NATO-ARW, Bad Windsheim, West Germany, 18 - 24 September 1988.
- [EFvZZ88] D. L. Evans, T. G. Farr, J. J. van Zyl, and H. A. Zebker. "Radar polarimetry: analysis tools and applications". *IEEE Transactions on Geoscience and Remote Sensing*, vol. 26 (6): pages 774–789, November 1988.
- [Fey96] R. P. Feynman. "*Six easy pieces*". Perseus Publishing, Cambridge, Massachusetts, USA, 1996.
- [FMYS97] A. C. Frery, H-J. Mueller, C. C. F. Yanasse, and S. J. S. Sant'Anna. "A model for extremely heterogeneous clutter". *IEEE Transactions on Geoscience and Remote Sensing*, vol. 35 (3): pages 648–659, May 1997.
- [Fre92] A. Freeman. "SAR calibration: an overview". *IEEE Transactions on Geoscience and Remote Sensing*, vol. 30 (6): pages 1107–1121, November 1992.

- [GGP⁺94] F. Gatelli, A. Monti Guarnieri, F. Parizzi, P. Pasquali, C. Prati, and F. Rocca. "The wavenumber shift in SAR interferometry". *IEEE Transactions on Geoscience and Remote Sensing*, vol. 32 (4): pages 855–864, July 1994.
- [Giu86] D. Giuli. "Polarization diversity in radars". *Proceedings of the IEEE*, vol. 74 (2): pages 245–269, February 1986.
- [Gra56] C. D. Graves. "Radar polarization power scattering matrix". *Proceedings of the IRE*, vol. 44 (5): pages 248–252, 1956.
- [Haj01] I. Hajnsek. "Inversion of surface parameters using polarimetric SAR". PhD thesis, Friedrich Schiller University, Jena, Germany, October 2001.
- [Hel00] M. Hellmann. "Classification of fully polarimetric SAR-data for cartographic applications". PhD thesis, Technical University of Dresden, Germany, April 2000.
- [HJ85] R. A. Horn and C. R. Johnson. "Matrix analysis". Cambridge University Press, New York, USA, 1985.
- [Hol84] A. R. Holt. "Some factors affecting the remote sensing of rain by polarization diversity radar in the 3- to 35-GHz frequency range". *Radio Science*, vol. 19 (5): pages 1399–1412, September-October 1984.
- [HUA95] J. O. Hagberg, L. M. H. Ulander, and J. Askne. "Repeat-pass SAR interferometry over forested terrain". *IEEE Transactions on Geoscience and Remote Sensing*, vol. 33 (2): pages 331–340, March 1995.
- [Hub94] J. H. Hubbert. "A comparison of radar, optic and specular null polarization theories". *IEEE Transactions on Geoscience and Remote Sensing*, vol. 32 (3): pages 658–671, May 1994.
- [Huy70] J. R. Huynen. "Phenomenological theory of radar targets". PhD thesis, Technical University of Delft, the Netherlands, December 1970.
- [IC01] M. Isola and S. R. Cloude. "Forest height mapping using space-borne polarimetric SAR interferometry". In *Proceedings of IGARSS 2001*, pages 1095–1097, Sydney, Australia, 9 - 13 July 2001.
- [IEE83] "IEEE standard definitions of terms for antennas". *IEEE Transactions on Antennas and Propagation*, vol. AP-31 (6): pages 1–26, 1983.
- [Jac75] J. D. Jackson. "Classical electrodynamics". John Wiley & Sons, New York, USA, 1975.
- [KB86] A. B. Kostinski and W-M. Boerner. "On foundations of radar polarimetry". *IEEE Transactions on Antennas and Propagation*, vol. AP-34 (12): pages 1395–1404, December 1986.
- [KC95] E. Krogager and Z. H. Czyż. "Properties of the sphere, diplane, helix decomposition". In *Proceedings of JIPR '95*, pages 106–114, Nantes, France, 21 - 23 March 1995.

- [Ken52] E. M. Kennaugh. "Polarization properties of radar reflections". Master's thesis, The Ohio State University, Columbus, Ohio, USA, March 1952.
- [Ken54] E. M. Kennaugh. "Effects of the type of polarization on echo characteristics". Technical Report 381-1 to 394-24, Antenna Laboratory, The Ohio State University Research Foundation, Columbus, Ohio, USA, 1949-1954.
- [Kon86] J. A. Kong. *"Electromagnetic wave theory"*. John Wiley & Sons, New York, USA, 1986.
- [Kro92] E. Krogager. *"Decomposition of the Sinclair matrix into fundamental components with applications to high resolution radar target imaging"*, pages 1459–1478. In *NATO-ASI C [eae92]*, 1992. Proceedings of the NATO-ARW, Bad Windsheim, West Germany, 18 - 24 September 1988.
- [Kro93] E. Krogager. *"Aspects of polarimetric radar imaging"*. PhD thesis, Technical University of Denmark, Electromagnetics Institute, Lyngby, Denmark, March 1993.
- [Mot92] H. Mott. *"Antennas for radar and communications: a polarimetric approach"*. John Wiley & Sons, New York, USA, 1992.
- [PAC⁺02] L. Pipia, V. Alberga, M. Chandra, M. Migliaccio, and K. Ben Khadhra. "Quantitative assessment of the efficiency of supervised classification using coherent and incoherent polarimetric SAR observables". In *Proceedings of EUSAR 2002*, pages 729–732, Cologne, Germany, 4 - 6 June 2002.
- [Pap65] A. Papoulis. *"Probability, random variables and stochastic processes"*. McGraw-Hill Book Company, New York, USA, 1965.
- [Pap99] K. P. Papathanassiou. *"Polarimetric SAR interferometry"*. PhD thesis, Technical University of Graz, Austria, January 1999.
- [PC01] K. P. Papathanassiou and S. R. Cloude. "Single-baseline polarimetric SAR interferometry". *IEEE Transactions on Geoscience and Remote Sensing*, vol. 39 (11): pages 2352–2363, November 2001.
- [PRC99a] K. P. Papathanassiou, A. Reigber, and S. R. Cloude. "Vegetation and ground parameter estimation using polarimetric interferometry - Part I: The role of polarisation". In *Proceedings of ESA CEOS SAR Workshop*, Toulouse, France, 26 - 29 October 1999. Paper available at: <http://www.estec.esa.nl/conferences/99b02/index.html>.
- [PRC99b] K. P. Papathanassiou, A. Reigber, and S. R. Cloude. "Vegetation and ground parameter estimation using polarimetric interferometry - Part II: Parameter inversion and optimal polarisations". In *Proceedings of ESA CEOS SAR Workshop*, Toulouse, France, 26 - 29 October 1999. Paper available at: <http://www.estec.esa.nl/conferences/99b02/index.html>.

- [PRGP94] C. Prati, F. Rocca, A. Monti Guarnieri, and P. Pasquali. "ERS-1 SAR interferometric techniques and applications". Technical Report ESA N.: 10179/93/YT/I/SC, Dept. of Electronics - Polytechnic of Milano, Italy, June 1994.
- [Qua98] M. Quartulli. "Teoria e applicazioni dell'interferometria SAR differenziale" (in Italian). Master's thesis, University of Bari, Italy, October 1998.
- [Rei01] A. Reigber. "Airborne polarimetric SAR tomography". PhD thesis, University of Stuttgart, Germany, October 2001.
- [Ric94] J. A. Richards. "Remote sensing digital image analysis". Springer-Verlag, Berlin, Germany, 1994.
- [RM92] E. Rodriguez and J. M. Martin. "Theory and design of interferometric synthetic aperture radars". *IEE Proceedings-F*, vol. 139 (2): pages 147–159, April 1992.
- [RM00] A. Reigber and A. Moreira. "First demonstration of airborne SAR tomography using multibaseline L-band data". *IEEE Transactions on Geoscience and Remote Sensing*, vol. 38 (5): pages 2142–2152, September 2000.
- [ROvZJ93] E. J. Rignot, S. J. Ostro, J. J. van Zyl, and K. C. Jezek. "Unusual radar echoes from the Greenland ice sheet". *Science*, vol. 261: pages 1710–1713, September 1993.
- [SAC⁺00] P. Spencer, V. Alberga, M. Chandra, D. Hounam, and W. Keydel. "SAR polarimetric parameters for land use classification". In *Proceedings of EU-SAR 2000*, pages 783–785, Munich, Germany, 23 - 25 May 2000.
- [Sag00] L. Sagués. "Surface and volumetric scattering analysis of terrains for polarimetric and interferometric SAR applications". PhD thesis, Polytechnic University of Catalonia, Dept. of Signal Theory and Communications, Barcelona, Spain, September 2000.
- [Sar92] K. Sarabandi. "Derivation of phase statistics from the Mueller matrix". *Radio Science*, vol. 27 (5): pages 553–560, September-October 1992.
- [SBAK79] T. A. Seliga, V. N. Bringi, and H. H. Al-Khatib. "Differential reflectivity measurements in rain: first experiments". *IEEE Transactions on Geoscience and Electronics*, vol. GE-17 (4): pages 240–244, October 1979.
- [SCM88] A. C. Schroth, M. S. Chandra, and P. F. Meischner. "A C-band coherent polarimetric radar for propagation and cloud physics research". *Journal of Atmospheric and Oceanic Technology*, vol. 5 (6): pages 803–822, December 1988.
- [Sin50] G. Sinclair. "The transmission and reception of elliptically polarized waves". *Proceedings of the IRE*, vol. 38 (2): pages 148–151, 1950.

- [Ste97] S. V. Stehman. "Selecting and interpreting measures of thematic classification accuracy". *Remote Sensing of Environment*, vol. 62: pages 77–89, 1997.
- [Str41] J. A. Stratton. *"Electromagnetic theory"*. McGraw-Hill Book Company, New York, USA, 1941.
- [TG74] J. T. Tou and R. C. Gonzalez. *"Pattern recognition principles"*. Addison-Wesley Publishing Company, Reading, Massachusetts, USA, 1974.
- [TMMvZ96] R. N. Treuhaft, S. N. Madsen, M. Moghaddam, and J. J. van Zyl. "Vegetation characteristics and underlying topography from interferometric radar". *Radio Science*, vol. 31 (6): pages 1449–1485, November-December 1996.
- [TS00] R. N. Treuhaft and P. R. Siqueira. "Vertical structure of vegetated land surfaces from interferometric and polarimetric radar". *Radio Science*, vol. 35 (1): pages 141–177, January-February 2000.
- [UHD⁺87] F. T. Ulaby, D. Held, M. C. Dobson, K. C. McDonald, and T. B. A. Senior. "Relating polarization phase difference of SAR signals to scene properties". *IEEE Transactions on Geoscience and Remote Sensing*, vol. GE-25 (1): pages 83–92, January 1987.
- [UMF82] F. T. Ulaby, R. K. Moore, and A. K. Fung. *"Microwave remote sensing - Volume II: Radar remote sensing and surface scattering and emission theory"*. Addison-Wesley Publishing Company, Reading, Massachusetts, USA, 1982.
- [vdH81] H. C. van de Hulst. *"Light scattering by small particles"*. Dover Publications, New York, USA, 1981.
- [vZ89] J. J. van Zyl. "Unsupervised classification of scattering behavior using radar polarimetry data". *IEEE Transactions on Geoscience and Remote Sensing*, vol. 27 (1): pages 36–45, January 1989.
- [vZ90] J. J. van Zyl. "Calibration of polarimetric radar images using only image parameters and trihedral corner reflector responses". *IEEE Transactions on Geoscience and Remote Sensing*, vol. 28 (3): pages 337–348, May 1990.
- [vZZ90] J. J. van Zyl and H. A. Zebker. "Imaging radar polarimetry". In J. A. Kong, editor, *Polarimetric remote sensing*, volume 3 of *PIER*, pages 277–326. Elsevier, New York, USA, 1990.
- [vZZE87] J. J. van Zyl, H. A. Zebker, and C. Elachi. "Imaging radar polarization signatures: theory and observation". *Radio Science*, vol. 22 (4): pages 529–543, July-August 1987.
- [ZV92] H. A. Zebker and J. Villasenor. "Decorrelation in interferometric radar echoes". *IEEE Transactions on Geoscience and Remote Sensing*, vol. 30 (5): pages 950–959, September 1992.

- [ZvZ91] H. A. Zebker and J. J. van Zyl. "Imaging radar polarimetry: a review". *Proceedings of the IEEE*, vol. 79 (11): pages 1583–1606, November 1991.
- [ZvZH87] H. A. Zebker, J. J. van Zyl, and D. N. Held. "Imaging radar polarimetry from wave synthesis". *Journal of Geophysical Research*, vol. 92 (B1): pages 683–701, January 1987.

Short résumé of Vito Alberga

PERSONAL DATA

DATE OF BIRTH	November, 2 nd 1970
CITIZENSHIP	Italian
OFFICE ADDRESS	German Aerospace Centre (DLR) - Microwaves and Radar Institute, P.O. Box 1116, D-82234 Wessling, Germany
E-MAIL	Vito.Alberga@DLR.de

EDUCATION

1998	Master's Degree in Physics (Laurea in Fisica): "The Use of SAR Data for Environmental-Risk Areas Monitoring". University of Bari, Italy
1998	Final Master's Research Work at the Institute of Intelligent Systems for Automation (ISSIA) of the National Research Council (CNR), Bari, Italy
1989	High School Leaving Certificate (Diploma di Maturità Scientifica), Bari, Italy

CONTINUING EDUCATION

2002	CCG Seminar "SAR Principles and Applications"; DLR, Oberpfaffenhofen, Germany
2001	Training Workshop "SAR Polarimetry and Polarimetric Interferometry"; University of Rennes, France
2000	Training Workshop "Polarimetric Radar Remote Sensing: Basic Concepts, Theory, Systems and Applications"; DLR, Oberpfaffenhofen, Germany
2000	Training Workshop "On the Foundations of Polarimetry and Basic Principles of Polarimetric Radar-Observations and Analysis"; JRC, Ispra (VA), Italy
1999	"IDL Intensive Course"; CREASO GmbH, Gilching bei München, Germany
1998	"Seminar on ERS SAR and Other Complementary Spaceborne Sensors for Land Use and Land Cover Applications"; ESA/ESRIN, Frascati (Roma), Italy
1998	CNR/ISIATA Summer School "Instrumental Techniques in Environmental Atmospheric Physics"; Castro Marina (LE), Italy

WORKING EXPERIENCE

2002 TO DATE	Performance Engineer for the project TerraSAR-X at the Microwaves and Radar Institute (HR) of the German Aerospace Centre; Oberpfaffenhofen, Germany
2002	Collaboration with Definiens-Imaging for the implementation of algorithms for the analysis of polarimetric SAR data into the Ecognition software
1999 - 2002	EU Fellow at DLR/HR. Research activity: studies on polarimetry and polarimetric SAR interferometry. Teaching activity: tutoring of students at Master's Degree level
PAST EXPERIENCES	Summer jobs abroad, private lessons of mathematics.